Thesis for the degree of Doctor of Philosophy

Molecular observations at high and low redshifts with the Odin satellite

CARINA M. PERSSON

Department of Radio and Space Science
CHALMERS UNIVERSITY OF TECHNOLOGY
Göteborg, Sweden 2008

Molecular observations at high and low redshifts with the Odin satellite

CARINA M. PERSSON
ISBN 978-91-7385-227-2

Doktorsavhandlingar vid Chalmers tekniska högskola
Ny serie Nr 2908
ISSN 0346-718X

Department of Radio and Space Science
Chalmers University of Technology
SE–412 96 Göteborg
Sweden
Phone: +46 (0)31–772 1000

Contact information:
Carina M. Persson
Onsala Space Observatory
Chalmers University of Technology
SE–439 92 Onsala, Sweden

Phone: +46 (0)31–772 5537
Fax: +46 (0)31–772 5590
Email: carina.persson@chalmers.se

Front cover: An illustration of the Odin satellite, part of its spectral scan towards the Orion KL region together with a comparison of $H_2^{18}O$ and SO, and water and ammonia towards the molecular cloud S140.
Back cover: A picture of the author taken during a summer school at La Palma, 2006. Photographer is Tine Bjørn.

Printed by Chalmers Reproservice
Chalmers University of Technology
Göteborg, Sweden 2008

This thesis is dedicated to my family
and especially my children

Andreas
Anna
Maria &
Rebecca

Molecular observations at high and low redshifts with the Odin satellite

CARINA M. PERSSON
Department of Radio and Space Science
Chalmers University of Technology

Abstract

The papers in this thesis have the aim of expanding our knowledge of different processes related to star formation in the early Universe and at present times. A complex chemistry occurs in star forming clouds and by observing molecules, information about the necessary physical and chemical conditions for star formation can be obtained. Our main focus is to observe the important water molecule using the Odin satellite since the strongest transition at 557 GHz is not observable using ground-based telescopes.

The first two papers describe a spectral line survey in a previous unobserved spectral range towards the well-known Orion KL star forming nebula, covering a 42 GHz wide frequency band. We found 280 spectral lines from 38 species, and additionally 64 lines which remain unidentified. Water is very abundant in the powerful molecular outflows, while less abundant in the extended quiescent gas cloud. In addition to H_2O, we observed $H_2^{18}O$ and, for the first time in the interstellar medium, also $H_2^{17}O$. Remarkable similarities are found between the outflow emission observed from the water isotopologues and those of SO_2 and SO.

The third paper covers observations towards the star forming region within the molecular cloud S140. Here we focused the observations on three species: H_2O, NH_3, and CO including the isotopologues ^{13}CO and $H_2^{18}O$. The observations were performed at five positions to reveal emission changes moving across the star forming center towards the edge of the cloud. The water abundance is found to be about 100 – 1 000 times lower in the outflows as compared to Orion KL, but is similar in the extended cloud. The emissions of water and ammonia in the extended cloud show a striking similarity.

Paper IV describes our searches for weak signals emitted from molecules before the first stars were born during the cosmic Dark Ages. Star formation during this epoch differs substantially from star formation at present times, due to the extremely low molecular abundances. No observational evidence exists today from this epoch, and the search is extremely difficult. A detection would, however, be of utmost importance and would for the first time give direct evidence about the beginning of structure and star formation in the Universe.

Keywords: ISM: abundances – ISM: molecules – ISM: individual (Orion KL) – ISM: individual (S140) – Radio lines: ISM – Submillimeter – Line: profiles – Line: formation – Cosmology: early Universe – Cosmology: observations

LIST OF PUBLICATIONS

This thesis is based on the work contained in the following papers, referred to by Roman numerals in the text:

I *A spectral line survey of Orion KL in the bands 486 – 492 and 541 – 577 GHz with the Odin satellite*
I. The observational data
A.O. Henrik Olofsson, Carina M. Persson, N. Koning, P. Bergman, P.F. Bernath, J.H. Black, U. Frisk, W. Geppert, T.I. Hasegawa, Å. Hjalmarson, S. Kwok, B. Larsson, A. Lecacheux, A. Nummelin, M. Olberg, Aa. Sandqvist, and E.S. Wirström
Astronomy & Astrophysics, 476, 791 (2007)

II *A spectral line survey of Orion KL in the bands 486 – 492 and 541 – 577 GHz with the Odin satellite*
II. Data analysis
Carina M. Persson, A.O.H. Olofsson, N. Koning, P. Bergman, P.F. Bernath, J.H. Black, U. Frisk, W. Geppert, T.I. Hasegawa, Å. Hjalmarson, S. Kwok, B. Larsson, A. Lecacheux, A. Nummelin, M. Olberg, Aa. Sandqvist, and E.S. Wirström
Astronomy & Astrophysics, 476, 807 (2007)

III *Water and ammonia abundances in S140 with the Odin satellite*
Carina M. Persson, M. Olberg, Å. Hjalmarson, M. Spaans, J.H. Black, U. Frisk,T. Liljeström, A.O.H. Olofsson, D.R. Poelman, and Aa. Sandqvist
Astronomy & Astrophysics, in press (2008)

IV *The first spectral line surveys searching for signals from the Dark Ages*
Carina M. Persson, R. Maoli, P. Encrenaz, Å. Hjalmarson, M. Olberg, G. Rydbeck, M. Signore, U. Frisk, Aa. Sandqvist, and Jean-Yves Daniel
Intended for Astronomy & Astrophysics (2009)

I have also participated in the following papers not included in the thesis:

Observational constraints on the formation of interstellar methanol
E.S Wirström, Carina M. Persson, Å. Hjalmarson, J.H. Black, P. Bergman, W. Geppert, M. Hamberg, E. Vigren
IAU Symposium 251: Organic Matter in Space, Hong Kong (2008)

From molecular oxygen to primordial molecules with the Odin satellite
C.M. Persson, P.J. Encrenaz, Å. Hjalmarson, Aa. Sandqvist, and the Odin team
Frontiers of Astrophysics: A Celebration of NRAO's 50th Anniversary
Astronomical Society of the Pacific Conference Series, Vol. 395 (2008)
Eds. Bridle, A.H., Condon, J.J., and Hunt, G.C.

On the progress in Odin's hunt for molecules
On behalf of the Odin team: Å. Hjalmarson, M. Olberg, H.-G. Florén, U. Frisk, S. Lundin, A.O.H. Olofsson, C.M. Persson, G. Persson, Aa. Sandqvist
AdSpR, 40, 630 (2007)

Upper limits to the water abundance in starburst galaxies
C.D. Wilson, R.S. Booth, A.O.H. Olofsson, M. Olberg, C.M. Persson, Aa. Sandqist, Å. Hjalmarson, V., Buat, P.J. Encrenaz, M. Fich, U. Frisk, M. Gerin, G. Rydbeck, and T. Wiklind
Astronomy & Astrophysics, 469, 121 (2007)

Odin CO and ^{13}CO $J=5-4$ mapping of Orion KL – a step towards accurate water abundances
E.S. Wirström, P. Bergman, A.O.H. Olofsson, U. Frisk, Å. Hjalmarson, M. Olberg, C.M. Persson, and Aa. Sandqvist
Astronomy & Astrophysics, 453, 979 (2006)

DEMON: a Proposal for a Satellite-Borne Experiment to study Dark Matter and Dark Energy
A. Berciano Alba, P. Borges de Silva, H. Eichelberger, F. Giovacchini, M. Godolt, G. Hasinger, M. Lerchster, V. Lusset, F. Mattana, Y. Mellier, M. Michalowski, C. Monteserin-Sanches, F. Noviello, C.M. Persson, A. Santovincenzo, P. Schneider, M. Zhang, and L. Östman
SPIE conference proceedings Vol. 6266, p. 91 (2006)
Space Telescopes and Instrumentation II: Ultraviolet to Gamma Ray (AS02)
Eds. M.J.L. Turner and G. Hasinger

Acknowledgements

I owe this thesis to many people. First, I am greatly indebted to my supervisors Michael Olberg and Åke Hjalmarson. I certainly would not have managed without you and I have really enjoyed our discussions and work during these five years. Being a supervisor is a kind of parenting and I hope that I have not given you too much headache and worries. And thanks a lot for giving me the chance to pursue a carrier in astrophysics which always has been my wish.

At our observatory there are so many helpful and friendly people: John Black always has an answer when I am confused about molecules and the interstellar medium, Gustaf Rydbeck has been an invaluable help about all cosmology issues and very helpful, thanks Gustaf, and Per Bergman has always been very supportive and has a great knowledge about radiative processes and observation techniques. Our Odin team would not have been complete without Henrik Olofsson. I miss our work and discussions and I look forward to work with you again. And without Margareta, Ingrid, Vivi, Eva N, Monica, Eva A, Paula (thanks for helping us move twice), Lars E, and Roger nothing would work at the observatory. I believe Roger can take care of just about anything. And neither Vårruset, parties, or coffee breaks would have been so much fun without all of you, or Cathy, Magnus, René, Kay, Susanne, Michael L, Gunnar, Glenn, Alessandro, John C, and all the staff members at the observatory. You have all created a friendly and stimulating environment. My fellow PhD students have also shown to be real good friends and support these years and I particularly want to mention my friend Eva for all our fun travels and discussions, and also Daniel and Per Bjerkeli (thanks for the proof-reading) for being such nice persons. And my recent work with the new astronomy exhibition together with Christer and Lasse has also proven to be a source of much fun. Thank you both for your work and friendly attitude. I also would like to thank the head of our observatory Hans Olofsson for giving me future work, and our former chief Roy Booth who I am indebted to for opening the door for a carrier in science for me. Thanks Roy.

Many thanks also to the Odin team member Pierre Encrenaz from Observatoire de Paris and our PriMol Onsala/Paris/Rome team which also include Monique Signore and Roberto Maoli. And thanks Pierre and Åke for your positive attitude and open minds which allow you to discover new territories in science. Many thanks also to the whole Odin team. Our meetings and workshops have always been a priority in my calendar. I have also enjoyed a lot to work with Marco Spaans, Groningen, a wonder of efficiency.

I am grateful to my former classmates Anna, Anders, Lars, and Daniel, my friends in the Löhf family in Storvreta, and my teachers at Uppsala University for all the support and encouragement you gave me. Especially the whole Astronomy department and the Galaxy group including Nils Bergvall, Erik Zackrisson, and Kjell Olofsson (now it is my turn to stay up all night writing on my thesis until the very last minute). Thanks also to Leif Karlsson at the Physics department in Uppsala and Johannes Ortner, director of the Alpbach Summer School in Austria who both always have been very supportive and friendly. Thanks to all of you for believing in me.

But without my family nothing would have been possible. My children – Andreas, Anna, Maria, and Rebecca have always, always been the joy of my life. Thank you for filling my life with love. And without my parents Arne and Stina, or brother and sister, Stefan and Eva, and her daughter Åsa, or my aunt Anita and her boyfriend Eddie, I certainly would not have survived my undergraduate studies at Uppsala, being a single parent with four children. Thanks a lot for all the times you took care of them when I had to go to exams, study or travel. (I guess I will pay for this within a few years when my children will leave their future children with me.) And thanks also to our new family members Håkan and Viviana for completing our family. Three years ago I was still not completely happy, but this changed fundamentally when I met Kaj and his daughter Felicia. Thank you so much for loving me. I could not have made this without you.

I am grateful to the Swedish National Space Board (SNSB) for support of this PhD project.

Carina
Onsala, December 2008

Contents

Preface

"If I had been present at the creation,
I would have recommended a simpler design for the Universe."

The Spanish monarch Alphonso X *(1221 – 1284) complained about the tedious work and difficult calculations required to revise the tables of planetary motions.*

One look at the stars a dark and clear night a long time ago and I was lost in the magic of the Universe. The infinity and the silence is the cradle for questions. What is really out there? What is our true place in the Universe? How did it all begin and will it have an end? What made our existence possible and does life on other planets exist? The more I learn, the more questions come into my mind. And I believe that this is the heart of science – to ask the right questions. When the Greek philosopher Thales 2 600 years ago asked the question "What is the Universe made of?" without resorting to supernatural explanations, the question became very powerful. Even though his answer was not correct; the Earth is a flat disk on an infinite ocean and the Universe basically consists of water; the *question* continued its own life. Even though some of our answers might be wrong or incomplete, the questions continue to drive our imagination and research. And the base of all our progress and efforts in history is the conviction that the Universe is inherently understandable and can be explained by simple physical laws which *apply throughout the Universe*. Today, we still do not know the complete answer to Thales' question about the Universe. The present dominating theory is, that in addition to the well-known normal matter, 24% of the Universe consists of an unknown form of dark matter. The remaining 72% of the Universe is composed of an even more mysterious ingredient referred to as dark energy.

The Greek community was the first known one that tried the scientific method. They were allowed to think creatively and most importantly: all new ideas were open to challenge. It was also during this time that mathematics, the language of science, started its first development. The Greeks also believed that ideas must be consistent with observations and be as simple as possible. Science is, however, performed by human beings who all have their own personal beliefs and biases. This may influence the way they perform the experiments or what questions they ask. But even if this sometimes may lead science in the wrong direction, eventually

other scientists will uncover the mistakes. Or if a new seemingly crazy idea is not accepted, if the idea is correct it will survive and eventually come up again. Around 260 B.C. the Greek scientist Aristarchos suggested a Sun-centered system, but he was not able to convince his contemporaries of his theory. After 1 800 years Nicholaus Copernicus developed the idea further, but still it did not fit the observations better than the old Earth-centered model since he believed that the planets moved in perfect circles. The lack of high-quality observations did not allow a verification of the planetary orbits. However, the theory provided a much *simpler* explanation of the apparent motion of planets, which was very appealing.

The required high-quality observations were finally performed by the Danish astronomer Tycho Brahe (1546 – 1601), which in 1610 enabled Johannes Kepler (1571 – 1630) to derive his famous laws about planetary motions still taught in class-rooms today. Kepler trusted Brahes' observations which forced him to abandon ancient ideas of perfect circular orbits in favour of elliptical orbits. This event marked another transition: models must fit the observations and even small deviations can lead to new discoveries.

Galileo Galilei (1564 – 1642) was a physicist who also was not satisfied with just trusting ancient beliefs without proof. Instead he performed experiments that later helped Isaac Newton (1643 – 1727) to formulate the laws of motion and gravity. This again demanded more insight of physics and further developed mathematics. Newton showed that Kepler's laws are natural consequences of the laws of motion and gravity, and explained *why* the planets moved in elliptical orbits. This is a good example of a scientific model that both explains and makes accurate and verifiable predictions about natural phenomena.

The year of 2009 is the International Year of Astronomy and marks the event 400 years ago when Galileo Galilei for the first time used a telescope, invented in 1608 by the German-Dutch lens maker Hans Lippershey, to discover the Universe. For the first time ever, the four moons orbiting the planet Jupiter, the sunspots on our Sun, craters on the surface of our Moon, and the phases of the planet Venus were seen. This was the absolute death blow for the Earth-centered view that had been believed in since ancient times. Galileo showed that the wandering lights on the sky were in fact real planets, new worlds other than our own, and that we indeed did not live at the center of the Universe. It took another 360 years until mankind actually *walked* on another world, our Moon, on July 20, 1969, and thus we celebrate the 40th anniversary of this event in 2009.

My hope is that the quest for knowledge is what characterises mankind. Those of us who are lucky enough to be able to study and practice science are led to wonder about the Universe and our place in it, even when each step towards new knowledge is bound up in tedious details.

Chapter 1

Setting the scene

On the Origin of Species by Means of Natural Selection was published by Charles Darwin in 1859 and provided an explanation of the evolution of life on Earth. But this is not the true beginning of the story. The true beginning lies in space with the creation of stars, planets and galaxies in the gas originating from the Big Bang.

Not so long ago it was believed that stars are eternal. But in the beginning of the 20th century, disturbing evidence began to show that the Universe is not static at all, but is constantly evolving much like living organisms. This includes the birth, life and death of stars.

Our galaxy, the Milky Way, consists of hundreds of billions of stars, and in between them there is an important component of gas and dust particles called the *Interstellar Medium* (ISM). Of all visible matter in our Galaxy approximately one sixth is composed of interstellar gas and dust. There are a number of good reasons to study the ISM. First, it all starts here. Deep within cold molecular clouds stars and planets are born. Without a good knowledge about the birth, life and death of stars, it is very difficult to learn anything about the rest of the Universe, including the origin of life and our own existence. Therefore, we need to know more about the formation of stars and their subsequent evolution which implies a study of the ISM.

Some 60 years ago the ISM was poorly known and star formation was still a big mystery. How is it possible for such huge objects as stars to form? The most natural explanation is gravity. But at the time it was a common belief that the density of atoms in the ISM was too low for molecules to form. The density of the interstellar medium was thought to be billions of billions less than the air we breathe. In such tenuous gas it would not be possible for gravity to form a star.

Since stars are born deep within dark clouds, opaque to visible light, and in addition so far away that we cannot resolve the stars, astronomers had to find clever ways to find some answers. A powerful tool is the nature of light. In the 19th and 20th centuries the interaction between electromagnetic radiation and matter became evident by a number of experiments. Molecules and atoms

radiate at precise wavelengths which form a unique fingerprint for each species. And though it had been believed to be impossible for molecules to exist at all in the ISM, the first detections of diatomic molecules were performed in the 1930s when absorption lines of the cyanide radical (CN), methylidyne (CH), and ionised methylidyne (CH^+) were found in the optical wavelength regime. But, still there was no evidence of larger molecules showing the existence of the even denser clouds needed for star formation, even though there were some indirect observations.

The most common radiation at short wavelengths in the optical and infrared regimes is from atoms, whereas molecules mostly radiate from cold molecular clouds at decimetre to millimetre wavelengths in the radio regime. This complicates observations since ordinary optical devices cannot be used for such long wavelengths. In addition, the extremely weak signals also demand very sensitive receivers. Hence, detections of larger molecules had to await the dawn of radio-astronomy starting in the 1950s. In 1963, the rapid development of radio detectors enabled the first detection of the OH molecule, which marks the beginning of molecular line radio astronomy. And finally, in 1968 and 1969, ammonia (NH_3) and water (H_2O) were discovered in the interstellar medium. This showed for the first time the existence of *dense* clouds, even though very thin compared to Earth standards.[1]

Any theory explaining star formation must also consider the temperature in addition to density. Any increase in temperature will counteract gravity, creating an outward pressure which will stop the collapse. If you have ever used a bicycle pump you know that it gets warmer when the air is compressed. This is a good example of thermodynamics and applies to bicycle pumps as well as the huge gas clouds in the ISM which can be as big as several light-years across. When a gas cloud contracts and the size decreases the temperature will increase, regardless of size. Thus the collapse will halt unless the cloud can somehow lose energy. This can be performed with the help of molecules.

When the temperature increases in a contracting gas cloud the molecules radiate away the increasing kinetic energy thereby keeping the temperature constant, which in turn allows further collapse. Molecular hydrogen (H_2), the most abundant molecule of them all, is able to cool the cloud to about 200° C. Star formation, however, requires several hundred degrees lower temperatures. Carbon-monoxide (CO), discovered in the 70s, is a well-studied and important molecule for many reasons, and has the ability to cool the gas to the required low temperatures. However, it cannot do the job alone.

Besides being key molecules for life, both water and molecular oxygen (O_2) have the potential of being important coolants in the star formation process, and hence in the evolution of the interstellar medium. As such they have drawn a lot of attention and many attempts have been made to observe these molecules. One major difficulty is though that they are very difficult to observe from ground

[1] Dense clouds in space are about as dense as our best vacuum on Earth!

since the atmosphere is completely opaque around the wavelengths of the most interesting transitions. Such observations therefore have to be performed from space. The first attempts were made with balloon experiments in the early 1990s with little success. A few years later space satellites were launched to observe water and molecular oxygen from orbits around the Earth: the ESA Infrared Space Observatory satellite (ISO, 1995-1998), the NASA Submillimeter Wave Astronomy Satellite (SWAS, 1998-2004), and the Swedish-led Odin sub-mm satellite (launched in 2001, see figure on the front cover).

The main goal of these space missions has been to determine the composition of interstellar clouds and the amounts of molecular oxygen and water, which also is important for the chemistry. Another purpose was to improve the understanding of the early stages of star formation by establishing the means by which these clouds cool as they collapse to form stars and planets. All three missions have been very successful in observing water in many different celestrial objects: cold, warm or shocked gas in star forming regions, the circumstellar environment around old stars, the thin atmospheres of Mars and Jupiter, as well as in comets.

At the Onsala Space Observatory we have been working with data from the Odin satellite resulting in a number of interesting scientific papers. One example is the detection of molecular oxygen which had been unsuccessful until 2007, when the Odin team could claim a detection in a molecular cloud after hundreds of hours of observation. The reason for the difficulty to detect molecular oxygen seems to be a several thousand times lower abundance than predicted by chemical models. In this thesis, molecular oxygen will not be discussed any further since most of my work has been focused on water in star forming regions.

The following chapters will expand this field into a more detailed level to give a background and introduction to the appended papers. A short introduction to radiative transport and explanation of some simple relations are found in the appendix for the non-familiar readers, followed by the references and a short list of useful databases.

Chapter 2

The Interstellar Medium

2.1 Introduction

What are the constituents of the ISM and how do they affect star formation? Does star formation in turn affect the ISM? Is there a connection between the chemistry of dense interstellar clouds and the cometary and planetary matter that could be their remnants?

The search for answers to questions like this is complicated by the fact that the ISM is certainly not a homogeneous medium with equal density and temperature, or constituents, spread evenly throughout the Galaxy. The very dilute gas is observable by means of its emission lines and by the absorption of starlight that travels through it. The signals are often very weak and the radiation and gas particles are mostly not in equilibrium with each other, which complicates the analysis. In addition, the composition of ISM also changes with time.

The origin of these changes can be tracked into the deep and hot interiors of stars. During their lives, the stars burn hydrogen and helium in different nucleosynthesis processes in their hot cores, creating heavier elements by which they enrich the ISM at the end of their lives. Gas is also lost in stellar winds by the stars during their entire lifetimes. Almost everything in the Universe is thus recycled, except for the collapsed remnants of stellar cores like white dwarfs, neutron stars, and black holes. The result of this recycling is that a small fraction of the chemical composition of the gas is altered by the nuclear processes.

From the beginning in the early Universe, the primordial composition of the ISM was, by mass, about three fourths of hydrogen and one fourth of helium, with trace amounts of lithium. Today, the relative amounts of hydrogen and helium are about the same, but with an additional small and very important fraction of $1-2\%$ of the heavier elements. These elements are created in different ways. Almost all elements from helium to iron in the periodic system are synthesized in nucleosynthesis processes in the hot cores of stars. For instance, in our Sun, the proton-proton chain which is effective for $T \gtrsim 10\,\text{million}\,\text{K}$, combines four

hydrogen nuclei into helium in a series of reactions. Synthesis of larger atoms demand even higher temperatures. To produce carbon or oxygen from helium in the triple alpha process temperatures above 100 million K is required. The creation of elements heavier than iron do not produce energy, but instead demand so much energy that the only way to synthesize them is in the moment when a very massive star explodes as a supernova. Our very existence therefore requires that a high-mass star has exploded as a supernova in the solar neighbourhood before the birth of our solar system. The dispersed elements from this supernova was later incorporated into our Sun and planetary system. Studies of the relative elemental abundances of the ISM can therefore give us information about the age of stars, chemical evolution in our Galaxy, and the history of star formation including different types of supernovae.

There also exists a complex chemistry in the envelope of old stars, on the surface of dust grains, in comets and planets, and in the gaseous clouds throughout the ISM that produce molecules. In fact the ISM can be considered as a unique chemical laboratory characterised by very low densities and temperatures not available on Earth. Species which are highly reactive and chemically unstable on Earth can therefore be quite abundant in some parts of the ISM. These include ions like HCO^+ and radicals like OH, CH and CN. In fact, the HCO^+ ion was first observed in the ISM and only later observed and confirmed in the laboratory. In this way studies of a chemistry otherwise not accessible is possible.

Determining atomic and molecular abundances in the ISM, of for example deuterium, is also a way to obtain information about what happened shortly after the Big Bang. When the Universe was only a few minutes old the three lightest elements hydrogen (H), helium (He), and lithium (Li) were created. Since the only known efficient process of deuterium production is the Big Bang Nucleosynthesis (BBN), almost all existing deuterium today must be a relic from the Big Bang. Measurements of the deuterium abundance may thus be used to constrain the event of the original production in the BBN.

2.2 Dust grains and ices

In addition to the gas the ISM contains approximately $\sim$1% by mass of small dust particles (0.01μm-1μm). These dust particles are solids composed mainly of silicate minerals, graphite, and amorphous carbon (soot). There is also evidence that the interstellar medium contains polycyclic aromatic hydrocarbons (PAHs), which show some properties of both gaseous molecules and small, solid particles. The distinction between gaseous molecules and solid-phase particles becomes blurred when 50 to 100 atoms are bound together. The dust grains form in the outer part of the atmosphere of old, low temperature stars together with molecules. The radiation pressure from the star on the dust grains drives a circumstellar wind away from the star which injects the dust and gas into the ambient ISM.

Supernova shock waves also distribute the dust over large scales, and thus the dust and gas are subsequently mixed into the ISM.

Dust particles are a very important part of the ISM for several reasons. For one, they can absorb and scatter energetic photons. This shields the interior parts of a cloud and enables molecules to survive. This absorption of ultra-violet (UV) and visible radiation heats the grains, causing them to radiate at infrared wavelengths, which in turn heats many molecules including water. Electrons can also be ejected from the grains, which is an additional important heating source of the gas.

Another important issue concerns the formation of molecules. Molecules can form in the gas-phase (see Sect. 2.3), but many reactions require a precursor molecule. These molecules can be provided by the complicated chemistry occurring *on the surface of dust grains*, including almost all of the production of molecular hydrogen. At low temperatures, a gas-phase atom may stick to a grain, migrate over the surface, and when a reaction partner is found a molecule may form. The probability for a reaction to occur increases on a dust grain since the environment prolongs the collision time of the elements. The formation rate of the molecules primarily depends on the nature of the grain surface, which can be very different, and temperature.

In colder regions the surface is often covered with a layer of volatile material. This is typically composed of ices of water (H_2O), carbon dioxide (CO_2), methanol (CH_3OH), carbon monoxide (CO), methane (CH_4), ammonia (NH_3), and carbonyl sulphide (OCS). Water ice is the dominant species and carbon dioxide the second most common with about 20 percent of the water abundance. Gas-phase carbon dioxide is, however, surprisingly rare. The icy grain mantles can be acquired through the slow, but efficient, accretion of species in the gas-phase. The time for removal from the gas-phase to the dust is about one billion years divided by the hydrogen number density. With a density of $10\,000\,\mathrm{cm}^{-3}$, the depletion time scale is only about 100 thousand years, which is less than the expected lifetime of the dense cores in Giant Molecular Clouds (more in Sect. 2.5). This depletion is very important to take into account when we make predictions of the molecular abundances in the gas-phase.

Molecules on the dust grains, created either on the grain or adsorbed from the gas-phase, will most likely not stay on the dust grain for ever. They can leave the dust grains by different methods, involving energy injections or destruction of the dust by shocks. Molecular hydrogen production releases a large amount of energy by which the H_2 molecules promptly desorb from the grain into gas-phase. This may also heat other parts of the grain which thereby may release other weakly bound molecules such as CO and N_2. Energetic radiation from newborn stars may also heat the grains, again causing molecular desorption. Since different species require different desorption temperatures, observations of star forming regions that are warming up, may use the observed relative molecular abundances as a "chemical clock" for the age and mass of the protostar.

2.3 Atoms, molecules and astrochemistry

Our understanding of the ISM is built upon observations of interstellar atoms, ions and molecules and the study of their formation routes – astrochemistry. More than 150 confirmed detections of molecules have been made in interstellar space, circumstellar envelopes of old stars, comets and on planets as seen in Table 2.1. Many more probably await future detections. Compounds of the elements which are chemically reactive and have high abundances; hydrogen (H), carbon (C), oxygen (O), and nitrogen (N); constitute the major part of the detected molecules. Even though helium (He) is present in large amounts in the ISM, this atom is very stable and does not easily take part in chemical reactions. Even though its chemical role is small, it must be taken into account when modelling excitation conditions in the gas-phase due to collisions between He and other species. The first molecule to form in the Universe was also likely composed of helium, He_2^+. Molecules that form from heavier refractory elements, such as sulphur (S), silicon (Si) or magnesium (Mg), often reside on dust particles.

The overwhelmingly most abundant molecule of them all is molecular hydrogen (H_2) which constitutes about 99.99% of all molecules. Despite its large abundance it is very difficult to detect. The easiest way of detection is to observe transitions radiating in UV, and such observations have provided a vast amount of information on diffuse and translucent molecular clouds. The rotational transitions radiating in the infrared, are on the other hand forbidden due to the symmetry of H_2, and are therefore intrinsically weak. These transitions have been observed, to study both cold, dense molecular gas in absorption and warm ($T \sim 1\,000\,K$) gas in emission. The H_2 emission from cold and dense clouds is, however, only visible in places where there are sufficiently bright, background infrared sources to allow absorption spectroscopy. As a consequence, much of the content in cold molecular clouds is invisible. The solution to this problem has been to observe the second most common molecule, carbon monoxide, which seems to have a co-spatial existence with H_2. The abundance of CO relative to H_2 is rather stable and is about one part in ten thousand. The CO molecule is easily excited at modest densities and temperatures and also very tightly bound, and is therefore an excellent probe of cold molecular clouds. Other very familiar molecules detected in the ISM include water, molecular oxygen, methanol, ethanol, ammonia, and formaldehyde.

Molecules can be produced in several ways, where one major formation process occurs on the surface of dust grains as described in the previous section. In *gas-phase* chemistry one major problem concerns energy, in addition to conservation of momentum and quantum mechanical symmetry considerations. Considering energetics, if two atoms collide, they will simply bounce off each-other unless they can lose energy somehow. This may happen for instance in a simultaneous collision with a third atom in a *three-body collision*. On Earth, the density is very high and molecules form easily in three-body collisions. In space, however, the density is

Table 2.1: 169 detected interstellar species as of November 2008[a]. Cyclic and linear forms are labelled *c*− and *l*−, respectively. A question mark labels unconfirmed detections.

Hydrogen compounds					**Oxygen**
H_2 [b,e]	HD [b]	H_3^+	H_2D^+	HD_2^+	O_2
Hydrogen & Carbon compounds					
C_2 [b,e]	CH_2	C_8H	C_2H_2 [e]	CH_3C_2H	*l*−C_3H
C_3 [e]	CH_3	C_2H	C_2H_4 [d]	CH_3C_4H	*c*−C_3H
C_4	CH_4 [e]	C_4H [e]	C_2H_6 [f]	CH_3C_6H	*l*−C_3H_2
C_5 [d]	C_5H	C_4H^-	C_3H_6	CH_2D^+?	*c*−C_3H_2
CH [c,e]	C_6H	C_6H^-	C_6H_6 [d]?	CH_2CHCH_3	*l*−H_2C_4
CH^+ [b,e]	C_7H [d]	C_8H^-	H_2C_6	*l*−HC_4H [d]?	*l*−HC_6H [d]?
Hydrogen, Oxygen & Carbon compounds					
CO [c e]	OH [c,e]	H_2O^+ [f]	HC_2CHO	CH_3OH [e]	$(CH_3)_2O$
CO^+ [e]	OH^+ [f]	H_3O^+ [e]	$(CH_2OH)_2$ [e]	CH_3CHO [e]	$(CH_3)_2CO$
CO_2 [e]	HCO [e]	H_2CO [e]	CH_2CHOH	CH_3OCHO [e]	*c*−C_2H_4O
CO_2^+ [f]	HCO^+ [e]	H_2COH^+	CH_2CHCHO?	CH_3COOH	*c*−H_2C_3O?
C_2O	HOC^+	$HOCO^+$	CH_2OHCHO	CH_3CH_2OH	$C_2H_5OCH_3$?
C_3O	H_2O [e]	H_2C_2O	HCOOH [e]	CH_3CH_2CHO	$HC(O)OCH_3$ [e]
Hydrogen, Nitrogen & Carbon compounds					
N_2 [b,g]	CN [c,e]	HNC_3 [e]	$HCNH^+$	CH_2CN	CH_3CN [e]
N_2H^+	C_3N	HC_3N [e]	HC_3NH^+	CH_2NH	CH_3NC
NH [b,e]	C_3N^-	HC_5N	HC_2N	CH_2CHCN	CH_3NH_2
NH_2 [b,e]	C_5N	HC_7N	HC_2NC	CH_2CCHCN	CH_3C_3N
NH_3 [e]	C_5N^-	HC_9N	H_2CN	CH_2CNH?	CH_3C_5N
HNC [e]	HCN [e]	$HC_{11}N$	H_2NCN	*l*−HC_4N [d]	CH_3CH_2CN
			H_2NCH_2CN		
Hydrogen, Nitrogen, Oxygen & Carbon compounds					
NO	N_2O	HNO	HNCO [e]	NH_2CHO [e]	$CH_3C(O)NH_2$
			HCNO	HC(O)CN	NH_2CH_2CN
Species containing: S, Si, Na, K, Cl, F, Al, Mg, Fe, P					
S_2 [f]	C_2S	PN	SiC [d]	CF^+	AlCl [d]
SO [e]	C_3S	PH_3?	SiN	HF	AlNC [d]
SO^+	HCS^+	PO	SiH?	NaCN [d]	NaCl [d]
SO_2 [e]	H_2CS [e]	CP [d]	SiO	MgNC [d]	KCl [d]
NS [e]	OCS [e]	CCP	SiNC [d]	MgCN [d]	AlF [d]
H_2S [e]	CS [e]	HCP	C_4Si [d]	SiH_4 [d]	HCl
H_2S^+ [f]	CS_2 [f]	FeO?	*c*−SiC_2	SiCN [d]	SiS
	CH_3SH	HNCS	*c*−SiC_3		
Polycyclic Aromatic Hydrocarbons (PAHs)					

[a]Data are from `http://www.cdms.de`, `http://www.astrochymist.org/`, `http://www.cv.nrao.edu/~awootten/allmols.html` and NASAs cosmic ice laboratory. [b]Detected in visible light & UV absorption. [c]Detected in visible light & UV absorption, and in the radio. [d]Only circumstellar species. [e]Also detected in comets. [f]Uniquely detected in comets. [g]Also in/on planets in our solar system.

much too low for this process to proceed rapidly, except in the circumstellar envelopes of cold AGB stars and in collapsing protostellar clouds. They offer a warm and dense environment producing a rich chemistry. As seen in Table 2.1, some molecules, such as C_5, C_7H, and HC_6H among others, are only detected in these regions. Another way to lose energy is by *radiative association* where emission of a photon is produced during the collision, which conserves momentum as well as energy. In this process, two atoms collide and form an excited molecule which radiatively decays to the ground state before it dissociates. But the probability for this to occur is generally very low. The symmetric H_2 molecule cannot form by radiative association of hydrogen atoms in their lowest state since this process is strongly forbidden on account of the symmetry properties.

The chemical reactions that drive most of the interstellar chemistry are instead the efficient *ion-molecule* and *neutral-neutral* reactions. The colliding species can be atoms, ions, electrons, molecules or cosmic rays (CRs). Cosmic rays are relativistic charged particles: protons, helium nuclei, electrons and 1% heavier nuclei, travelling with a speed close to the speed of light. These particles play a very important role in the ISM and constitute a cornerstone of gas-phase chemistry. They originate from stars and the most energetic mostly from supernovae and very massive stars. During their travel through the ISM they may be accelerated further by shock waves, turbulence or magnetic fields. Since the CRs are charged they are affected and trapped by magnetic fields which permeate the ISM.

Neutral-neutral reactions possess energy barriers which can require temperatures above 100 K. At low temperatures they are only about 1% as likely to occur as the ion-molecule reactions, but they often become increasingly more efficient at higher temperatures.

Destruction of molecules occurs again by different processes, for instance by *energetic radiation* or by *cosmic rays*. Molecules do not survive in general at high temperatures above 3 000 K. In dense regions very complex molecules can be produced since the outer layer of the cloud, consisting of both gas and dust, is an effective shield against the energetic UV-radiation. On the other hand, if the clouds are diffuse, the incoming UV-photons will destroy large molecules faster than they can be produced. Therefore only small and simple molecules may survive in diffuse clouds. Some molecules also have the ability to protect themselves by *self-shielding*. Molecular hydrogen and carbon-monoxide have this capacity since their photo-destruction occurs through narrow spectrum lines rather than the broad-band continuous absorption destroying most other molecules. In the case of H_2 and CO the the radiation outside these bands does not affect the molecules. Another destruction source is *dissociative recombination*. An ambient free electron recombines with a molecular ion and creates an energetic and unstable neutral molecule. The molecule can ionise by itself, and thereby lose the electron again, or fall apart into its neutral species.

2.4 Molecular environments affect the chemistry

Within the Milky Way, a typical spiral galaxy, the average density is about 1 particle per cm^3. Several billion solar masses of neutral hydrogen is found everywhere in the Galactic disc, and is observable at 21 cm (1420 MHz). A low-probability transition in the ground energy level emits radiation at this wavelength when the electron changes its spin relative to the proton. The vast amount of hydrogen compensates for the low-probability, and allows the detection and mapping of the spiral arms in our Galaxy. This line was detected for the first time in 1951 and represents a very important part of radio astronomy. Molecular hydrogen is also widespread, even though it resides mostly in discrete molecular clouds in the spiral arms as mapped by their CO and ^{13}CO rotational line emission.

Several classifications of molecular clouds exist with no clear boundary between the different regions and one classification is shown in Table 2.2. As seen in this table, there is a huge range in sizes, temperatures and densities between the different types of clouds. Dense, star forming clouds in the ISM have about one million particles in each cm^3.

On small scales the ISM forms a multi-phase medium with three different coexisting phases. Low density, neutral and ionised gas with a high temperature of 1 000 –10 000 K is in pressure equilibrium with high density, low temperature $\lesssim$100 K neutral and molecular gas. The third phase is shock heated by supernovae to temperatures of about 1 million K and is therefore ionised. This gas occupies most of the volume in the ISM, but most of the mass is in the dense phase. The gas material passes continuously between the different phases.

Many of these different molecular environments in the ISM have chemical characteristics which are connected to the formation and evolution of stars. The process of star formation will significantly alter the chemical composition in the region due to the increasing density and temperature of the collapsing cloud. In the early stages of star formation the temperature may rise from about 10 – 15 K to 100 K, and at later stages powerful outflows and shocks from the new-born star can elevate the temperature locally to several thousands of kelvin. At these high temperatures neutral-neutral reactions can dominate the chemistry and produce other molecules than the ion-molecule chemistry at low temperatures. In addition, molecules that previously were frozen in the ice on dust grains will evaporate into the gas phase at high temperatures. The evaporated species may have been formed through chemical reactions on the surface of dust grains, for instance methanol, or in the gas-phase before they condensed onto the dust grains. This transformation of chemical composition in a protostellar nebula will be small in the outer part where the temperature is lower. In the inner part, which is heated by the protostar, a major reprocessing of grains and molecules will occur.

The gas in the ISM is thus continuously changing and passing through different phases involving a possible change of chemistry and thereby constituents. But do

the molecules have the ability to survive when passing through these phases, or do they always transform and evolve to other species? An interesting question concerns how much of the organic material present in the comets of our own Solar system is pristine interstellar material, and to what extent has it has been processed. Is it possible that the molecular abundances are the same in the ISM gas-phase, on the icy dust grains, in our Solar system comets and on Earth? Observing molecules in all these different regions and comparing abundances gives us valuable clues on how our Solar system once was born.

The origin of life is an even more difficult subject than the origin of stars and planets. A very popular subject is to search for large, complex, carbon-based molecules and possible precursors to DNA. Organic molecules necessary for the origin of life have been shown to exist throughout the ISM. One such pre-biotic molecule is the amino acetonitrile molecule, NH_2CH_2CN, detected in 2008. This molecule is chemically related to the simplest amino acid commonly found in proteins, glycine. Would it be possible for these pre-biotic molecules to be transported via comets to newly formed planets, thereby allowing the building blocks of life to be widely spread? This is a fascinating thought, even though the probability that these molecules would be destroyed during the impact on a planet is high.

As illustrated above, the molecular chemistry is affected by the environment, but the reverse is also true, the initial molecular abundances and the level of ionisation affect the star formation process. Thus, the chemistry both controls the evolution of the molecular clouds and is a diagnostic of their physical conditions.

2.5 A few molecular environments

A short description of a few of the different classes of clouds that are important in the appended papers follows:

Giant Molecular Clouds (GMCs) are the most massive individual objects in our Galaxy typically found in the spiral arms. In these clouds the majority of all stars form. More than half of the total gas mass in the Galaxy is found in GMCs, and once a GMC forms the formation of stars starts almost immediately. Thousands of low-mass stars may form, and in addition, a number of high-mass stars which cannot form elsewhere. These huge clouds are self-gravitating objects, which means that they are bound together by the mass of the molecular gas within them. The internal structure is inhomogeneous with fragments of dense sheets, filaments, cores and large low-density voids. Clumps of even higher than average density gas fill a fraction of the volume, and the stars form only in the very densest central parts of the most tightly gravitationally bound clumps (see Sect. 2.6). An example of a well-known GMC is the Orion Molecular Cloud (paper I and II).

The lifetimes of GMCs are only about a few to tens of million years. The short lifetime is due to the formation of very massive and hot stars. The route of

Table 2.2: Characteristics of molecular clouds in the ISM after van Dishoeck et al. (1993).

Region	Density $[cm^{-3}]$	Temp. [K]	Mass $[M_\odot]$	Size [pc]
Diffuse clouds	100 – 800	30 – 80	1 – 100	1 – 5
Translucent clouds	500 – 5000	15 – 50	3 – 100	0.5 – 5
Cold dark clouds				
complex	$10^2 - 10^3$	$\gtrsim$10	$10^3 - 10^4$	6 – 20
clouds	$10^2 - 10^4$	$\gtrsim$10	$10 - 10^3$	0.2 – 4
cores	$10^4 - 10^5$	$\approx$10	0.3 – 10	0.05 – 0.4
Giant Molecular Clouds				
complex	$10^2 - 10^3$	15 – 20	$10^5 - 10^6$	20 – 80
clouds	$10^2 - 10^4$	$\gtrsim$20	$10^3 - 10^5$	3 – 20
warm clumps	$10^4 - 10^7$	25 – 70	$1 - 10^3$	0.05 – 3
hot cores	$10^6 - 10^9$	100 – 200	$10 - 10^3$	0.05 – 1

destruction may start once a bright O or B star is formed. These stars have surface temperatures between 10 000 – 60 000 K and produce intense UV-radiation with photon energies above 13.6 eV. This energy is high enough to both dissociate and ionise molecules and atoms and will produce large *HII regions* or *emission nebulae*. The name refers to the radiation in visible light from ionised hydrogen. These fully ionised clouds are signposts of massive star formation, and their distribution points to a concentration in the spiral arms of our Galaxy. However, the very massive O and B stars cannot maintain the UV-flux for more than a few million years, since they have a very short lifetime. One of the best studied examples of a rather close HII region is M42 in the Orion Nebula.

Farther away from the ionising star, a transition region between the ionised gas and the cold and dense cloud will appear: a *Photo Dissociation Region* (PDR). The energies of the photons have now dropped below the necessary hydrogen ionising energy and are called Far Ultra Violet (FUV) photons. These photons have energies between 6 – 13.6 eV and dominate the heating and chemistry processes in the PDRs. The most efficient heating occurs in the outer parts, where the heated dust grains radiate strongly in the infrared producing most of the non-stellar infrared radiation from galaxies. Deeper in the cloud, cosmic rays are the main heating source. The cooling occurs mostly from fine-structure lines of abundant atoms and ions, such as ionised carbon and neutral oxygen. The structure is determined by the density and the intensity of the incident radiation field. At the edge of the PDR, where the temperature can be thousands of kelvin, there is a thin transition region where ionising UV-photons are absorbed by the dust and

molecules. In this zone, hydrogen atoms recombine from being almost fully ionised to almost fully neutral. The remaining FUV-photons will dissociate molecular hydrogen and ionise carbon, and thus this region is composed of H, C^+, and O. Deeper in the cloud, neutral atoms and molecules form subsequently in the order of their ionisation and dissociation energies: molecular hydrogen, carbon, carbon-monoxide, oxygen and molecular oxygen will appear in this order, before the cold and dark molecular cloud begins.

In paper III we report observations of water, ammonia, and carbon-monoxide in the PDR of the well-studied molecular cloud S140. Other well-known PDRs include the Orion Bar and extended PDR, which is the interface PDR between the Orion KL molecular cloud and the M42 HII region.

In the *cold and dark clouds* the gas is mostly molecular, with H_2 as the dominant species. Due to the high density there is no penetration by visible or UV-photons, and the ionisation is low. The chemistry is driven by cosmic rays that are able to penetrate deep into the clouds producing the necessary ions for the ion-molecule chemistry. Over 60 molecules have been detected in these regions, mostly at long wavelengths. Here the largest molecules are found in the form of carbon chains, for example HC_7N, HC_9N, and $HC_{11}N$. Typically one or two low-mass stars can be formed in dense cores in these clouds.

Hot cores are warm, dense, rather small, and are believed to harbour a protostellar object. The warm environment gives rise to a complex and rich chemistry with a different chemical composition than in the cold and dark clouds. The abundances of hydrogenated molecules, such as NH_3, H_2O, H_2S, CH_3OH, and $(CH_3)_2O$, are very high. Hot cores also show an enhancement in the abundance of deuterated species, for instance the ratio of HDO to H_2O is higher here than normal. Molecular ions are less abundant which suggests a low degree of ionisation. The high temperatures found in hot cores allow chemical reactions with an energy barrier, for example the neutral-neutral reactions. The Orion KL nebula has a well studied hot core (paper II).

A *shock* occurs whenever a disturbance through the medium has a speed greater than the speed of sound, which is about $1\,\mathrm{km\,s^{-1}}$ in a neutral gas with temperature below 100 K. The energy of a shock with a velocity about $10-30\,\mathrm{km\,s^{-1}}$ or energetic outflows from a protostar can elevate the temperature to thousands of kelvin, and this largely affects the chemistry. One source of shocks are the *molecular outflows* from newly born stars still embedded inside their parental could. On large scales bipolar molecular outflows are often seen. Paper II and III report on observations of water in the outflows from the Orion KL nebula and the S140 molecular cloud.

2.6 Star formation at high and low redshifts

The basic processes that govern star formation at both present times and in the early Universe are the same even if the details differ a lot. The main stages are:

Building a home Forming a gravitationally bound molecular cloud core.

Conception The gravitational collapse, accretion of infalling material and circumstellar disk-formation.

Birth The on-set of thermo-nuclear processes in the core of the star.

Leaving home The dispersal of the parental molecular cloud by a stellar wind and outflows.

The standard theory describes the gravitational collapse of a cold and dense cloud core. The forces to be taken into account are gravity, and the opposing thermal pressure. A cloud will collapse by gravitation if the mass of a cloud *exceeds* the Jeans mass.

$$M_{\rm J} \simeq 22\, M_{\odot} \left(\frac{T}{20\,{\rm K}}\right)^{3/2} \left(\frac{n}{10^4\,{\rm cm}^{-3}}\right)^{-1/2}, \tag{2.1}$$

where T is the local temperature of the cloud, and n is the density. This equation shows the importance of a high density and a low temperature, emphasising the importance of cooling. The dense cores inside the GMCs fulfill the above conditions and star formation will naturally occur.

Even though the gravitational collapse scenario qualitatively explains the formation of stars, the actual details depend on the physical conditions in the star forming cloud. This also determines the efficiency of star formation, the mass of the resulting star, and if a binary star or a planetary system will form. From observations we know that stars have masses between 0.08 and $\sim$100 $\rm M_{\odot}$ where most of the stars have masses comparable to our Sun or less, and more than half of all stars are binary star systems. The fraction of stars with planetary systems is unknown, but there is a possibility that a large fraction of all stars has a planetary system, even in binary star systems.

The star formation rate varies a lot between galaxies, and also within our Galaxy, but here is in total $\sim$2 – 3 $\rm M_{\odot}$ each year. This has posed a problem since our Galaxy contains about one billion $\rm M_{\odot}$ of molecular gas, and most of the gas resides in GMCs. These clouds are gravitationally unstable and this should produce a star formation rate higher than about 200 $\rm M_{\odot}$ each year. Since the observations show a rate which is about a hundred times lower, an additional force must be counteracting the gravitational collapse

This additional force is supplied by the non-uniform magnetic fields that permeate and support the clouds. This magnetic pressure is at least comparable to the thermal pressure and sometimes many times stronger. In order for gravitational collapse to start, the gas cloud must first lose this magnetic support. This is done by a process called ambipolar diffusion, which is the drift of the neutral relative to the charged particles. The magnetic field tends to push the charged

particles outwards, while the neutral particles, carrying most of the mass, are only affected by the inward gravitational force. The friction between the outward and inward drifting species will reduce their velocities and retard a collapse. If the ionisation is high, the time for the neutral species to drift inwards through the ionised component will be longer than in the case of low ionisation. The effectiveness of a cloud collapse is therefore governed by the fractional ionisation in the cloud, which in turn is controlled mainly by the penetration of the clouds by cosmic rays.

It is believed that stars are formed by different physical processes in isolated star forming regions, producing stars with masses $\lesssim 3\,\mathrm{M}_\odot$, and in cluster-forming regions (GMCs) where also high-mass stars may form. The environment in the different regions of the ISM also creates a turbulent behaviour of the gas acting against star formation. The turbulence exists on all scales, and may on large scales be created when a molecular cloud experiences the differential rotation in our Galaxy. Both gas and stars in the Galaxy disc are rotating around its center, but the speed differs with distance from the galactic center creating a differential rotation. Shock waves from supernovae, energetic radiation, stellar winds and outflows from massive O- and B-stars generate turbulence on intermediate scales. On the smallest scales, turbulence is driven by stellar winds and outflows from low-mass stars. Such a scale-free turbulence predicts structure in the ISM on all scales, which is indeed observed. The clouds are clumpy on every scale observed and this has implications for our observations (read more in Chapter 3).

The actual onset of a collapse in the Milky Way may be triggered by collisions between clouds streaming across a spiral arm, or when powerful outflows and shocks from supernovae and massive stars slam into the surrounding cloud, compressing the gas to higher densities. It may also be triggered by the decay of turbulence or loss of magnetic support.

In the early Universe the lack of dust and heavy elements makes it very difficult to explain the formation of the first stars, called population III stars (read more in Chapter 6). They are believed to have formed some hundred million years after the Big Bang. During this time the magnetic fields and turbulence are believed to have been very low, and star formation was therefore mainly governed by the competition between gravity and thermal pressure. The necessary cooling was very inefficient since there were no heavy elements and only a few molecular species with very low abundances. Cooling agents were species like H_2 and HD, which only allow cooling to temperatures of 100 K or higher. As a consequence, the first generation of stars must have been very massive, $\sim 100 - 1\,000\,\mathrm{M}_\odot$, and hence very short-lived. This first generation of stars seeded the early Universe with trace amounts of elements like carbon, nitrogen, and oxygen in powerful supernovae explosions. Thus, the pregalactic gas gradually became enriched with heavier elements than hydrogen and helium, and therefore a wider variety of stars could form.

The emerging picture of star formation is thus a very complex ecosystem of many variables such as temperature, density, degree of ionisation, content of molecules and heavy atoms, and magnetic fields. In addition, star formation is also affected by the environment creating turbulence on all scales prohibiting gravitational collapse. Due to the complexity, even small variations of the initial variables will produce very different results. In the early Universe, the first stars were many times more massive than stars today, owing to the lack of efficient molecular cooling.

2.7 Summary

The Universe and the interstellar medium (ISM) are indeed far from sterile. The ISM is a unique laboratory where a complex and surprisingly rich chemistry, totally different from chemistry on Earth, can be studied. A revolution of our knowledge started in 1963 when astronomers first detected simple molecules in the ISM. Today more than 150 molecules have been found in space, some even before they were discovered on Earth. The chemistry producing the molecules depend on the environment: temperature, density, radiation from new-born stars, cosmic rays, magnetic fields, turbulence, shocks and stellar winds. The chemistry in turn affects the environment. Without molecules, stars and planetary systems would not be able to form since star formation depends to a high degree on the cooling properties of molecules.

Chapter 3

Water and cooling

Besides molecular oxygen, very few molecules are attached with such an emotional interest as the water molecule. This is of course based on the fact that water is absolutely indispensable for the evolution of life as we know it. Moreover, water also seems to be of equal importance to the chemical evolution of the ISM.

3.1 Water in space

One of the important properties of water, granting a status as a key molecule for life, is the ability to act as a universal solvent. On Earth, atoms and molecules demand liquid water as a solvent to be able to form larger species. The hydrogen bonds between the water molecules redistribute constantly and rapidly, and this creates an excellent environment where molecules can form. This is not the case when water is in the form of ice, occurring at temperatures below 273 K on Earth. The water molecules are then ordered in a rigid crystalline structure which recoils other species. In interstellar space the temperatures are mostly much lower than this, and it therefore seems impossible for large molecules to form in the ice. But at the extremely low densities in the ISM, paired with a temperature below 135 K, an *amorphous ice* will form which behaves differently than ordinary ice. This form has similar properties to liquid water found on Earth and is the most commonly form of ice in the ISM.

The Infrared Space Observatory (ISO) satellite has observed ices on dust grains between wavelengths of $2-200\,\mu$m towards a number of sources including star forming regions, quiescent dark clouds and diffuse clouds in the ISM. The water content is shown to account for about 2/3 of the ice in most sources. The remaining 1/3 is composed primarily of CO_2 and with smaller amounts of $^{13}CO_2$, CO, CH_3OH, CH_4, and possibly SO_2, OCS, H_2CS, and NH_3 (read more about dust grains in Chapter 2.2).

Water ice is also very abundant in comets, which are believed to be pristine objects from the original solar nebula. These objects may be very important for

the emergence of life on a planet, since there is a possibility that they can deliver large amounts of water and complex molecules to a young planet. Water ice is in fact by far the most abundant condensed-phase species in space, and is a major constituent of all the planets, satellites, comets, and asteroids from Jupiter and outwards in our Solar system.

Trace amounts of water are found in the atmospheres of Venus and Mars, and has even been found in dark spots on our Sun with temperatures of 3 200 K with a possible origin from infalling comets. It is also believed that water is important in planetary formation by delineating the "snow-line" which is the distance from a new-born star to where the condensation begins. Life supporting environments on planets outside our solar system have been searched for since the first detection of an exoplanet in 1995. In 2007, a major step in this direction was made with the claimed detection of water vapour and methane in the atmosphere of the exoplanet HD 189733b. Liquid water can exist on the surface of solid planets and in the interior of planetary bodies, such as the Jupiter moon Europa or the Saturn moon Enceladus, if the temperature and pressure are right. So far Earth is the only known place with liquid water, although there are indications that liquid water has been present in the past history of planet Mars.

The first detection of water in space was due to a special kind of radiation process, a maser. This is an acronym for Microwave Amplification by Stimulated Emission of Radiation, which is an amplification process for radio waves analogous to a laser in visible light. The detected transition was a high-energy masering transition at 22 GHz. Maser radiation comes from certain very small amplifying regions of high-excitation gas in star forming regions and also from regions close to evolved stars. The analysis is often difficult, demanding sophisticated maser models, and is not treated any further in this thesis. The problem with water observations is that the only available transitions using ground-based telescopes are more or less masering in nature. This is because the Earth's atmosphere is completely opaque around all other lines. Observations by ground-based telescopes of the isotopologue $H_2^{18}O$ and deuterated water HDO have therefore been performed to estimate water abundances in different regions. These observations are attached to large uncertainties due to contaminating atmospheric lines and unknown isotopologue ratios.

With the launch of the ISO satellite in 1995, a wealth of highly excited $H_2^{16}O$ transitions were observed from hot molecular regions at wavelengths in the infrared spectral regime. The water abundance was measured both in vapour and solid form. The subsequent launches of SWAS in 1998 and Odin 2001, enabled observations of the ground rotational state transition of one of the two forms of water, *ortho*-H_2O (see Sec. 3.3). Using its tunable receivers, Odin was also able to observe the isotopologue *ortho*-$H_2^{17}O$ for the first time in the ISM, in addition to the previously observed *ortho*-$H_2^{18}O$ by SWAS. These water transitions require less energy to be excited than the observed ISO transitions, hence colder and more ex-

tended regions are probed. In paper I and II we also report a detection of an HDO transition and one highly excited transition of the other form of water, *para*-H_2O.

3.2 Water formation

Water is composed of one oxygen and two hydrogen atoms. The maximum abundance of water is therefore set by the number of oxygen atoms in the ISM. Oxygen is the third most abundant element in interstellar space with a solar abundance relative to hydrogen of about 7×10^{-4} and, as such, is a very important element in astrochemistry. The most common gas-phase oxygen-bearing molecule is CO with water as the second most common molecule in many environments.

There are three different major routes of water formation. At cold temperatures the main water production is taking place on the *surface of dust grains*. Typical abundances of water ice were observed by ISO to be about 10^{-4} with respect to the total hydrogen content. This implies that much of the oxygen is locked into water ice at low temperatures. If the temperature rises above $\sim$110 K the ice sublimates, thereby enriching the gas-phase water abundance by orders of magnitude.

The major route of gas-phase production at low temperatures $\lesssim$400 K, is the *neutral-ion process* and involves a chain of processes:

$$\begin{aligned}
H_3^+ + O &\rightarrow H_2 + OH^+ \\
OH^+ + H_2 &\rightarrow OH_2^+ + H \\
OH_2^+ + H_2 &\rightarrow H_3O^+ + H \\
H_3O^+ + e^- &\rightarrow H_2O + H
\end{aligned}$$

where the H_3^+ ion is produced from the ionisation of H_2 by cosmic rays and X-rays. This gas-phase chemistry produces a theoretical water abundance of a few times 10^{-7} relative to hydrogen.

In hot core regions or in shocked gas where the average temperature is higher than $\sim$400 K, the gas-phase *neutral-neutral reaction* rapidly produces water using all available oxygen not locked into the very stable CO molecule with the major sequence:

$$\begin{aligned}
O + H_2 + 3\,150\ \mathrm{K} &\rightarrow OH + H \\
OH + H_2 + 1\,736\ \mathrm{K} &\rightarrow H_2O + H
\end{aligned}$$

where the temperatures involved are the energy barriers. These reactions produce a water abundance of a few times 10^{-4}. Note, that a high molecular hydrogen content is required to prevent "back reactions" with atomic H, which will destroy the water molecules.

The required high temperatures for the neutral-neutral reactions to occur are easily reached in hot cores, outflows or shocks in star forming regions. A shock velocity of $\sim10-30\,\mathrm{km\,s^{-1}}$ will elevate the temperature to several thousand Kelvin without destroying the molecules. This produces a perfect environment for a rapid

water production within a few hundred years which is about the same time scale as the cooling time for the shocked gas. These shocks produce about $100-1\,000$ times more water than the neutral-ion process. Even though the temperature quickly decreases, the water abundance will remain at a high level some hundred thousands years, before *freezing out* on the dust grains. This also implies that a high water abundance in a cold molecular gas is a sensitive probe of previous shocks.

The highest gas-phase abundances of water are therefore found in warm regions were the ice desorbs from the dust grains and the neutral-neutral reactions additionally form abundant water directly in the gas-phase. This also implies that water is not an important coolant on large scales, while it still may be very important locally. Observations of water confirm high abundances in shocks and outflows in star forming regions, with the Orion KL star forming region being a good example (paper I and II). On the other hand, observations in cold and quiescent regions indicate a much lower water abundance of about $10^{-8}-10^{-9}$ than predicted by the theoretical models, with an example in paper III. One idea to solve this discrepancy is to include the gas and grain interaction in the chemical models, where the molecules and atoms will freeze out on the dust grains on a timescale of $10^9/n_{\rm H}$ years, where $n_{\rm H}$ is the hydrogen density in cm^{-3}. Thus, in cold, old and high density clouds the depletion will be high and the water abundance will be low.

Another suggestion to solve the discrepancy on large scales within a low density medium, is to include the *clumpy structure* of the interstellar clouds. The ISM displays a clumpy structure on all scales, and this structure will allow the energetic radiation and cosmic rays to penetrate deeper in the cloud and thereby dissociating water to a larger depth. The water emission most likely arises from a rather narrow region from each clump within the cloud. Too close to the surface, water is photodestroyed by the UV-radiation, and deeper in the dense and cold clumps it depletes onto grains. Since the clumps only fill a fraction of the observed region the average observed emission will be much lower than in the case of a homogeneous cloud thereby decreasing the derived water abundance. In paper II and III a clumpy structure is indeed required to recover the observed water emission. Paper III also finds a much higher water abundance on the surface of the high-density clumps than in the low-density inter-clump medium.

3.3 Water transitions

A spectrum of a species depends on its structure and the participating elements. The two hydrogen atoms in the water molecule are symmetric with respect to each other. Their nuclear spins may be anti-parallel or parallel aligned and this causes energy level splitting into two different subspecies, *para*- and *ortho*-water. For high temperatures the *ortho*-levels are three times more populated than *para*.

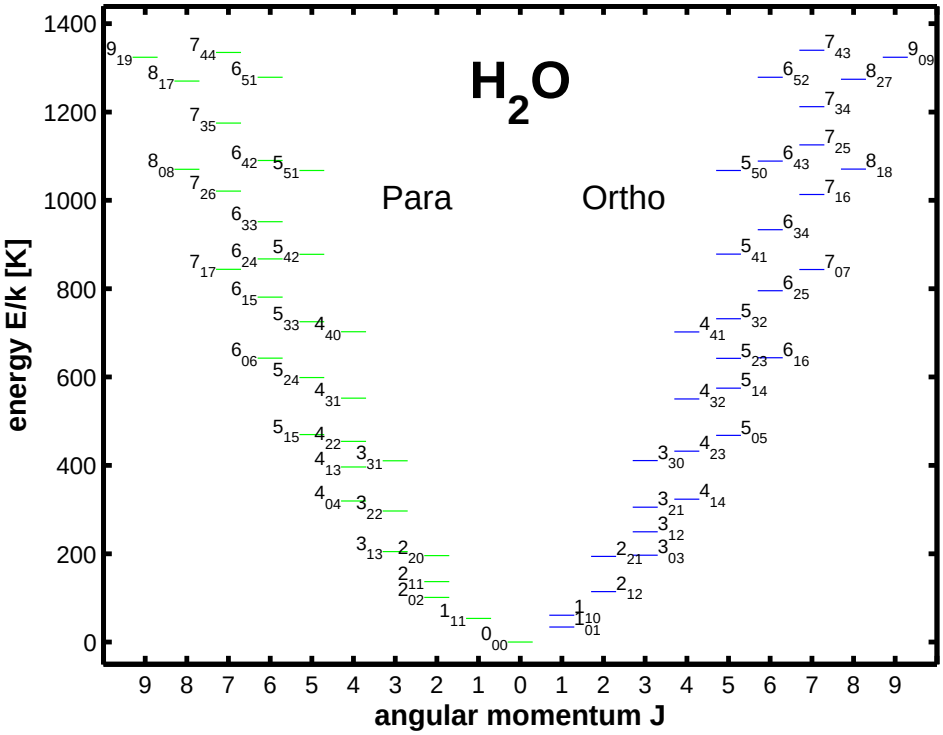

Figure 3.1: Energy level diagram of *ortho*- and *para*-H_2O.

Radiative transitions between *para*- and *ortho*-states are forbidden.

In radio astronomy, molecular radiation arises when the molecules change their rotational energy, described by the rotation quantum number J. Water is an asymmetric top which means that it has three unequal principal axes of rotation. Therefore, two additional quantum numbers K_A and K_C are needed for a full description of all possible energy levels. Figure 3.1 shows the *ortho*- and *para*-H_2O energy level diagram up to energies $E/k = 1\,400\,\mathrm{K}$ and describes the different levels of rotational energy the water molecule may have. The dipole selection rules allow J to change by 0 or ± 1, while the quantum numbers K_A or K_C can change by ± 1 or ± 3. The *ortho*-transitions have even K_A and odd K_C (e, o) which can only change to a state with an odd K_A and even K_C, (o, e). Similarly, for *para* states the quantum numbers must go from (e, e) to (o, o). Note, that collisional transitions may occur between any level within each *ortho* and *para* sub-species. The rotational ground state *ortho*-water transition observed with Odin is labelled $1_{1,0} - 1_{0,1}$ and occurs at 556.936 GHz.

The water transitions have high Einstein A-coefficients and therefore need a high density to be collisionally excited. The $1_{1,0} - 1_{0,1}$ transition has $A = 0.0035\,\mathrm{s}^{-1}$

giving a critical density of $\sim 10^8 - 10^9$ cm^{-3} depending on temperature. Most molecular environments have densities much lower than this and this transition is therefore said to be subthermally excited.

The opacity for the $1_{1,0} - 1_{0,1}$ transition is high even for rather low abundances and this has implications on the analysis of the water emission. If a transition is optically thick we only see the "surface" of the cloud where $\tau \sim 1$. Thus, observations of this transition cannot tell if there is more water behind the optically thick surface. Instead, other higher lying, optically thin transitions may serve this purpose. The subthermal excitation of the ground state transition may on the other hand allow this line to be considered as "effectively optically thin". In this limit, every collisional excitation will always result in a photon that eventually escapes the cloud, even if repeatedly scattered. This approximation is, however, most likely only valid if the opacity is $\lesssim 10$, since the probability of being collisionally de-excited increases with number of scatterings as measured by the opacity.

A high optical depth of the *ortho*-H_2O $1_{1,0} - 1_{0,1}$ transition often results in self-absorption from lower excitation foreground gas. This is clearly seen in the water observations shown in paper I and II. The high opacity and self-absorption also prevent a correct abundance estimation. For this reason the optically thin *ortho*-$H_2^{17}O$ and *ortho*-$H_2^{18}O$ transitions are often used as substitutes for column density and abundance determinations. This requires knowledge of the isotopologue ratios in the respective source and introduces additional uncertainties.

3.4 Heating and cooling

The temperature in a molecular cloud is determined by the balance between heating and cooling processes. This is especially important in the context of star formation since the increasing temperature released in the gravitational contraction counteracts a gravitational collapse. Heating and cooling occur by a variety of processes with radiation as the dominant transport mechanism. When a collisionally excited species radiatively decays before another collision occurs, energy will be lost. The kinetic energy will be transferred to radiation that escapes the cloud resulting in decreasing temperature. The gas may also be heated if exposed to a radiation field. An energetic photon may ionise a species and transfer kinetic energy to the released electron. The electron will later share this energy with the other gas particles through collisions, thereby heating the gas. Cosmic rays are another very important heating source, with their ability to reach deep into dense and dark clouds where radiation otherwise is blocked by molecules and dust particles.

To be an efficient coolant a species must have a high abundance and possess energy levels comparable to the average kinetic energy in the cloud. In diffuse clouds with high temperatures and in PDRs, the most important coolants are fine-structure transitions of ionised carbon, neutral carbon, neutral oxygen, and ionised

Table 3.1: A few important cooling species and transitions.

Species	Transition	Wavelength [μm]	E_u^a [K]	A-coeff^b [s^{-1}]
[OI]	$^3P_1 - {}^2P_2$	63	228	8.91×10^{-5}
[CII]	$^2P_{3/2} - {}^2P_{1/2}$	158	91	2.30×10^{-6}
C	$^3P_1 - {}^3P_0$	609	24	7.88×10^{-8}
H_2	$J = 2-0$	28.2	510	2.94×10^{-11}
HD	$J = 1-0$	112.2	128	5.32×10^{-8}
CO	$J = 5-4$	520.6	83	1.22×10^{-5}
^{13}CO	$J = 5-4$	544.5	79	1.10×10^{-5}
C^{18}O	$J = 5-4$	546.6	79	1.06×10^{-5}
H_2O	$J_{K_a,K_c} = 1_{1,0} - 1_{0,1}$	538.7	27	3.46×10^{-3}
$H_2^{18}O$	$J_{K_a,K_c} = 1_{1,0} - 1_{0,1}$	547.8	27	3.29×10^{-3}

^{a}The upper state energy. ^{b}Einstein A-coefficient.

silicon. In Table 3.1, a few important atomic and molecular cooling transitions are listed. The square brackets around the oxygen and carbon transitions denote that these transitions are magnetic dipole transitions (also known as forbidden lines) and provide important sources of cooling. Molecules have more low energy levels available, as compared to atoms, which are readily excited through collisions. At high temperatures and low densities, H_2 is the dominant coolant because of its large abundance, while generally unimportant below 100 K or at high densities. The reason is the lack of low-lying transitions, and very low A-coefficients, which will cause collisional de-excitations to happen before a radiative transition has a chance to occur.

Other well known molecular gas coolants are H_2O, OH, and CO where the latter is the most important coolant at low temperatures and densities. CO has closely spaced rotational levels, is easily excited, and is the second most abundant molecule after H_2. With higher density and temperature, water becomes increasingly more important as a coolant. Under these conditions it dominates the cooling due to its high A-coefficients and high abundance.

If the cloud is not optically thin at the frequency of the emitted photon, the photon will be re-absorbed and trapped within the cloud. This decreases the cooling ability of the transition, and is often the case for the ground state rotational transition of water. In this case the $H_2^{18}O$ isotopologue will become more important. The same problem applies to CO with the $J = 1-0$ transition, always being optically thick in molecular clouds. When the number density of molecular hydrogen is about $10^3\,\mathrm{cm}^{-3}$ the isotopologue ^{13}CO starts contributing to the cooling.

Despite the 40 – 100 times lower abundance compared to ^{12}CO, the cooling by both these species may be of the same order of magnitude.

Interstellar dust grains also serve as important coolants by converting the absorbed energetic UV or FUV radiation to infrared thermal emission from the heated dust grains. This radiation may in turn serve as an important excitation for the water transitions. In addition to their role as coolants, the dust grain may also heat the gas at the same time they absorb UV-radiation and liberate electrons from their surface.

3.5 Summary

The water molecule seems to be indispensable for the chemistry and the evolution of the ISM. It is an important coolant in regions of high density and temperature, it plays an active part in the chemistry, and constitutes the major component of the ices on dust grains where it shields molecules and allows their formation. It is also a valuable diagnostic of shocks and outflows due to the high sensitivity to temperature and density, including the age of the shocks. A high water abundance is a typical signpost of star formation, shocks and outflows.

Chapter 4

Introduction to Papers I & II: A spectral line survey of the Orion KL nebula

A very important part of all research is to compare theory with observations. Sometimes it is the small deviations from an otherwise perfect result that will lead to new unexpected discoveries. It is therefore very important to perform high-quality observations.

An unbiased spectral line survey in a previous unobserved spectral range is a very efficient way to discover new species. If this is performed towards different kind of objects, we obtain valuable information about the chemistry occuring in different environments. Some sources may emit lines from numerous molecules, while the detection rate is very low in other regions. This is a consequence of the response by the molecules to the physical conditions in the medium, including temperature, density, abundance, and the background radiation. Some molecules need very high densities to be excited by collisions with other species, e.g. CN, HCN, or CS. These molecules therefore radiate most strongly when the density is high and are therefore excellent tracers of high-density cloud cores. Other molecules, such as CO, only demand low densities and temperatures for excitation of their lowest transitions and are thus easily observed across extended regions.

A molecule can radiate in many transitions and the strength of each transition is determined by the environment, in addition to the molecular properties. These properties depend on the size, symmetry and the participating elements of the molecule, which also determine the number of allowed transitions. Small molecules have less allowed number of transitions than large, complex molecules. This implies that one of the difficulties to detect large molecules is that the number of lines is very high, and may look like a dense "forest" of weak lines, easily confused with noise.

The accurate determination of oxygen and water abundances in the ISM has

posed a severe observational difficulty: due to the absorption by the same species the terrestrial atmosphere is completely opaque around the strongest transitions at 119 and 557 GHz. Any observations in these spectral regions therefore had to await space or balloon experiments.

4.1 The Odin satellite

The Odin sub-millimetre wave spectroscopy satellite is especially designed to solve these problems. Odin is a small, low-cost, and successful spacecraft with a clever design. By the use of advanced technology two scientific disciplines are combined on a single satellite: astronomy and aeronomy.

The astronomical scientific objectives are to study the water and oxygen chemistry in the ISM and star formation regions, comets and circumstellar envelopes, while the aeronomers study molecules relevant to ozone depletion. Additional species like ammonia and carbon monoxide, including their rarer isotopologues, are also observable to aid the analysis of water and oxygen.

The decision to start the Odin project was made by the Swedish National Space Board (SNSB) in 1994. The development was performed by the Swedish Space Corporation (SSC), on behalf of SNSB, together with the space agencies of Canada (CSA), Finland (TEKES) and France (CNES). The launch took place on 20 February 2001 by a Start-1 rocket from Svobodny in far-eastern Russia. The orbit is sun-synchronous at an altitude of about 600 km.

By now, Odin has successfully been operating almost eight years while the promised lifetime was only two years. Nordh et al. (2003) and the subsequent papers in the A&A Special Letters Edition: *First Science with the ODIN satellite* describe the satellite and its first science in some detail. More recent progress is discussed by Hjalmarson et al. (2005, 2007). The last regular astronomy observations were, however, performed during fall 2007, observing the primordial molecules for paper IV. Since then only aeronomy observations are performed by Odin. At the time of writing this chapter; 19 Nov 2008 at 6.15 PM; the number of days in space for Odin counts to 2 830. The number of orbits around the Earth are 42 214, and of these 2 500 have been used to perform the necessary observations for the presented papers in this thesis.

The Odin satellite is a next sensitive step after NASA's SWAS satellite, which had a $3\farcm3\times4\farcm5$ beam size, and non-tunable receivers (Melnick et al. 2000 and subsequent ApJ letters in that issue). Odin is equipped with an offset Gregorian telescope of diameter 1.1 m, with beam widths of $2\farcm1$ and $10\farcm0$ at 557 GHz and 119 GHz, respectively. The receiver package is actively cooled to about 140 K and consists of four tunable sub-mm Schottky mixers. The frequency bands covered are 486 – 504 and 541 – 581 GHz. In addition, a fixed-tuned HEMT receiver at 118.750 GHz for sensitive O_2 searches was added in a late phase. Any combination of three receivers can be simultaneously used together with a broadband acousto-

optical spectrometer (AOS); bandwidth of 1 050 MHz and resolution 0.6 MHz; and two flexible hybrid autocorrelation spectrometers (AC1 and AC2); bandwidth of 100 – 800 MHz and a resolution of 0.125 – 1 MHz. The main beam antenna efficiency is close to 0.9 which makes the intensity calibration very accurate.

The Odin satellite addresses several key-questions in common with the European Space Agency's Herschel satellite, to be launched in 2009. It will be located at the second Lagrange point of the Earth-Sun system, and will cover the full far infrared and sub-millimetre wave-band (60–670 μm). Herschel will have an order of a magnitude more sensitive SIS mixers compared to Odin, and, in addition, a 3.5 m mirror which is the largest civilian mirror ever deployed in space. The Odin science can therefore serve as important pilot studies with all the studied objects in this thesis as good, and hopefully very useful, examples.

4.2 The Orion KL nebula

In the following two papers, we present the results of an unbiased spectral line survey in a previously unobserved spectral range towards the Orion Kleinmann-Low (KL) nebula.

At a distance of only ∼450 pc, the Orion KL region is the closest high mass star forming region, where O and B star formation is on-going (see Genzel & Stutzki 1989 and references therein for a review). Thousands of stars, including stars many times more massive than our Sun, are produced in this vigorous star forming cloud. It is very complex and chemically structured and contains extremely young and massive embedded stars, not yet visible due to the surrounding dust. All these bright hidden protostars heat the dust which radiates in infrared, producing the brightest infrared region in the 1° large Orion Molecular Cloud OMC-1 complex.

The position on the sky is easy to find, situated about 1′ NW of the Trapezium stars, which is close to the middle star of the sword in the Orion constellation. The brightest object has a spectral type O6 and a mass of 33 $M_\odot$. These stars are found close to the centre of a dense cluster, where the stellar density near the centre is about 10 000 stars per pc^3. This can be compared to our solar neighbourhood where only a few stars in each pc^3 are found. The UV-radiating O stars have cleared much of the ambient gas, allowing about half of the cluster members to be visible in optical light. Their intense radiation has also ionised the surrounding gas in the M42 HII region in front of OMC-1, and the interface between M42 and OMC-1 constitutes one of the famous PDRs in Orion.

The chemical richness in a star forming region like Orion KL, together with its proximity, have made this object an ideal target for spectral line surveys at millimetre and sub-mm wavelengths. And indeed, this is one of the best studied regions of the interaction of young massive stars and their parental molecular cloud. Fig. 4.1 shows a colour composite image of the Orion Nebula. The Odin beam is drawn around the central position of our observations, which is the position of the

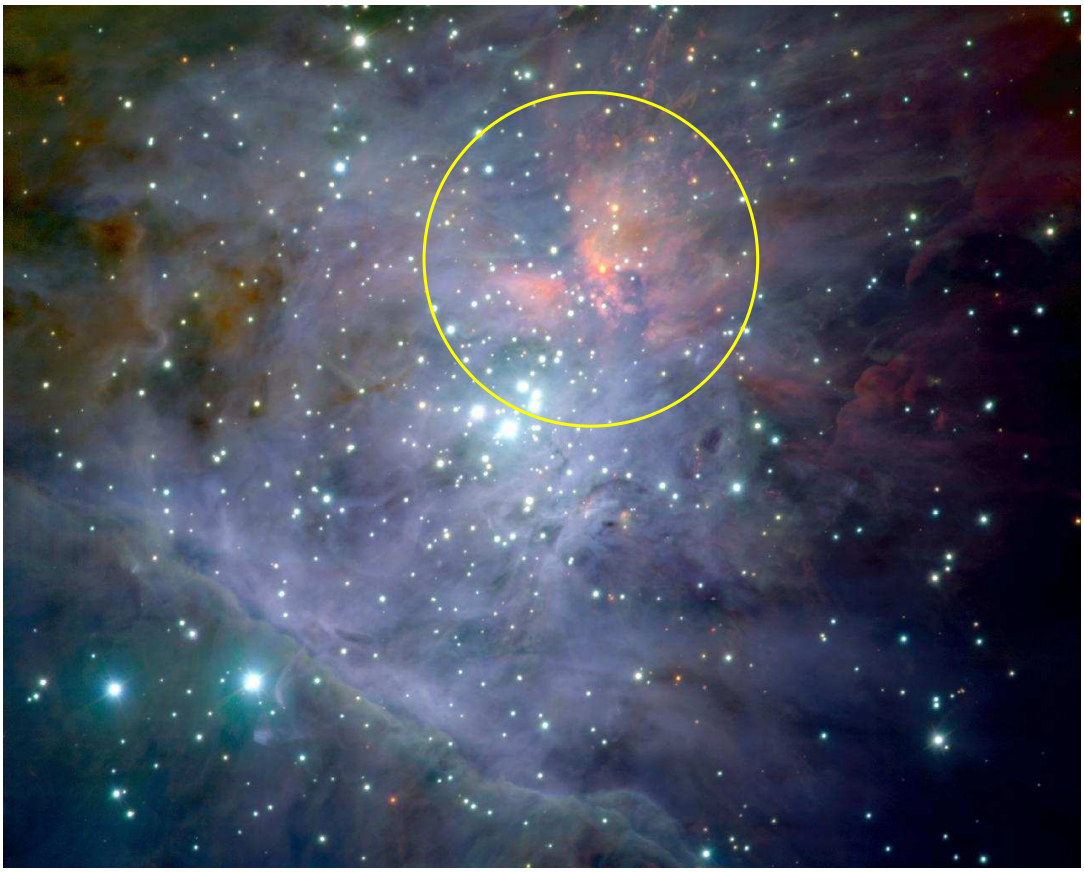

Figure 4.1: The Odin beam overlaid on a colour composite image of the central part of the Orion Nebula, M42, also showing the BN/KL region, based on 81 images obtained with the infrared multi-mode ISAAC instrument on the ESO Very Large Telescope (VLT) at the Paranal Observatory (ESO PR photo 03a/01 2001). The red emission at 2 μm comes from shock excited H_2 caused by a strong bipolar outflow wind from a very young massive star newly born. This is addressed in considerable detail in paper II.

most luminous infrared object in the region Orion KL region, IRc2.

In addition to the chemical structure, the Orion KL region also has a complicated velocity field. The large Odin beam (2′.1 at 557 GHz) encompasses the following subsources: the bipolar *low-* and *high-velocity outflows*, the *hot core*, the *compact ridge* and *extended ridge*, as well as the extended *PDR* region. These regions have different sizes, different centre velocities, and have different velocity fields. This will produce lines with characteristic line widths and shapes at characteristic centre velocities from each subregion, which allow a separation of the emission into its constituent parts.

4.3 Results of Paper I and II

The spectral survey required approximately 1 100 revolutions of observations towards one position in the centre of the star forming cloud. Each orbit gives about one hour of astronomical observations. In the end a 42 GHz wide frequency band was covered between 486 – 492 GHz and 541 – 577 GHz, thereby filling the gaps between previous ground-based spectral line surveys.

The power of a spectral line survey is the detection of numerous lines from many species *with the same beam and calibration* at the same time, thereby reducing uncertainties arising from beam-filling and technical considerations.

Some results:

1. We detect a total of 280 lines from 38 different molecular species. In addition, we detect 64 unidentified lines, representing 19% of the total.

2. The total beam-averaged emission in our survey is dominated by CO, *o*-H_2O, SO_2, SO, ^{13}CO and CH_3OH. Species with the largest number of lines are CH_3OH, $(CH_3)_2O$, SO_2, $^{13}CH_3OH$, CH_3CN and NO.

3. Six water lines are detected, including the ground state rotational transition $1_{1,0} - 1_{0,1}$ of *o*-H_2O, its isotopologues *o*-$H_2^{18}O$ and, for the first time in the ISM, *o*-$H_2^{17}O$, which shows emission from the Low- & High Velocity Flow, and the Compact Ridge. Hot Core emission from water is observed from the *p*-H_2O $6_{2,4} - 7_{1,7}$ transition with an upper state energy of 867 K. We have also observed the HDO $2_{0,2} - 1_{1,1}$ transition from the Low Velocity Flow, Compact Ridge and the Hot Core.

4. Line profiles:
   The *o*-H_2O line has a central asymmetry that suggests strong self-absorption in the blue Low Velocity Flow by lower excitation foreground gas. The remarkable similarity of the line profiles of *o*-$H_2^{18}O$, *o*-$H_2^{17}O$, and SO_2 suggests a similar origin and chemistry of the water isotopologues and SO_2 in the Low Velocity Flow, with additional High Velocity Flow emission mainly in the

red wings. Comparison of the *o*-$H_2^{18}O$ and SO line profiles shows an almost identical line profile in the red wing, suggesting an elevated water and SO production from shock chemistry in the red outflow, which is moving into the molecular cloud. In the blue outflow, which is leaving the molecular cloud, an elevated abundance is only found for SO and not for water, implying an absence of shock chemistry. Contrary, to SO and SO_2, comparing CO with *o*-H_2O, we find that the very broad line profiles, strongly dominated by outflow in both species, are almost identical in the blue wing, while water shows excess emission in the red wing.

5. Clumpy medium:
   The analysis shows that the water outflow emission is most likely emitted from a clumpy medium, filling about a quarter of the Odin beam.

6. We detect the $1_0 - 0_0$ transitions of NH_3 and the isotopologue $^{15}NH_3$. The main isotopologue shows emission from both the Hot Core, Low Velocity Flow and Compact Ridge, while the rarer isotopologue only exhibits emission from the Hot Core where the ammonia abundance is high.

7. Isotopologue abundance ratios of D/H, $^{12}C/^{13}C$, $^{32}S/^{34}S$, $^{34}S/^{33}S$ and $^{18}O/^{17}O$ are calculated, as well as the molecular abundance ratio of O/S, all in agreement with previous findings.

8. Different methods are used to obtain rotation temperatures and column densities. For eight different species with at least four lines and a sufficient energy range in the transitions, the rotation diagram method and the forward model are applied. The LTE approximation is used for all other species.

9. Abundances in each subregion are estimated for all species, and we find very high gas-phase abundances of H_2O, NH_3, SO_2, SO, NO, and CH_3OH. An important fact here is that all our abundance determinations, including those for water vapour, are based upon the same methodology.

10. Since our abundance estimates agree rather well with the results from earlier ground-based spectral surveys, we believe that the water abundances in the various subregions, determined from our Odin observations, also should be accurate.

11. A comparison of our estimated gas-phase abundances with the ice inventory of ISO, sheds new light on the chemical origins of H_2O, CH_3OH, NH_3 and SO_2 in the various Orion KL subregions.

Paper I

A spectral line survey of Orion KL in the bands 486 – 492 and 541 – 577 GHz with the Odin satellite

I. The observational data

A.O.H. Olofsson, Carina M. Persson, N. Koning, P. Bergman, P.F. Bernath, J.H. Black, U. Frisk, W. Geppert, T.I. Hasegawa, Å. Hjalmarson, S. Kwok, B. Larsson, A. Lecacheux, A. Nummelin, M. Olberg, Aa. Sandqvist, and E.S. Wirström

Astronomy & Astrophysics, 476, 791 (2007)

A&A 476, 791–806 (2007)
DOI: 10.1051/0004-6361:20077229

Astronomy & Astrophysics

A spectral line survey of Orion KL in the bands 486–492 and 541–577 GHz with the Odin⋆ satellite⋆⋆

I. The observational data

A. O. H. Olofsson[1,2], C. M. Persson[1], N. Koning[3], P. Bergman[1,4], P. F. Bernath[5,6,7], J. H. Black[1], U. Frisk[8], W. Geppert[9], T. I. Hasegawa[3,10], Å. Hjalmarson[1], S. Kwok[3,11], B. Larsson[12], A. Lecacheux[13], A. Nummelin[14], M. Olberg[1], Aa. Sandqvist[12], and E. S. Wirström[1]

[1] Onsala Space Observatory (OSO), 43992 Onsala, Sweden
e-mail: henrik@oso.chalmers.se
[2] LERMA, Observatoire de Paris, 61 Av. de l'Observatoire, 75014 Paris, France
[3] Department of Physics and Astronomy, University of Calgary, Calgary, AB T2N 1N4, Canada
[4] European Southern Observatory, Alonso de Cordova 3107, Vitacura, Casilla 19001, Santiago, Chile
[5] Department of Chemistry, University of Arizona, Tucson, AZ 85721, USA
[6] Department of Chemistry, University of Waterloo, Waterloo, ON N2L 3G1, Canada
[7] Department of Chemistry, University of York, Heslington, York YO10 5DD, UK
[8] Swedish Space Corporation, PO Box 4207, 17104 Solna, Sweden
[9] Molecular Physics Division, Department of Physics, Stockholm University AlbaNova, 10691 Stockholm, Sweden
[10] Institute of Astronomy and Astrophysics, Academia Sinica, PO Box 23-141, Taipei 106, Taiwan, R.O.C.
[11] Department of Physics, University of Hong Kong, Hong Kong, PR China
[12] Stockholm Observatory, AlbaNova University Center, 10691 Stockholm, Sweden
[13] LESIA, Observatoire de Paris, Section de Meudon, 5 place Jules Janssen, 92195 Meudon Cedex, France
[14] Computer science and engineering, Chalmers University of Technology, 41296 Göteborg, Sweden

Received 2 February 2007 / Accepted 30 August 2007

ABSTRACT

Aims. Spectral line surveys are useful since they allow identification of new molecules and new lines in uniformly calibrated data sets. The subsequent multi-transition analysis will provide improved knowledge of molecular abundances, cloud temperatures and densities, and may also reveal previously unsuspected blends of molecular lines, which otherwise may lead to erroneous conclusions. Nonetheless, large portions of the sub-millimetre spectral regime remain unexplored due to severe absorptions by H_2O and O_2 in the terrestrial atmosphere. The purpose of the measurements presented here is to cover wavelength regions at and around 0.55 mm – regions largely unobservable from the ground.

Methods. Using the Odin astronomy/aeronomy satellite, we performed the first spectral survey of the Orion KL molecular cloud core in the bands 486–492 and 541–576 GHz with rather uniform sensitivity (22–25 mK baseline noise). Odin's 1.1 m size telescope, equipped with four cryo-cooled tuneable mixers connected to broad band spectrometers, was used in a satellite position-switching mode. Two mixers simultaneously observed different 1.1 GHz bands using frequency steps of 0.5 GHz (25 h each). An on-source integration time of 20 h was achieved for most bands. The entire campaign consumed ~1100 orbits, each containing one hour of serviceable astro-observation.

Results. We identified 280 spectral lines from 38 known interstellar molecules (including isotopologues) having intensities in the range 80 to 0.05 K. An additional 64 weak lines remain unidentified. Apart from the ground state rotational $1_{1,0}$–$1_{0,1}$ transitions of *ortho*-H_2O, $H_2^{18}O$ and $H_2^{17}O$, the high energy $6_{2,4}$–$7_{1,7}$ line of *para*-H_2O (E_u = 867 K) and the HDO($2_{0,2}$–$1_{1,1}$) line have been observed, as well as the 1_0–0_1 lines from NH_3 and its rare isotopologue $^{15}NH_3$. We suggest assignments for some unidentified features, notably the new interstellar molecules ND and SH^-. Severe blends have been detected in the line wings of the $H_2^{18}O$, $H_2^{17}O$ and ^{13}CO lines changing the true linewidths of the outflow emission.

Key words. ISM: individual: objects: Orion KL – ISM: lines and bands – ISM: molecules – line: identification – submillimeter – surveys

1. Introduction

Being the most popular target for spectral line surveys, in the Orion KL position OMC-1 has been the focal point of at least ~20 observational efforts in the mm and submm bands over the last 20 years, starting with Johansson et al. (1984, 1985), and in the frequency range 72–91 GHz. White et al. (2003) provide an extensive list of this earlier work in their introduction. Using the James Clerk Maxwell Telescope (JCMT),

⋆ Odin is a Swedish-led satellite project funded jointly by the Swedish National Space Board (SNSB), the Canadian Space Agency (CSA), the National Technology Agency of Finland (Tekes), and the Centre National d'Études Spatiales (CNES, France). The Swedish Space Corporation (SSC) was the industrial prime contractor and is also responsible for the satellite operation.

⋆⋆ Appendix B is only available at electronic form at http://www.aanda.org

White et al. (2003) surveyed the bands 455–469 and 492–507 GHz, surrounding the lowest frequency range of our Odin spectral scan (486–492 GHz). The frequency range 607–725 GHz, just above the Odin spectral scan band 542–576 GHz, has been surveyed by Schilke et al. (2001) using the Caltech Submillimeter Observatory (CSO).

More recent additions include 159.7–164.7 GHz (Lee & Cho 2002), 795–903 GHz (Comito et al. 2005), 260–328 GHz (Yoshida & Phillips IAU 231[1]), and an IRAM 30 m survey (168 GHz in three windows between 80 and 281 GHz) by Tercero et al. (IAU 231[1]).

The first imaging line survey of Orion KL in the submm range (337.2–339.2 and 347.2–349.2 GHz) was recently reported by Beuther et al. (2005), who used the Submillimeter Array interferometer. They later employed the same instrument to make measurements around 680 and 690 GHz with similar bandwidths (Beuther et al. 2006).

The luminous Orion Kleinmann-Low infrared nebula (Orion KL; $L \approx 10^5\,L_\odot$), and its surrounding molecular cloud, is the nearest (distance of 450 pc) and probably most studied massive star formation region in the sky. A very useful review has been written by Genzel & Stutzki (1989); for reference updates see e.g., Olofsson et al. (2003), and Wirström et al. (2006). Here we summarise some source component designations and dynamical properties particularly relevant to the molecular line identification work in the current presentation of our Odin spectral scan data, which includes our molecular line assignments (in the Online Table 6).

Odin's circa 126″ antenna beam is centred on the most prominent infrared "point" source in the KL nebula, IRc 2 (RA $05^{\rm h}35^{\rm m}14\overset{\rm s}{.}36$, Dec. $-05°22'29\overset{''}{.}6$ (J2000)). The Orion *hot core* source, with a size of only ≈10″ and centred only 2″ S of IRc 2, is a warm (≈200 K, or even higher; cf. Sempere et al. 2000), dense ($\approx 10^7$ cm^{-3}) clump or rather collection of clumps, characterised by a spectral line width of 5–15 km s^{-1} centred on $v_{\rm LSR}$ = 3–6 km s^{-1} and exhibiting emission from nitrogen-containing species at markedly enhanced abundances. The outflowing gas, or the *plateau source*, with a size of 40–60″, may be characterised in terms of a bipolar *high-velocity flow* elongated in the SE-NW direction (reaching velocities of ±100 km s^{-1}), and a SW-NE extended *low-velocity flow* (the "18 km s^{-1} flow") of size 15–30″, centred on 10 and 5 km s^{-1}, respectively. Further details on the complex structure of the outflow – such as a central jet and localised "bullet" type emission within the high velocity flow – are nicely revealed by the IRAM 30-m CO J = 2–1 maps by Rodríguez-Franco et al. (1999). Within the Odin 126″ antenna beam there is also an N-S extended quiescent molecular cloud structure (the *ridge*), with densities of 10^4–10^6 cm^{-3} and temperatures in the range 20–60 K, and characterised by line widths of 3–5 km s^{-1} and an abrupt velocity shift across the KL nebula from $v_{\rm LSR}$ = 8 km s^{-1} (in the south) to 10 km s^{-1} (in the north). The large-scale chemical structure of many important ridge molecules is outlined in Ungerechts et al. (1997).

The interaction between the bipolar high-velocity outflow and the surrounding ridge gas produces shock heating and shock enhanced chemistry, markedly visible in terms of bright H_2 emission, strong high-J CO lines and uniquely strong emission from abundant H_2O (Melnick et al. 2000; Olofsson et al. 2003). Also the roughly orthogonal low-velocity outflow component appears to interact with the ambient gas, creating density, temperature and column density enhancements in the ridge gas. One such feature is the *compact ridge cloud* (Δv = 3 km s^{-1}; $v_{\rm LSR} \approx 8$ km s^{-1}) situated only 10–15″ S of IRc 2, on the northern tip of the 8 km s^{-1} ridge cloud, where complex oxygen-containing molecules have been observed to be abundant. The hot core itself might also be a result of shock-induced compression. A recent finding along these lines is enhanced [CI] forbidden line ($^3P_2$–$^3P_1$) emission north and south of IRc 2 (in a shell of radius ≈20″, where the outflow encounters ambient gas), and proposed to result from CO dissociation in shocks (Pardo et al. 2005).

Although the major source constituents are commonly discussed in the literature as outlined above, we caution readers that observations yielding higher spatial resolutions (e.g. Blake et al. 1996; Wright et al. 1996; Beuther et al. 2005, all employing aperture synthesis) reveal that the KL core composition is in fact more complex and breaks down into further sub-structures of sizes $\lesssim 10^3$ AU.

We present here the observational results and line identifications. Numerical analyses such as column density and rotation temperature estimates are included in an accompanying paper in this A&A issue (Persson et al. 2007, Paper II hereafter).

2. Observations

The present data-set was obtained in a four-part campaign running over 1.5 years, starting in spring 2004 (Feb.–Apr.), followed by fall 2004 (Aug.–Oct.) and continuing in the same manner in 2005. This division naturally arises from the combination of source coordinates and Odin's orbital plane (Sun-synchronous low Earth orbit) leading to seasonal visiblilty constraints for low-declination sources such as the Orion nebula.

The dedicated observing period spanned over ∼1100 revolutions with a very high success rate due to consistently stable spacecraft performance. Each orbit allows 61 min of astronomical observations, whereas the source line-of-sight is occulted by the Earth and its atmosphere for the remaining 35 min of the orbital period. We employed position switching (PSW) in order to acquire cold sky reference spectra. This was implemented by regularly reorienting the entire spacecraft by −15′ in RA with a cycle time of 1 min, carried out by the onboard momentum wheels. The resulting efficiency penalty for slew time was low (<20%).

The beam size and main beam efficiency of Odin's 1.1 m offset Gregorian telescope at 557 GHz are 2′1 and 0.9, respectively, as measured in continuum observations of Jupiter assuming a Jovian brightness temperature of 145 K and a disc-like source geometry (Frisk et al. 2003).

The pointing is maintained in real time by the attitude control system, assisted by two star trackers with an angular separation of 40°. It has been empirically established that the reconstructed attitude uncertainty is ≤15″ most of the time.

There are four tunable submm receivers of single-sideband (SSB) type in the radiometer, all of which were employed for these measurements. Image band rejection is achieved using Martin-Puplett filters with cooled termination absorbers and Schottky mixers are used for frequency down-conversion. The channels have centre frequencies of 495, 549, 555, and 572 GHz and the design of the receiver system allows simultaneous use of RX555 and RX572, or RX549 and RX495 (Frisk et al. 2003).

The tuning range of 14 GHz was not fully exploited in all channels although the combined results from the complementary pair RX549 and RX555 cover all their accessible frequency range. System temperatures in the passband centres were around

[1] Poster contributions at Symposium No. 231 of The International Astronomical Union, Asilomar 2005. Abstracts available at `http://asilomar.caltech.edu/`

3000–3500 K with few exceptions as measured by switching between the main beam and a hot load at room temperature. For a given tuning, $T_{\rm sys}$ does not change in time by more than a few percent due to the stable conditions and no interfering atmosphere.

The observing strategy was to tune the receivers in 0.5 GHz steps and observe for 25 orbits. The resulting overlap in between adjacent tunings gives a net on-source integration time of $50 \times 61 \times 0.8/2 \approx 20$ h per channel. This commonly used approach was adopted to reduce potential impacts of artificial spectral patterns/transients or baseline effects which could arise in one tuning but conceivably not in both.

Three spectrometers were used: one acousto-optical spectrometer (AOS) and two hybrid autocorrelators (AC1/2). The former has a bandwidth of 1.1 GHz and a channel spacing of 620 kHz, while the latter two can be used in several modes. In the low resolution mode used here, the bandwidth is 700 MHz with 1 MHz channel spacing. The AOS and the ACs have rather different characteristics and therefore we have used slightly different approaches in building the final spectra, hence the division into two parts of the next section.

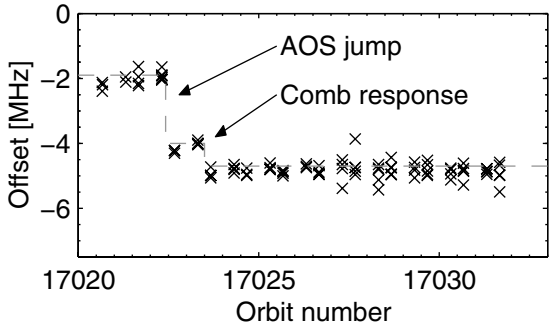

Fig. 1. Tracing the frequency deviation using the telluric $H_2^{17}O$ line. As is evident, there was an early sudden shift of the line position, corresponding to an AOS laser mode jump during warming up – a small penalty because of our shared astronomy/aeronomy mission. The times of such shifts can be determined accurately since they affect the total power levels of the spectrometer. The gray dashed line shows the correction applied to the data from this sample observation.

3. Data reduction

The data reduction has been performed in two parallell, independent efforts by members of the Odin Team situated at the Onsala Space Observatory and in the University of Calgary. The spectra presented in this paper are the products of the data reduction at Onsala. The very similar Calgary results have been used to verify the quality of the spectra shown here. Although a few differences were found for lines at a level below 0.1 K (or below 4σ in terms of the baseline noise), we are encouraged to believe that the majority of such weak lines are real.

3.1. AOS and data from RX549/RX555

3.1.1. Calibration and averaging

There were essentially three complicating factors that needed special consideration in these data sets.

Frequency correction: by using telluric ozone and water (and occasionally rarer lines during the occultation phase, the capability exists to check the frequency setting to a very high accuracy, as is illustrated in Fig. 1. It was found that there was an offset of 0–5 MHz from the commanded value leaning towards the upper value most of the time. Furthermore, on a few occasions the offset was seen to change instantaneously by 2–3 MHz in mid-observation between two apparently stable offset levels. Thus it was deemed necessary to register telluric frequency references at all times and correct the astronomical spectra accordingly. If no atmospheric lines were present in a particular tuning, overlapping astronomical lines inherent to a different but adjacent tuning with a known frequency correction, were cross-correlated to find the proper correction. This method gave consistently positive results and we now believe that the absolute frequency uncertainty is 1 MHz ($\approx$0.5 km s^{-1}) at worst.

Channel dependent RMS: probably owing to the large bandwidth of the AOS, the system temperature profiles had rather steep gradients towards the upper and lower edges, often leading to noise temperatures in these portions twice the mid-spectrum values. When averaging together two adjacent tunings, the low-noise central channels from one tuning will be combined with the high-noise edge channels of the other. This has been taken into account in the weighting procedure by letting the most recently measured $T_{\rm sys}$ profile represent the formal noise *in each channel* of the the next spectrum to be included in the average. Provided that the integration times and resolutions are all the same, and that we have a good linear correlation between $T_{\rm sys}$ and the channel RMS, this approach is easily justified.

Side-band suppression: In general, we have very good suppression of the undesired image band ($\gtrsim$20 dB in at least one tuning). In the RX555 tunings, there is one exception where the appearance of an image SO line indicates a suppression of only 10 dB. Similarly poor SSB suppression was seen more frequently in the RX549 data through the emergence of telluric image ozone lines in occultation phase data. As is evident in the final result, we had in general more problems with high $T_{\rm sys}$ and unexplained baseline ripples in this front-end/backend configuration, probably related to the poorer SSB performance. In those cases where image lines were seen in the final average (almost exclusively due to the strong H_2O and ^{13}CO lines at 557 and 551 GHz, respectively), the appropriate channels were excluded to remove the interference. The complementary tunings certified that no gaps were created in the total average, although the noise is visibly higher in these portions due to less net observing time. Potential low-level image line intrusions are in general sufficiently weakened not to be seen in our baseline noise, owing to the satellite motion Doppler correction which serves to disperse image band signals.

Other pre-averaging measures consisted of first linearising the readouts of the AOS aided by internal frequency comb measurements, then resampling the AOS spectra to whole MHz to match the AC resolution.

The individual spectra each represent one on-source observation in the PSW cycle which is equivalent to 24 s integration time. During one such observation, the variation of the projected satellite orbital velocity in the direction of the source is not taken into account which introduces a slight spectral smearing of astronomical lines. However, the magnitude of the Doppler shift change *at most* amounts to $\sim$200 m s^{-1} and is considerbly less for the major part of the orbit.

The baseline stability was very good (Sect. 3.1.2) and no fits were subtracted from the spectra in the averaging procedure.

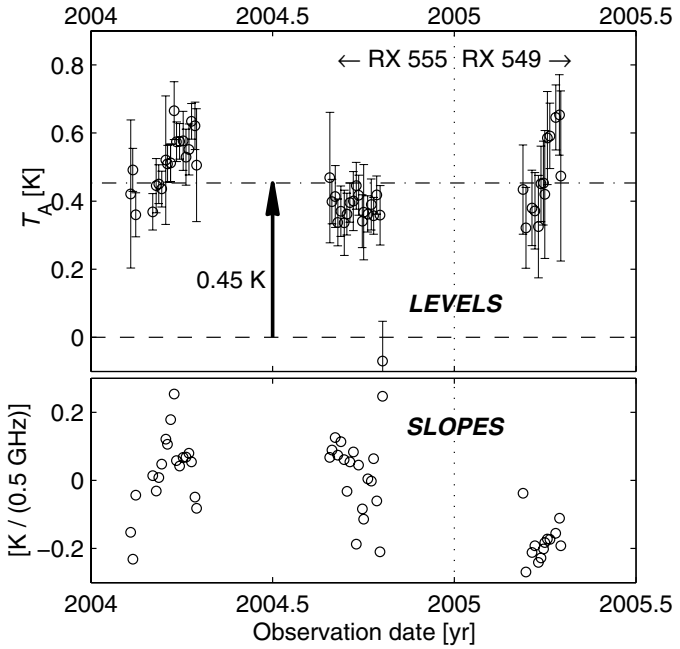

Fig. 2. Baseline levels and slopes in 52 RX555 and RX549 observations before any baseline subtractions. The error bars in the upper panel correspond to 3σ. The slopes are measured as the level difference of two halves of the spectra whose centres are separated by 496 MHz. This figure indeed highlights the stability of the receiver/AOS/calibration chain, but the upwards trends of the levels towards the ends of both spring observing runs remain unexplained. There is also an observation that inexplicably appears to lack continuum signal (while telluric spectral lines could still be detected).

However, to obtain accurate line property estimates for the very weak features, we opted to subtract a piecewise linear fit from the broadband end products, putting the baseline level at zero around clearly detected emission lines.

3.1.2. Baseline stability/continuum level

We have estimated the dust continuum beam averaged antenna temperature around 550 GHz using the spectra from the RX549 and RX555 receivers. One value was extracted for each tuning as shown in Fig. 2 and the average amounted to $T_{\rm A} = 0.45$ K (1800 Jy beam^{-1}).

Due to the crowding of strong lines in some tunings, this calculation relied on noise statistics and did *not* require that the positions of lines were known beforehand. The assumptions made were instead i) at least half the channels in a spectrum were largely unaffected by emission lines, ii) the baselines are largely flat compared to the noise scatter of the intensity in individual spectra, and iii) the noise is Gaussian and the RMS is well described by its formal value derived from the radiometer formula.

The simple procedure was then to sort all channels according to increasing intensity and select the bottom half of the distribution (the top half is "contaminated" by emission lines). Statistically, the expectation value of the distribution is then found by adding $0.8 \times {\rm RMS}_{\rm formal}$ to the mean value of the selected low-intensity channels.

To further remove effects of baseline variations, and to get a handle on the baseline stability, each spectrum was divided into two 500 MHz subspectra on which the calculation described above were performed. The average difference between the two halves in each tuning then additionally supplied an indication of the first order trend (or slope) of the baselines. Figure 2 also illustrates the results found here. Although it is obvious that a systematic baseline pattern was present throughout the RX549 observations, the RX555 baseline performance is quite satisfactory.

3.2. ACs and data from RX495/RX572

The 700 MHz AC spectra are created by stitching together seven 112 MHz portions. To achieve the double coverage of each frequency interval as we do with the AOS, one AC was split into two portions, 3+4 subbands, and placed on each side of the other AC that covered the central 700 MHz in the passband.

Each such sub-band is typically "well behaved" in terms of having Gaussian noise and a uniform gain curve. However, in the PSW observing mode there is for unknown reasons a linear falloff in channel intensity from the start of each on and off sequence. Due to the inescapable slight asymmetry between on and off measurements, and to the fact that the drift rate changes gradually over the channels in one sub-band, the calibrated spectra end up with a low-level curved saw tooth-like appearance with two sub-bands forming each tooth. This pattern has been removed by using high-order polynomials after careful comparisons with the results obtained by calibrating each sub-band separately. Around the extremely broad CO line at 576.3 GHz, this method failed and the corresponding two tunings were instead cured by employing a corrective procedure that nullifies the effects of the intensity drift mentioned above but is very time-consuming.

The uppermost 200 MHz of the RX495 spectrum were acquired from a tuning that suffered instability; the LO alternated between being properly locked and oscillating between frequency offsets of ±33 MHz. Using the recorded IF current and the amplitudes of the [CI] forbidden line line at 491.7 GHz (visible in individual spectra, $T_{\rm A} \approx 6$ K) as guides, about ten minutes of integration was recovered. In spite of the higher noise level thus obtained, we chose to include this spectral section since it contains two strong lines, the [CI] and a low-energy methanol transition ($T_{\rm A} \approx 1.2$ K).

We did not find any evidence of image band lines interfering in the signal side band for these two receivers, nor did we find any significant frequency offsets (at most ≈ 1 MHz) from nominal values in telluric line position controls in sample tunings.

4. Results

4.1. Summary

Table 1 lists some general figures and characteristics for the survey as a whole. As is evident from this Table, our integrated intensity is dominated by the continuum emission by a ratio of 5:1 (see Sect. 3.1.2 for details). The line-to-continuum ratio found here, 20%, is much lower than that at 350 GHz, 50%, but rather close to the 15% found at 650 GHz (Schilke et al. 2001). For a larger telescope (such as the Herschel Space Observatory) one can expect this value to increase somewhat due to increased intensity from the abundant lines from the compact line sources ($<10''$) compared to the dust continuum source whose KL component is about $30''$ as seen in for example the 345 GHz bolometer map of Siringo et al. (2004).

Table 1. Survey overview.

Property	Value
Bandwidth covered	42 GHz
Number of lines detected[a]	344
Line density	8 GHz^{-1} (range: 4–20)
Line intensity range	0.05–80 K
Number of species detected[b]	38
Typical RMS reached	~25 mK/1 MHz channel
Total $\int T_A\,dv$	2 455[c]/2 525[d] K km s^{-1}
Total line luminosity[e,f]	5×10^{26} W
Mean line-to-continuum ratio[g]	0.2

[a] Incl. U- and T-lines (see Sect. 4.4). [b] Including isotopologues and C I. [c] Over all lines detected. [d] Over all measured frequencies. [e] Using the expression $2.65 \times T_r \times \theta/\lambda$ where $\theta = 2.1'$ and λ is given in centimetres, to find the flux density per beam. [f] Using a beam-filling correction factor of 1.25 for data near 490 GHz. [g] Near 550 GHz.

4.2. Spectra and identifications

The final spectral scan results from the four receivers can be seen in Figs. A.1–A.4. The frequency scale is counted w.r.t. a source velocity of $v_{LSR} = +8$ km s^{-1}, and markers are placed at the laboratory rest frequencies of the transitions attributed to the line features.

The general method for identification was to select the most plausible species after comparisons with available molecular databases[2] (SLAIM03: Lovas 2003; CDMS: Müller et al. 2001; JPL: Pickett et al. 1998) of predicted/calculated or directly measured transition frequencies (SLAIM03 contains both kinds wherever available). The selection criteria included: frequency coincidence, expected abundance, line strength, line width, line velocity, and upper state energy. Where possible we have also used rotation diagram analysis (cf. Goldsmith & Langer 1999) to guide our identification, as discussed in Paper II.

In the case of marginally detected line features suspected to arise from more complex molecules such as dimethyl ether and methyl formate, we also required that other lines of similar expected emission characteristics be visible at other frequencies within the observed bands.

It is important to note that any conceivable artificial sharp features produced in the radiometer would likely be stable in the sky frequency rest frame and thus would be significantly smeared here since the satellite motion Doppler correction of each spectrum varies between –7 and +7 km s^{-1} over one orbit.

The line counts, upper state energy ranges and total integrated intensities for each detected molecule are listed in Table 2. All identifications (molecule and laboratory rest frequency) can be found in Table 6 (available on line).

Also of interest here are the spectral offsets of the measured lines relative to the laboratory frequencies. We have estimated these from the value found at the peak intensity channel of the lines (assuming a systemic emission velocity of +8 km s^{-1}) and they are listed in full in Paper II. The average offset per molecule is −0.6 MHz but this cannot be used as a quality measure of the data fidelity nor the accuracy of tabulated rest frequencies since different molecules emit at different velocities (as is likely reflected by the high dispersion, 3.2 MHz). In addition, these emission velocities are often instrument-dependent due to varying beam fillings of the different source components. Nonetheless, by choosing the 35 strongest lines of methanol (which conveniently has narrow emission lines), we minimise this effect and get a dispersion of only 1.1 MHz. While this is slightly higher than the stated estimated frequency uncertainty of our spectra, there are a number of possible remaining explanations aside from data error such as lab measurement/calculation error and line blending.

[2] On line locations at `http://www.cdms.de/` (CDMS) `http://spec.jpl.nasa.gov/` (JPL) (SLAIM03 is not available on line but some of its content is maintained under `http://physics.nist.gov/PhysRefData/`).

Table 2. Summary of all detected species.

Species	Number	Energy range [K]	$\int T_A\,dv$ [K km s^{-1}]
CH_3OCH_3	47	106–448	18.3
SO_2	42	75–737	239.9
$^{34}SO_2$	5	79-457	2.6
SO	5	71–201	181.5
^{33}SO	3	191–199	6.5
^{34}SO	2	191–197	15.6
CH_3OH $v_t = 1$	42	332-836	
CH_3OH	34	38–863	108.6
$^{13}CH_3OH$	21	37–499	6.8
$^{13}CH_3OH$ $v_t = 1$	2	373–670	
CH_3CN	17	410–1012	9.3
NO	12	84–232	11.1
CN	8	54	8.5
H_2CS	5	138–343	1.7
H_2CO	3	106–133	38.5
$H_2^{13}CO$	1	130	0.6
HDCO	3	114–141	2.8
OCS	3	604–658	1.3
o-H_2O	1	61	320.3
p-H_2O	1	867	2.2
o-$H_2^{17}O$	1	61	9.4
o-$H_2^{18}O$	2	60–430	16.2
HDO	1	66	10.7
HC_3N	2	648–799	0.6
CO	1	83	1100
^{13}CO	1	79	174.3
$C^{17}O$	1	81	6.0
$C^{18}O$	1	79	24.3
C	1	24	38.7
NH_3	1	27	20.6
$^{15}NH_3$	1	27	0.7
HNC	1	91	10.7
N_2H^+	1	94	1.5
H_2S	1	166	4.4
CS	1	129	24
^{13}CS	1	173	v blend
SiO	1	190	17.6
^{29}SiO	1	187	1.4
^{30}SiO	1	185	0.5
HCS^+	1	186	v blend
NS	1	442	v blend
U-line	28	–	9.1
T-line	36	–	7.2

4.3. Important line blends

A means to identify and subsequently remove "interfering" lines is helpful, particularly in the detailed study of line shapes (where the signal-to-noise ratios of the lines are such that this is feasible).

It now seems convincingly clear that the line wings of the rarer isotopologues of water and carbon monoxide are affected by emission from SO_2, $^{34}SO_2$, CH_3OH and CH_3CN. Fortunately,

the emission from these species can be accurately modelled due to the wealth of other lines from these species present in our band, allowing determinations of column densities and excitation temperatures. We have in the course of our analysis tried to reconstruct the true shapes of some lines by subtracting polluting emissions from our spectra, and in Paper II one successful example is demonstrated ($H_2^{17}O$).

We caution that this approach is only useful in contexts where the interfering lines emit in an optically thin portion of the main line (or if the gas is stratified so that the optically thin line arises in the near side of the gas column). For instance, we do not find it likely that the SO_2 line at 556.960 GHz significantly alters the profile of the main water line (at 556.936 GHz) since i) the optical depth towards the centre of the water line is very large, and ii) according to the interpretation in Olofsson et al. (2003) the High Velocity Flow as seen in water is located in front of (or around) the Low Velocity Flow from which the sulphur oxide lines mainly originate, as evidenced by their line widths and source size.

4.4. Unidentified line features

We have defined U-lines – clearly detected lines well distinguished from the baseline noise – and T-lines, which are only marginally visible (T for "Tentative") against the noise, or in an apparent line blend. The lines of both types are marked in the spectra and listed in Table 3.

We have in some cases found candidate species (Table 3) which have not fulfilled all our criteria for an unequivocal designation and they are kept as U- or T-lines. Some of the more interesting scenarios are discussed below.

4.4.1. New SO^+ lines?

Interstellar SO^+ was first detected in the shocked clump IC443G, presumably being formed in the dissociative shock caused by the supernova remnant (Turner 1992). Our weak unidentified lines at 486.845 and 487.209 GHz tentatively can be identified as the $J = 21/2$–$19/2$ e and f doublet of the reactive radical SO^+ in its $^2\Pi_{1/2}$ ground state (JPL; Amano et al. 1991). The suggested assignment is consistent with the detection in Orion KL of lower energy SO^+ lines at 115.804, 116.180, 208.590, and 255.353 GHz (Turner 1994). Our assignment is further strengthened by the U-line at 347.743 GHz observed by Schilke et al. (1997) which we identify here with the $J = 15/2$–$13/2$ e transition of SO^+ at 347.740 GHz. However, the corresponding f transition at 348.115 GHz is hidden in a blend with $^{13}CH_3OH$ and $^{34}SO_2$.

4.4.2. Other notable frequency coincidences: SH^- and ND

Our weak, slightly broad lines near 546.138 and 546.176 GHz could be associated with the $N_J = 1_1$–0_1 hyperfine transition cluster of the ND radical in its $X^3\Sigma^-$ ground vibronic state (CDMS; Saito & Goto 1993; Takano et al. 1998). If so, the strongest component is at a blue-shifted position closer to the Hot Core velocity, in agreement to what is seen in other nitrogen hydrides such as NH_2 (which we tentatively conclude to be blue-shifted after studying the 900 GHz spectral survey of Comito et al. 2005 in detail). NH_3 on the other hand – discussed further in Paper II – has a ∼60% Hot Core contribution but this is heavily masked by its optical depth in both the Hot Core and in the Compact Ridge. Unfortunately, the predicted shape of the line bundle as a whole does not match the observation and one would need to invoke non-LTE excitation to explain this difference.

A weak unidentified line at 564.418 GHz may originate in the $J = 1-0$ rotational transition of SH^- in its $X^1\Sigma^+$ ground state, measured to fall at the frequency 564.422 GHz (Civiš et al. 1998). A new interstellar anion would be of utmost interest since only one has been found previously, namely the discovery of C_6H^- which was recently reported by McCarthy et al. (2006). Thus – although our line is not strong enough to claim a detection (∼3.5σ relative to the local noise) – we chose to perform a very simple column density calculation (or an upper limit thereof if the line turned out false). By employing the LTE assumption with full beamfilling, an excitation temperature of 100 K, and a dipole moment of 0.273 D (adopted from the ab initio calculations of Senekowitsch et al. 1985), we arrive at a figure of $N_{SH^-} = 2 \times 10^{13}$ cm^{-2}. The scenario used would be consistent with SH^- residing in the extended OMC-1/M42 face-on PDR (discussed in Wirström et al. 2006). Should the origin of the line (if real) be any of the smaller Orion KL components – as indeed the observed line width ($\Delta v_{FWHM} = 11$ km s^{-1}) seems to indicate – the column density rises by a factor of ∼200. We deem at least the PDR column density to be a reasonably low value in light of the rather unknown chemistry of similar hydrides in

Table 3. Unidentified (U) and/or marginally detected (T) lines.

Frequency [MHz]	Type [U/T]	Sugg. ident.
486 845	T	SO^+
487 209	U	SO^+
487 507	T	CH_3CHO
488 477	T	–
488 598	U	CH_3OCHO
488 633	U	CH_3CHO
489 193	T	–
489 709	T	SiS
491 496	U	CH_3OCHO
491 892	U	–
541 926	T	–
541 981	U	CH_3OCHO
542 945	U	–
543 873	U	–
544 016	T	SiS
546 138	U	ND
546 176	T	ND
546 662	T	–
546 805	T	–
547 080	T	–
547 162	T	–
547 262	T	HNCO
549 142	T	HNCO
549 199	T	HNCO,H_2CS
549 449	U	–
549 719	T	SO_2,$(CH_3)_2O$
550 132	T	SO_2
552 308	U	–
552 846	T	–
553 667	U	CH_3OCHO
553 716	U	–
555 312	T	–

Table continued

Frequency [MHz]	Type [U/T]	Sugg. ident.
555 914	T	–
555 933	T	–
556 267	T	–
556 633	T	–
559 239	U	CH_3OCHO
559 816	T	HDO
559 861	U	CH_3OCHO
559 913	U	–
560 753	T	–
561 971	U	–
562 118	T	–
562 960	U	–
563 033	U	–
563 481	T	HNCO
564 105	U	–
564 418	T	SH^-
566 066	U	–
567 485	U	–
569 138	U	HNCO
570 303	U	–
570 335	T	–
570 790	T	–
570 814	T	–
571 151	T	HNCO
571 217	T	HNCO
571 477	T	$H_2C^{18}O$
572 596	U	–
572 678	U	–
574 184	U	–
575 397	T	–
576 446	U	–
577 160	T	–

the interstellar medium. The SH radical, for instance, has only been found in the atmosphere of a Mira variable through mid-IR transitions (Yamamura et al. 2000). Nevertheless, a possible contribution from SH in a C_3 spectrum towards Sgr B2 has been reported by Cernicharo et al. (2000). We also note that a formation pathway exists involving H_2S (via dissociative electron attachment), a molecule observed by Odin in the present survey and treated in Paper II.

Both these candidates (marked by gray arrows in the spectra figures) can be confirmed or ruled out by the forthcoming Herschel mission (discussed further in Sect. 5). For the case of ND, the triplets of NH at 947 and 1000 GHz are also relevant.

4.5. Non-detections

Two notable non-detections have been indicated by gray arrows in our spectra: the PH and O_2 molecules. The PH line (a hyperfine transition within the $N_J = 1_1$–0_1 group at 553.363 GHz) has also been searched for in IRC + 10216 by Odin to a much higher sensitivity by Bernath et al. (2007), and we refer to them for details on the PH physical and chemical properties and its role in the circum- and interstellar medium. The O_2 line at 487.249 GHz has previously been searched for by the SWAS satellite (having a larger beam size) down to a sensitivity of 6.4 mK (Goldsmith et al. 2000) without success. Both O_2 non-detections are consistent with the Odin upper limit from the ground state transition at 118.750 GHz by Pagani et al. (2003).

4.6. Improvements of existing spectroscopic data

In the case of our rather weak H_2CS lines, we did at first find frequency offsets between 6 and 14 MHz systematically redwards of the expected values (as given in the JPL database which indeed stated high uncertainties for these calculated H_2CS frequencies). Prompted by private communication, an entry for this molecule was subsequently inserted into CDMS and the new calculated rest frequencies found there gave very good agreements with our measured positions in all but one line. This is an encouraging result proving that large measured frequency offsets are likely not to be spurious and may in some cases indicate that the existing tabulated spectroscopy data are off the mark.

In the case of H_2CS, new extensive laboratory spectroscopy work has kindly been performed by Eric Herbst and his collaborators. The resulting H_2CS database will be crucial for Herschel Space Observatory.

In general, we hope that our measured line parameters (listed in bulk in Paper II) may be useful for accurate determination of molecular data such as rotational constants.

5. Discussion of future observations

No further Odin observations of this kind are currently planned and the observation time cost for significant noise reduction would in any case be prohibitive. However, the spectral portions presented here will be reobserved by the Herschel space observatory[3] and is of interest to briefly discuss what they could obtain. Herschel is a European Space Agency (ESA) satellite mission aimed at launching a 3.5 m telescope equipped with very low noise submm/far-IR heterodyne receivers in 2008.

Most of the identified lines in this survey belong to species already observed at other transitions (at both lower and higher frequencies) and source size estimates for the corresponding emission components are available in the literature (e.g. references in Sect. 1 and Paper II). A rough Herschel beam-filling estimate based on these source sizes reveals that those lines will be 1–10 times stronger in the Herschel spectrum, with the majority leaning towards the higher end. Assuming further an observation time of only one hour in combination with recent figures for the Herschel receiver system sensitivity, one finds that the signal-to-noise ratio will be increased by up to a factor of 20 in such a case. This will be particularly useful for the weakest lines (5–10σ) seen in the Odin survey which will be possible to study in some detail in the Herschel spectrum. It is in this group we find nearly all the unidentified lines and the potential for new discoveries among them is obvious. The interesting frequency coincidences of SH^- and ND described earlier are good examples. The interpretation of these and even weaker lines runs, however, the risk of being hampered by line crowding and blending (already up to 20 lines/GHz in our spectrum) due to the plethora of lines that will emerge from the noise compared to the Odin spectrum. This in turn will put high demands on the system baseline stability in order to correctly disentangle the emissions. The pollutive contributions in the key water isotopologue lines discussed above will also be worsened (due to differential beam-fillings) and on a side note one can predict that this problem will arise in most sources where Herschel observes these species.

6. Conclusions

We have conducted a spectral survey in two submillimetre windows largely inaccessible from the ground due to atmospheric opacity. The frequency ranges covered are: 486.4–492.3 and 541.5–577.6 GHz. This was achieved using the Odin submm satellite.

The spacecraft performance was generally excellent in terms of high observing efficiency and good sideband suppression most of the time (within the SSB receivers).

The baseline stability has been shown to be satisfactory, albeit high-order polynomials being required in about 50% of the data to remove a fixed pattern arising in the autocorrelators in this particular observation setup.

Careful attention has been paid to the frequency alignment of our data resulting in an estimated frequency error of $\lesssim$1 MHz.

Thus, high confidence is warranted in the fidelity of the reduced spectra. To ascertain the calibration accuracy, some lines have also been compared to previous or later targeted Odin observations using markedly different instrumental setups.

We found a total of 280 identified emission lines (some of which include multiple transitions), and 28 unidentified lines. We have also pointed out a further 36 borderline detected features which in some cases have interesting candidate assignments such as SH^- and SO^+.

Among the 38 detected molecules, we have four water isotopologues seen in at least five emssion lines. These data are used in Paper II to make a water abundance analysis.

Column density estimates for all species are presented in Paper II, as well as abundance, source size, and rotation temperature estimates for a selection of molecules.

Acknowledgements. Generous financial support from the Research Councils and Space Agencies in Sweden, Canada, Finland and France is gratefully acknowledged. We sincerely thank Frank Lovas for a CD containing his molecular spectroscopy database SLAIM03, and the dedicated scientists at Cologne (CDMS) and at JPL for undertaking the all-important work of providing spectroscopic data through the internet.

[3] `http://www.esa.int/science/herschel`

References

Amano, T., Amanao, T., & Warner, H. E. 1991, J. Mol. Spectrosc., 146, 519
Bernath, P., Kwok, S., Koning, N., et al. 2007, ApJ, submitted
Beuther, H., Zhang, Q., Greenhill, L. J., et al. 2005, ApJ, 632, 355
Beuther, H., Zang, Q., Reid, M. J., et al. 2006, ApJ, 636, 323
Blake, G. A., Mundy, L. G., Carlstrom, J. E., et al. 1996, ApJ, 472, L49
Cernicharo, J., Goicoechea, J. R., & Caux, E. 2000, ApJ, 534, L199
Civiš, S., Walters, A., Yu Tretyakov, M., Bailleux, S., & Bogey, M. 1998, J. Chem. Phys., 108, 8369
Comito, C., Schilke, P., Phillips, T. G., et al. 2005, ApJS, 156, 127
Frisk, U., Hagström, M., Ala-Laurinaho, J., et al. 2003, A&A, 402, L27
Genzel, R., & Stutzki, J. 1989, ARA&A, 27, 41
Goldsmith, P. F., & Langer, W. D. 1999, ApJ, 517, 209
Goldsmith, P. F., Melnick, G. J., Bergin, E. A., et al. 2000, ApJ, 539, L123
de Graauw, Th., & Helmich, F. P. 2000, in Proc. Symp., The Promise of the Herschel Space Observatory, ed. G. L. Pilbratt, J. Cernicharo, A. M. Heras, T. Prusti, & R. Harris, 45
Johansson, L. E. B., Andersson, C., Elldér, et al. 1984, A&A, 130, 227
Johansson, L. E. B., Andersson, C., Elldér, et al. 1985, A&AS, 60, 135
Lee, C. W., & Cho, S.-H. 2002, JKAS, 35, 187
Lovas, F. J. 2003, Spectral Line Atlas for Interstellar Molecules (SLAIM) Ver. 1, private communication
McCarthy, M. C., Gottlieb, C. A., Gupta, H., & Thaddeus, P. 2006, ApJ, 652, L141
Melnick, G. J., Ashby, M. L. N., Plume, R., et al. 2000, ApJ, 539, L87
Müller, H. S. P., Thorwirth, S., Roth, D. A., & Winnewisser, G. 2001, A&A, 370, L49
Olofsson, H., Elldér, J., Hjalmarson, Å., & Rydbeck, G. 1982, A&A, 113, L18
Olofsson, A. O. H., Olofsson, G., Hjalmarson, Å., et al. 2003, A&A, 402, L47
Pagani, L., Olofsson, A. O. H., Bergman, P., et al. 2003, A&A, 402, L77
Pardo, R. P., Cernicharo, J., Herpin, F., et al. 2001, ApJ, 562, 799
Pardo, J. R., Cernicharo, J., & Phillips, T. G. 2005, ApJ, 634, L61
Persson, C. M., Olofsson, A. O. H., Koning, N., et al. 2007, A&A, 476, 807 (Paper II)
Pickett, H. M., Poynter, R. L., Cohen, E. A., et al. 1998, J. Quant. Spectrosc. & Rad. Trans., 60, 883
Rodríguez-Franco, A., Martín-Pintado, J., & Wilson, T. L. 1999, A&A, 344, L57
Schilke, P., Groesbeck, T. D., Blake, G. A., & Phillips, T. G. 1997, ApJS, 108, 301
Saito, S., & Goto, M. 1993, ApJ, 410, L53
Schilke, P., Benford, D. J., Hunter, T. R., Lis, D. C., & Phillips, T. G. 2001, ApJS, 132, 281
Sempere, M. J., Cernicharo, J., Leflouch, B., & González-Alfonso, E. 2000, ApJ, 530, L123
Senekowitsch, J., Werner, H.-J., Rosmus, P., Reinsch, E.-A., & ONeil, S. V. 1985, J. Chem. Phys., 83, 4661
Siringo, G., Kreysa, E., Reichertz, L. A., & Menten, K. M. 2004, A&A, 422, 751
Takano, S., Klaus, T., & Winnewisser, G. 1998, J. Mol. Spectrosc., 192, 309
Turner, B. E. 1992a, ApJ, 396, L107
Turner, B. E. 1992b, ApJ, 430, 727
Ungerechts, H., Bergin, E. A., Goldsmith, P. F., et al. 1997, ApJ, 482, 245
White, G. J., Araki, M., Greaves, J. S., Ohishi, M., & Higginbottom, N. S. 2003, A&A, 407, 589
Wirström, E. S., Bergman, P., Olofsson, A. O. H., et al. 2006, A&A, 453, 979
Wright, M. C. H., Plambeck, R. L., & Wilner, D. J. 1996, ApJ, 469, 216
Yamamura, I., Kawaguchi, K., & Ridgway, S. T. 2000, ApJ, 528, L33
Zuckerman, B., & Palmer, P. 1975, ApJ, 199, L35

Appendix A: Spectra

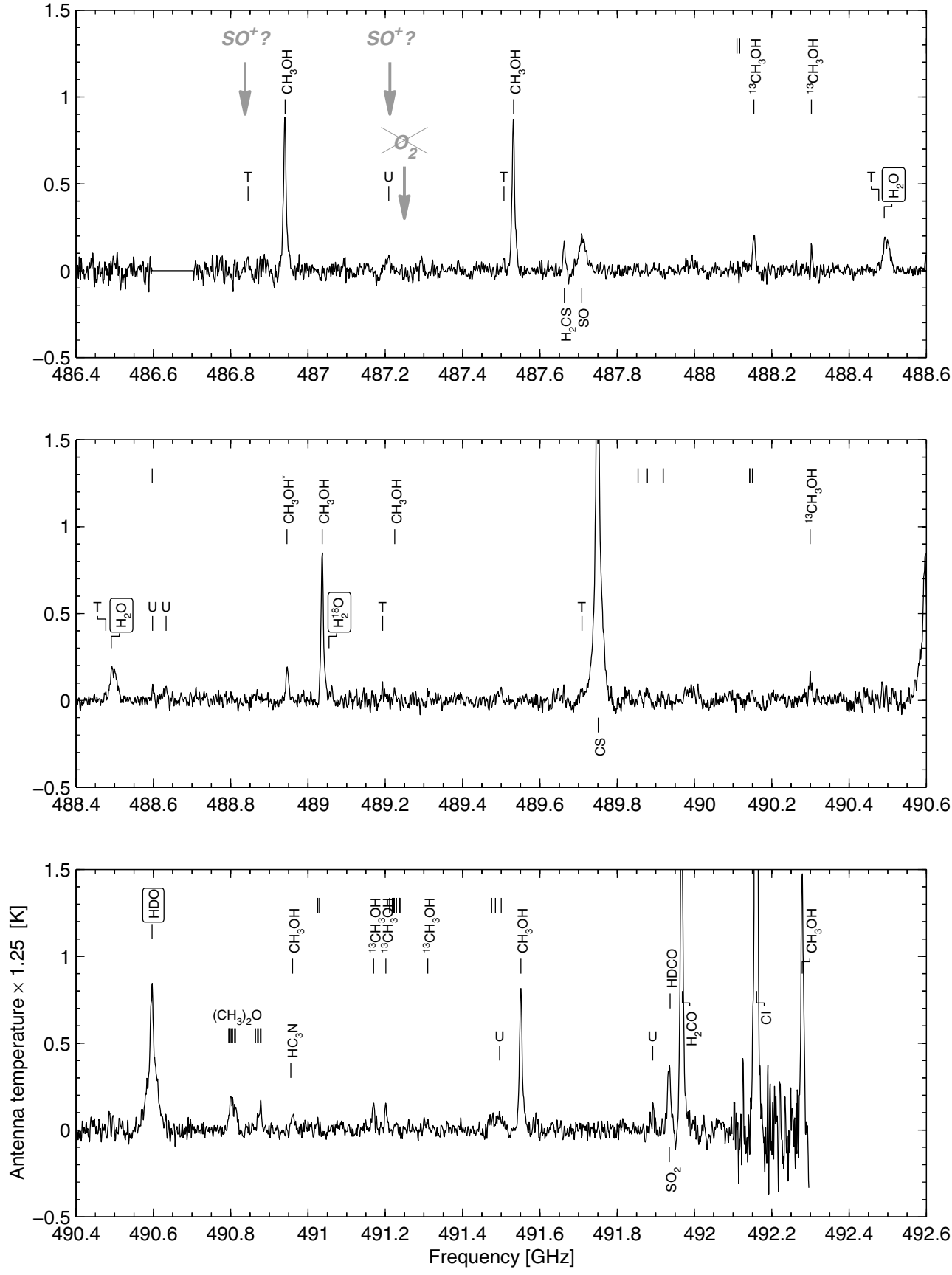

Fig. A.1. The Odin spectral survey between 486.4 and 492.1 GHz (RX495). Note the intensity scaling factor of 1.25 to approximately deconvolve the spectrum to the beam size near 557 GHz (assuming a point source). Empty markers at the intensity level of 1.25 K denote CH_3OCHO lines.

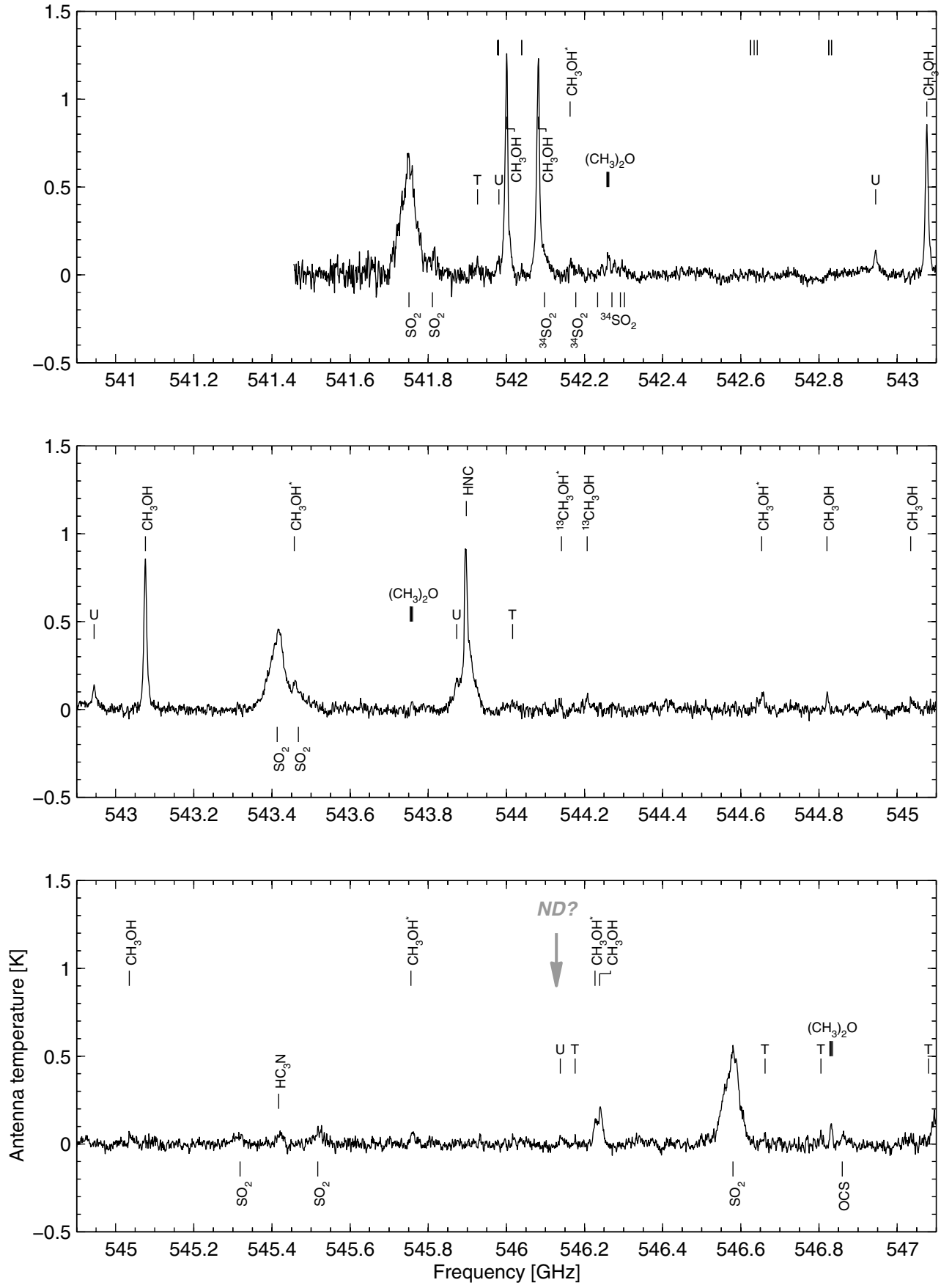

Fig. A.2. The Odin spectral survey between 541.4 and 547.1 GHz (RX549). Empty markers at the intensity level of 1.25 K denote CH_3OCHO lines. A star denotes a transition within a vibrationally excited state: $v_t = 1$ for methanol, and $\nu_2 = 1$ for SO_2.

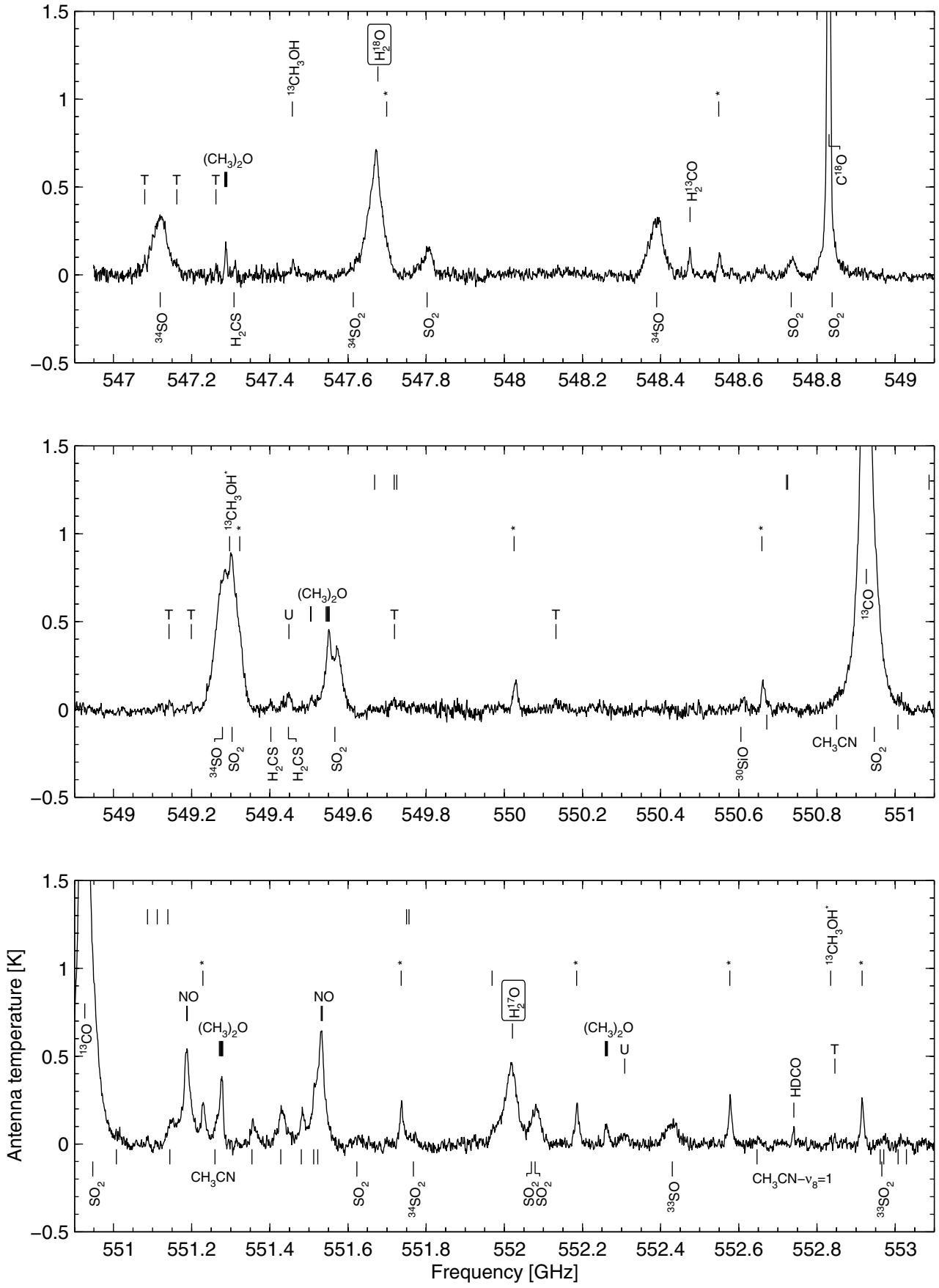

Fig. A.3. The Odin spectral survey between 546.9 and 563.1 GHz (RX555). Unlabelled markers at intensity levels –0.1, 0.5, 0.9, and 1.25 K, belong to SO_2, $(CH_3)_2OH$, CH_3OH, and CH_3OCHO, respectively. A star denotes a transition within a vibrationally excited state: $v_t = 1$ for methanol, and $\nu_2 = 1$ for SO_2. Two sets of markers immediately below the spectrum baseline belong to ground state and vibrationally excited CH_3CN.

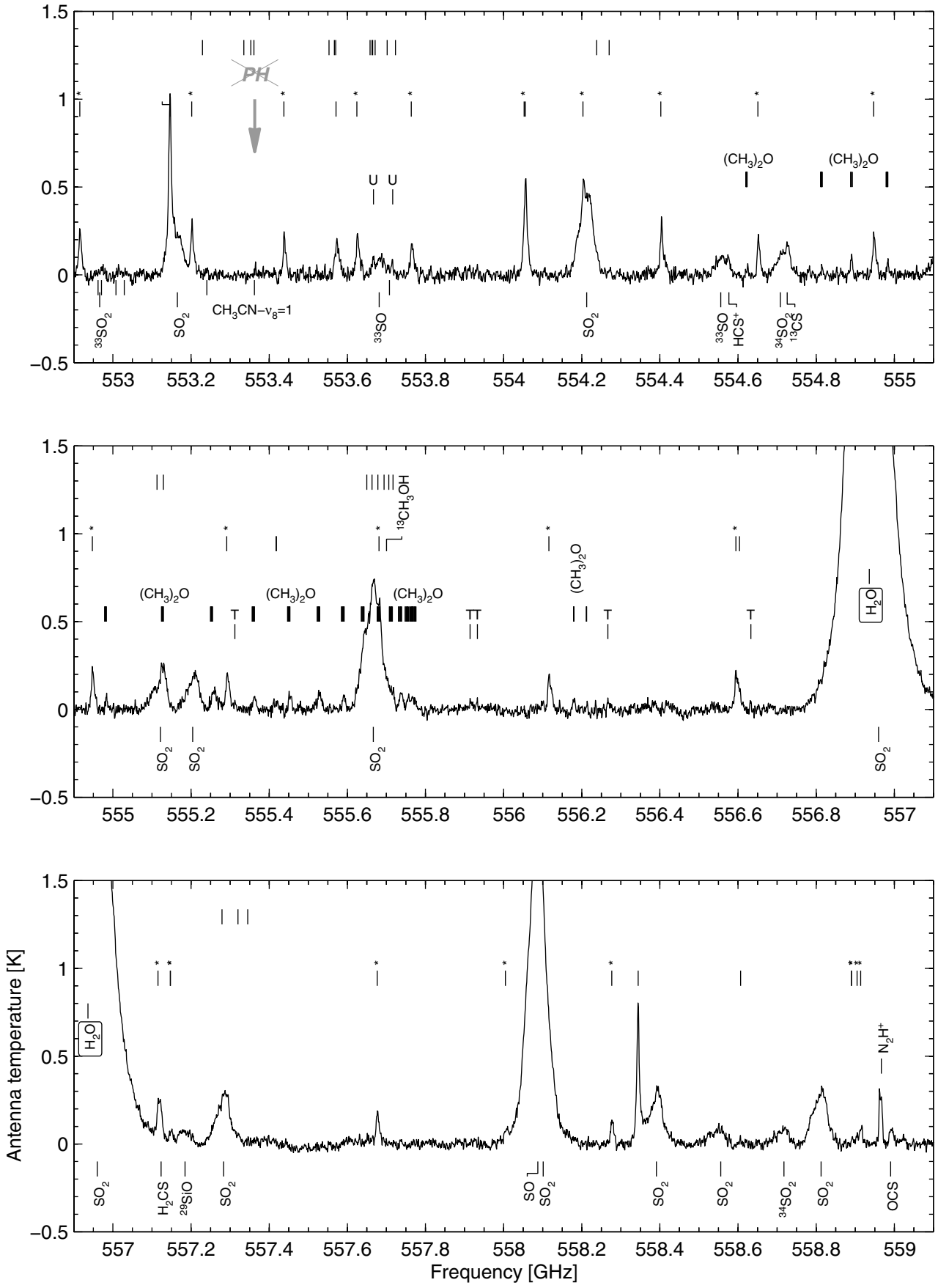

Fig. A.3. continued.

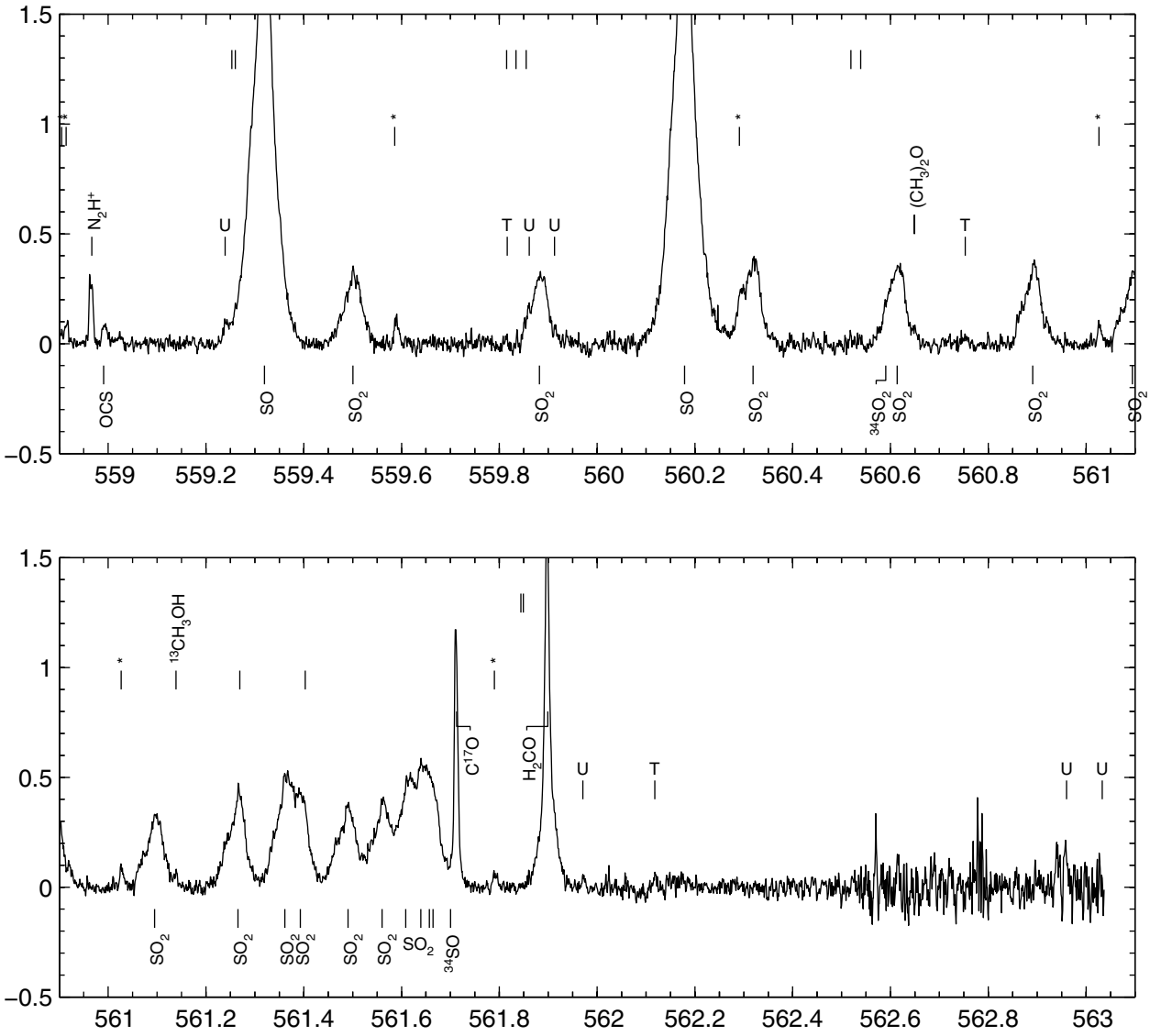

Fig. A.3. continued.

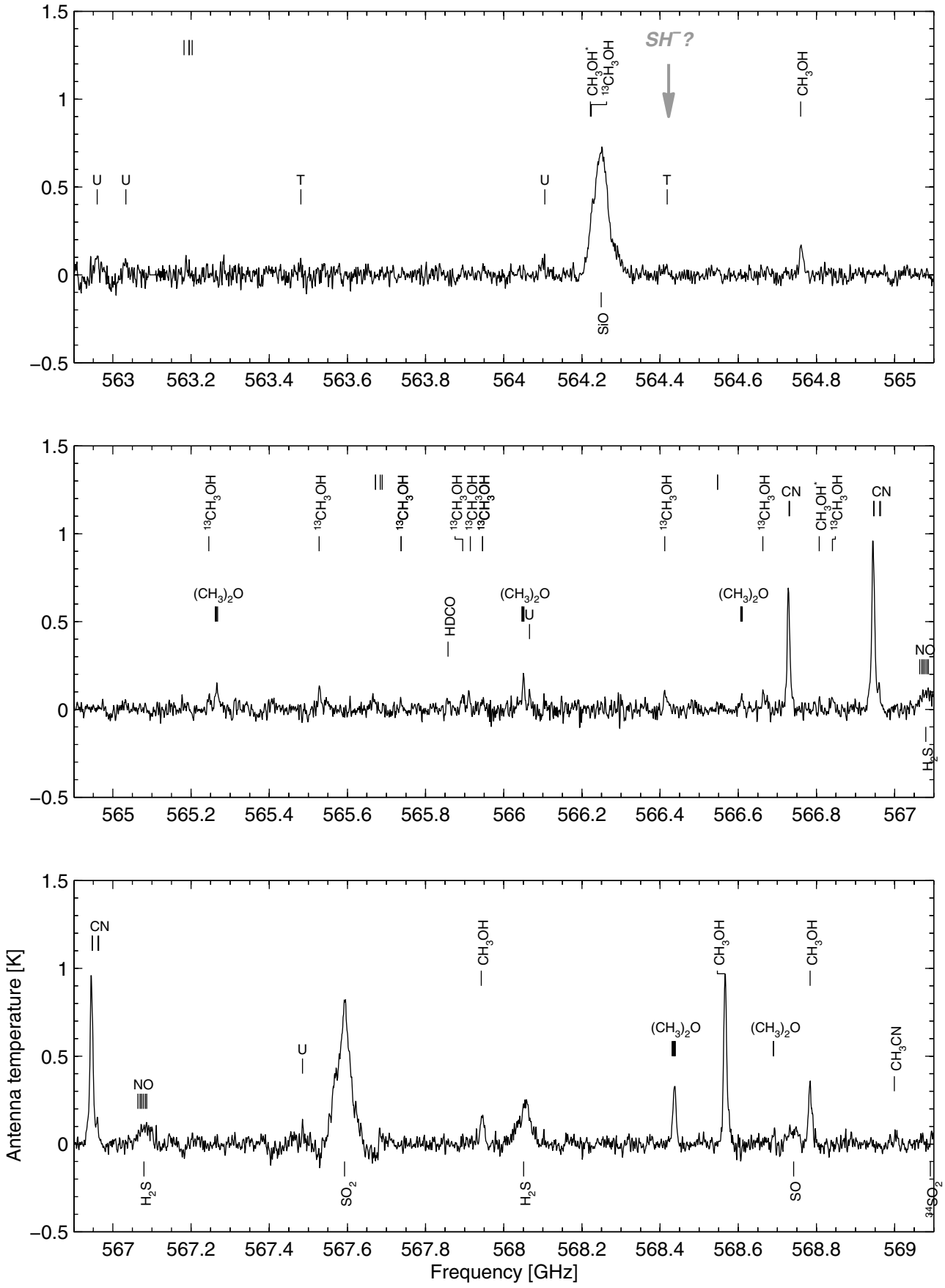

Fig. A.4. The Odin spectral survey between 562.9 and 577.6 GHz (RX572). Empty markers at the intensity level of 1.25 K denote CH_3OCHO lines.

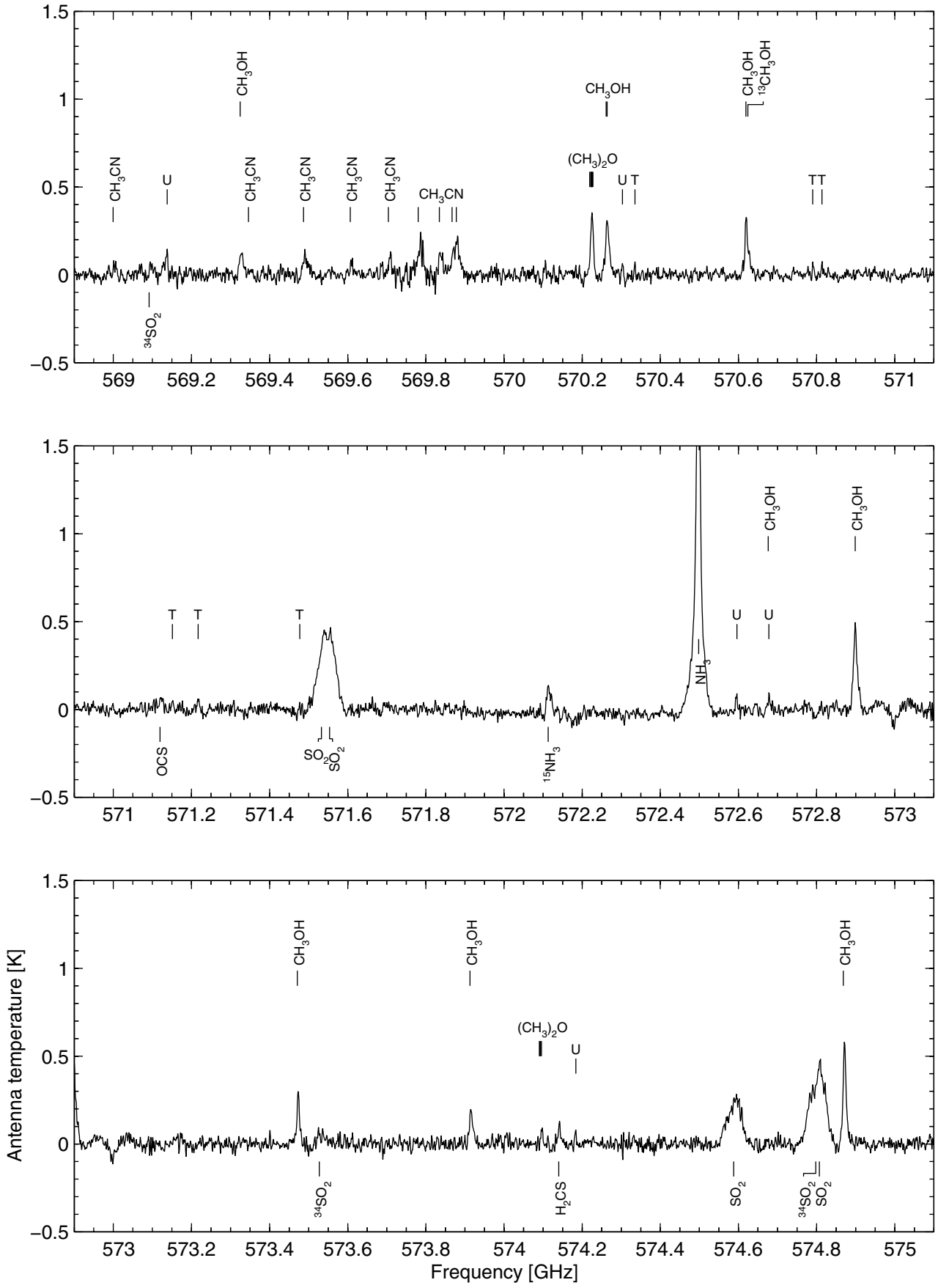

Fig. A.4. continued.

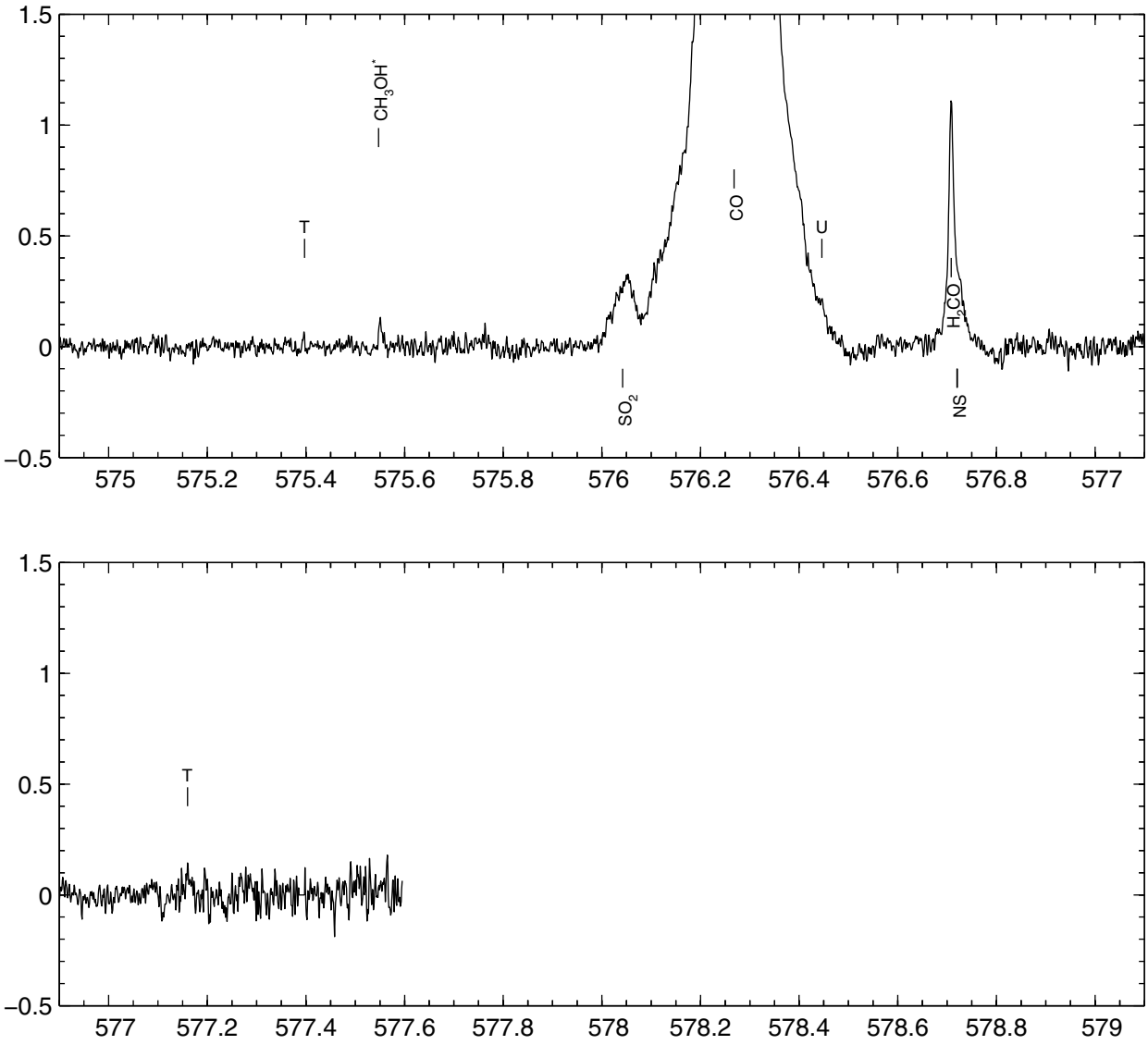

Fig. A.4. continued.

Online Material

Appendix B: Electronic table on lines

Table B.1. Lines detected towards Orion KL listed in order of laboratory frequency.

Frequency [MHz]	Molecule or U/T-line
486 845	T-line
486 940.9	CH_3OH
487 209	U-line
487 507	T-line
487 531.9	CH_3OH
487 663.4	H_2CS
487 708.5	SO
488 153.5	$^{13}CH_3OH$
488 302.6	$^{13}CH_3OH$
488 477	T-line
488 491.1	*para*-H_2O
488 598	U-line
488 633	U-line
488 945.5	CH_3OH
489 037.0	CH_3OH
489 054.3	*ortho*-$H_2^{18}O$
489 193	T-line
489 224.3	CH_3OH
489 709	T-line
489 751.1	CS
490 299.4	$^{13}CH_3OH$
490 596.7	HDO
490 795.3	CH_3OCH_3
490 795.3	CH_3OCH_3
490 797.5	CH_3OCH_3
490 798.3	CH_3OCH_3
490 801.3	CH_3OCH_3
490 804.3	CH_3OCH_3
490 804.7	CH_3OCH_3
490 810.3	CH_3OCH_3
490 811.4	CH_3OCH_3
490 812.1	CH_3OCH_3
490 864.4	CH_3OCH_3
490 869.8	CH_3OCH_3
490 871.5	CH_3OCH_3
490 877.2	CH_3OCH_3
490 877.6	CH_3OCH_3
490 878.3	CH_3OCH_3
490 955.7	HC_3N
490 960.0	CH_3OH
491 170.0	$^{13}CH_3OH$
491 201.3	$^{13}CH_3OH$
491 310.1	$^{13}CH_3OH$
491 496	U-line
491 550.9	CH_3OH
491 892	U-line
491 934.7	SO_2
491 937.0	HDCO
491 968.4	H_2CO
492 160.7	C
492 278.7	CH_3OH
541 750.9	SO_2
541 810.6	SO_2
541 926	T-line
541 981	U-line
542 000.9	CH_3OH
542 081.9	CH_3OH
542 097.7	$^{34}SO_2$
542 163.0	CH_3OH
542 177.4	$^{34}SO_2$
542 233.5	$^{34}SO_2$
542 257.7	CH_3OCH_3
542 257.7	CH_3OCH_3
542 260.1	CH_3OCH_3
542 262.4	CH_3OCH_3
542 270.1	$^{34}SO_2$
542 291.7	$^{34}SO_2$
542 302.3	$^{34}SO_2$
542 945	U-line
543 076.1	CH_3OH
543 413.5	SO_2
543 457.3	CH_3OH
543 467.7	SO_2
543 753.9	CH_3OCH_3
543 753.9	CH_3OCH_3
543 756.9	CH_3OCH_3
543 759.8	CH_3OCH_3
543 873	U-line
543 897.6	HNC
544 016	T-line
544 140.5	$^{13}CH_3OH$
544 206.7	$^{13}CH_3OH$
544 653.1	CH_3OH
544 820.5	CH_3OH
545 034.8	CH_3OH
545 318.5	SO_2
545 417.1	HC_3N
545 517.3	SO_2
545 755.6	CH_3OH
546 138	U-line
546 176	T-line
546 226.8	CH_3OH
546 239.0	CH_3OH
546 579.8	SO_2
546 662	T-line
546 805	T-line
546 827.8	CH_3OCH_3
546 829.2	CH_3OCH_3
546 831.5	CH_3OCH_3
546 834.5	CH_3OCH_3
546 859.8	OCS
547 080	T-line
547 119.6	^{34}SO
547 162	T-line
547 262	T-line
547 284.8	CH_3OCH_3
547 286.2	CH_3OCH_3
547 287.8	CH_3OCH_3
547 290.1	CH_3OCH_3
547 308.2	H_2CS
547 457.8	$^{13}CH_3OH$
547 613.5	$^{34}SO_2$
547 676.4	*ortho*-$H_2^{18}O$
547 698.9	CH_3OH
547 802.2	SO_2
548 389.8	^{34}SO
548 475.2	$H_2^{13}CO$
548 548.7	CH_3OH
548 734.3	SO_2
548 831.0	$C^{18}O$
548 838.9	SO_2
549 142	T-line
549 199	T-line
549 278.7	^{34}SO
549 297.1	$^{13}CH_3OH$
549 303.3	SO_2
549 322.8	CH_3OH
549 402.4	H_2CS
549 447.5	H_2CS
549 449	U-line
549 504.7	CH_3OCH_3
549 504.7	CH_3OCH_3
549 504.9	CH_3OCH_3
549 505.2	CH_3OCH_3
549 543.8	CH_3OCH_3
549 546.5	CH_3OCH_3
549 547.4	CH_3OCH_3
549 547.7	CH_3OCH_3
549 550.4	CH_3OCH_3
549 550.6	CH_3OCH_3
549 550.8	CH_3OCH_3
549 551.7	CH_3OCH_3
549 566.4	SO_2
549 719	T-line
550 025.2	CH_3OH
550 132	T-line
550 605.2	^{30}SiO
550 659.3	CH_3OH
550 671.7	CH_3CN
550 850.0	CH_3CN
550 926.3	^{13}CO
550 946.7	SO_2
551 007.4	CH_3CN
551 143.9	CH_3CN
551 187.3	NO
551 187.5	NO
551 188.8	NO
551 228.6	CH_3OH
551 259.6	CH_3CN

Table B.1. continued.

Frequency [MHz]	Molecule or U/T-line
551 270.8	CH_3OCH_3
551 273.6	CH_3OCH_3
551 275.1	CH_3OCH_3
551 275.1	CH_3OCH_3
551 276.5	CH_3OCH_3
551 276.5	CH_3OCH_3
551 277.9	CH_3OCH_3
551 279.4	CH_3OCH_3
551 354.2	CH_3CN
551 427.9	CH_3CN
551 480.6	CH_3CN
551 512.2	CH_3CN
551 522.7	CH_3CN
551 531.5	NO
551 534.0	NO
551 534.1	NO
551 622.9	SO_2
551 736.2	CH_3OH
551 767.4	$^{34}SO_2$
551 968.8	CH_3OH
552 021.0	*ortho*-$H_2^{17}O$
552 069.4	SO_2
552 078.9	SO_2
552 184.8	CH_3OH
552 258.9	CH_3OCH_3
552 258.9	CH_3OCH_3
552 261.4	CH_3OCH_3
552 264.0	CH_3OCH_3
552 308	U-line
552 429.8	^{33}SO
552 577.2	CH_3OH
552 646.6	CH_3CN
552 740.9	HDCO
552 835.1	$^{13}CH_3OH$
552 846	T-line
552 915.4	CH_3OH
552 970.8	CH_3CN
553 007.8	CH_3CN
553 029.1	CH_3CN
553 146.3	CH_3OH
553 164.9	SO_2
553 201.6	CH_3OH
553 240.3	CH_3CN
553 362.2	CH_3CN
553 437.5	CH_3OH
553 570.9	CH_3OH
553 624.5	CH_3OH
553 667	U-line
553 681.3	^{33}SO
553 707.6	CH_3CN
553 716	U-line
553 763.7	CH_3OH
554 052.7	CH_3OH

Frequency [MHz]	Molecule or U/T-line
554 055.5	CH_3OH
554 202.9	CH_3OH
554 212.8	SO_2
554 402.5	CH_3OH
554 555.6	^{33}SO
554 576.6	HCS^+
554 619.8	CH_3OCH_3
554 619.8	CH_3OCH_3
554 621.0	CH_3OCH_3
554 621.5	CH_3OCH_3
554 622.1	CH_3OCH_3
554 622.6	CH_3OCH_3
554 622.6	CH_3OCH_3
554 623.2	CH_3OCH_3
554 650.9	CH_3OH
554 708.2	$^{34}SO_2$
554 726.0	^{13}CS
554 811.5	CH_3OCH_3
554 811.5	CH_3OCH_3
554 812.7	CH_3OCH_3
554 813.4	CH_3OCH_3
554 813.9	CH_3OCH_3
554 814.6	CH_3OCH_3
554 814.6	CH_3OCH_3
554 815.3	CH_3OCH_3
554 888.3	CH_3OCH_3
554 888.3	CH_3OCH_3
554 890.4	CH_3OCH_3
554 892.5	CH_3OCH_3
554 947.4	CH_3OH
554 979.1	CH_3OCH_3
554 979.1	CH_3OCH_3
554 980.4	CH_3OCH_3
554 981.2	CH_3OCH_3
554 981.7	CH_3OCH_3
554 982.5	CH_3OCH_3
554 982.5	CH_3OCH_3
554 983.3	CH_3OCH_3
555 121.5	SO_2
555 124.5	CH_3OCH_3
555 124.5	CH_3OCH_3
555 125.9	CH_3OCH_3
555 126.8	CH_3OCH_3
555 127.3	CH_3OCH_3
555 128.2	CH_3OCH_3
555 128.2	CH_3OCH_3
555 129.1	CH_3OCH_3
555 204.1	SO_2
555 249.8	CH_3OCH_3
555 249.8	CH_3OCH_3
555 251.3	CH_3OCH_3
555 252.3	CH_3OCH_3
555 252.7	CH_3OCH_3

Frequency [MHz]	Molecule or U/T-line
555 253.8	CH_3OCH_3
555 253.8	CH_3OCH_3
555 254.9	CH_3OCH_3
555 291.1	CH_3OH
555 312	T-line
555 356.8	CH_3OCH_3
555 356.8	CH_3OCH_3
555 358.3	CH_3OCH_3
555 359.5	CH_3OCH_3
555 359.9	CH_3OCH_3
555 361.1	CH_3OCH_3
555 361.1	CH_3OCH_3
555 362.3	CH_3OCH_3
555 417.7	CH_3OH
555 418.5	CH_3OH
555 447.3	CH_3OCH_3
555 447.3	CH_3OCH_3
555 448.9	CH_3OCH_3
555 450.2	CH_3OCH_3
555 450.6	CH_3OCH_3
555 451.9	CH_3OCH_3
555 451.9	CH_3OCH_3
555 453.1	CH_3OCH_3
555 522.9	CH_3OCH_3
555 522.9	CH_3OCH_3
555 524.6	CH_3OCH_3
555 526.0	CH_3OCH_3
555 526.4	CH_3OCH_3
555 527.8	CH_3OCH_3
555 527.8	CH_3OCH_3
555 529.2	CH_3OCH_3
555 585.3	CH_3OCH_3
555 585.3	CH_3OCH_3
555 587.1	CH_3OCH_3
555 588.6	CH_3OCH_3
555 589.0	CH_3OCH_3
555 590.4	CH_3OCH_3
555 590.4	CH_3OCH_3
555 591.9	CH_3OCH_3
555 635.9	CH_3OCH_3
555 635.9	CH_3OCH_3
555 637.9	CH_3OCH_3
555 639.4	CH_3OCH_3
555 639.8	CH_3OCH_3
555 641.4	CH_3OCH_3
555 641.4	CH_3OCH_3
555 642.9	CH_3OCH_3
555 666.3	SO_2
555 676.3	CH_3OCH_3
555 676.3	CH_3OCH_3
555 678.3	CH_3OCH_3
555 679.9	CH_3OCH_3
555 680.3	CH_3OCH_3

Table B.1. continued.

Frequency [MHz]	Molecule or U/T-line
555 681.0	CH_3OH
555 681.9	CH_3OCH_3
555 681.9	CH_3OCH_3
555 683.6	CH_3OCH_3
555 700.1	$^{13}CH_3OH$
555 707.6	CH_3OCH_3
555 707.6	CH_3OCH_3
555 709.7	CH_3OCH_3
555 711.4	CH_3OCH_3
555 711.8	CH_3OCH_3
555 713.5	CH_3OCH_3
555 713.5	CH_3OCH_3
555 715.2	CH_3OCH_3
555 731.2	CH_3OCH_3
555 731.2	CH_3OCH_3
555 733.4	CH_3OCH_3
555 735.2	CH_3OCH_3
555 735.5	CH_3OCH_3
555 737.3	CH_3OCH_3
555 737.3	CH_3OCH_3
555 739.1	CH_3OCH_3
555 748.2	CH_3OCH_3
555 748.2	CH_3OCH_3
555 750.5	CH_3OCH_3
555 752.3	CH_3OCH_3
555 752.7	CH_3OCH_3
555 754.6	CH_3OCH_3
555 754.6	CH_3OCH_3
555 756.4	CH_3OCH_3
555 759.7	CH_3OCH_3
555 759.7	CH_3OCH_3
555 762.1	CH_3OCH_3
555 764.0	CH_3OCH_3
555 764.4	CH_3OCH_3
555 766.3	CH_3OCH_3
555 766.3	CH_3OCH_3
555 766.8	CH_3OCH_3
555 766.8	CH_3OCH_3
555 768.2	CH_3OCH_3
555 769.2	CH_3OCH_3
555 771.2	CH_3OCH_3
555 771.6	CH_3OCH_3
555 773.5	CH_3OCH_3
555 773.5	CH_3OCH_3
555 775.5	CH_3OCH_3
555 914	T-line
555 933	T-line
556 115.8	CH_3OH
556 179.4	CH_3OCH_3
556 179.4	CH_3OCH_3
556 179.4	CH_3OCH_3
556 179.5	CH_3OCH_3
556 212.0	CH_3OCH_3
556 212.0	CH_3OCH_3
556 212.1	CH_3OCH_3
556 212.2	CH_3OCH_3
556 267	T-line
556 594.4	CH_3OH
556 603.7	CH_3OH
556 633	T-line
556 936.0	*ortho*-H_2O
556 959.9	SO_2
557 115.2	CH_3OH
557 123.2	H_2CS
557 147.0	CH_3OH
557 147.0	CH_3OH
557 184.4	^{29}SiO
557 283.2	SO_2
557 676.6	CH_3OH
558 004.6	CH_3OH
558 087.7	SO
558 101.2	SO_2
558 276.8	CH_3OH
558 344.5	CH_3OH
558 390.9	SO_2
558 555.8	SO_2
558 606.4	CH_3OH
558 717.5	$^{34}SO_2$
558 812.5	SO_2
558 890.2	CH_3OH
558 890.2	CH_3OH
558 904.6	CH_3OH
558 914.0	CH_3OH
558 966.6	N_2H^+
558 990.5	OCS
559 239	U-line
559 319.8	SO
559 500.4	SO_2
559 586.1	CH_3OH
559 816	T-line
559 861	U-line
559 882.1	SO_2
559 913	U-line
560 178.7	SO
560 291.0	CH_3OH
560 318.9	SO_2
560 590.2	$^{34}SO_2$
560 613.5	SO_2
560 648.9	CH_3OCH_3
560 648.9	CH_3OCH_3
560 649.0	CH_3OCH_3
560 649.0	CH_3OCH_3
560 753	T-line
560 891.0	SO_2
561 026.4	CH_3OH
561 094.8	SO_2
561 138.5	$^{13}CH_3OH$
561 265.6	SO_2
561 269.1	CH_3OH
561 361.4	SO_2
561 392.9	SO_2
561 402.9	CH_3OH
561 490.5	SO_2
561 560.3	SO_2
561 608.6	SO_2
561 639.3	SO_2
561 656.7	SO_2
561 664.2	SO_2
561 700.4	^{34}SO
561 712.8	$C^{17}O$
561 789.7	CH_3OH
561 899.3	H_2CO
561 971	U-line
562 118	T-line
562 960	U-line
563 033	U-line
563 481	T-line
564 105	U-line
564 221.6	CH_3OH
564 223.7	$^{13}CH_3OH$
564 249.2	SiO
564 418	T-line
564 759.8	CH_3OH
565 245.2	$^{13}CH_3OH$
565 262.1	CH_3OCH_3
565 262.8	CH_3OCH_3
565 265.2	CH_3OCH_3
565 267.9	CH_3OCH_3
565 527.8	$^{13}CH_3OH$
565 737.4	$^{13}CH_3OH$
565 737.4	$^{13}CH_3OH$
565 857.5	HDCO
565 895.0	$^{13}CH_3OH$
565 914.4	$^{13}CH_3OH$
565 946.2	$^{13}CH_3OH$
566 046.6	CH_3OCH_3
566 047.3	CH_3OCH_3
566 049.3	CH_3OCH_3
566 051.7	CH_3OCH_3
566 066	U-line
566 411.9	$^{13}CH_3OH$
566 606.7	CH_3OCH_3
566 606.7	CH_3OCH_3
566 608.5	CH_3OCH_3
566 610.4	CH_3OCH_3
566 662.8	$^{13}CH_3OH$
566 729.9	CN
566 730.7	CN
566 730.8	CN

Table B.1. continued.

Frequency [MHz]	Molecule or U/T-line
566 840.7	$^{13}CH_3OH$
566 946.8	CN
566 946.9	CN
566 947.2	CN
566 962.0	CN
566 963.7	CN
567 064.2	NO
567 069.6	NO
567 073.4	NO
567 077.9	NO
567 079.6	H_2S
567 082.7	NO
567 086.6	NO
567 485	U-line
567 592.7	SO_2
567 942.6	CH_3OH
568 050.7	H_2S
568 430.6	CH_3OCH_3
568 432.6	CH_3OCH_3
568 433.9	CH_3OCH_3
568 435.3	CH_3OCH_3
568 436.3	CH_3OCH_3
568 437.2	CH_3OCH_3
568 437.7	CH_3OCH_3
568 439.2	CH_3OCH_3
568 566.1	CH_3OH
568 690.1	CH_3OCH_3
568 690.1	CH_3OCH_3
568 690.3	CH_3OCH_3
568 690.4	CH_3OCH_3
568 741.6	SO
568 783.6	CH_3OH
568 999.3	CH_3CN
569 091.6	$^{34}SO_2$
569 138	U-line
569 324.5	CH_3OH
569 486.9	CH_3CN
569 606.3	CH_3CN
569 704.0	CH_3CN
569 780.1	CH_3CN
569 834.5	CH_3CN
569 867.1	CH_3CN
569 878.0	CH_3CN
570 219.1	CH_3OCH_3
570 221.9	CH_3OCH_3
570 223.3	CH_3OCH_3
570 223.3	CH_3OCH_3
570 224.7	CH_3OCH_3
570 224.7	CH_3OCH_3
570 226.1	CH_3OCH_3
570 227.5	CH_3OCH_3
570 261.5	CH_3OH
570 264.0	CH_3OH
570 303	U-line
570 335	T-line
570 619.0	CH_3OH
570 624.2	$^{13}CH_3OH$
570 790	T-line
570 814	T-line
571 119.7	OCS
571 151	T-line
571 217	T-line
571 477	T-line
571 532.6	SO_2
571 553.3	SO_2
572 112.8	$^{15}NH_3$
572 498.2	NH_3
572 596	U-line
572 676.2	CH_3OH
572 678	U-line
572 898.8	CH_3OH
573 471.1	CH_3OH
573 527.3	$^{34}SO_2$
573 912.7	CH_3OH
574 090.9	CH_3OCH_3
574 090.9	CH_3OCH_3
574 093.3	CH_3OCH_3
574 095.7	CH_3OCH_3
574 140.0	H_2CS
574 184	U-line
574 587.8	SO_2
574 797.9	$^{34}SO_2$
574 807.3	SO_2
574 868.5	CH_3OH
575 397	T-line
575 547.2	CH_3OH
576 042.1	SO_2
576 267.9	CO
576 446	U-line
576 708.3	H_2CO
576 720.2	NS
577 160	T-line

Paper II

A spectral line survey of Orion KL in the bands 486 – 492 and 541 – 577 GHz with the Odin satellite

II. Data analysis

Carina M. Persson, A.O.H. Olofsson, N. Koning, P. Bergman, P.F. Bernath, J.H. Black, U. Frisk, W. Geppert, T.I. Hasegawa, Å. Hjalmarson, S. Kwok, B. Larsson, A. Lecacheux, A. Nummelin, M. Olberg, Aa. Sandqvist, and E.S. Wirström

Astronomy & Astrophysics, 476, 807 (2007)

A&A 476, 807–828 (2007)
DOI: 10.1051/0004-6361:20077225

Astronomy & Astrophysics

A spectral line survey of Orion KL in the bands 486-492 and 541-577 GHz with the Odin⋆ satellite⋆⋆

II. Data analysis

C. M. Persson[1], A. O. H. Olofsson[1,2], N. Koning[3], P. Bergman[1,4], P. Bernath[5,6,7], J. H. Black[1], U. Frisk[8], W. Geppert[9], T. I. Hasegawa[3,10], Å. Hjalmarson[1], S. Kwok[3,11], B. Larsson[12], A. Lecacheux[13], A. Nummelin[14], M. Olberg[1], Aa. Sandqvist[12], and E. S. Wirström[1]

[1] Onsala Space Observatory (OSO), Chalmers University of Technology, 43992 Onsala, Sweden
e-mail: carina@oso.chalmers.se
[2] LERMA, Observatoire de Paris, 61 Av. de l'Observatoire, 75014 Paris, France
[3] Department of Physics and Astronomy, University of Calgary, Calgary, AB T2N 1N4, Canada
[4] European Southern Observatory, Alonso de Cordova 3107, Vitacura, Casilla 19001, Santiago, Chile
[5] Department of Chemistry, University of Waterloo, Waterloo, ON N2L 3G1, Canada
[6] Department of Chemistry, University of Arizona, Tucson, AZ 85721, USA
[7] Department of Chemistry, University of York, Heslington, York YO10 5DD, UK
[8] Swedish Space Corporation, PO Box 4207, 17104 Solna, Sweden
[9] Molecular Physics Division, Department of Physics, Stockholm University AlbaNova, 10691 Stockholm, Sweden
[10] Institute of Astronomy and Astrophysics, Academia Sinica, PO Box 23-141, Taipei 106, Taiwan, R.O.C.
[11] Department of Physics, University of Hong Kong, Hong Kong, PR China
[12] Stockholm Observatory, AlbaNova University Center, 10691 Stockholm, Sweden
[13] LESIA, Observatoire de Paris, Section de Meudon, 5 place Jules Janssen, 92195 Meudon Cedex, France
[14] Computer science and engineering, Chalmers University of Technology, 41296 Göteborg, Sweden

Received 2 February 2007 / Accepted 17 September 2007

ABSTRACT

Aims. We investigate the physical and chemical conditions in a typical star forming region, including an unbiased search for new molecules in a spectral region previously unobserved.
Methods. Due to its proximity, the Orion KL region offers a unique laboratory of molecular astrophysics in a chemically rich, massive star forming region. Several ground-based spectral line surveys have been made, but due to the absorption by water and oxygen, the terrestrial atmosphere is completely opaque at frequencies around 487 and 557 GHz. To cover these frequencies we used the Odin satellite to perform a spectral line survey in the frequency ranges 486−492 GHz and 541−577 GHz, filling the gaps between previous spectral scans. Odin's high main beam efficiency, $\eta_{\rm mb} = 0.9$, and observations performed outside the atmosphere make our intensity scale very well determined.
Results. We observed 280 spectral lines from 38 molecules including isotopologues, and, in addition, 64 unidentified lines. A few U-lines have interesting frequency coincidences such as ND and the anion SH^-. The beam-averaged emission is dominated by CO, H_2O, SO_2, SO, ^{13}CO and CH_3OH. Species with the largest number of lines are CH_3OH, $(CH_3)_2O$, SO_2, $^{13}CH_3OH$, CH_3CN and NO. Six water lines are detected including the ground state rotational transition $1_{1,0}$–$1_{0,1}$ of o-H_2O, its isotopologues o-$H_2^{18}O$ and o-$H_2^{17}O$, the Hot Core tracing p-H_2O transition $6_{2,4}$–$7_{1,7}$, and the $2_{0,2}$–$1_{1,1}$ transition of HDO. Other lines of special interest are the 1_0–0_0 transition of NH_3 and its isotopologue $^{15}NH_3$. Isotopologue abundance ratios of D/H, $^{12}C/^{13}C$, $^{32}S/^{34}S$, $^{34}S/^{33}S$, and $^{18}O/^{17}O$ are estimated. The temperatures, column densities and abundances in the various subregions are estimated, and we find very high gas-phase abundances of H_2O, NH_3, SO_2, SO, NO, and CH_3OH. A comparison with the ice inventory of ISO sheds new light on the origin of the abundant gas-phase molecules.

Key words. ISM: abundances – ISM: individual objects: Orion KL – ISM: molecules – line: formation – line: identification – submillimeter

1. Introduction

To study the important ground-state rotational transition of water (including isotopologues), which traces shocks and heated star forming regions, is one of the main astronomy goals of the Odin satellite (Nordh et al. 2003, and subsequent papers in the A&A "Special Letters Edition: First Science with the Odin satellite") and hence also of this spectral line survey towards the Orion KL region. The first observations of this water line were performed by SWAS in 1998 (NASA's Submillimeter Wave Astronomy

⋆ Odin is a Swedish-led satellite project funded jointly by the Swedish National Space Board (SNSB), the Canadian Space Agency (CSA), the National Technology Agency of Finland (Tekes) and Centre National d'Etudes Spatiales (CNES). The Swedish Space Corporation was the prime contractor and also is responsible for the satellite operation.

⋆⋆ Section 10, Figs. 25–47 and Tables 5–35 are only available in electronic form at http://www.aanda.org

Satellite; Melnick et al. 2000 and subsequent ApJ papers in that issue). The Odin satellite provides a smaller beam than SWAS (2.1′ vs. 3.3′ × 4.5′), and our tunable SSB receivers enable a full line survey in this spectral window, including the water isotopologues ($H_2^{16}O$, $H_2^{17}O$, $H_2^{18}O$ and HDO), and a high energy p-H_2O transition.

A spectral scan offers an unbiased search for new molecules. It also creates opportunities to observe multiple transitions of the same species as a uniformly calibrated data set, and this can be used to calculate rotation temperatures, column densities, abundances, source sizes, optical depths, and isotopic elemental abundance ratios of the observed gases. The latter are important constraints for models of the Galactic chemical evolution. These models predict the elemental abundance evolution as a function of star formation history, stellar nucleosynthesis, and the degree of mixing of the gas in the ISM (Wilson & Rood 1994).

The Orion Molecular Cloud (OMC-1) is a well known massive star forming region (see Genzel & Stutzki 1989, for a review), and an ideal target for spectral line surveys at millimetre and submillimetre wavelengths due to its chemical richness and proximity (∼450 pc). The Kleinmann-Low nebula (Orion KL) is the brightest infrared region in the OMC-1 and is situated about 1′ NW of the Trapezium cluster. This region enables studies of the interaction between young massive stars and their parental molecular cloud. Powerful outflows, shocks and turbulence cause a very complex and chemically structured source, consisting of several distinct subsources.

There are five different components of radial velocity (e.g. Olofsson et al. 1981; Olofsson et al. 1982; Johansson et al. 1984; Friberg 1984; Genzel & Stutzki 1989; Wright et al. 1996; Schilke et al. 2001; Beuther et al. 2005; Olofsson et al. 2007, hereafter Paper I) within the ∼126″ Odin beam:

- *The ambient medium/Extended Ridge* (ER) with $\upsilon_{\rm LSR}$ ∼ 8 km s^{-1} in the south and an abrupt velocity shift across the KL region to $\upsilon_{\rm LSR}$ ∼ 10 km s^{-1} in the north. This extended emission is larger than our beam with quiescent, cool gas of narrow line widths of $\Delta\upsilon$ ∼ 3−5 km s^{-1}, a temperature of ∼20−60 K, and densities of 10^4−10^6 cm^{-3}.
- *The Plateau*: the out-flowing gas, centred close to IRc2 contains two outflows (Greenhill et al. 1998). The bipolar *High Velocity Flow* (HVF) in the SE-NW direction at $\upsilon_{\rm LSR}$ ∼ 10 km s^{-1} reaches velocities of 150 km s^{-1} and covers 40−70″. The second is a *Low Velocity Flow* (LVF) in the SW-NE direction at $\upsilon_{\rm LSR}$ ∼ 5 km s^{-1}, widths of ∼18 km s^{-1} ("the 18 km s^{-1} flow", Genzel et al. 1981), and a size of 15−30″. The temperature and density are 100−150 K and ∼10^5 cm^{-3}, respectively.
- *The Compact Ridge* (CR): a compact warm clump in the northern tip of the southern ER was first discovered by Johansson et al. (1984), approximately 10−15″ southwest of IRc2 with $\upsilon_{\rm LSR}$ ∼ 8 km s^{-1}, and line widths of $\Delta\upsilon$ ∼ 3 km s^{-1}. It may be the result of an interaction between the LVF and the ER that compressed the gas to higher densities ∼10^6 cm^{-3}, temperatures of 100−150 K, and to a small size of 6−15″.
- *The Hot Core* (HC): a warm star forming region which is heated internally, probably by one (or more) young massive protostars. The total size is ∼5−10″ (Hermsen et al. 1988a; Wilson et al. 2000) with smaller, very dense (n ∼ 10^7 cm^{-3}) clumps (Beuther et al. 2005). It is centred only 2″ from IRc2, at a projected distance of 10″ from the CR. The velocity is centred on $\upsilon_{\rm LSR}$ ∼ 3−6 km s^{-1} with line widths of $\Delta\upsilon$ ∼ 5−15 km s^{-1}. The range of temperatures obtained from inversion transitions of NH_3 is 165−400 K (Wilson et al. 2000).
- *Photo Dissociation Region* (PDR): the extended interface region between the molecular cloud and the foreground M42 HII region (Rodríguez-Franco et al. 1998, 2001; Wirström et al. 2006, and references therein) at velocities 8−10 km s^{-1}.

The various cloud components have been displayed in Fig. 6 of Genzel & Stutzki (1989), and Fig. 7 of Irvine et al. (1987). Figure 1 of Greenhill et al. (1998) shows a model of the bipolar High Velocity Flow and the Low Velocity Flow.

The Odin satellite has a large beam and covers high frequencies. This gives our survey the opportunity to simultaneously observe both the small, hot and dense regions, and the extended, cooler regions. Because of the complex source structure encompassed by our large antenna beam, we will compare our data with interferometric images for each species (see Paper I for an extensive list of spectral line survey references). In this way the origin and source sizes of our detected species can be checked.

The complete submm spectrum observed by Odin together with the proposed identification of each line can be found in Paper I. In the present paper we give a short description of our data in Sect. 2, and of the different analysis methods in Sect. 3. In Sect. 4 we present the results in tables and rotation diagrams together with spectra of typical or particularly important transitions. Tables of observed transitions can be found as electronic Tables in the online material (Tables 9 to 33). Tables 34 and 35 list our unidentified and tentatively identified lines. Section 4 also includes a short analysis for each molecule. The important water and CO lines are analysed in Sects. 5 and 6. An attempt to obtain molecular abundances in the different subregions of Orion KL and comparison with abundances in ice mantles of dust grains is found in Sect. 7. We end this paper with a discussion of source sizes and source structure in Sect. 8, followed by a short summary.

2. The line survey data

The observational method is presented in Paper I, and the data is analysed in this paper. These data were obtained with the Odin satellite from spring 2004 to autumn 2005 during four different runs. The spectral scan covers frequencies between 486–492 and 541–577 GHz and includes 280 spectral features from 38 species including isotopologues. The lines were identified using the Lovas SLAIMØ3 molecular line catalogue[1] (Lovas 2003), the Cologne Database for Molecular Spectroscopy[2] (CDMS, Müller et al. 2001) and the Jet Propulsion Laboratory[3] database (JPL, Pickett et al. 1998). Identifications are based not only on frequency coincidence, but also expected abundance, line strength, width and velocity, upper state energy, and the presence of other expected transitions of the molecule.

Most lines in our survey (205 out of 280 identified lines) are due to CH_3OH, $^{13}CH_3OH$, $(CH_3)_2O$, SO_2, and CH_3CN (Table 5, online material). A total of 64 lines (19% of all lines) could not be uniquely identified, although from frequency coincidences we have suggestions for a few identifications such as ND, the interstellar anion SH^-, SO^+, HNCO and CH_3OCHO (see Sect. 4 and Paper I). The spectroscopy still is sparse at higher frequencies

[1] Not available online, but some of its content is maintained under http://physics.nist.gov/PhysRefData/

[2] http://www.cdms.de

[3] http://spec.jpl.nasa.gov/

and a number of U-lines are likely to be poorly known transitions of the identified molecules and their isotopologues, including their vibrationally or torsionally excited states.

At 557 GHz the Odin 1.1 m mirror has a circular beam with FWHM of 2.′1. The main beam efficiency is $\eta_{\rm mb} = 0.9$. This in addition to being outside the atmosphere makes our intensity calibration very accurate. The intensity scale is expressed in terms of antenna temperature $T_{\rm A}^{*}$. In all calculations of the column densities the main beam efficiency is properly taken into account. The reconstructed pointing uncertainty is <15″ during most of the time. The coordinates of Orion KL in our survey are RA $05^{\rm h}35^{\rm m}14.^{\rm s}36$, Dec $-05°22'29.''6$ (J2000), and the frequency scale is set in relation to a source LSR velocity of +8 km s^{-1}. The spectral resolution is 1 MHz, and the typical rms reached is ∼25 mK per 1 MHz channel.

3. Data analysis methods – a simplified approach

The observed line emission is not restricted to one single subregion in Orion KL, but may be a complicated blend from several subregions with a complex line profile. Thus, when we attempt to derive column densities and abundances, we have to separate the emission into its constituent parts. The most simple approach whenever several emission features are clearly present, is to use least-square fits of Gaussians to the line profiles to separate their relative contributions. This can give a first order input to modelling attempts including current and future knowledge of the source structure. The resulting parameters are found in the online tables and in fitted spectra (Sect. 4). This is based on the assumptions that either all emissions are optically thin or that the emission subregions do not overlap each other spatially, and also that the velocity distributions are Gaussian.

The formal errors obtained from the rotation diagram method and forward model are given in each subsection. The formal errors obtained from the single line analysis and from the Gaussian decomposition of the lines are mostly below 20%, with weak lines having higher formal errors. We estimate the accuracy of our column densities results to be within a factor of 2−3. The uncertainties in the derived abundances can be higher because the adopted H_2 column density is also uncertain (see also Sect. 7). Details, definitions and additional uncertainties of the methods not discussed below are found in the online Sect. 10.

3.1. Single line analysis

With the assumption of optically thin emission, neglecting the background radiation, and assuming that the source fills the antenna main beam, the *beam averaged upper state* column density can be calculated as

$$N_{\rm u}^{\rm thin} = \frac{8\pi k \nu_{{\rm u}l}^2}{hc^3}\frac{1}{A_{{\rm u}l}}\int T_{\rm mb}\,{\rm d}\upsilon, \tag{1}$$

where k is the Boltzmann constant, $\nu_{{\rm u}l}$ is the frequency of the transition, h is the Planck constant, c is the speed of light, $A_{{\rm u}l}$ is the Einstein A-coefficient for the transition, and $T_{\rm mb}$ is the main beam brightness temperature. As customary the frequency ν has been converted to a Doppler velocity υ.

For a Boltzmann distribution, and with corrections for opacity and beam-filling, the true *total source-averaged* column density can be calculated as

$$N_{\rm LTE} = \frac{C_\tau}{\eta_{\rm bf}}\frac{8\pi k \nu_{{\rm u}l}^2}{hc^3}\frac{1}{A_{{\rm u}l}}\frac{Q(T)}{g_{\rm u}}{\rm e}^{E_{\rm u}/kT_{\rm ex}}\int T_{\rm mb}\,{\rm d}\upsilon, \tag{2}$$

where C_τ and $\eta_{\rm bf}$ are the opacity and beam-filling correction factors, $Q(T)$ is the partition function, g_u and E_u are the statistical weight and energy of the upper state, respectively, and $T_{\rm ex}$ is the excitation temperature for the transition.

For molecules where one or few transitions are observed, the column density is calculated using Eq. (2). If no information about optical depth or source-size is available these corrections are not taken into account, thus producing a *beam-averaged* and *not opacity corrected* column density.

3.2. Multiple line analysis

3.2.1. The rotation diagram method

When we have observed a number of lines with a wide range of upper-state energies, the rotation diagram method can be used according to

$$\ln\frac{N_{\rm u}^{\rm thin}}{g_{\rm u}} = \ln\frac{N_{\rm tot}}{Q(T)} - \frac{E_{\rm u}}{kT_{\rm ex}}. \tag{3}$$

To create a rotation diagram we plot $\ln(N_{\rm u}^{\rm thin}/g_{\rm u})$ as a function of the upper state energy $E_{\rm u}$ in a semi-log plot. A least squares fit to the data will then produce a straight line with slope $-1/T_{\rm ROT}$. If we extrapolate the line to $E_{\rm u} = 0$ K, we obtain the total column density from the intersection of the y-axis, y_0, and derive the total column density as

$$N_{\rm ROT} = Q(T)\,{\rm e}^{y_0}. \tag{4}$$

To correct for beam-filling, the right hand side of Eq. (4) is multiplied by $1/\eta_{\rm bf}$. Note that this constant does not change the rotation temperature. However, the optical depths can change the slope, and therefore the rotation temperature estimated from the rotation diagram.

The error bars shown in our rotation diagrams (Sect. 4) include 10% calibration error and the observed rms-noise.

3.2.2. The forward model (χ^2-method)

This model matches calculated opacity-corrected LTE integrated intensities and beam-filling in a χ^2 sense, to observed intensities vs. $E_{\rm u}$ (Nummelin et al. 1998; Nummelin et al. 2000; Lampton et al. 1976; Bevington 1969). Equation (3) in this case is modified to include optical depth and beam-filling corrections

$$\ln\frac{N_{\rm u}}{g_{\rm u}} + \ln C_\tau + \ln\frac{1}{\eta_{\rm bf}} = \ln\frac{N_{\rm tot}}{Q(T)} - \frac{E_{\rm u}}{kT_{\rm ex}}. \tag{5}$$

The intensity of each transition can be calculated using Eq. (12), with a specific set of free parameters $\eta_{\rm bf}$, $T_{\rm ROT}$ and $N_{\rm tot}$. The best fit to all the data, is obtained by finding the minimum of the reduced χ^2, which is defined as

$$\chi^2 = \frac{1}{n-p}\sum_{i=1}^{n}\left(\frac{I_i^{\rm obs} - I_i^{\rm calc}}{\sigma_i^{\rm obs}}\right)^2. \tag{6}$$

Here n is the number of data points, p is the number of free parameters, $\sigma_i^{\rm obs}$ is the 1σ uncertainty of the observed line intensity, $I_i^{\rm obs}$ and $I_i^{\rm calc}$ are the observed and calculated integrated intensities.

Note that the column density obtained with this method will be somewhat lower than that calculated from a simple rotation

diagram, since solutions producing $I_i^{\rm calc} < I_i^{\rm obs}$ are favoured compared to the opposite. This can be seen from the contribution to the χ^2-value from each transition giving χ_i^2.

$$\chi_i^2 = \left(\frac{I_i^{\rm obs} - I_i^{\rm calc}}{\sigma_i^{\rm obs}}\right)^2 \rightarrow \left(\frac{I_i^{\rm obs}}{\sigma_i^{\rm obs}}\right)^2 \quad (7)$$

when $I_i^{\rm calc} \rightarrow 0$. But if $I_i^{\rm calc} > I_i^{\rm obs}$, χ^2 will be unlimited, and this favours the lower model intensities (Nummelin et al. 1998).

4. Results

A summary of the observed features for all the species is presented in the online Table 5; the number of observed lines, the range in upper state energy, and the total integrated intensity.

A mean line-to-continuum ratio of 0.2 is reported in Paper I. The largest emission comes from CO with approximately 45% of the total spectral line emission. The second strongest emitter is H_2O (13%), followed by SO_2 (10%), SO (7%), ^{13}CO (7%) and CH_3OH (4%). The remaining species emit ∼14% of the total. However, these are *beam-average* values. Since the sizes of the SO_2, SO and CH_3OH emitting regions are much smaller than the extended CO emission, the relative amount of emission will change with a smaller beam, and will in addition not be the same for the different subregions.

The resulting column densities and rotation temperatures are shown in Tables 1 and 2, together with results from the ground-based submillimetre spectral scans by White et al. (2003, hereafter W03) from 455 to 507 GHz, Schilke et al. (2001, hereafter S01) from 607 to 725 GHZ, and Comito et al. (2005, hereafter C05) from 795 to 903 GHz. The number of lines used in our calculations are listed in parenthesis after the species in Table 1.

Differences may arise between the comparison surveys and ours due to the different beam-fillings. The comparison surveys W03 and S01 mostly use beam-averaged (with HPBW of 10″−12″) and not opacity-corrected column densities, while our results are corrected for beam-filling and optical depth, when possible. A second source of discrepancy is our effort to separate the emissions from different subregions, while the column densities in the comparison surveys are calculated from the total integrated intensity. Most of our column densities have therefore been calculated using the total integrated intensity and a source size of the main emitting component as a first approximation and comparison to S01 and W03. The column densities for the different subregions, are also calculated when possible, and have been corrected for opacity (if known) and beam-filling. In C05 beam-filling and optical depth correction are taken into account as well as separation into different subregions.

The listed source sizes are either calculated with Eq. (12), the χ^2-method, or taken from the literature. The size of the ER is assumed to be larger than our beam, although the East-West extent of the molecular ridge is rather limited (cf. Goldsmith et al. 1997). As excitation temperatures we use the population distribution temperatures $T_{\rm ROT}$ obtained from rotation diagrams. These temperatures are also used for species with similar excitation conditions. If no similar species exist, the temperatures are assumed to have the typical value for the emitting region: 100 K for the LVF, HVF and PDR, 60 K for the ER, 115 K for the CR, and 200 K for the HC. The rotation diagram technique as well as the forward model have been applied to all species that have a broad upper state energy range and four lines or more; SO_2, $^{34}SO_2$, SO, CH_3CN, CH_3OH, $^{13}CH_3OH$, H_2CS, and CH_3OCH_3; to calculate $N_{\rm ROT}$ and N_{χ^2}. Only in the methanol case, the forward model directly leads to a beam-filling and hence a source size. For the other species it was impossible to discriminate between solutions for different beam size/optical depth combinations.

In the online Table 6 our estimated isotopologue abundance ratios are listed, as well as comparisons with several other studies.

4.1. Outflow molecules

Sulphur-bearing species are considered to be tracers of massive *outflows* from a newly formed star. The high temperatures caused by the intense radiation from the driving source, or by shocks, can enhance the production of SO_2, SO and SiO. The line profile of the outflow shows a characteristic triangular line shape with broad wings as seen in examples of SO in Fig. 27, SiO in Fig. 28, SO_2 in Fig. 29, and in a comparison of SO_2 and SO in Fig. 41 (online material). The Orion outflows are also traced by other molecules like H_2O and CO: see Sects. 5 and 6, where also comparisons of $H_2^{18}O$, SO and SO_2 are shown.

4.1.1. Sulphur dioxide (SO_2/ $^{34}SO_2$)

We have observed 42 SO_2, and five $^{34}SO_2$ transitions. Typical line profiles are shown in Fig. 29 (online material) with different upper state energies. As proposed by Johansson et al. (1984) the complicated SO_2 and isotopologue line shapes suggest the presence of at least two velocity components, even though the emission primarily occurs in the outflow. Figure 1 shows a three-component Gaussian fit of a typical SO_2 line with line widths of ∼5 km s^{-1}, 18 km s^{-1} and 35 km s^{-1} from the CR, LVF and HVF, respectively. This is very similar to the Gaussian components of SO (Fig. 2), SiO (Fig. 3), and $H_2^{18}O$ (Fig. 36).

Figure 42 (online material) shows the size of the SO_2 emitting region vs. energy for each transition (Eq. (12)). The mean size is found to be 8″, which is consistent with the aperture synthesis mapping of Wright et al. (1996). This size is used for beam-filling corrections.

The high line density and the broadness of the SO_2 lines result in blends between the numerous transitions as well as with other species. There are 31 SO_2 transitions and four $^{34}SO_2$ transitions without blends, which are used in a rotation diagram shown in Fig. 43 (online material) producing $N_{\rm ROT} = (3.9 \pm 0.6) \times 10^{17}$ cm^{-2}, $T_{\rm ROT} = (132 \pm 8)$ K and $N_{\rm ROT} = (5.4 \pm 2.0) \times 10^{16}$ cm^{-2}, $T_{\rm ROT} = 125 \pm 30$ K for SO_2 and $^{34}SO_2$, respectively.

However, almost all of the SO_2 transitions are optically thick which lowers the SO_2 column density. The opacity is calculated using the same excitation temperature for all transitions and the column density obtained from the $^{34}SO_2$ rotation diagram (using an isotope ratio of 22.5, Table 6) and is found to be around 2–4 for most transitions. The opacity corrected rotation diagram is shown in Fig. 4 together with $^{34}SO_2$. The column density $N_{\rm ROT}^{\tau-{\rm corr}}$ increases to $(1.5 \pm 0.2) \times 10^{18}$ cm^{-2} and the temperature is lowered to 103 ± 3 K.

The isotopologue $^{34}SO_2$ is optically thin, hence no opacity correction is needed. But since the lines are weak and only four, the temperature from SO_2 is applied to the rotation diagram, which increases the $^{34}SO_2$ column slightly to 6.5×10^{16} cm^{-2}.

As a consistency check we also use Eq. (2) together with the single optically thin SO_2 line. This $16_{3,13}-16_{0,16}$ transition has an upper state energy of 148 K, and $\tau \sim 0.2$. The column density $N_{\rm LTE}$ obtained is 1.4×10^{18} cm^{-2}, in agreement with $N_{\rm ROT}^{\tau-{\rm corr}}$ and $N_{\rm ISO}$ from $^{34}SO_2$.

Table 1. Resulting column densities and rotation temperatures as well as comparison with W03, S01 and C05.

Species (No.)	Region	N [cm^{-2}]	T_{ex} [K]	Size[a] [″]	W03[b,c] N [cm^{-2}]	W03[b,c] T_{ex} [K]	S01[b,c] N [cm^{-2}]	S01[b,c] T_{ex} [K]	C05[d] N [cm^{-2}]	C05[d] T_{ex} [K]
SO_2 (31)	Total[c]	1.5×10^{18} [e]	103[e]	8[f]	1×10^{17}	136	6×10^{16}	187	9×10^{16}	130
	CR[g]	2.0×10^{17} [h]	(115)[i]	5[f]						
	LVF[g]	6.0×10^{17} [h]	103[j]	8[f]						
	HVF[g]	9.0×10^{17} [h]	103[j]	8[f]						
$^{34}SO_2$ (4)	Total[c] (outflow)	6.5×10^{16} [k]	103[j]	8[l]	8×10^{15}	156	8×10^{15}	192		
SO (5)	Total[c]	1.6×10^{17} [e]	132[e]	18[f]	3×10^{17}	(72)[i]	2×10^{17}	64	5×10^{16}	150
	CR[g]	1.7×10^{16} [h]	(115)[i]	6[f]						
	LVF[g]	9.3×10^{16} [h]	132[m]	11[n]						
	HVF[g]	8.5×10^{16} [h]	(100)[i]	18[n]						
^{33}SO (3)	Total[c] (outflow)	1.7×10^{15} [o]	132[m]	18[p]						
^{34}SO (2)	Total[c] (outflow)	8.4×10^{15} [o]	132[m]	18[p]	1×10^{16}	89				
SiO (1)	Total[c]	4.0×10^{15} [q]	(100)[i]	14[f]			5×10^{14}	110	1×10^{15}	(150)[i]
	LVF[g]	3.3×10^{15} [h]	(100)[i]	10[n]						
	HVF[g]	1.8×10^{15} [h]	(100)[i]	14[r]						
^{29}SiO (1)	Total[c] (outflow)	2.0×10^{14} [o]	(100)[i]	14[r]						
H_2S (1)	LVF[g]	4.5×10^{16} [o]	(100)[i]	(15)[i]			1×10^{16}	129	4×10^{16}	140
	HC[g]	2.7×10^{16} [o]	(200)[i]	(10)[i]						
CH_3CN (9)	Total[c] (HC)	5.0×10^{15} [k]	137[k]	(10)[i]	3×10^{15}	227			4×10^{15}	250
HC_3N (2)	Total[c] (HC)	1.8×10^{15} [o]	(200)[i]	(10)[i]	1×10^{15}	164				
OCS (3)	Total[c] (HC)	1.7×10^{16} [o]	(200)[i]	(10)[i]	9×10^{16}	106				
NO (1)	Total[c] (HC)	2.8×10^{17} [o]	(200)[i]	(10)[i]			1×10^{17}	90	2×10^{17}	150
NH_3 (1)	CR[g]	4.0×10^{16} [h]	(115)[i]	17[f]						
	HC[g]	1.6×10^{18} [q]	(200)[i]	8[f]						
$^{15}NH_3$ (1)	Total[c] (HC)	3.5×10^{15} [o]	(200)[i]	8[s]						
CH_3OH (50)	Total[c]	3.4×10^{18} [e]	116[e]	6[f,t]	9×10^{16}	599	5×10^{16}	303		
	HC[g]	7.9×10^{17} [u]	178[u]	6[n]					3×10^{16}	220
	CR[g]	2.4×10^{18} [u]	98[u]	6[f]					5×10^{16}	160
$^{13}CH_3OH$ (14)	Total[c] (CR)	5.9×10^{16} [k]	115[k]	6[v]			1×10^{16}	229		
$(CH_3)_2O$ (37)	Total[c] (CR)	1.3×10^{17} [k]	112[k]	6[v]	1×10^{16}	157	3×10^{16}	360	2×10^{16}	160
H_2CS (4)	Total[c] (CR)	1.3×10^{15} [k]	93[k]	14[x]						
H_2CO (3)	LVF[g]	4.3×10^{15} [o]	(100)[i]	(15)[i]	1×10^{16}	(166)[i]	3×10^{15}	190	2×10^{15}	155
	CR[g]	2.0×10^{16} [q]	(115)[i]	14[f]						
$H_2^{13}CO$ (1)	Total[c] (CR)	3.3×10^{14} [o]	(115)[i]	14[x]	1×10^{15}	(166)[i]				
HDCO (2)	Total[c](CR)	2.7×10^{14} [o]	(115)[i]	14[x]						
CS (1)	LVF[g]	3.6×10^{15} [o]	(100)[i]	(15)[i]			1×10^{15}	127	3×10^{15}	100
	HC[g]	2.9×10^{15} [o]	(200)[i]	(10)[i]					1×10^{16}	190
	N as CR[g]	8.0×10^{15} [q]	(115)[i]	20[f]						
	N as ER[g]	4.2×10^{14} [q]	(60)[i]	...						
^{13}CS (1)	Total[c] as CR	1.3×10^{14} [o]	(115)[i]	20[y]	2×10^{14}	(120)[i]				
	Total[c] as ER	7.1×10^{12} [o]	(60)[i]	...						
HNC (1)	LVF[g]	3.6×10^{14} [o]	(100)[i]	(15)[i]					5×10^{14}	(150)[i]
	HC[g]	4.4×10^{14} [o]	(200)[i]	(10)[i]						
	ER[g]	1.9×10^{12} [o]	(60)[i]	...						
CN (2)	PDR/ER[g]	4.9×10^{13} [o]	(100)[i]	...						
	HC[g]	7.9×10^{15} [o]	(200)[i]	(10)[i]						
N_2H^+ (1)	Total[c] (ER)	1.0×10^{12} [o]	(60)[i]	...						

[a] The column density is a source-average if a source size is given, else it is a beam-average. [b] HPBW is 10–12″ in comparison surveys, and the column densities are beam-averaged and not corrected for opacity. [c] From the total integrated intensity of the line(s). [d] Beam-filling and opacity corrected, as well as separation into components. [e] From an opacity-corrected rotation diagram. [f] From optically thick line(s). [g] From Gaussian decomposition. [h] N_{LTE}, opacity corrected. [i] Not calculated by the authors. [j] Temperature from SO_2 opacity-corrected rotation diagram. [k] From a non opacity-corrected rotation diagram. [l] Size from SO_2. [m] Temperature from a SO opacity-corrected rotation diagram. [n] Opacity corrected. [o] N_{LTE}. [p] Size from SO total integrated intensity. [q] N_{ISO}. [r] Size from SiO total integrated intensity. [s] Size from NH_3. [t] From the forward model. [u] From an opacity corrected two-component rotation diagram. [v] Size from CH_3OH. [x] Using H_2CO calculated source size. [y] Using size from CS.

Our column densities of both isotopologues are much larger than in the comparison surveys. This can partly be caused by our beam-filling correction with a rather small size, and the non-correction for opacity in W03 and S01. However, Johansson et al. (1984) and Serabyn & Weisstein (1995) obtain a column density of about 1×10^{18} cm^{-2} (corrected for our source size) in agreement with our value.

Column densities for each subregion are estimated from the Gaussian components shown in Fig. 1 (Table 1). The rarer isotopologues are too weak for a Gaussian decomposition so

Table 2. Column density results for water, C, CO and H_2.

Species	Region	T_{ex} [K]	N_{LTE} [cm^{-2}]	N_{ISO} [cm^{-2}]	N_{H_2} [cm^{-2}]	Size[a] [']	τ
C		100	5.6×10^{17}			...	
CO	PDR[b]	100	1.6×10^{17}	1.6×10^{18} [c]	2.0×10^{22}	...	
	LVF	100		2.5×10^{19} [c]	3.2×10^{23}	(30)[d]	
	HVF	100	1.2×10^{18}	3.1×10^{18} [e]	3.9×10^{22}	70[f]	
^{13}CO	PDR/ER[b]	100	5.7×10^{16}	5.4×10^{16} [c]		...	
	LVF	100	3.9×10^{17}	4.2×10^{17} [c]		30	
	HVF	100	5.2×10^{16}			70	
C^{17}O	PDR/ER[b]	100	2.5×10^{15}			...	0.07
	LVF	100	2.0×10^{16}			30	0.1
C^{18}O	PDR/ER[b]	100	8.9×10^{15}	9.8×10^{15} [c]		...	0.3
	LVF	100	6.7×10^{16}	7.7×10^{16} [c]		30	0.3
H_2O	Total[g]	72		1.7×10^{18} [h]		(15)[d]	~1100
	CR	115		5.6×10^{17} [h]		(6)[d]	~860
	LVF	72		8.7×10^{17} [h]		(15)[d]	~1900
	HVF	72	8.0×10^{17} [i]	8.8×10^{17} [h]		70[f]	~910
	HC	200	1.2×10^{19} [j]			10	0.3[k]
$H_2^{17}O$	Total[g]	72	1.3×10^{15} [l]			15	0.9
	CR	115	4.4×10^{14} [l]			6	0.7
	LVF	72	6.7×10^{14} [l]			15	1.5
	HVF	72	6.8×10^{14} [l]			15	0.7
$H_2^{18}O$	Total[g]	72	5.0×10^{15} [l]	5.0×10^{15} [h]		15	3.4
	CR	115	1.8×10^{15} [l]	1.7×10^{15} [h]		6	2.6
	LVF	72	2.7×10^{15} [l]	2.6×10^{15} [h]		15	5.9
	HVF	72	2.8×10^{15} [l]	2.7×10^{15} [h]		15	2.8
HDO	Total[g]	72	9.1×10^{15}			15	1.5[k]
	CR	115	1.8×10^{16}			6	3[k]
	LVF	72	4.5×10^{15}			15	0.3[k]
	HC	200	1.5×10^{16}			10	0.5[k]

[a] The column density is a source-average if a source size is given, else it is a beam-average. [b] The narrow component from CO isotopologues contains emission from both PDR and ER, the CO narrow component only from the PDR, hence the PDR column density for CO here is divided by two as motivated in Sect. 5. [c] Using C^{17}O together with [^{18}O/^{17}O] = 3.9, [^{16}O/^{18}O] = 330, and [^{12}CO/^{13}CO] = 60. [d] Indirect size estimated using isotopologues. The full size may be larger. [e] Using ^{13}CO together with [^{12}CO/^{13}CO] = 60. [f] Hjalmarson et al. (2005). [g] From the total integrated intensity of the line. [h] Using opacity and beam-filling corrected *o*-$H_2^{17}O$ together with [^{18}O/^{17}O] = 3.9 and [^{16}O/^{18}O] = 330. [i] From HVF Gaussian fit of *o*-H_2O, opacity and beam-filling corrected. [j] Using beam-filling corrected *p*-H_2O. [k] Calculated with Eq. (15). [l] Opacity and beam-filling corrected.

opacities cannot be calculated by comparison with isotopologues. Still, the components are likely to be optically thick and therefore the sizes of the emitting regions are calculated with T = 115 K for the CR, and T = 103 K for the LVF and HVF. The source sizes are found to be 5″ for the CR and 8″ for both the LVF and HVF. These sizes correspond to optical depths of about 2–3. The opacity-corrected column densities become 2×10^{17} cm^{-2}, 6×10^{17} cm^{-2}, and 9×10^{17} cm^{-2} for the CR, LVF and HVF, respectively.

The elemental isotopic ratio of [^{32}S/^{34}S] can be estimated from a comparison of the optically thin column densities. In this way we obtain an isotopic ratio of 23 ± 7, in agreement with most other comparison studies listed in Table 6.

As expected, no vibrationally excited lines were found. The $5_{5,1}-4_{4,0}$ v_2 bending mode transition has the lowest upper state energy (822 K) of all v_2 lines in our spectral range. The calculated expected peak temperature of this line is 34 mK, with an expected line width of 23 km s^{-1}. Such weak and broad lines are marginally below our detection limit.

4.1.2. Sulphur monoxide (SO/^{33}SO/^{34}SO)

Typical line profiles are shown in Fig. 27 (online material). The line profiles of the high energy transitions show an even broader outflow emission, and with more pronounced high velocity line wings than does SO_2 (comparison in Fig. 41 in the online material). As for SO_2, the emission is primarily from the Plateau, and Friberg (1984) has shown the bipolar nature of the HVF component. The ratios of SO_2 and SO emission lines vs. velocity, also show a high degree of similarity between the line profiles except in the high velocity regime between −30 to −5 km s^{-1}. At these velocities SO has stronger emission than SO_2.

Figure 2 shows the $13_{12}-12_{11}$ transition with a three-component Gaussian fit. The broad HVF component has a FWHM width of ~35 km s^{-1} at υ_{LSR} ~ 9 km s^{-1}. The LVF component has widths of 18 km s^{-1} at υ_{LSR} ~ 8 km s^{-1}. In addition to the LVF and HVF components a third from the CR appears with a width of 5 km s^{-1} at υ_{LSR} ~ 9–10 km s^{-1}.

The most likely source size is 18″, calculated using the three optically thick SO lines. This is in agreement with the aperture synthesis mapping by Beuther et al. (2005), and Wright et al. (1996), who find a larger source size for SO than for SO_2. The source size 18″ is used for beam-filling correction.

The rotation diagram in Fig. 5 (calculated with the total integrated intensity of the lines) displays our five SO lines. The rotation temperature without any corrections is (59 ± 2 K) and the column density N_{ROT} is (1.5 ± 0.2) × 10^{17} cm^{-2}. However, the three higher energy lines have optical depth of ~3, whereas

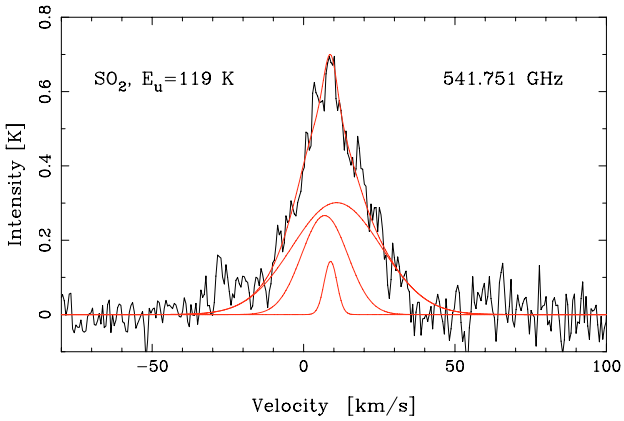

Fig. 1. The $14_{3,11}$–$13_{2,12}$ SO_2 transition with a three-component Gaussian fit shown together with the individual Gaussians. The line widths are 5 km s^{-1}, 18 km s^{-1} and 35 km s^{-1} from the CR, LVF and HVF, respectively.

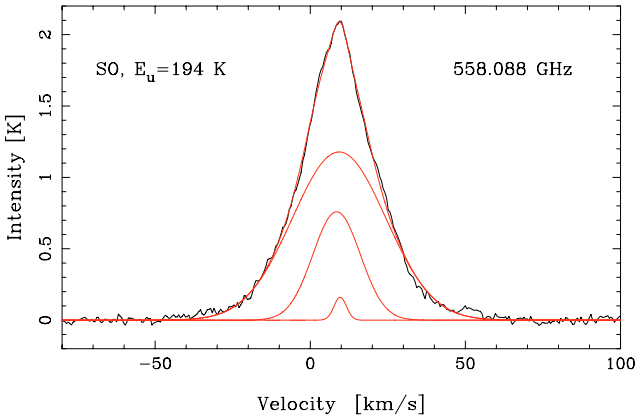

Fig. 2. The 13_{12}–12_{11} SO transition with a three-component Gaussian fit shown together with the individual Gaussians. The line widths are 5 km s^{-1}, 18 km s^{-1} and 35 km s^{-1} from the CR, LVF and HVF, respectively.

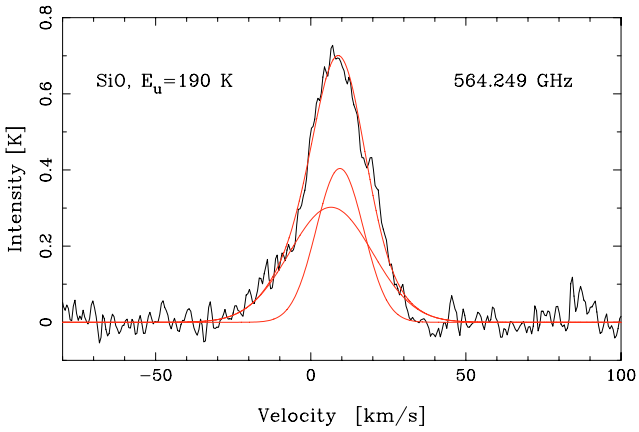

Fig. 3. The J = 13–12 SiO transition with a two-component Gaussian fit shown together with the individual Gaussians. The line widths are 18 km s^{-1} and 31 km s^{-1} from the LVF and HVF, respectively.

the two low energy transitions are optically thin with $\tau \sim 0.1$ (Eq. (15)). We make an optical depth correction for all five transitions and plot them again in Fig. 5 together with a new fit. Note that the correction is substantial for the high energy, optically thick lines (cf. Serabyn & Weisstein 1995). The rotation temperature obtained is higher than without corrections, 132 ± 22 K, but the resulting column density is only slightly higher than that found without the corrections, $N_{\rm ROT}^{\tau-{\rm corr}} = (1.6 \pm 0.5) \times 10^{17}$ cm^{-2}. This is in agreement with the column density obtained from ^{34}SO, $N_{\rm ISO} = 1.9 \times 10^{17}$ cm^{-2} (using 22.5 for [^{32}S/^{34}S]). The two optically thin SO transitions gives $N_{\rm LTE} = 1.8 \times 10^{17}$ cm^{-2}. The column densities for both isotopologues are calculated with the rotation temperature from SO.

The isotopologues, two ^{33}SO and three ^{34}SO transitions, are optically thin with opacities around 0.02 and 0.13, respectively. These transitions are plotted in Fig. 5 with the integrated intensities multiplied by appropriate isotopic ratios (5.5 for [^{34}S/^{33}S], Table 6). As seen in Fig. 5, the result of the isotopic ratio corrections is consistent with the optical depth corrected SO transitions.

As for SO_2 the column densities for each SO subregion are estimated from the Gaussian components shown in Fig. 2. Opacities cannot be calculated by comparison with the rarer isotopologues since they are too weak for a Gaussian decomposition. However, the components are likely to be optically thick and therefore the sizes of the emitting regions are calculated with T = 115 K for the CR, T = 132 K for the LVF, and T = 100 K for the HVF. The source sizes of the CR, LVF and HVF are found to be 6″, 10″ and 14″, respectively. These sizes may be larger if the opacities are low. Combining calculations of source size, optical depths, and column densities, the sizes for the LVF and HVF increase slightly to 11″ and 18″, respectively. These sizes correspond to optical depths of about 2.5 and 1.0 for respective region. The opacity-corrected column densities become 1.7×10^{16} cm^{-2}, 9.3×10^{16} cm^{-2}, and 8.5×10^{16} cm^{-2} for the CR, LVF and HVF, respectively.

The elemental isotopic ratio of [^{32}S/^{34}S] and [^{34}S/^{33}S] can be estimated from comparisons of the column densities of the isotopologues and the optically thin SO transitions. We obtain isotopic ratios of 21.0 ± 6 and 4.9, respectively in agreement with most other comparison studies listed in Table 6.

4.1.3. Silicon monoxide (SiO/^{29}SiO/^{30}SiO)

We have observed the transition J = 13–12 for each isotopologue, and we show the SiO and ^{29}SiO transitions in Fig. 28 (online material). As for SO_2 and SO, the complicated line profile of SiO suggests emission from both the LVF and the bipolar HVF (present in aperture synthesis maps of Wright et al. 1996), with widths of 18 and 31 km s^{-1} at $v_{\rm LSR}$ velocities of 9 and 7 km s^{-1}, respectively. Figure 3 shows the two-component Gaussian fit to SiO. The ^{29}SiO transition is located in the high-velocity wing of o-H_2O (at $v_{\rm LSR} \sim -130$ km s^{-1}). The width is 21 km s^{-1} at a centre velocity of ~9 km s^{-1}. The ^{30}SiO transition is a questionable assignment due to its narrow line width of 7.5 km s^{-1}.

Comparison of the peak antenna temperatures of SiO and ^{29}SiO shows that the SiO transition has an optical depth of ~1.0. The source size (Eq. (12)) is found to be 14″. This is used as beam-filling correction. Using a LVF temperature of 100 K (about the same temperature as the SO_2 rotation temperature), the total integrated intensity, and the simple LTE approximation, the opacity-corrected column density is found to be 4.0×10^{15} cm^{-2} for SiO.

The decomposition into subregions results in LVF and HVF source sizes of 8″ and 7″ with temperatures of 100 K for both sources. The rather small values are most likely due to the low opacity in these components and are therefore only lower

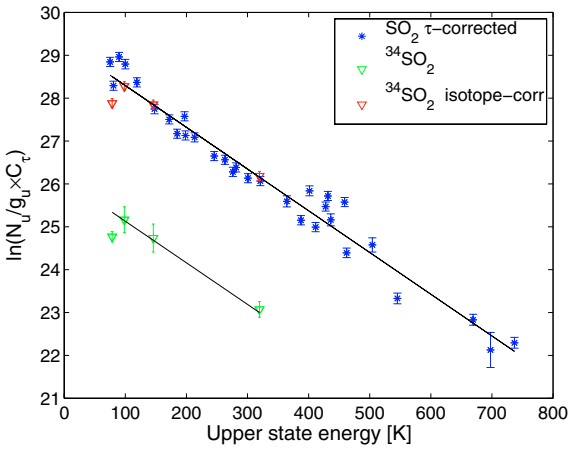

Fig. 4. Rotation diagram for SO_2 produces T_{ROT} = 103 K (extended source). The $^{34}SO_2$ fit uses the SO_2 rotation temperature.

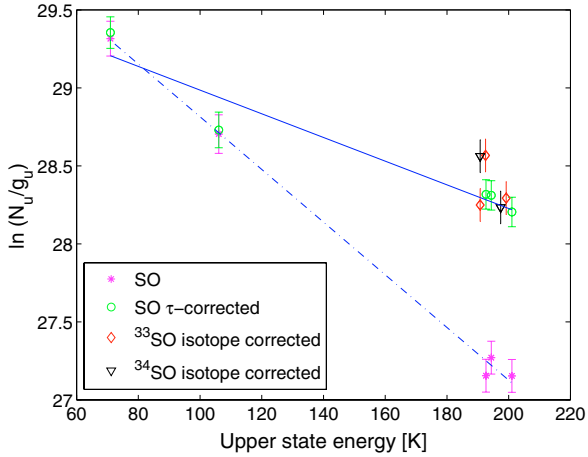

Fig. 5. Rotation diagram for SO and isotopologues (extended source). The isotopologues are plotted multiplied by respective isotopic ratio. Two fits are made: the first (dashed-dotted line) is not opacity corrected (T_{ROT} = 59 K), while the second (solid line) is corrected for opacity (T_{ROT} = 132 K).

limits. Assuming that the opacity in the LVF is about the same as for the total integrated emission, the LVF opacity-corrected source size increases to 10″. The opacity in the HVF is most likely less than in the LVF. As an upper limit the size is assumed to be the same as for the total integrated emission, which results in an HVF opacity of about 0.4. The sizes are consistent with Beuther et al. (2005). Note the similarity of the SO and SiO source sizes. In Sect. 6 the $H_2^{18}O$ sizes will also be shown to be similar. These source sizes are used to correct for beam-filling, and the resulting LVF and HVF opacity-corrected column densities are 3.3×10^{15} and 1.8×10^{15} cm^{-2}, respectively.

4.2. Outflow and Hot Core molecule

The *Hot Core* is a collection of warm (≳200 K) and dense ($n \sim 10^7$ cm^{-3}) clumps of gas. The dominating species are oxygen-free, small, saturated nitrogen-bearing molecules such as CH_3CN and NH_3. Most N-bearing molecules are strong in the HC, while the oxygen-bearing molecules peak toward the CR (e.g. Blake et al. 1987, hereafter B87; Caselli et al. 1993; Beuther et al. 2005). CH_3OH is an exception with pronounced emissions from the HC as well as from the CR. In addition, high levels of deuterium fractionation are found here. Since the HC region

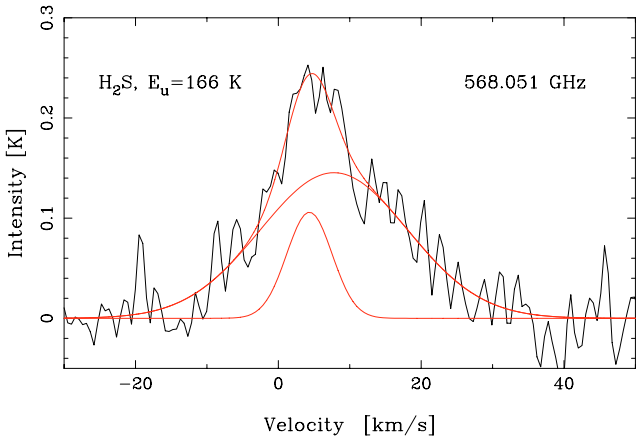

Fig. 6. The H_2S $3_{3,1}$–$3_{2,2}$ transition with a two-component Gaussian fit shown together with the individual Gaussians. The line widths are 8 km s^{-1} and 24 km s^{-1} from the HC and outflow, respectively.

probably contains one or more massive protostars it presents an ideal opportunity to study active gas-phase chemistry. And due to the high temperatures in both the HC and CR, the gas-phase chemistry will get a significant contribution of molecules from grain surface chemistry through evaporation of the icy mantles caused by the intense UV radiation from newly formed stars.

4.2.1. Hydrogen sulphide (H_2S)

We observe only the $3_{3,1}$–$3_{2,2}$ transition of H_2S, with emission from the HC and LVF, illustrated by a Gaussian decomposition in Fig. 6. The emission from the HC component has a width of ∼8 km s^{-1} at $\upsilon_{LSR} \sim 5$ km s^{-1} between velocities −5 to +15 km s^{-1}. The LVF emission has a width of ∼24 km s^{-1} at $\upsilon_{LSR} \sim 8$ km s^{-1}. The line is also shown in the bottom of Fig. 25 (online material) together with other comparison HC molecules.

The column densities are consistent with the comparison surveys assuming typical source sizes and temperatures.

4.3. Hot Core molecules

4.3.1. Methyl cyanide (CH_3CN)

Previous observations of the high density tracer CH_3CN (e.g. Blake et al. 1986; Wilner et al. 1994) have shown that the low-J transitions in the vibrational ground state appears to be a mix of CR and HC emission, while the high-J transitions and all the vibrationally excited lines originate in the HC only. This is also confirmed in our survey where we observe the 30_K–29_K transitions with K = 0–9, and 31_K–30_K with K = 0–6 and 9. These lines suggest an origin in the HC at $\upsilon_{LSR} \sim 5$–6 km s^{-1} and widths of ∼8–9 km s^{-1}, also consistent with W05 and C05. The 30_4–29_4 ground state transition is shown in Fig. 25 (online material). In addition we see a number of weak vibrational lines from the $\upsilon_8 = 1$ bending mode with 30_K–29_K where K = 0–3. In total we observe 17 line features from this molecule. Nine of these are free from blends and are used in the rotation diagram (Fig. 7). Due to the weak lines the rotation temperature of 137 ± 25 K and the column density of $(5.0 \pm 3.6) \times 10^{15}$ cm^{-2} are comparatively uncertain. The temperature is rather low compared to W03 who estimate the temperature to 227 K, and C05 to 250 K. Still, the column density agrees well with B87, Sutton et al. (1995, hereafter S95), W03, and C05.

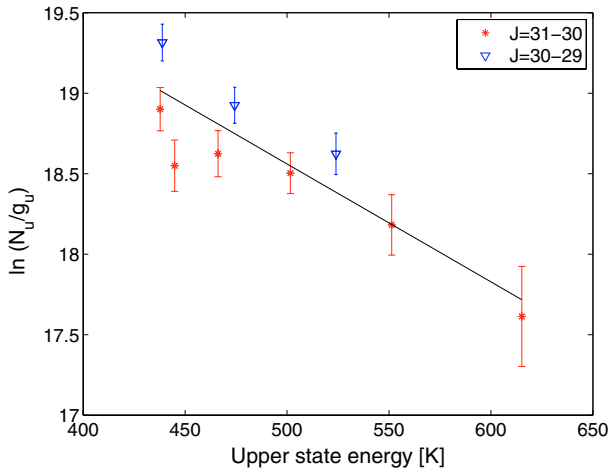

Fig. 7. Rotation diagram for CH_3CN producing T_{ROT} = 137 K (extended source).

Wilner et al. (1994) find an opacity of the HC emission of at most a few for the main lines. This could explain the rather low [$^{13}C/^{12}C$] ratios in Blake et al. (1986) and Turner (1991). Sutton et al. (1986) suggests significant opacity from their statistical equilibrium calculations, if the HC is as small as 10″. This would give even higher column densities in the HC.

The partition function is calculated as recommended in Araya et al. (2005).

4.3.2. Cyanoacetylene (HC_3N)

Two transitions of cyanoacetylene are seen, of which J = 54–53 is a blend with CH_3OH. The transition J = 60–59 is shown in Fig. 25 (online material). HC emission is here evident at v_{LSR} ~ 5–6 km s^{-1} and a line width of ~10 km s^{-1}. The column density is calculated with the simple LTE approximation and is in agreement with W03.

4.3.3. Carbonyl sulphide (OCS)

We have identified three transitions from carbonyl sulphide, J = 47–46, J = 45–44, and J = 46–45 (shown in the online Fig. 25). The emission has its origin in the HC with v_{LSR} ~ 6 km s^{-1}, and a width of ~6 km s^{-1}.

The estimated column density is about five times lower than found by both W03 and S95.

4.3.4. Nitric oxide (NO)

We observe three features with $^2\Pi_{3/2}$, J = 11/2–9/2, and $^2\Pi_{1/2}$, J = 11/2–9/2 from both e and f species, which are composed of twelve non-resolved hyperfine transitions. No separation into components is possible due to blends between the hyperfine transitions and other species. Our estimated rotation temperature from our transitions with upper state energies of 84 K and 232 K is found to be 75 K. This is highly uncertain due to the severe blends in both low energy transitions. Since S01 and C05 observed HC emission we therefore use a typical HC temperature of 200 K and source size of 10″. The resulting column density (using the high energy line) is in agreement with S01 and C05.

4.4. Hot Core and Compact Ridge molecules

The *Compact Ridge* is a more quiescent region as compared to the Hot Core. Here we find high abundances of oxygen-bearing species such as CH_3OH, $(CH_3)_2O$ and HDO (B87; Caselli et al. 1993; Beuther et al. 2005). As in the HC, the evaporation of the icy mantles in the warm CR will release molecules produced by grain surface chemistry into the gas-phase.

4.4.1. Ammonia ($NH_3/^{15}NH_3$)

The symmetric top ammonia molecule is a valuable diagnostic because its complex energy level structure covers a very broad range of critical densities and temperatures (see Ho & Townes 1983, for energy level diagram and review).

Many observations have been made of the NH_3 inversion lines at cm wavelengths since the first detection by Cheung et al. (1968). The upper state energy of the lowest metastable inversion lines are 24 K and 64 K comparable to 28 K for the rotational ground state transition 1_0–0_0 at 572 GHz. The critical density is very different though, and is 3.6 × 10^7 cm^{-3} (calculated for 20 K) for the rotational ground state transition, and about 10^3 cm^{-3} for the inversion lines. The non-metastable inversion lines also trace higher excitation and density regions. Comparison of all these transitions could therefore give valuable information about both high- and low-density and temperature regions. The previous low quantity of observations of rotational transitions is due to the fact that they fall into the submillimetre and infrared regimes, which are generally not accessible from the ground and therefore has to be observed from space.

Observations of both metastable and non-metastable inversion lines (e.g. Batrla et al. 1983; Hermsen et al. 1988a,b; Migenes et al. 1989) have shown NH_3 in the HC, CR, ER and LVF regions. The existence of an outflow component was however questioned by Genzel et al. (1982) since the hyperfine satellite lines could cause the broadness of the line if the opacity is large.

The rotational ground state transition was first and solely detected twenty-four years ago with the Kuiper Airborne Observatory (Keene et al. 1983). Note that the Kuiper Airborne Observatory had a similar beam size (2′) to that of Odin (2.′1). Using Odin, sensitive observations have been made recently for example towards Orion KL and the Orion Bar (Larsson et al. 2003), the ρ Oph A core (Liseau et al. 2003), Sgr B2 (Hjalmarson et al. 2005), as well as the molecular cloud S140. The resulting NH_3 abundance in the Orion Bar is 5 × 10^{-9} (Larsson et al. 2003).

In this spectral survey we have observed the rotational ground state 1_0–0_0 transitions of NH_3 and $^{15}NH_3$, which are shown in Fig. 25 (online material). We show the NH_3 transition twice to emphasize the line wings. Our peak temperature agrees to within 5% with Larsson et al. (2003) who used a rather different Odin observational setup, demonstrating the excellent calibration of the Odin data. The vibrational transition v_2 = 1 of this line at 466 GHz has previously been observed by Schilke et al. (1992).

Figure 8 shows our two-component Gaussian fit to the NH_3 line which has pronounced features of the CR and a broad component. The line widths are 5 and 16 km s^{-1} at LSR velocities 8, and 9 km s^{-1} for the CR and broad components, respectively. The CR emission was also observed by Keene et al. (1983), while the broader component clearly seen in our Odin data, was only marginally present in their lower signal-to-noise data. Our $^{15}NH_3$ spectrum shows only evidence of the

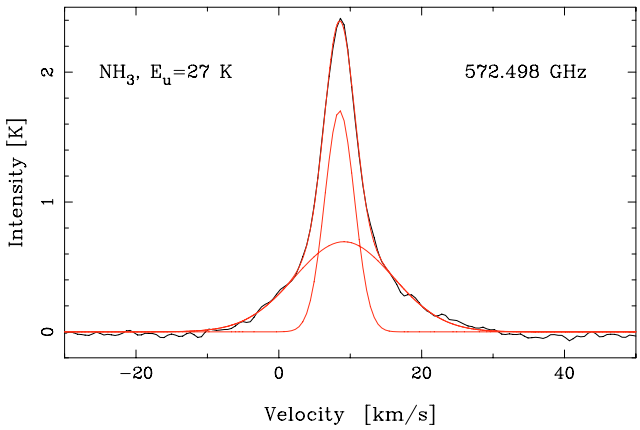

Fig. 8. The NH_3 transition with a two-component Gaussian fit shown together with the individual Gaussians. The line widths are 5 km s^{-1} and 16 km s^{-1} from the CR and HC/outflow, respectively.

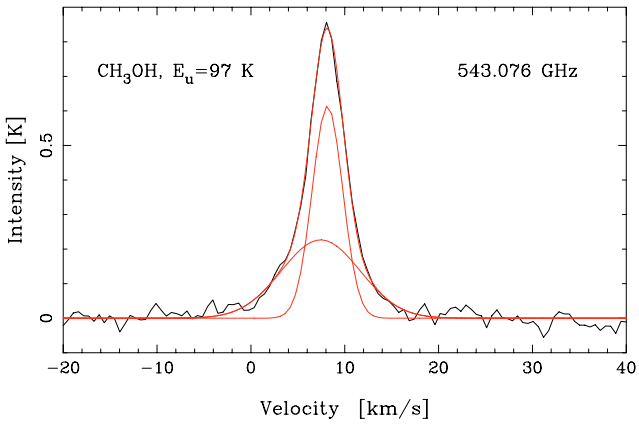

Fig. 9. Methanol line with a two-component fit shown together with the individual Gaussians. The line widths are 4 km s^{-1} and 10 km s^{-1} from the CR and HC, respectively.

HC component (cf. Hermsen et al. 1985), with a width of ∼7 km s^{-1} at $v_{LSR} \approx 7$ km s^{-1}. The width of the broad NH_3 component may seem too large to have an origin in the HC. However, the broadness of the line may be caused by opacity broadening (Eq. (21); cf. Phillips et al. 1979). From Eq. (16) combined with an assumed $^{14}N/^{15}N$ isotope ratio of 450 (Table 6), we estimate optical depths of ∼100 and ∼0.3 in the NH_3 and $^{15}NH_3$ HC lines, respectively. According to Eq. (21) this will broaden the optically thick NH_3 emission line by approximately 2.6 times from a line width comparable to the optically thin $^{15}NH_3$ HC emission to a resulting width of ∼17 km s^{-1}. This is very close to the width of our Gaussian HC component, 16 km s^{-1}. However, the high opacity in this component will cause the line profile to be flat topped with little or no line wings. Hence our broad Gaussian component not only contains the opacity broadened HC emission but also the outflow component seen by e.g. Wilson et al. (1979) and Pauls et al. (1983), in our spectrum visible as pronounced line wings. Alternatively it could be that the HC emission is hidden by optically thick NH_3 LVF emission just as in case of water (cf. Sect. 6.2.2).

The NH_3 source sizes of the CR and HC regions are found to be 17″ and 8″, respectively, and are used as beam-filling corrections. The rather large CR size as compared to the 6″ mean source size obtained for CH_3OH, might be due to the low upper state energy of 27 K for NH_3. Figure 12 shows the decreasing methanol source size with upper state energy, where the lowest methanol transitions with upper state energies of 40−100 K reach a source size of ∼11″. Hermsen et al. (1988b) find source sizes of 15″ and 6″ for the CR and HC, respectively, in agreement with our calculations. VLA maps by Migenes et al. (1989) also show that the HC emission is clumped on 1″ scales.

Hermsen et al. (1988b) find a HC temperature of 160 ± 25 K and a CR temperature above 100 K. In addition Wilson et al. (2000) detect an even hotter HC component with a temperature of about 400 K. Using HC and CR temperatures of 200 K and 115 K, respectively, we find a NH_3 HC column density (calculated from the optically thin $^{15}NH_3$ line) of 1.6×10^{18} cm^{-2}. Our comparison surveys have no observations of this molecule, but our result agrees with Genzel et al. (1982), who report column densities of NH_3 that reach 5×10^{18} cm^{-2} from the HC, with size 10″ and temperatures about 200 K. Their observations also confirmed increasing line width with increasing optical depth. Hermsen et al. (1988b) and Pauls et al. (1983) find values of 1×10^{18} cm^{-2} for the HC.

The optically thick NH_3 CR column density is found to be 3.4×10^{15} cm^{-2}. Optical depth broadening is used to estimate the opacity in this component. Batrla et al. (1983) found an intrinsic velocity width of 2.6 km s^{-1} by ammonia inversion lines observations. From a comparison with the observed line width, the opacity is estimated to be about 12 in the CR component. The opacity-corrected CR column density then becomes 4.0×10^{16} cm^{-2}. This is in agreement with the estimation of Hermsen et al. (1988b) who find a column density in the range 8×10^{15}−8×10^{16} cm^{-2} from the metastable (6,6) inversion line.

4.4.2. Methanol ($CH_3OH/^{13}CH_3OH$)

Methanol is an organic asymmetric top molecule with many energy levels (see energy level diagram in Nagai et al. 1979), and behaves like two different species labelled A and E for symmetry reasons.

We have observed 76 methanol lines of which 42 are from the $v_t = 1$ state, which is the first excited vibrational state of the torsional motion of the CH_3 group relative to the OH group. In the online Fig. 32 we have collected a number of examples of typical line profiles of CH_3OH, with different upper state energies and A-coefficients. The rarer isotopologue $^{13}CH_3OH$ is seen with 23 lines, of which two are vibrationally excited. Three typical line profiles are shown in the online Fig. 30.

The CH_3OH lines show evidence of two velocity components. One narrow, likely from the CR, with a line width of ∼3−4 km s^{-1}, and average velocity ∼8 km s^{-1}. The other broader component with a probable origin in the HC has a line width of ∼6−10 km s^{-1}, and average velocity ∼7 km s^{-1} (see an example of a two-component Gaussian fit in Fig. 9). This is consistent with the findings of Menten et al. (1988), S95, C05, and also of Beuther et al. (2005) who locate the methanol emission to the HC as well as the CR in their SMA aperture synthesis maps. According to recent CRYRING storage ring measurements (Geppert et al. 2005; Millar 2005) the dissociative recombination of a parent ion $CH_3OH_2^+ + e^- \rightarrow CH_3OH + H$ is so slow that gas-phase formation of methanol is unable to explain the abundance of this molecule, even in dark clouds where it is rare. Instead we have to rely on efficient hydrogenation reactions on grain surfaces, and subsequent release of the methanol into gas-phase. In this scenario the presence of very large amounts of CH_3OH in the compact, heated CR and HC sources is indeed expected.

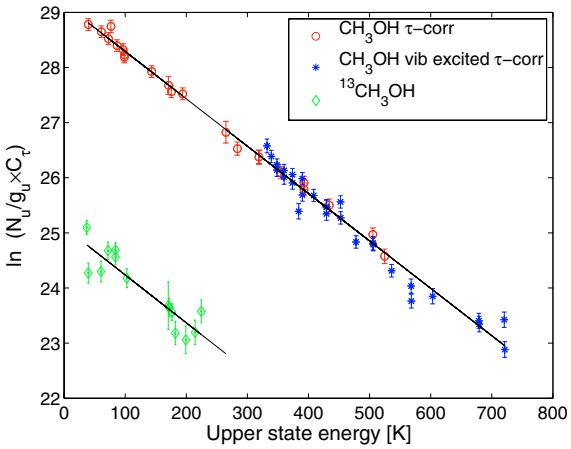

Fig. 10. CH_3OH opacity corrected rotation diagram producing T_{ROT} = 116 K (extended source). The opacity is calculated with varying source-sizes with energy. The $^{13}CH_3OH$ rotation diagram gives a temperature of 115 K.

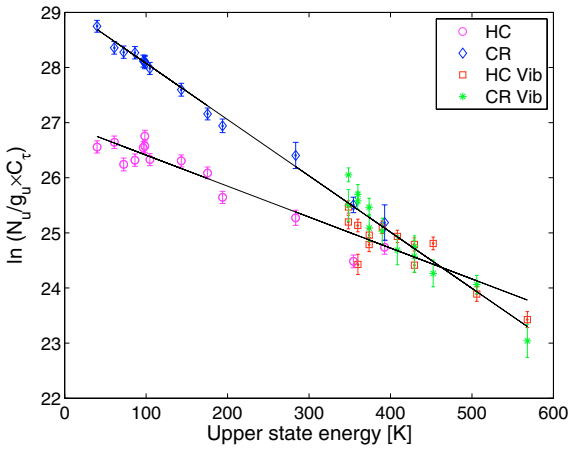

Fig. 11. Two component CH_3OH opacity corrected rotation diagram producing T_{ROT} = 178 K and 98 K for the HC and CR, respectively (extended source). The opacity is calculated with the same parameters together with varying source-size with energy.

The isotopologue $^{13}CH_3OH$ show only evidence of the narrow component, which can be well fitted by a single Gaussian with $\Delta v \approx 3$ km s^{-1} at $v_{LSR} \approx 8$ km s^{-1}. This is also consistent with Menten et al. (1988) and Beuther et al. (2005). The slight broadening of the CH_3OH narrow components compared with that of $^{13}CH_3OH$ might be caused by optical depth broadening. The $^{13}CH_3OH$ from the HC is expected to be well below our detection limit. There are 14 $^{13}CH_3OH$ lines free from blends with an upper state energy range between 37–225 K, which are used in a rotation diagram (Fig. 10). No corrections for optical depths are needed since the $^{13}CH_3OH$ transitions are optically thin. The rotation temperature is found to be 115 ± 16 K, and the column density $(5.9 \pm 1.5) \times 10^{16}$ cm^{-2}.

If we exclude blended and very weak lines we have 50 CH_3OH lines with an upper state energy range from 40 to 721 K. The large number of lines and the wide temperature range make methanol well suited to be used in a rotational diagram. However, one difficulty that may occur with this method is that the optical depths may vary considerably between the CH_3OH transitions. In the rotation diagram seen in Fig. 44 (online material) the lines are plotted (using the total integrated intensity) without any attempt to correct for optical depth or beam-dilution. As can be seen there is a large scatter of the CH_3OH lines. Three transitions with upper state energies of 77, 171 and 265 K lie clearly very high above the others due to their low transition probability and low opacity. A separate fit of these three lines is made and the resulting beam-filling corrected column density becomes $(2.6 \pm 0.4) \times 10^{18}$ cm^{-2}. This is about 3 times higher than the resulting column density from all the lines, $(9.3 \pm 1.1) \times 10^{17}$ cm^{-2}. This indicates that opacity correction needs to be included in the rotation diagram.

Using the forward model, which includes opacity and beam-filling correction (see Fig. 45 in the online material), we find a column density of $(1.3 \pm 0.1) \times 10^{18}$ cm^{-2} in a source size of 6″. (This size is used as beam-filling correction in all calculations of the column densities above.) The scatter in the rotation diagram is reduced and approaches the column density obtained from the three (assumed) optically thin lines. However, since this method has a tendency to underestimate the column density we proceed with opacity correction of the traditional rotation diagram. We note that most of the low energy lines seem to be optically thick (opacities between ~1–6) and most of the high energy lines seem to be optically thin (opacities between ~0.3–1.5). The rotation temperature would be too high if not opacity corrected.

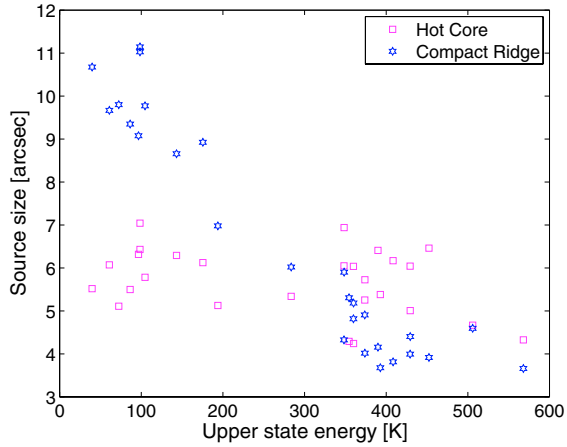

Fig. 12. Source size variation with energy for the CR and HC components of CH_3OH (opacity-corrected with $N_{CR} = 1.7 \times 10^{18}$ cm^{-2}, T_{CR} = 120 K and $N_{HC} = 7.9 \times 10^{17}$ cm^{-2}, T_{HC} = 200 K).

An additional complication is that the extent of the emitting regions may be different for lines of different energy (cf. Menten et al. 1986). This is affecting our estimation of the opacity since we need a total column density (corrected for beam-filling) in the calculations. The online Fig. 46 shows that the source size of the low-energy lines varies between 5–12″, whereas the size of the high-energy lines is almost constant (about 6″), based on Eq. (14) at T_{ROT} = 120 K.

In Fig. 10 we show the opacity corrected rotation diagram. The opacity is calculated using the column density obtained from the three optically thin lines corrected for different beam-fillings for each transition, and the same excitation temperature for all lines (120 K). The scatter in the plot is even more reduced than in the forward model and the resulting column density becomes $(3.4 \pm 0.2) \times 10^{18}$ cm^{-2}. This is much higher than in our comparison surveys, but consistent with Johansson et al. (1984), Menten et al. (1986), and S01 using the $^{13}CH_3OH$ column density (all corrected for our source size).

The rotation temperature is 116 ± 2 K with opacity correction which is the same as produced by the $^{13}CH_3OH$ rotation diagram (115 ± 16 K) and the optically thin fit (120 ± 10 K).

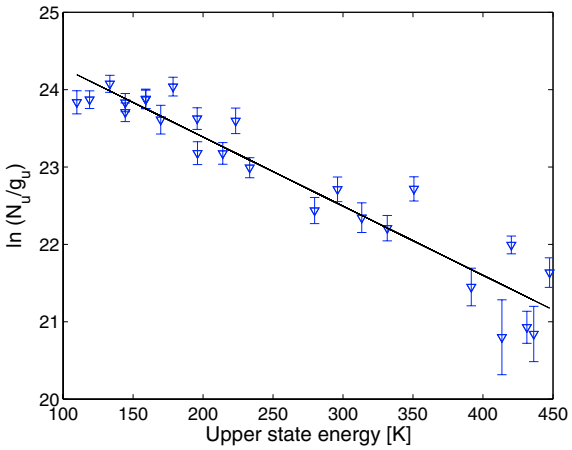

Fig. 13. Rotation diagram for $(CH_3)_2O$ producing T_{ROT} = 112 K (extended source).

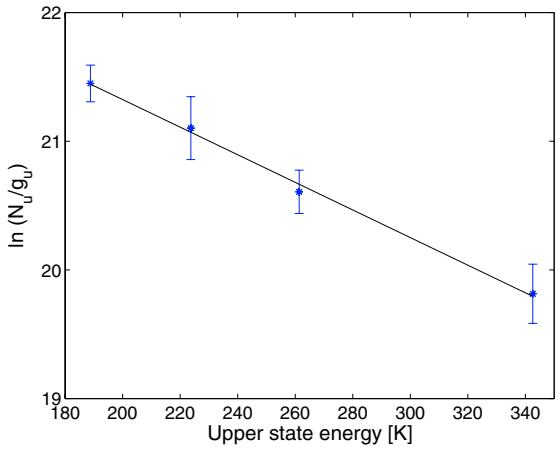

Fig. 14. Rotation diagram for H_2CS producing T_{ROT} = 93 K (extended source).

The forward model produces a slightly higher temperature (136 ± 4 K), which suggests that the opacity correction is too low with this method.

There is also a possibility that the high- and low energy lines are emitted from different regions even though our rotation diagram does not indicate a change of rotation temperature. Using the Gaussian decomposition of the 27 strongest lines, we note that the integrated intensity of the low energy lines is dominated by the narrow CR component, and the high energy lines by the broad HC emission.

When calculating the opacity of the components we again take into account the varying source size with energy. However, Fig. 12 shows that the pronounced variation in size is only true for the narrow component. The broad component seems to have approximately the same size as the energy increases. This again supports the scenario in which the narrow component arises in the CR, which is denser and hotter in the central parts. Hence only the central parts have the ability to emit the high energy lines. The broad component keeps the small size across the transition energy range, supporting an origin in the HC. This source is small and hot and thus can emit all transitions throughout the whole region. The opacity of the CR component is found to be higher than in the HC component which is about 1 or less.

Plotting the components in a opacity corrected rotation diagram (Fig. 11), produces column densities and rotation temperatures for each region: $N_{ROT} = (2.4 \pm 0.2) \times 10^{18}$ cm^{-2}, T_{ROT} = 98 ± 2 K and $(7.9 \pm 1.0) \times 10^{17}$ cm^{-2}, T_{ROT} = 178 ± 11 K for the CR and HC, respectively. Both column densities are much higher than in our comparison surveys, but agrees well with S95 (corrected for our source size). The calculated temperatures are lower than in the comparison surveys, but the high apparent rotation temperatures may be caused by high opacity. Hollis et al. (1983) found that the ground-state transitions originate in a 90 K region, while the torsionally excited transitions come from a 200 K region.

The isotopic ratio of $^{12}C/^{13}C$ can be estimated from the ratio of the optically thin CH_3OH and $^{13}CH_3OH$ column densities, and is found to be 57 ± 14. This is consistent with previous estimates (Table 6).

4.5. Compact Ridge molecules

4.5.1. Dimethyl ether ($(CH_3)_2O$)

This molecule is affected by two internal rotors which are the origin of the fine structure lines of the AA, AE, EE and EA symmetries (Groner et al. 1998). The emission only shows characteristics of the CR with narrow widths of 3−4 km s^{-1} at υ_{LSR} velocities of ∼6−8 km s^{-1}.

Since we cannot resolve these fine structure transitions, we treat them as one single line. The statistical weights and the partition function are changed accordingly. We observe 47 quartets out of which 37 are free from blends and hence can be used in the rotation diagram shown in Fig. 13. The resulting beam-filling corrected column density is $(1.3 \pm 0.3) \times 10^{17}$ cm^{-2} and the rotation temperature is 112 ± 8 K, which is higher than in the comparison line surveys (Table 1). The adopted source size is the same as obtained for CH_3OH, since these molecules most likely have a rather similar origin in the CR. This is also verified when calculating the source size with Eq. (14), assuming an opacity larger than unity. For a temperature of 112 K we find a CR size of 5−6″. This is also indicating optically thick lines which could increase the column density even further.

4.5.2. Thio-formaldehyde (H_2CS)

Five transitions of the CR-emitting H_2CS are observed, of which the $16_{3,13}-15_{3,12}$ transition is a blend with a U-line. The line profile of the $14_{1,13}-13_{1,12}$ transition is shown in Fig. 33 (online material). The four lines with no blends are used in the rotation diagram shown in Fig. 14, producing a rotation temperature, very similar to that of CH_3OH, T_{ROT} = (93 ± 4) K. The resulting beam-filling corrected column density is $(1.3 \pm 0.2) \times 10^{15}$ cm^{-2}, with a source size of 14″ guided by our calculations for the H_2CO optically thick CR emission (see Sect. 4.6.1).

A comparison of the H_2CS and the optically thin $H_2^{13}CO$ results in a molecular abundance ratio of $H_2CO/H_2CS \sim 15$. This is lower than the quoted [O/S] ratio of 35 (online Table 6) from Grevesse et al. (1996). From the comparison of H_2O and H_2S in Sect. 6 we obtain a similar value of ∼20.

4.5.3. Thioformyl cation (HCS^+)

The thioformyl cation previously has not been seen either by W03 nor S01, and here we only observe the J = 13−12 transition as a visible blend with ^{33}SO. Due to the blend we cannot analyse this transition further, but this emission is most likely emitted in the same small hot and dense CR source as CH_3OH and $(CH_3)_2O$.

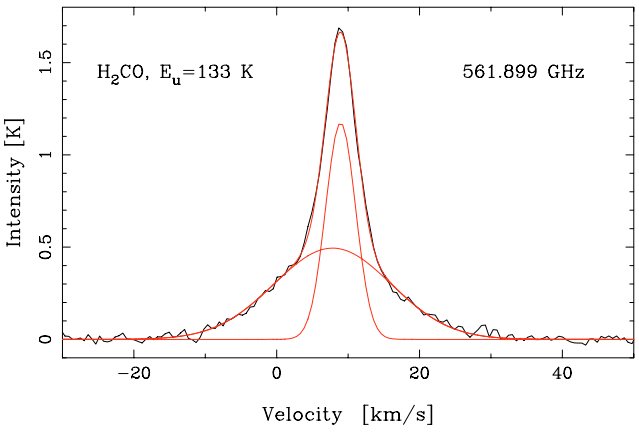

Fig. 15. The H_2CO $8_{1,8}$–$7_{1,7}$ transition with a two-component Gaussian fit shown together with the individual Gaussians. The line widths are 5 km s^{-1} and 19 km s^{-1} from the CR and LVF, respectively.

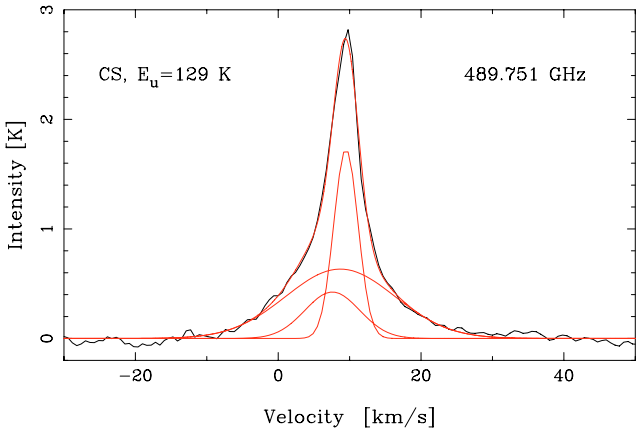

Fig. 16. The CS J = 10–9 transition with a three-component Gaussian fit shown together with the individual Gaussians. The line widths are 4 km s^{-1}, 9 km s^{-1}, and 18 km s^{-1} from the CR/ER, the HC and LVF, respectively.

4.6. Outflow and Compact Ridge molecule

4.6.1. Formaldehyde (H_2CO/$H_2^{13}CO$/HDCO)

We detect three transitions from each of H_2CO and HDCO, and one transition from $H_2^{13}CO$. Since the energy range is small (106–133 K), no rotation diagram can be made. The $8_{1,8}$–$7_{1,7}$ transition of H_2CO is shown in Fig. 33 (online material), together with the same transition of $H_2^{13}CO$ and the $9_{1,9}$–$8_{1,8}$ transition of HDCO. The H_2CO $8_{0,8}$–$7_{0,7}$ transition shows a blend with Hot Core NS at 576.720 GHz. The $8_{1,7}$–$7_{1,6}$ transition of $H_2C^{18}O$ is tentatively found at 571.477 GHz.

The H_2CO lines show two velocity components. Figure 15 shows a two-component Gaussian fit. The narrow component from the CR has widths of ∼5 km s^{-1} at υ_{LSR} ∼ 8.5 km s^{-1}, and the broader component from the LVF has widths of ∼19 km s^{-1} at υ_{LSR} ∼ 8 km s^{-1}. $H_2^{13}CO$ and HDCO show only emission from the CR with similar widths and LSR velocities as for the narrow H_2CO component. Comparison of the CR component of the H_2CO $8_{1,8}$–$7_{1,7}$ transition with the same $H_2^{13}CO$ transition, results in optical depths of ∼6.6 and ∼0.1, respectively (using [^{12}C/^{13}C] = 60).

Since the CR component is optically thick in H_2CO, this source size is calculated with Eq. (14) and is found to be as large as 14″ for a temperature of 115 K, in agreement with Mangum et al. (1990). The LVF source size becomes 10″, which might be caused by a low opacity. Hence a LVF size of 15″ is used for beam-filling correction. The resulting CR and LVF column densities are 3.0×10^{15} cm^{-2} and 4.3×10^{15} cm^{-2}, respectively. With the use of the optically thin $H_2^{13}CO$ the CR column density increases to 2.0×10^{16} cm^{-2}, in agreement with Turner (1990), Mangum et al. (1990), and S95.

Since H_2CO is optically thick we cannot calculate the [^{12}C/^{13}C] elemental ratio. But with the use of the optically thin $H_2^{13}CO$ and HDCO, the abundance ratio of D/H is estimated to ∼0.01, which implies a high deuterium fractionation in the CR. Turner (1990) derived a ratio of HDCO/H_2CO = $0.14^{+0.12}_{-0.07}$ and D_2CO/HDCO = $2.1^{+1.2}_{-0.5} \times 10^{-2}$ for the CR. These large abundance ratios were interpreted as a result of active grain surface chemistry.

4.7. Outflow, Hot Core and Compact/Extended Ridge molecules

4.7.1. Carbon monosulfide (CS/^{13}CS)

Figure 16 shows a three-component Gaussian fit to the observed J = 10–9 transition of CS. Emission is seen from a narrow component, the HC and the LVF at LSR velocities 9, 7 and 10 km s^{-1} with widths 4, 9 and 18 km s^{-1}, respectively. The narrow component may have an origin either from the ER or the CR, hence the column density is calculated with both alternatives. The CS line is also compared to H_2CS and isotopologues of H_2CO in Fig. 33 (online material).

The ^{13}CS J = 12–11 transition is observed with emission from a narrow (ER or CR) component, but is blended with a $^{34}SO_2$ transition. This makes the Gaussian fit with a width of 5 km s^{-1}, at LSR velocity 7 km s^{-1} approximate. Comparison of peak antenna temperatures of the isotopologues (using a ^{12}C/^{13}C ratio of 60) suggests that the narrow CS component is optically thick (τ ∼ 6–12). The source size of an ER component is calculated with Eq. (14) and is found to be 30″ for at temperature of 60 K. This suggests that either the emission of this component is rather extended and clumpy (see Sect. 8), or has an origin in the CR. For a typical CR temperature of 115 K, we find a size of 20″.

The resulting column densities are listed in Table 1. The column density of the LVF agrees well with B87, S95, S01 and C05, and the HC column also agrees with S95, but is lower than found in C05. The narrow component from either the CR och ER is more difficult to compare. Our ER column agrees rather well with B87, but is an order of magnitude lower than found by S95. As CR emission it agrees with S95. The differences may arise due to opacity, beam-sizes and energy levels.

4.7.2. Hydrogen isocyanide (HNC)

Figure 17 shows a four-component Gaussian fit of the HNC J = 6–5 transition with an upper state energy of 91 K, and a U-line seen in the red-ward LVF line wing at a velocity of 22 km s^{-1}. As for CS, three velocity components, from the ER, HC, and LVF, are clearly seen at υ_{LSR} = 9, 6 and 7 with widths of 4, 9 and 27 km s^{-1}, respectively. The sizes and temperatures for the subregions are taken to be representative of typical values

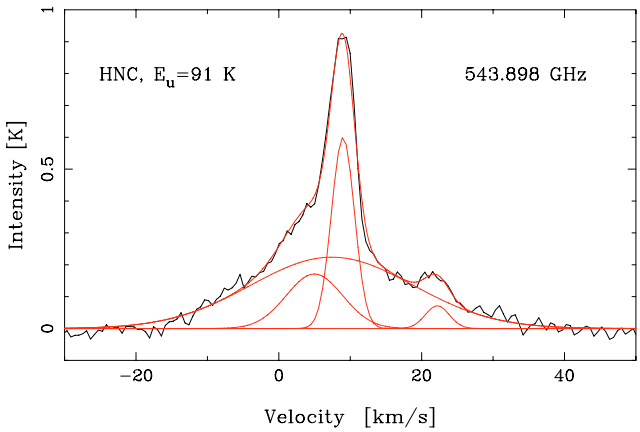

Fig. 17. The HNC J = 6−5 transition and a U-line at 543.873 GHz with a four-component Gaussian fit shown together with the individual Gaussians. The line widths are 4 km s^{-1} for the U-line, 4 km s^{-1}, 9 km s^{-1}, and 27 km s^{-1} for the HNC ER, HC and outflow components, respectively.

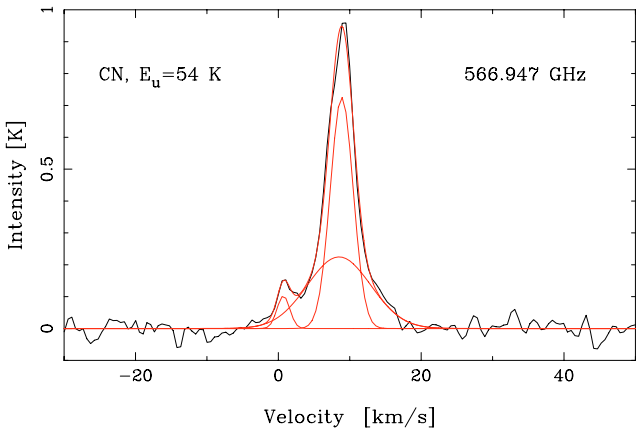

Fig. 18. CN with a three-component Gaussian fit of five unresolved hyperfine-structure lines shown together with the individual Gaussians. The widths are 4 km s^{-1} and 11 km s^{-1} for the PDR/ER and HC components of the three strong hyperfine-structure lines, respectively, and 2 km s^{-1} for the weak transitions at a velocity of 0 km s^{-1}.

(see Table 1). The HNC line is also shown in Fig. 31 (online material).

4.8. PDR/Extended Ridge and Hot Core molecule

4.8.1. The cyanide radical (CN)

The main CN emission has its origin in the PDR/ER region and the HC (Rodríguez-Franco et al. 1998) at $\upsilon_{\rm LSR}$ ∼ 9 and 8.5 km s^{-1} with widths of ∼4 and ∼10 km s^{-1}, respectively. In total we have observed three lines with 8 non-resolved hyperfine structure features. Figure 31 (online material) shows one of the N = 5−4 transitions, consisting of three non-resolved hyperfine structure lines, with two additional ones in the line wing at a velocity of 1 km s^{-1}. The same transitions are shown in Fig. 18 with a three-Gaussian fit of the five transitions. No rotation diagram is made since the upper state energy of 54 K is the same for all transitions.

Using Gaussian fits, the LTE approximation and typical temperatures and source sizes, the column densities for the HC and PDR/ER regions are estimated to be 7.9×10^{15} cm^{-2}, and 4.9×10^{13} cm^{-2} for the HC and PDR/ER, respectively. Our comparison surveys have no observations of CN, but Rodríguez-Franco et al. (2001) obtained column densities by CN mapping, ranging from 10^{13} cm^{-2} in the Trapezium region to 10^{14}−10^{15} cm^{-2} in the Ridge region. S95 find $N = 1 \times 10^{15}$ cm^{-2} with a 14″ beam, and B87 also find the same CN column density with a 30″ beam.

4.9. Extended Ridge molecule

4.9.1. Diazenylium (N_2H^+)

The diazenylium transition J = 6−5 is shown in Fig. 31 (online material). The width of ∼5 km s^{-1} at $\upsilon_{\rm LSR} \approx 9$ km s^{-1} indicates an ER origin of the emission, in agreement with mapping of the J = 1−0 transitions by Womack et al. (1990) and Ungerechts et al. (1997). The column density of 1.0×10^{12} cm^{-2}, that we calculate using the simple LTE approximation, is much lower than that found by Ungerechts et al. (1997), 8.4×10^{12} cm^{-2}.

4.10. Unidentified line features

We observe 64 unidentified line features. Tentative assignments have been given to 26 lines, such as the first tentative detections of ND, and of the anion SH^- (see Fig. 34, Tables 34, and 35 in the online material and Table 3 in Paper I). There are 28 U-lines, i.e. clearly detected lines, and 36 T-lines, which means that they are only marginally visible against the noise or in a blend. The tentative assignments also include the species SO^+, CH_3CHO, CH_3OCHO, SiS, HNCO, $H_2C^{18}O$, and a high energy HDO line. For details see Paper I.

The strongest U-line is found at 542.945 GHz with a peak intensity of 140 mK. The line appears to show emission from two components, probably the CR and the HC (see Fig. 34 in the online material).

5. Carbon monoxide (CO/^{13}CO/C^{17}O/C^{18}O), carbon (C) and H_2 column densities

We have observed the J = 5−4 transition of CO, ^{13}CO, C^{17}O, and C^{18}O (Fig. 26). The CO line is the most intense single line in our 42 GHz wide band. The FWZP (Full Width Zero Power) of CO is approximately 230 km s^{-1}, as compared to 120 km s^{-1} reported in Wirström et al. (2006, hereafter W06), a result of our much lower noise level. Since W06 also used Odin but with another observation mode, we can again demonstrate the high accuracy of the Odin calibration with a comparison of the amplitudes, which agree within less than five percent.

As pointed out in W06 it is clear that CO J = 5−4 has emission from at least three different components – LVF, HVF and a narrow component. The high brightness temperature of the last component suggests that this emission originates in the extended and warm PDR, whereas the narrow components from the optically thin isotopologues have approximately equal emission from the PDR and the colder ER gas behind it. We observe all three components in the CO and ^{13}CO emission, but only the narrow ER/PDR component and the LVF for the C^{17}O and C^{18}O isotopologues (W06). The Gaussian components are given in Tables 8 and 32 in the online material, and agree well with W06, especially when our higher signal-to-noise ratio is taken into account, which enables us to see line wings that were previously unobserved.

A summary of the resulting column densities, estimated optical depths, used source sizes and temperatures is found in Table 2, and also in more detail in the online Table 8. Here also column densities calculated from all isotopologues are given together with the parameters of the Gaussian fits. Note that the column density for the CO narrow component (calculated from $C^{17}O$) is lowered by a factor of two, since this component only has emission from the PDR, while the isotopologues have approximately equal emission from both the PDR and ER. For detailed arguments see W06.

The only observed atomic species in this survey is the $^3P_1$–$^3P_0$ transition of C at 492.1607 GHz. It shows a narrow line profile from an extended emission with a width of 4.5 km s^{-1}, at LSR velocity ∼9 km s^{-1}. Due to the loss of orbits during this observation, the noise level here is 200 mK, as compared to our average level of 25 mK in the rest of the spectral survey. This makes it impossible to distinguish a possible broad emission in this transition. Our beam-averaged column density of C is 5.6×10^{17} cm^{-2}. Tauber et al. (1995) find a lower limit for a beam-averaged C column density of $\sim 7 \times 10^{17}$ cm^{-2} (beam size 17″) in the Orion bar. Ikeda et al. (1999) find a column density very similar to ours (6.2×10^{17} cm^{-2}) from observations of the 492.1607 GHz transition with the Mount Fuji submillimetre-wave telescope towards the Orion KL position, in a HPBW of 2.′2. The optical depth was estimated to be 0.2. B87 find $N \gtrsim 7.5 \times 10^{17}$ cm^{-2} with a 30″ beam towards the Orion KL region. Plume et al. (2000) presented maps of the same transition, obtained with the SWAS satellite, resulting in an average column density of 2×10^{17} cm^{-2}.

When estimating abundances we need comparison column densities of H_2 for each subregion (results also given in Table 2). This is provided by $C^{17}O$ for the PDR/ER and LVF components, using $[CO]/[H_2] = 8 \times 10^{-5}$ (e.g. Wilson & Matteucci 1992), an isotope ratio $[^{18}O]/[^{17}O] = 3.9$ (Table 6), together with $[^{16}O]/[^{18}O] = 330$ (Olofsson 2003). The latter value was found from high S/N $S^{18}O$ observations of molecular cloud cores. This is somewhat lower than the usually quoted value of 560 (Wilson & Rood 1994), valid for the local ISM and estimated from H_2CO surveys in 1981 and 1985. A likely explanation for the lower value is a local enrichment of ^{18}O relative to ^{16}O by the ejecta from massive stars. For the HVF component we use ^{13}CO since $C^{17}O$ has no HVF emission.

The resulting H_2 column density from the LVF is 3.2×10^{23} cm^{-2}. This is close to the limits given by Masson et al. (1987) $(3–10) \times 10^{22}$ cm^{-2}, as well as 1×10^{23} cm^{-2} by Genzel & Stutzki (1989). Wright et al. (2000) find a beam-averaged H_2 column density of 2.8×10^{23} cm^{-2} from observations of the 28.2 μm H_2 0–0 S(0) line for a temperature of 130 K (beam size 20″ × 33″).

Our resulting HVF H_2 column density is 3.9×10^{22} cm^{-2}, in agreement with the Genzel & Stutzki value of 5×10^{22} cm^{-2}. In contrast, Watson et al. (1985) found that the HVF column of warm shock heated H_2 is only 3×10^{21} cm^{-2}, a result based upon their KAO observation of high-J CO lines.

Tauber et al. (1995) reported an average H_2 column density of $\sim 3 \times 10^{22}$ cm^{-2} from the Orion Bar (calculated from ^{13}CO mapping). This is in agreement with our total narrow component, which we find to be 4×10^{22} cm^{-2}. When we calculate the abundances in Sect. 7, we divide this value by two, since there are about equal contributions from the PDR and ER to the $C^{17}O$ emission (W06). Our value is also consistent with the results of Goldsmith et al. (1997) convolved with the 2.′1 Odin beam.

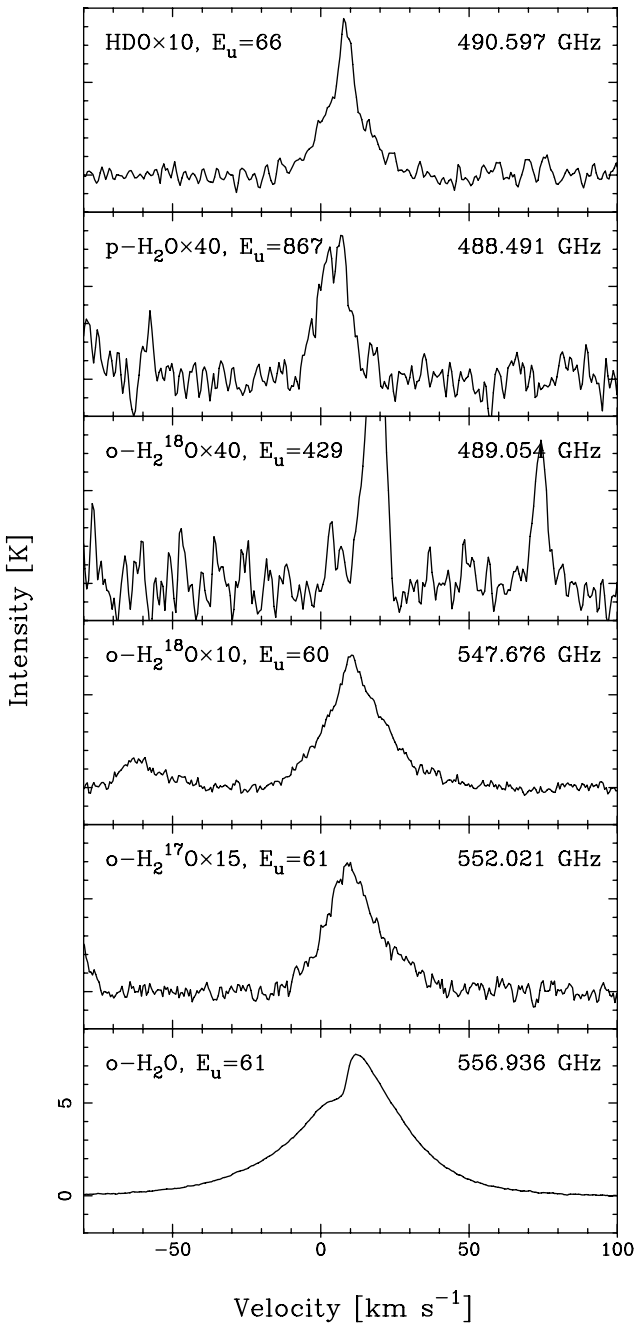

Fig. 19. Water and isotopologues. The o-$H_2^{17}O$ is reconstructed spectra with blending lines subtracted. An intensity scale factor is given after the molecular species.

6. Water (o-$H_2^{16}O$, p-$H_2^{16}O$, o-$H_2^{17}O$, o-$H_2^{18}O$, HDO)

6.1. Correcting the water emission lines for blends

Because of the large number of methanol and sulphur dioxide lines observed, they cause the most common blends in all lines. Since we are particularly interested in water, we attempt to reconstruct the water isotopologues without blends. We use observed transitions in our survey with similar parameters (E_u, A-coefficient and g_u), and scale them with the parameters of the blending lines before removal from the water isotopologue line of interest. The molecular line parameters of the blending transitions are found in the online Tables 9, 10 and 20.

Two lines are blended with the o-$H_2^{18}O$ $1_{1,0}$–$1_{0,1}$ ground state rotational transition. The $^{34}SO_2$ $21_{3,19}$–$20_{2,18}$ transition is blended with the red wing, and in the blue wing there is an overlapping methanol line, $15_{1,15}$–$15_{2,14}$, $v_t = 1$. However, since the simultaneous observations of o-$H_2^{17}O$ show that the $H_2^{18}O$ transition is optically thick even in the line wings (see next section), we do not attempt to remove these blending transitions.

The o-$H_2^{17}O$ ground state rotational transition is, however, optically thin in the line wings, and we therefore remove three blending lines. In Fig. 38 (online material) we show two of the blending lines together with the o-$H_2^{17}O$ line. In the blue o-$H_2^{17}O$ wing the blending SO_2 transition $26_{6,20}$–$26_{5,21}$ is overlapping. In the red wing there are two blends. One from the $6_{6,1}$–$7_{5,3}$ methanol transition shown, and one from the very weak SO_2 $34_{1,33}$–$34_{0,34}$ transition.

6.2. Water analysis

We have observed the $1_{1,0}$–$1_{0,1}$ ground state rotational transition of o-H_2O and its isotopologues o-$H_2^{18}O$ and o-$H_2^{17}O$, which mainly show emission from the Plateau. A very weak feature at 489.054 GHz is tentatively identified as the HC-tracing $4_{2,3}$–$3_{3,0}$ transition of o-$H_2^{18}O$ with an upper state energy of 429 K. The HC-tracing p-H_2O transition $6_{2,4}$–$7_{1,7}$ with an upper state energy of 867 K, is also observed, as well as the $2_{0,2}$–$1_{1,1}$ HDO transition showing emission from the CR, HC and LVF. Figure 19 shows all detected water lines after removal of some blends in $H_2^{17}O$ as discussed in the previous section.

The optical depths, column densities, assumed source sizes and excitation temperatures are found in Table 2, and in more detail in Table 7 (online material), together with the parameters of the Gaussian fits.

Both the o-$H_2^{18}O$ and o-$H_2^{17}O$ ground state rotational transition show features of a weak, narrow component from the CR, a broad stronger component from the LVF, and with HVF emission mainly in the red wing. Figures 35 and 36 (online material) show three-component Gaussian fits to the water isotopologues. The emission from the ER and PDR is considered to be very low since the water mainly will be frozen onto the dust grains at the rather low temperatures in this region.

The o-H_2O line is very optically thick at all velocities as seen in Fig. 39 (online material) which displays the ratio of o-H_2O and o-$H_2^{18}O$. The excitation conditions for these two isotopologues are therefore very different. A similar figure of the ratio of o-$H_2^{18}O$ and o-$H_2^{17}O$ (Fig. 40 in the online material) shows an almost constant ratio of 1.5 for velocities between −10 and +30 km s^{-1}. This demonstrates that the two line profiles are almost identical, and that the o-$H_2^{18}O$ emission is rather optically thick at all velocities since $[^{18}O/^{17}O] = 3.9$. By comparison of column densities from the total integrated intensities, the optical depths for o-$H_2^{17}O$ and o-$H_2^{18}O$, are 0.9 and 3.4, respectively. The small changes of the ratio with velocity as seen in Fig. 40 also are consistent with our decomposition into Gaussian components. The LVF is optically thick in both isotopologues, whereas the HVF and CR have lower optical depths causing increase of the ratio at their emission velocities.

6.2.1. *Ortho*-H_2O from the low- and high velocity flow and the Compact Ridge

The similarity of the line profiles is also illustrated in Fig. 20 showing a comparison of o-$H_2^{17}O$, o-$H_2^{18}O$ and the $19_{3,17}$–$18_{2,16}$ SO_2 transition, all normalised to their respective peak temperature. The remarkable similarity of the line profiles suggests a very similar origin and chemistry of the water isotopologues and SO_2: the LVF and with additional HVF emission mainly in the red wings.

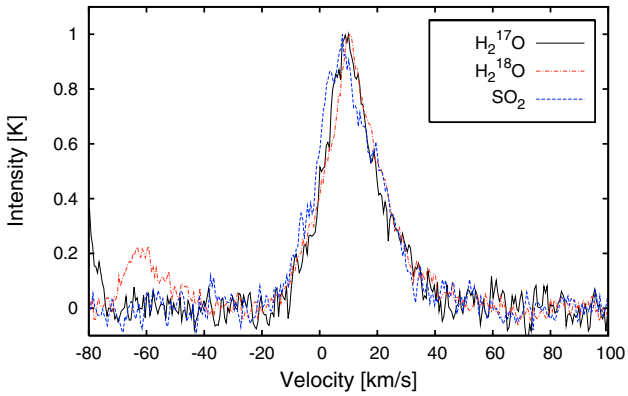

Fig. 20. Comparison of $H_2^{18}O$, with $H_2^{17}O$, and the $19_{3,17}$–$18_{2,16}$ SO_2 transition, all normalised with respective peak temperature. The high degree of similarity of all three line profiles suggests an origin in the same gas and velocity fields, mainly from the LVF with additional emission from HVF in the red wings.

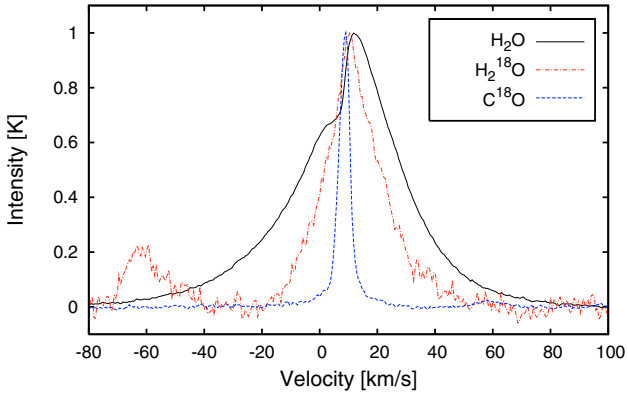

Fig. 21. Comparison of the optically thick self-absorbed o-H_2O with o-$H_2^{18}O$ and $C^{18}O$ $J = 5$–4, all normalised with respective peak intensity. The LVF self-absorption of o-H_2O in the blue wing is seen when compared to o-$H_2^{18}O$, which shows LVF emission in both wings and HVF emission mainly in the red wing.

The resulting column densities (found in Table 2 and in the online Table 7) are calculated with the simple LTE approximation and for an *ortho*/*para* ratio of 3. As a first approximation of the column density we have used the full integrated intensity of the lines, assuming the Plateau to be the main emitting source (with $T_{ex} = 72$ K and a source size of 15″, see below). We have also calculated the column densities for the different subregions using the Gaussian components. In addition, the o-$H_2^{17}O$ and o-$H_2^{18}O$ column densities are calculated with and without optical depth corrections. Since the o-H_2O transition is highly optically thick, we calculate the column density from o-$H_2^{17}O$ and o-$H_2^{18}O$. With isotope ratios of $[^{18}O]/[^{17}O] = 3.9$ and $[^{16}O]/[^{18}O] = 330$ (Table 6), we determine the opacity-corrected column density of H_2O to be 1.7×10^{18} cm^{-2}. The opacity-corrected LVF and HVF column densities, obtained from the Gaussian fits of the isotopologues, are 8.7×10^{17} cm^{-2} and 8.8×10^{17} cm^{-2}, respectively. These calculations assume LVF and HVF source sizes for the isotopologues of 15″ (cf. Olofsson et al. 2003), which is the same extent as the submillimetre HDO emission from the

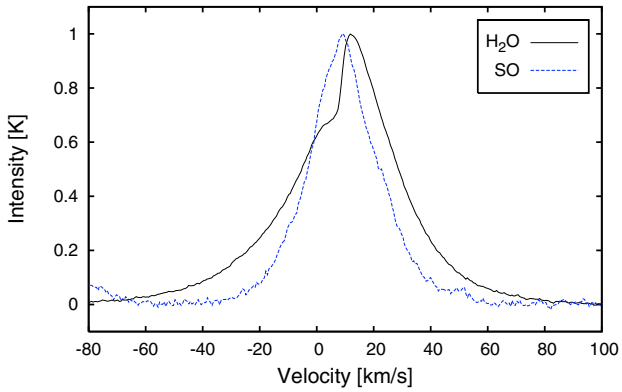

Fig. 22. Comparison of the 13_{13}–12_{12} SO transition and o-H_2O, both normalised with respective peak intensity. Both species show emission from the LVF and the HVF, but the water LVF is self-absorbed in the blue-shifted emission.

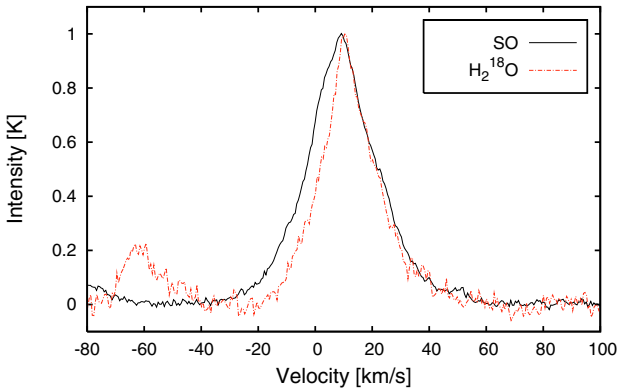

Fig. 23. Comparison of the 13_{13}–12_{12} SO transition, and o-$H_2^{18}O$ normalised with respective peak intensity.

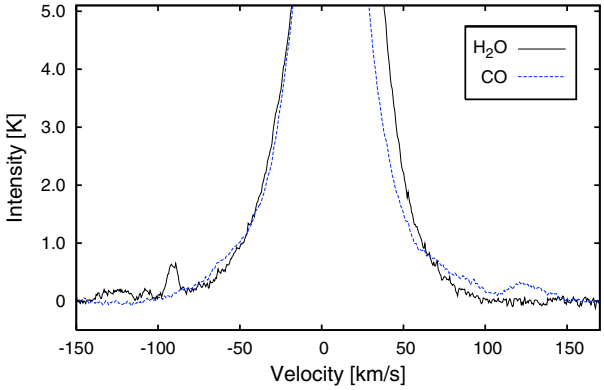

Fig. 24. Comparison of the broad HVF emission in the line wings of CO and o-H_2O scaled 2.5 times. Note the large velocity scale.

LVF mapped by Pardo et al. (2001). As excitation temperature for both LVF and HVF we use 72 K as found by Wright et al. (2000). We also calculate the H_2O HVF column density from the Gaussian fit to H_2O itself, and with opacity-correction (calculated from the isotopologues) almost the same value is obtained as from the isotopologues. The size of the H_2O HVF is assumed to have an extent of 70″ (Olofsson et al. 2003; Hjalmarson et al. 2005).

The opacity-corrected column density for the H_2O CR is 5.6×10^{17} cm^{-2}. For the CR we use the temperature and size obtained from our CH_3OH rotation diagram of 115 K and 6″. This is also consistent with our calculation of the excitation temperature from the optically thick $H_2^{18}O$ CR component, if a source size of 6″ is assumed.

The o-H_2O line has a central asymmetry that suggests strong self-absorption in the blue LVF by lower excitation foreground gas. The steep change in the self-absorption occurs in the velocity range of 2 to 12 km s^{-1}. Figure 21 compares the self-absorbed o-H_2O transition both with o-$H_2^{18}O$, and with the narrow emission from the $C^{18}O$ $J = 5$–4 line, all normalised to their respective peak temperature. The LVF self-absorption of o-H_2O in the blue wing is seen when compared to o-$H_2^{18}O$, which shows LVF emission in both wings, and HVF emission mainly in the red wing. Figure 22 shows a similar comparison between o-H_2O and an optically thick SO transition at 559.320 GHz. Both species display emission from LVF and HVF, although the blue water LVF emission is self-absorbed.

In Fig. 23 we show the same SO 13_{13}–12_{12} transition again, but this time compared to o-$H_2^{18}O$. In the blue wing SO has excess emission as compared to the water emission, whereas the red wings of SO and o-$H_2^{18}O$ are almost identical. This might be caused by shock chemistry in the red HVF which is pushing into the ambient molecular cloud (Genzel & Stutzki 1989), thereby producing a high water abundance. In the blue HVF, which is leaving the molecular cloud, no such shock chemistry seems to be present. The water abundance in this part of the HVF is likely due to evaporation from icy dust grains, which produces less water than shock chemistry. In contradiction to this, the SO emission is symmetric in both wings, suggesting that shock chemistry is not required to produce high SO abundances.

The similarity of the broad HVF emissions from CO and H_2O is shown in Fig. 24. The FWZP of the broad component is ∼230 km s^{-1} for o-$H_2^{16}O$, 50 km s^{-1} for the isotopologues, and 35 km s^{-1} for HDO.

6.2.2. *Para*-H_2O from the Hot Core

In the main o-H_2O $1_{1,0}$–$1_{0,1}$ line spectrum (Fig. 19) possible emission from the HC and CR would be blended with the much stronger and broader component from the LVF. Melnick et al. (2000) concluded that the HC contributes negligibly to the water emission within the SWAS beam, and the CR would contribute less than 5–10%. The highest energy levels in the ISO data presented by Lerate et al. (2006) and Cernicharo et al. (2006) may have a contribution from the HC, but those authors remark that the large far-IR line-plus-continuum opacity probably would hide most of this emission.

However, our detected optically thin p-H_2O $6_{2,4}$–$7_{1,7}$ transition with upper state energy 867 K, clearly reveals the emission from the HC. The width of the line is 12 km s^{-1} at $\upsilon_{\rm LSR}$ ∼ 4.4 km s^{-1}, between velocities −8 and 15 km s^{-1}. When column densities are calculated using the simple LTE approximation, we find values in the range $(3.7–12) \times 10^{18}$ cm^{-2} for a temperature range of 200–500 K and a typical source size of 10″. Since no clear HC emission is seen from the ground rotational state transition in $H_2^{17}O$, either the temperature in the HC is high enough to result in the negligible emission of this transition from the HC, or the $H_2^{17}O$ transition has an optically thick LVF emission which is blocking possible HC emission. If the temperature is 500 K, the emission from the HC would only be about 10% of the total (if no optical depths are taken into account), and therefore would be hidden in the stronger and broader LVF emission even if $H_2^{17}O$ is optically thin. However, if the temperature in the HC is about 200 K, the $H_2^{17}O$ LVF emission has to have an optical depth larger than unity. Since our estimated value is about

1.5, this is consistent with a HC temperature of 200 K and a column density of HC H_2O 1.2×10^{19} cm^{-2}. This is in agreement with the only previous observation of H_2O emission from the HC made by S01. They detected the vibrationally excited $1_{1,0}-1_{0,1}$ $v_2 = 1$ transition and found a HC column density of 3×10^{19} cm^{-2} with a temperature of 200 K and a water abundance of 1×10^{-5}. Gensheimer et al. (1996) estimated the HC $H_2^{18}O$ column density to be 2.7×10^{16} cm^{-2} from $H_2^{18}O$ mapping of the quasi-thermal $3_{1,3}-2_{2,0}$ transition with the IRAM telescope (12″ beam). This column density translates to 1.3×10^{19} cm^{-2} for H_2O (corrected for source size and isotopologue ratio differences), in excellent agreement with our result, even though their observations suffered from severe blends. Their HC water mapping also showed that the emission from both $H_2^{18}O$ and HDO were unresolved by their beam, and the HDO mapping showed sizes of 6–8″.

Our tentative detection of the optically thin HC emitting o-$H_2^{18}O$ $4_{2,3}-3_{3,0}$ transition, with an upper state energy of 430 K, results in a HC H_2O column density of about 4×10^{19} cm^{-2}.

6.2.3. Comparisons of outflow column densities

Our column density results for the Plateau agrees excellently with those of Wright et al. (2000), who observed 19 pure rotational lines in absorption using the Short Wavelength Spectrometer (SWS) on board the Infrared Space Observatory (ISO), with a beam size of 14″ × 20″ to 20″ × 30″. Their rotation diagram, including a generalised curve-of-growth method, results in a rotation temperature of 72 K, and a beam-averaged column density (from the total emission) of 1.5×10^{18} cm^{-2}. They also conclude that the observed water arises from an outflow centred near IRc2.

Lerate et al. (2006) observed more than 70 far-IR pure rotational $H_2^{16}O$ lines, and 5 $H_2^{18}O$ lines, with the ISO LWS (Long Wavelength Spectrometer) between ~43 and 197 μm (beam size about 80″). Their rotation diagram of the total emission from $H_2^{18}O$ results in a beam-averaged column density of $(2-5) \times 10^{14}$ cm^{-2}, and a rotation temperature of 60 K. For a 15″ outflow source, their result translates to $(1.8-4.7) \times 10^{18}$ cm^{-2} for $H_2^{16}O$, also in good agreement with our value. In the analysis by Cernicharo et al. (2006) of this data set, they concluded that most of the water emission and absorption arises from an extended flow of gas with velocity 25 ± 5 km s^{-1}, with an inferred kinetic gas temperature of 80–100 K.

6.2.4. HDO from the Compact Ridge, low velocity flow and the Hot Core

The deuterated species HDO is observed in the $2_{0,2}-1_{1,1}$ transition with $E_u = 66$ K, and shows evidence of CR, LVF, and also HC emission as is observed by W03. Figure 37 shows a three-component Gaussian fit. Pardo et al. (2001) reported detections of the $2_{1,2}-1_{1,1}$ and $1_{1,1}-1_{0,0}$ lines in the 850–900 GHz spectral region, which seem to trace the Plateau gas and not the HC. Their conclusion is that the HC component is hidden behind the optically thick HDO LVF in their transitions, which is supporting our analysis of the non-detection of HC emission in the ground state rotational water transitions.

A T-line at 559.816 GHz tentatively is identified as the high energy (580 K) HDO transition $6_{2,4}-6_{2,5}$.

Our estimated column density of HDO, assuming that the main emission originates in the outflows, is 9.1×10^{15} cm^{-2}, which is about the same value as reported by Lerate et al. (2006), 8.5×10^{15} cm^{-2} (corrected for source size). The column density reported by Pardo et al. (2001) is higher, 5×10^{16} cm^{-2}, calculated from an LVG model with a source size of 15″, and opacities of 3.7 and 6.7 for their two lines.

We also calculate the column densities for the CR, LVF and HC separately, which are found to be 1.8×10^{16} cm^{-2}, 4.5×10^{15} cm^{-2}, and 1.5×10^{16} cm^{-2}, respectively. With correction for source-size, this is 2–4 times lower than found in Olofsson (1984) by mapping the $1_{1,0}-1_{1,1}$ transition with a 47″ beam (at Onsala Space Observatory); 3×10^{16} cm^{-2}, 1×10^{16} cm^{-2}, and 7×10^{16} cm^{-2}, respectively.

6.2.5. Molecular abundance ratios

The [D/H] ratio calculated from from HDO/H_2O is 0.005, 0.001 and 0.03 in the LVF, HC, and CR, respectively (Table 6). The CR ratio may be compared to the HDCO/$H_2^{13}CO$ ratio from which we obtain a similar [D/H] value of 0.01 (see Sect. 4.6.1). Lerate et al. (2006) found [D/H] values in the range 0.004–0.01.

The column densities for H_2O and H_2S from the LVF are also used to estimate the molecular abundance ratio of O/S to ~20 (Table 6). Using the $H_2CS/H_2^{13}CO$ ratio we obtain a similar value of ~15 (see Sect. 4.5.2).

7. Molecular abundance estimates

7.1. Gas-phase abundances from the Odin spectral line survey

Our estimated abundances for each subregion are summarised in Table 3, together with comparison abundances mostly from B87 and S95. We find very high gas-phase abundances of H_2O, NH_3, SO_2, SO, NO, and CH_3OH. Note that both our LVF and HC abundances are source averages. S95 use beam-averaged abundances (with a HPBW of 14″), and B87 use a HC size of 10″ and a Plateau size of 20″, while we separate the LVF and HVF emissions with a slightly smaller size for the LVF (15″). The beam-averaged CR abundances in both B87 and S95 are corrected to our source-sizes to allow an easier comparison.

A large source of uncertainty in these calculations is the adopted H_2 column densities. Whenever possible we have used our own calculated H_2 column densities (for the ER, LVF, HVF, Table 2). For the HC and CR we have adopted $N(H_2) = 1 \times 10^{24}$ cm^{-2} (calculated for a HC size of 10″ in B87), and $N(H_2) = 2 \times 10^{23}$ cm^{-2} (Wilson et al. 1986; B87; Goldsmith et al. 1997), respectively. In case of the HVF we also compare the (shocked) water column with the column density of the hot (shocked) H_2, where $N_{HVF} = 3 \times 10^{21}$ cm^{-2} (Watson et al. 1985). When we calculate the abundances we assume that the derived H_2 column density spatially coincides with the emission from the species of interest.

Most of our abundances, listed in Table 3, are in very good agreement with B87 and S95. However, there are a few exceptions – a 4–15 times higher abundance for SO_2 in the LVF, and 2–5 times higher abundances in general in the CR than in B87 and S95. The differences may arise because our observed transitions probe higher density and more compact regions in the CR. Since we cannot discriminate between CR or ER emission for CS, the abundance is calculated with both alternatives. It turns out that the CS abundance is about the same for either source of emission. However, the high ER abundance of CS compared to that of B87 is to a large extent due to the very different H_2 column densities used in our survey

Table 3. Derived abundances and comparisons.

Region	Species	X[g] [$\times 10^7$]	B87 X[h] [$\times 10^7$]	S95 X[i] [$\times 10^7$]
LVF[a]	H_2O	29		
	HDO	0.15	0.17	
	SO_2	20	5.2	1.3
	SO	3.1	5.2	2
	SiO	0.11	0.28	0.08
	H_2S	1.5	0.98	
	H_2CO	0.14	0.31	1.1
	CS	0.12	0.22	0.04
	HNC	0.012		
HVF	H_2O/Total H_2[b]	220	200–300[j]	
	H_2O/Hot H_2[c]	2900	2000–5000[k]	
	SO_2	225		
	SO	21		
	SiO	0.45		
HC[d]	H_2O	120	140[l]	
	HDO	0.15	0.5	0.14
	H_2S	0.27	0.3[m]	
	CH_3CN	0.05	0.078	0.04
	NH_3	16	10[n]	
	HC_3N	0.018	0.016	0.018
	OCS	0.17		1.1
	CH_3OH	7.9[o]	1-10[p]	1.4
	HNC	0.0044		
	CS	0.029		0.06
	CN	0.079		0.008
	NO	2.8	2.0[m]	
CR[e]	H_2O	28		
	HDO	0.87		0.93
	NH_3	2.0		
	CH_3OH	120[o]	30	22
	$(CH_3)_2O$	6.5	2.5	1.0
	H_2CO	1.0	0.6	0.46
	HDCO	0.014		
	H_2CS	0.065	0.06	0.014
	SO_2	10		
	SO	0.85		
	CS as CR	0.40		0.1
ER[f]	CS as ER	0.21	0.025	0.11
	HNC	0.001	0.005	
	N_2H^+	0.0005		
PDR[f]	H_2O	$\gtrsim$1.1[q]	0.33[r]	
	CN	0.02	0.03	
	NH_3	0.05[s]		

[a] LVF $N(H_2) = 3 \times 10^{23}$ cm^{-2} (this work). [b] HVF total $N(H_2) = 4 \times 10^{22}$ cm^{-2} (this work). [c] HVF hot $N(H_2) = 3 \times 10^{21}$ cm^{-2} (Watson et al. 1985). [d] HC $N(H_2) = 1 \times 10^{24}$ cm^{-2} (B87). [e] CR $N(H_2) = 2 \times 10^{23}$ cm^{-2} (Wilson et al. 1986; Goldsmith et al. 1997). [f] For both the ER and PDR: $N(H_2) = 2.0 \times 10^{22}$ cm^{-2} (this work, see Sect. 5). [g] Source averages with sizes given in Tables 1 and 2. [h] Source averages from Blake et al. (1987). [i] Source averages from Sutton et al. (1995). [j] Plateau abundance (both LVF and HVF), Cernicharo et al. (2006). [k] Wright et al. (1996). [l] Gensheimer et al. (1996). [m] C05. [n] Hermsen et al. (1988a). [o] Estimated from the CH_3OH two-component rotation diagram. [p] Menten et al. (1988). [q] W06. [r] Melnick et al. (2000). [s] Larsson et al. (2003) towards the Orion Bar.

and B87, $N(H_2) = 2 \times 10^{22}$ cm^{-2} and $N(H_2) = 3 \times 10^{23}$ cm^{-2}, respectively.

Our HVF H_2O abundance, as compared to the total H_2 density in the flow, is 3×10^{-5}, in agreement with the water abundance in the Plateau estimated by Cernicharo et al. (2006). If we compare the HVF water abundance to the hot shocked H_2 it is consistent with Wright et al. (2000) and Melnick et al. (2000), who estimate the shocked Plateau water abundance to be $(2-5) \times 10^{-4}$.

The HC H_2O abundance is in agreement with the mapping of $H_2^{18}O$ towards the Orion Hot Core with the IRAM telescope (12″ beam) by Gensheimer et al. (1996). Their estimated abundance is 1.4×10^{-5}. S01 estimate the water abundance to be $\sim 1.0 \times 10^{-5}$ from their observation of the vibrationally excited H_2O $1_{1,0}-1_{0,1}$ $v_2 = 1$ transition, also in accordance with our value.

High water abundances in high temperature regions, for example in outflows, PDRs, and hot cores are consistent with both water and deuterated water forming on grains at low temperatures, and subsequently evaporating from the grain surfaces at high temperatures above ~90 K. At temperatures above ~400 K, easily reached in shocks, neutral-neutral reactions produce even higher water abundances (cf. Neufeld et al. 1995). Hence, our high abundance in the HC of H_2O can be the result of evaporation from grain surfaces, which also applies to CH_3OH and NH_3, as is discussed in more detail in Sect. 7.2. The water abundance in the CR and LVF is about the same, and lower than in the HC. This might be a natural consequence of a lower temperature in these regions with less evaporation from grain surfaces, which also applies to the PDR region. This is also the cause of the non-detection of water in the ER which has a temperature below the sublimation temperature. The highest water abundance is found in the HVF, which is suggestive of an even more efficient production in shocks.

Table 4. Relative abundances ratios and comparisons with ice abundances.

Abundance ratio	LVF	HC	CR	Ice abundances[a]	
	$N/N(H_2O) \times 100$			Orion IRc2	W33A
CH_3OH/H_2O		7	430	10	11–17
HDO/H_2O	0.52	0.13	3.2		0.3
$HDCO/H_2CO$			1.2		
NH_3/H_2O		13	7		15
SO_2/H_2O	69		36		~1.6
H_2CO/H_2O	0.5		3.6		~3
SO/H_2O	11		3.0		
OCS/H_2O		0.14		<0.2	0.2
CS/H_2O	0.41	0.02	1.4		
H_2S/H_2O	5.2	0.22			

[a] Gibb et al. (2000) and (2004).

7.2. Gas-phase vs. grain surface abundances

Ratios of our observed gas-phase column densities in the Orion LVF, HC and CR sources (as derived from Tables 1 and 2) and the water column density is found in Table 4. These ratios are compared with the corresponding grain-surface abundance ratios towards two of the sources observed by ISO (Gibb et al. 2000, 2004), Orion IRc2 and the embedded high-mass protostar W33A.

Some suggestions from these comparisons are:

– Both CH_3OH and H_2O are very abundant in the dense and warm HC, and their gas-phase abundance ratio is very similar to that in the grain-surface ice of Orion IRc2 and W33A. This strongly points at a dominant production via hydrogenation on cold grain surfaces and subsequent evaporation in the warm and hot cores (cf. Brown et al. 1988; Caselli et al. 1993; Stantcheva & Herbst 2004; Garrod & Herbst 2006;

Chang et al. 2007), especially so since gas-phase production of CH_3OH has been shown to be very inefficient (cf. Geppert et al. 2005; Millar 2005; Garrod et al. 2007). In the CR the CH_3OH/H_2O ratio is about 60 times higher than in the HC and in ices, caused by the four times decrease of the water abundance, and the 15 times higher methanol abundance as compared to the HC. This may suggest that H_2O is consumed in the formation of CH_3OH in accordance with the recent laboratory study of methanol formation from electron-irradiated mixed H_2O/CH_4 ice at 10 K by Wada et al. (2006).

- The rather similar gas-phase HDO/H_2O abundance ratios in the LVF and HC compared with the ice ratio in W33A most likely suggest efficient deuteration reactions on grain surfaces as the cause of the high water deuteration level. This is supported by our previous conclusions about the grain surface origin of the high water abundances. The much higher HDO/H_2O ratio found in the CR, as well as the similar $HDCO/H_2CO$ ratio, at least partly is caused by a decreasing H_2O abundance – possibly a result of H_2O consumption in the efficient grain-surface formation of CH_3OH in this source.
- Likewise, the gas-phase abundance ratios of NH_3 and H_2O in the CR and HC are similar to the W33A ice abundance ratio, again strongly suggesting that both these abundant species originate primarily from hydrogenation on cold grain surfaces with subsequent evaporation (cf. Stantcheva & Herbst 2004; Garrod et al. 2007).
- The high SO_2/H_2O abundance ratio observed in the LVF is contrasted with a low ice ratio in W33A. The latter ratio is most likely explained by rather inefficient gas-phase formation of SO_2 and subsequent adsorption onto already icy grain mantles formed by efficient hydrogenation on the cold grains. The high gas-phase H_2O abundance in the LVF may directly result from evaporation caused by the strong radiation from the nearby LVF driving source. This heating also could release S and Si atoms from the grains. Subsequent gas-phase reactions, based upon undepleted elemental abundances, then could lead to the elevated abundances of SO_2, SO, H_2S and SiO observed in the LVF. These abundances are several orders of magnitude higher than those in quiescent clouds where the abundances of S and Si appear to be depleted (B87; Irvine et al. 1987). In this scenario the ISO observations of OH at high abundance in the LVF (Goicoechea et al. 2006) are important. Low velocity shocks also may play a role here (cf. Mitchell 1984; Pineau des Forêts et al. 1993).
- The very similar CR H_2CO/H_2O gas-phase and W33A ice abundances most likely just tells us that both abundance ratios have the same main origin.
- The similarity of the HC gas-phase OCS/H_2O abundance ratio and the corresponding ratio in the W33A ice, also might hint at a grain surface origin of OCS. However, the comparatively low OCS abundance is accommodated by current ion-molecule reaction models and the ice content then likely is a result of adsorption.

8. Discussion – source sizes and source structure

We have in our column density and molecular abundance calculations in all cases treated the various Orion KL subregions, probed by the large Odin antenna beam, as homogeneous sources having specified average temperatures, densities and equivalent circular sizes and beam-filling factors.

However, the *High Velocity Outflow* is known to be bi-polar with a FWHP size of 60−70″, as estimated from simultaneous Odin mapping of the H_2O and CO $J = 5-4$ brightness distributions (Olofsson et al. 2003; Hjalmarson et al. 2005). As seen from the radiative transfer equation, the H_2O excitation temperature corresponding to a size of 70″ is only 26 K, while a temperature of 72 K as found by Wright et al. (2000) corresponds to a size of only 32″. This indicates a very clumpy H_2O brightness distribution, and that this source is filled with approximately one fourth of water emission. Similar results are obtained investigating the size-temperature relation of CO. In fact, the appearance of the HVF may be similar to the clumpy, finger-like emission seen in shock-excited H_2 (Salas et al. 1999)[4].

The *Low Velocity Outflow* has a NE-SW elongated structure, roughly orthogonal to the HVF, which also must have small scale structure (Genzel et al. 1981; Greenhill et al. 1998). If we guide ourselves by the optically thick HDO lines observed by Pardo et al. (2001) and use a HPBW size of 15″ for $H_2^{18}O$, the corresponding excitation temperature is only 40 K. The size corresponding to 72 K is 10″ which suggests that this source is filled with about one half of radiating gas-phase water. Similar results are found for all optically thick outflow species.

The *Compact Ridge* and *Hot Core* size-temperature relations are more consistent with the assumed values, although we know from Beuther et al. (2005) that both sources are very clumpy. This might be caused by their much smaller size as compared to the outflows, where the clumping affects larger scales. As seen from the CH_3OH Fig. 46 (online material) and Fig. 12, the source size of the CR also varies with the upper state energies of the lines. This might indicate considerable temperature and density variations within the CR.

Considering the uncertainties discussed above and in Sects. 3 and 10.2 (Appendix), the striking agreement with B87 and S95 strengthens our confidence of our results.

9. Summary

We present first results from a spectral line survey towards Orion KL in a frequency range inaccessible from the ground covering 487−492 and 542−577 GHz.

Some of the results from this survey:

1. We detect a total of 280 lines from 38 different molecular species.
2. In addition we detect 64 unidentified lines, which represents 19% of the total. Some tentative assignments of a few of them have been made such as the interstellar anion SH^-, ND, SO^+, and CH_3OCHO.
3. The total *beam-averaged* emission in our survey is dominated by CO, *o*-H_2O, SO_2, SO, ^{13}CO and CH_3OH. Species with the largest number of lines are CH_3OH, $(CH_3)_2O$, SO_2, $^{13}CH_3OH$, CH_3CN and NO.
4. Six water lines are detected, including the ground state rotational transition $1_{1,0}-1_{0,1}$ of *o*-H_2O, and its isotopologues *o*-$H_2^{18}O$ and *o*-$H_2^{17}O$, which shows emission from the Low- and High Velocity Flow and the Compact Ridge. Hot Core emission from water is observed from the *p*-H_2O transition $6_{2,4}-7_{1,7}$ with an upper state energy 867 K, and from a weak line feature at 489.054 GHz identified as the $4_{2,3}-3_{3,0}$ transition of *o*-$H_2^{18}O$ with an upper state energy of 430 K. We have also observed the HDO $2_{0,2}-1_{1,1}$ transition from the Low

[4] See also www: `http://subarutelescope.org/Science/press-release/9901/OrionKL_300.jpg`

Velocity Flow, Compact Ridge and the Hot Core, and have a tentative detection of the high energy transition (581 K) $6_{2,4}-6_{2,5}$ of HDO.

5. We detect the 1_0–0_0 transitions of NH_3 and the isotopologue $^{15}NH_3$. The main isotopologue shows emission from both the Hot Core, LVF and Compact Ridge, while the rarer isotopologue only exhibits emission from the Hot Core.
6. Isotopologue abundance ratios of D/H, $^{12}C/^{13}C$, $^{32}S/^{34}S$, $^{34}S/^{33}S$ and $^{18}O/^{17}O$ are calculated, as well as the molecular abundance ratio of O/S, all in agreement with previous findings.
7. Different methods are used to obtain rotation temperatures and column densities. For eight different species with at least four lines and a sufficient energy range in the transitions, the rotation diagram method and the forward model are applied. The LTE approximation is used for all the other species.
8. Abundances are estimated for the observed species from the different subregions, and we find very high gas-phase abundances of H_2O, NH_3, SO_2, SO, NO, and CH_3OH. An important fact here is that all our abundance determinations, including those for water vapour, are based upon the same methodology.
9. A comparison of our estimated gas-phase abundances with the ice inventory of ISO is shedding new light on the chemical origins of H_2O, CH_3OH, NH_3 and SO_2 in the various Orion KL subregions.
10. The line density in our survey is 4–20 per GHz, with a mean of 8 per GHz. This is comparable with larger telescopes ($\sim$10 GHz^{-1}), showing the excellent performance of the Odin satellite.

Acknowledgements. Generous financial support from the Research Councils and Space Agencies in Sweden, Canada, Finland and France is gratefully acknowledged. We sincerely thank Frank Lovas for a CD containing his molecular spectroscopy database SLAIMØ3, and are very grateful to the dedicated scientists supporting the molecular spectroscopy database the Cologne Database for Molecular Spectroscopy (CDMS) and the Jet Propulsion Laboratory (JPL) for making the difficult but absolutely necessary molecular spectroscopy available on the Internet. We also thank the referees whose constructive comments led to significant improvements of the paper.

References

Araya, E., Hofner, P., Kurtz, S., Bronfman, L., & DeDeo, S. 2005, ApJS, 157, 279
Batrla, W., Wilson, T. L., Bastien, P., & Ruf, K. 1983, A&A, 128, 279
Bensch, F., Pak, I., Wouterloot, J. G. A., Klapper, G., & Winnewisser, G. 2001, ApJ, 562, L185
Beuther, H., Zhang, Q., Greenhill, L. J., et al. 2005, ApJ, 632, 355
Bevington, P. R. 1969, Data Reduction and Error Analysis for the Physicas Sciences (McGraw-Hill book company)
Blake, G. A., Sutton, E. C., Masson, C. R., & Phillips, T. G. 1986, ApJS, 60, 357
Blake, G. A., Sutton, E. C., Masson, C. R., & Phillips, T. G. 1987, ApJ, 315, 621 (B87)
Brown, P. D., Charnley, S. B., & Millar, T. J. 1988, MNRAS, 231, 409
Caselli, P., Hasegawa, T. I., & Herbst, E. 1993, ApJ, 408, 548
Cernicharo, J., Goicoechea, J. R., Daniel, F., et al. 2006, ApJ, 649, 33
Chang, Q., Cuppen, H. M., & Herbst, E. 2007, A&A, 469, 973
Cheung, A. C., Rank, D. M., Townes, C. H., Thornton, D. D., & Welch, W. J. 1968, Phys. Rev. Lett., 21, 1701
Chin, Y.-N., Henkel, C., Whiteoak, J. B., Langer, N., & Churchwell, E. B. 1996, A&A, 305, 960
Comito, C., Schilke, P., Phillips, T. G., et al. 2005, ApJS, 156, 127 (C05)
Friberg, P. 1984, A&A, 132, 265
Garrod, R. T., & Herbst, E. 2006, A&A, 457, 927
Garrod, R. T., Wakelam, V., & Herbst, E. 2007, A&A, 467, 1103
Gensheimer, P. D., Mauersberger, R., & Wilson, T. L. 1996, A&A, 314, 281
Genzel, R., & Stutzki, J. 1989, ARA&A, 27, 41
Genzel, R., Reid, M. J., Moran, J. M., & Downes, D. 1981, ApJ, 244, 884
Genzel, R., Downes, D., Ho, P. T. P., & Bieging, J. 1982, ApJ, 259, L103
Geppert, W., Hellberg, F., Österdahl, et al. 2005, IAU Symp. 231, ed. D. C. Lis, G. A. Blake, & E. Herbst (Cambridge University Press), 117
Gibb, E. L., Whittet, D. C. B., Schutte, W. A., et al. 2000, ApJ, 536, 347
Gibb, E. L., Whittet, D. C. B., Boogert, A. C. A., & Tielens, A. G. G. M. 2004, ApJS, 151, 35
Goicoechea, J. R., Cernicharo, J., Lerate, M. R., et al. 2006, ApJ, 641, L49
Goldsmith, P. F., & Langer, W. D. 1999, ApJ, 517, 209
Goldsmith, P. F., Bergin, E. A., & Lis, D. C. 1997, ApJ, 491, 615
Greenhill, L. J., Gwinn, C. R., Schwartz, C., Moran, J. M., & Diamond, P. J. 1998, Nature, 396, 650
Grevesse, N., Noels, A., & Sauval, A. J. 1996, ASP Conf. Ser., 99, 117
Groner, P., Albert, S., Herbst, E., & de Lucia, F. C. 1998, ApJ, 500, 1059
Hermsen, W., Wilson, T. L., Walmsley, C. M., & Batrla, W. 1985, A&A, 146, 134
Hermsen, W., Wilson, T. L., & Bieging, J. H. 1988a, A&A, 201, 276
Hermsen, W., Wilson, T. L., Walmsley, C. M., & Henkel, C. 1988b, A&A, 201, 285
Hjalmarson, Å., Bergman, P., Biver, N., et al. 2005, Adv. Space Res., 36, 1031
Ho, P. T. P., & Townes, C. H. 1983, ARA&A, 21, 239
Hollis, J. M., Lovas, F. J., Suenram, R. D., Jewell, P. R., & Snyder, L. E. 1983, ApJ, 264, 543
Ikeda, M., Maezawa, H., Ito, T., et al. 1999, ApJ, 527, L59
Irvine, W. M., Schloerb, F. P., Hjalmarson, Å., & Herbst, E. 1985, in Protostars and Planets II, ed. D. C. Black, & M. S. Matthews (University of Arizona Press), 579
Irvine, W. M., Goldsmith, P. F., & Hjalmarson, Å. 1987, in Interstellar Processes, ed. D. J. Hollenbach, & H. A. Thronson, Jr. (Reidel Publishing Co), 561
Johansson, L. E. B., Andersson, C., Elldér, J., et al. 1984, A&A, 130, 227
Kahane, C., Gomez-Gonzalez, J., Cernicharo, J., & Guélin, M. 1988, A&A, 1988, 190, 167
Keene, J., Blake, G. A., & Phillips, T. G. 1983, ApJ, 271, L27
Lampton, M., Margon, B., & Bowyer, S. 1976, ApJ, 208, 177
Larsson, B., Liseau, R., Bergman, P., et al. 2003, A&A, 402, L69
Lerate, M. R., Barlow, M. J., Swinyard, B. M., et al. 2006, MNRAS, 370, 597
Liseau, R., Larsson, B., Brandeker, A., et al. 2003, A&A, 402, L73
Lovas, F. J. 2003, Spectral Line Atlas for Interstellar Molecules (SLAIMØ3) Ver.1, private communication of a CD
Mangum, J. G., Wootten, A., Loren, R. B., & Wadiak, E. J. 1990, ApJ, 348, 542
Masson, C. R., Lo, K. Y., Phillips, T. G., et al. 1987, ApJ, 319, 446
Melnick, G. J., Stauffer, J. R., Ashby, M. L. N., et al. 2000, ApJ, 539, L77
Menten, K. M., Walmsley, C. M., Henkel, C., et al. 1986, A&A, 169, 271
Menten, K. M., Walmsley, C. M., Henkel, C., & Wilson, T. L. 1988, A&A, 198, 253
Migenes, V., Johnston, K. J., Pauls, T. A., & Wilson, T. L. 1989, ApJ, 347, 294
Millar, T. J. 2005, IAU Symp., 231, ed. D. C. Lis, G. A. Blake, & E. Herbst (Cambridge University Press), 77
Mitchell, G. F. 1984, ApJ, 287, 665
Müller, H. S. P., Thorwirth, S., Roth, D. A., & Winnewisser, G. 2001, A&A, 370, L49
Nagai, T., Kaifu, N., Nagane, K., & Akaba, K. 1979, PASJ, 31, 317
Neufeld, D. A., Lepp, S., & Melnick, G. J. 1995, ApJS, 100, 132
Neufeld, D. A., Green, J. D., Hollenbach, et al. 2006, ApJ, 647, L33
Nordh, H. L., von Schéele, F., Frisk, U., et al. 2003, A&A, 402, L21
Nummelin, A., Dickens, J. E., Bergman, P., et al. 1998, A&A, 337, 275
Nummelin, A., Bergman, P., Hjalmarson, Å., et al. 2000, ApJS, 128, 213
Olofsson, H. 1984, A&A, 134, 36O
Olofsson, H., Hjalmarson, Å., & Rydbeck, O. E. H. 1981, A&A, 100, L30
Olofsson, H., Elldér, J., Hjalmarson, Å., & Rydbeck, O. E. H. 1982, A&A, 113, L18
Olofsson, A. O. H. 2003, Thesis, Chalmers University of Techonology, ISBN 91-7291-341-X
Olofsson, A. O. H., Olofsson, G., Hjalmarson, Å., et al. 2003, A&A, 402, L47
Olofsson, A. O. H., Persson, C. M., Koning, N., et al. 2007, A&A, 476, 791 (Paper I)
Pardo, J. R., Cernicharo, J., Herpin, F., et al. 2001, ApJ, 562, 799
Pauls, T. A., Wilson, T. L., Bieging, J. H., & Martin, R. N. 1983, A&A, 124, 23
Penzias, A. A. 1981a, ApJ, 249, 513
Penzias, A. A. 1981b, ApJ, 249, 518
Phillips, T. G., Wannier, P. G., Scoville, N. Z., & Huggins, P. J. 1979, ApJ, 231, 720
Pickett, H. M., Poynter, R. L., Cohen, E. A., et al. 1998, J. Quant. Spectrosc. & Rad. Transfer, 60, 883
Pineau des Forêts, G., Roueff, E., Schilke, P., & Flower, D. R. 1993, MNRAS, 262, 915

Plume, R., Bensch, F., Howe, J. E., et al. 2000, ApJ, 539, L133
Rodríguez-Franco, A., Martín-Pintado, J., & Fuente, A. 1998, A&A, 329, 1097
Rodríguez-Franco, A., Wilson, T. L., Martín-Pintado, J., & Fuente, A. 2001, ApJ, 559, 985
Salas, L., Rosando., M., Cruz-González, I., et al. 1999, ApJ, 511, 822
Savage, C., Apponi, A. J., Ziurys, L. M., & Wyckoff, S. 2002, ApJ, 578, 211
Schilke, P., Güsten, R., Schulz, A., Serabyn, E., & Walmsley, C. M. 1992, A&A, 261, L5
Schilke, P., Benford, D. J., Hunter, T. R., Lis, D. C., & Phillips, T. G. 2001, ApJS, 132, 281 (S01)
Schöier, F. L., van der Tak, F. F. S., van Dishoeck, E. F., & Black, J. H. 2005, A&A, 432, 369
Serabyn, E., & Weisstein, E. 1995, ApJ, 451, 238
Stantcheva, T., & Herbst, E. 2004, A&A, 423, 241
Sutton, E. C., Blake, G. A., Genzel, R., Masson, C. R., & Phillips, T. G. 1986, ApJ, 311, 921
Sutton, E. C., Peng, R., Danchi, W. C., et al. 1995, ApJS, 97, 455 (S95)
Tauber, J. A., Lis, D. C., Keene, J., Schilke, P., & Büttgenbach, T. H. 1995, A&A, 297, 567
Turner, B. E. 1990, ApJ, 362, L29
Turner, B. E. 1991, ApJS, 76, 617
Ungerechts, H., Bergin, E. A., Goldsmith, et al. 1997, ApJ, 482, 245
Wada, A., Mochizuki, N., & Hiraoka, K. 2006, ApJ, 644, 300
Watson, D. M., Genzel, R., Townes, C. H., & Storey, J. W. V. 1985, ApJ, 298, 316
White, G. J., Araki, A., Greaves, J. S., Ohishi, M., & Higginbottom, N. S. 2003, A&A, 407, 589 (W03)
Wilner, D. J., Wright, M. C. H., & Plambeck, R. L. 1994, ApJ, 422, 642
Wilson, T. L., & Matteucci, F. 1992, A&ARv., 4, 1
Wilson, T. L., & Rood, R. 1994, ARA&A, 32, 191
Wilson, T. L., Downes, D., & Bieging, J. 1979, A&A, 71, 275
Wilson, T. L., Serabyn, E., Henkel, C., & Walmsley, C. M. 1986, A&A, 158, L1
Wilson, T. L., Gaume, R. A., Gensheimer, P., & Johnston, K. J. 2000, ApJ, 538, 665
Wirström, E. S., Bergman, P., Olofsson, A. O. H., et al. 2006, A&A, 453, 979 (W06)
Womack, M., Ziurys, L. M., Wyckoff, S., & Sage, L. 1990, BAAS, 22, 1329
Wouterloot, J. G. A., Brand, J., & Henkel, C. 2005, A&A, 430, 549
Wright, M. C. H., Plambeck, R. L., & Wilner, D. J. 1996, ApJ, 469, 216
Wright, C. M., van Dishoeck, E. F., Black, J. H., et al. 2000, A&A, 358, 689

Online Material

10. Data analysis methods

10.1. Single line analysis

With the assumption of optically thin emission, neglecting the background radiation, and assuming that the source fills the antenna main beam, the beam averaged upper state column density is calculated as

$$N_{\rm u}^{\rm thin} = \frac{8\pi k \nu_{{\rm u}l}^2}{hc^3} \frac{1}{A_{{\rm u}l}} \int T_{\rm mb}\, {\rm d}\upsilon, \tag{8}$$

where k is the Boltzmann constant, $\nu_{{\rm u}l}$ is the frequency of the transition, h is the Planck constant, c is the speed of light, $A_{{\rm u}l}$ is the Einstein A-coefficient for the transition, and $T_{\rm mb}$ is the main beam brightness temperature. As customary the frequency axis ν has been converted to a velocity axis υ using the speed of light.

The total column density of each species can then be found assuming LTE (Local Thermodynamic Equilibrium), where the excitation temperatures, $T_{\rm ex}$, for all the energy levels are the same. The molecular population of each level is then given by the Boltzmann equation, which also defines $T_{\rm ex}$

$$N_{\rm u} = N_{\rm tot} \frac{g_{\rm u}}{Q(T)}\, {\rm e}^{-E_{\rm u}/kT_{\rm ex}}, \tag{9}$$

where $g_{\rm u}$ is the statistical weight of the upper state, and $Q(T)$ is the partition function, which only depends on temperature and molecular constants and hence differs for different kinds of species. The A-coefficients, statistical weights, partition functions and upper state energy levels are available via the databases JPL, CDMS, Leiden[5] (Schöier et al. 2005) or SLAIMØ3. For a few molecules, e.g. $(CH_3)_2O$, we calculate the A-coefficients using line strengths found in SLAIMØ3 as

$$A_{{\rm u}l} = \frac{16\,\pi^3\,\nu_{{\rm u}l}^3\,\mu^2}{3\,\epsilon_0\,h\,c^3} \frac{S_{{\rm u}l}}{g_{\rm u}} \tag{10}$$

where $S_{{\rm u}l}$ is the rotational part of the line strength, and μ is the molecular dipole moment.

From Eqs. (9) and (1), we obtain *the beam-averaged total column density*

$$N_{\rm tot}^{\rm thin} = \frac{8\pi k \nu_{{\rm u}l}^2}{hc^3} \frac{1}{A_{{\rm u}l}} \frac{Q(T)}{g_{\rm u}} {\rm e}^{\,E_{\rm u}/kT_{\rm ex}} \int T_{\rm mb}\, {\rm d}\upsilon \tag{11}$$

assuming optically thin emission.

The solution of the radiative transport equation, neglecting background radiation and with a constant source function, is

$$T_{\rm A}^* = T_{\rm b}\,\eta_{\rm mb}\,\eta_{\rm bf} = J(T_{\rm ex})\,(1-{\rm e}^{-\tau})\,\eta_{\rm mb}\,\eta_{\rm bf}, \tag{12}$$

where the beam-filling factor $\eta_{\rm bf} = \theta_{\rm s}^2/(\theta_{\rm s}^2+\theta_{\rm mb}^2)$, assuming that both the source brightness distribution and the antenna response are circularly symmetric and Gaussian. The radiation temperature, $J(T_{\rm ex})$ is

$$J(T_{\rm ex}) = \frac{h\nu}{k} \frac{1}{{\rm e}^{h\nu/kT_{\rm ex}}-1} \approx T_{\rm ex}, \tag{13}$$

where the approximation is valid only if $h\nu \ll kT_{\rm ex}$. For the appropriate temperatures in this region, $T \approx 100{-}200$ K, and frequencies ~550 GHz, the radiation temperature will differ from $T_{\rm ex}$ by approximately 10−15%. Accordingly, we use $J(T_{\rm ex})$ and not $T_{\rm ex}$ in our calculations.

[5] http://www.strw.leidenuniv.nl/~moldata/

If the emission is optically thick ($\tau \gg 1$) Eq. (12) simplifies to

$$T_{\rm A}^* = J(T_{\rm ex})\,\eta_{\rm mb}\,\eta_{\rm bf} = J(T_{\rm ex})\,\eta_{\rm mb}\,\frac{\theta_{\rm s}^2}{\theta_{\rm s}^2+\theta_{\rm mb}^2}. \tag{14}$$

Using this equation the beam-filling, and hence the approximate source size, can be determined without relying on correctly calculated optical depths. The variation in $T_{\rm A}^*$ that is seen mainly will be due to variations in the beam-filling factor, but there can also be variations in $T_{\rm ex}$, both along the path and between different states, which cannot be determined.

Since molecular clouds are known to be clumpy down to very small scales, it is indeed likely that the source does not fill the beam. This is especially true in case of the large Odin beam, and the total column density from Eq. (11) will be too low by a factor of $1/\eta_{\rm bf}$. Variations in beam-filling between the different transitions of the same molecule also are probable. Hence, when we are comparing other observations (e.g. interferometry mapping) with ours to estimate the beam-filling, by necessity we have to compare transitions with similar parameters tracing the same gas.

The optical depth at the centre of the line can be calculated, assuming LTE and a Gaussian line profile, using

$$\tau_{\rm max} = \sqrt{\frac{\ln 2}{16\,\pi^3}} \frac{c^3}{\nu_{{\rm u}l}^3\,\Delta\upsilon}\, A_{{\rm u}l}\, N_{\rm tot}\, \frac{g_{\rm u}}{Q(T)}\, {\rm e}^{-E_{\rm u}/kT_{\rm ex}}\, ({\rm e}^{h\nu_{{\rm u}l}/kT_{\rm ex}}-1) \tag{15}$$

where $\Delta\upsilon$ is the width of the line, and $E_{\rm u}$ is the upper state energy. However, this approach demands knowledge of the total column density. If we have observations of isotopologues, and if the isotopologue abundance ratio R is known, then the optical depths can be determined by means of Eq. (12). If the excitation temperatures are about the same for both isotopologues, and the optical depth of isotopologue one is larger than isotopologue two by a factor R, we then will have

$$\frac{T_{\rm A,1}}{T_{\rm A,2}} = \frac{(1-{\rm e}^{-\tau_1})\,\eta_{\rm bf,1}}{(1-{\rm e}^{-\tau_2})\,\eta_{\rm bf,2}} = \frac{(1-{\rm e}^{-R\,\tau_2})\,\eta_{\rm bf,1}}{(1-{\rm e}^{-\tau_2})\,\eta_{\rm bf,2}}. \tag{16}$$

This will give the mean optical depths of both species. If the emissions are co-spatial the beam-filling factors cancel.

Once a transition has become optically thick, the value of $N_{\rm u}/g_{\rm u}$ cannot increase any further. The derived total column density will then be too low and needs an optical depth correction factor C_τ, which will be one or larger

$$C_\tau = \frac{\tau}{1-{\rm e}^{-\tau}}. \tag{17}$$

With corrections for optical depth and beam-filling the *true total source averaged column density* will be

$$N_{\rm tot} = \frac{C_\tau}{\eta_{\rm bf}} \frac{8\pi k \nu_{{\rm u}l}^2}{hc^3} \frac{1}{A_{{\rm u}l}} \frac{Q(T)}{g_{\rm u}} {\rm e}^{E_{\rm u}/kT_{\rm ex}} \int T_{\rm mb}\, {\rm d}\upsilon = \frac{C_\tau}{\eta_{\rm bf}}\, N_{\rm tot}^{\rm thin}. \tag{18}$$

If no information about optical depth is available this correction is not taken into account. For the excitation temperature in Eqs. (14) and (18), we use an adopted temperature that fits the species (Table 1), or the calculated rotation temperature $T_{\rm ROT}$ (see Sect. 3.2.1).

Note the importance of the partition function $Q(T)$, and the statistical weight $g_{\rm u}$ in Eq. (18). If the statistical weights include the *ortho*/*para* ratio whenever these molecular sub-divisions exist, the partition function must include them. It is also important to use the same statistical weights $g_{\rm u}$ in Eq. (18) when the partition function $Q(T)$ is calculated.

10.2. Additional limitations

If there are deviations from the basic assumptions, errors will occur in the calculations for all models (cf. Goldsmith & Langer 1999). These effects can to some extent be corrected for, like optical depth effects and beam-filling, as discussed above. In addition we have:

1. *Several excitation temperatures/non-LTE.* The population distribution may not be characterised by a single rotational temperature. The temperature can vary due to density, excitation gradients along the line-of-sight, IR flux, subthermal excitation etc. Since our beam is very large and encompasses a variety of different conditions, we may expect emission from several different sources, each with different temperature.
2. *Adopted excitation temperature.* Whenever we have too few lines to use the rotation diagram method or forward model we use the LTE approximation for a single line. The excitation temperature is then adopted from a rotation temperature of a similar species in our survey, or taken from the literature. This can create errors if the adopted temperature is not appropriate.
3. *Source structure.* The beam-filling correction are calculated assuming a homogenous source (see also Sect. 8). Clumping and substructures can introduce errors in the beam-filling corrections. Vastly different opacitites between the isotopologues (with NH_3 and H_2O as good examples) also complicate the analysis, as the beam-filling factors may be very different.
4. *Gaussian decomposition.* Errors in our Gaussian decompositions can introduce errors in the calculated optical depths and the column densities.
5. *H_2 column densities.* The largest source of uncertainty in the abundances in Sect. 7 is the adopted H_2 column densities and the assumption that the H_2 emission and the molecule of interest spatially coincides. This can create errors by orders of magnitude.
6. *Observational errors.* Errors may exist in the measured line intensities due to misidentifications, unresolved blends, or pointing and calibration. However, the errors must be rather large to create significant errors in the column density obtained from the rotation diagram and forward model.
7. *Background radiation.* The background radiation, for example emission from warm dust, may be too large to be neglected. If the condition $T_{\rm ex} \gg T_{\rm bg}$ is violated, shifts along the ordinate in the rotation diagram with a factor of $\ln(1-T_{\rm bg}/T_{\rm ex})$ will occur. The dust continuum radiation will for example affect the level populations of water, and must be included in accurate calculations for these transitions.

10.3. Determination of relative chemical abundances

The definition of molecular abundance of a species with respect to H_2 is the ratio of the volume densities. This demands detailed knowledge of the geometry of the emitting region. If this is not known, column densities can be used as a substitute, with the assumption that the two species are well mixed and emitted from the same region, to obtain average abundances along the line of sight

$$X_{\rm species} = \frac{N_{\rm species}}{N_{\rm H_2}}. \tag{19}$$

The use of column densities will provide a higher degree of accuracy than the use of volume densities (Irvine et al. 1985). As long as the molecules are emitted from the same region with approximately the same source size, there is no dependence of beam-filling. In addition, since we have a uniformly calibrated set of data, uncertainties in calibration will not affect the result.

The relative isotopologue abundance R can be determined in the same way as the molecular abundances,

$$R = \frac{N_1}{N_2}, \tag{20}$$

when we have observations of optically thin isotopologues, or opacity-corrected column densities.

10.4. Optical depth broadening

If the intrinsic line shape is Gaussian, a high line opacity will increase the observed line width (cf. Phillips et al. 1979) as

$$\Delta\upsilon \approx \Delta\upsilon_i \left(\frac{\ln\tau_{\rm p}}{\ln 2}\right)^{1/2} \tag{21}$$

where $\Delta\upsilon_i$ is the intrinsic velocity width of the line and $\tau_{\rm p}$ ($\gg$1) is the peak optical depth in the line.

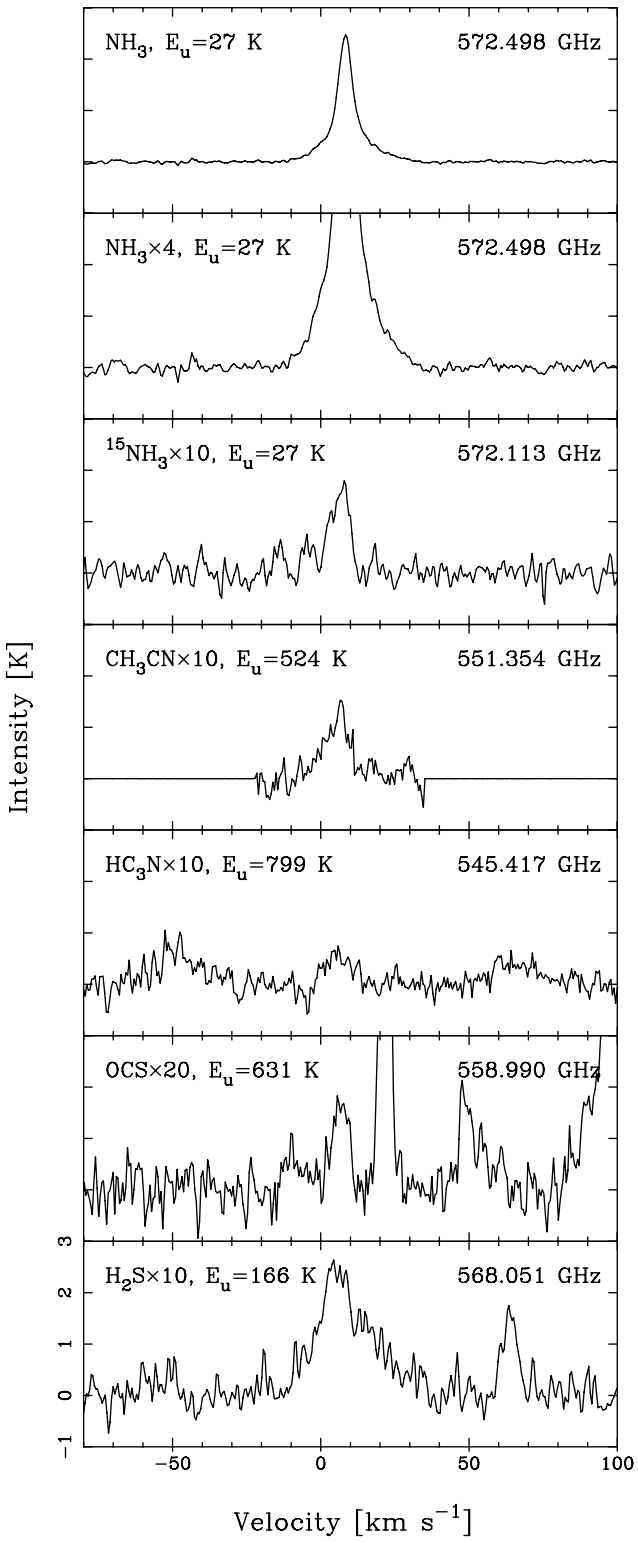

Fig. 25. Top figure shows the NH_3 line, the second figure shows four times magnified NH_3 line wings. The NH_3 line profile shows emission from the CR and HC. The $^{15}NH_3$, CH_3CN, HC_3N and OCS transitions suggest emission from the HC, and H_2S from both the HC and LVF. An intensity scale factor is given after the molecular species.

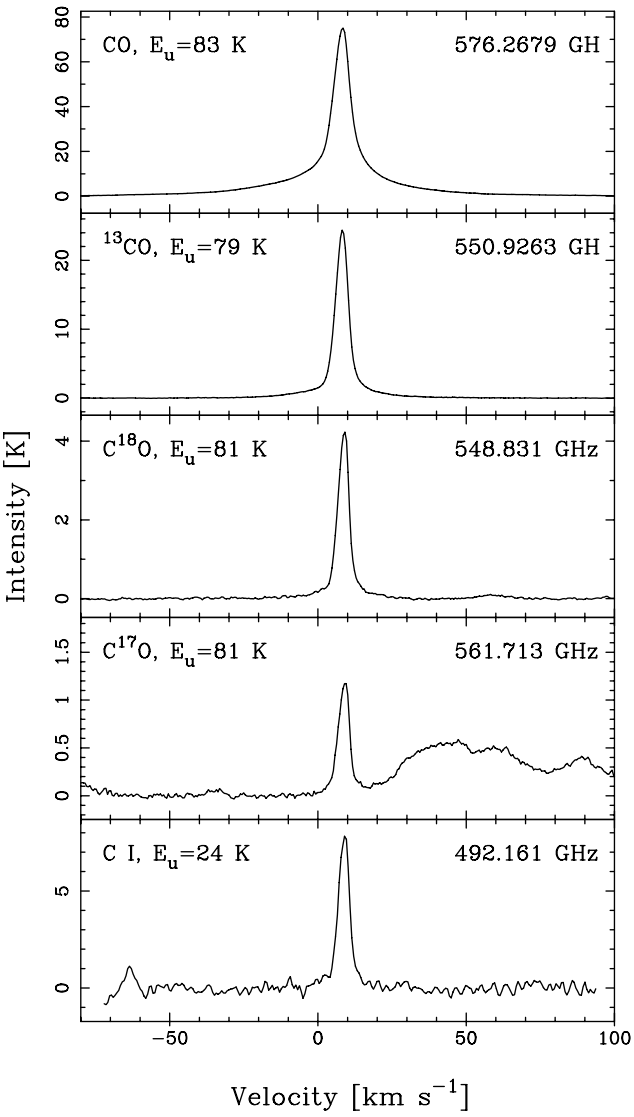

Fig. 26. CO, isotopologues and atomic C. Note the different intensity scales.

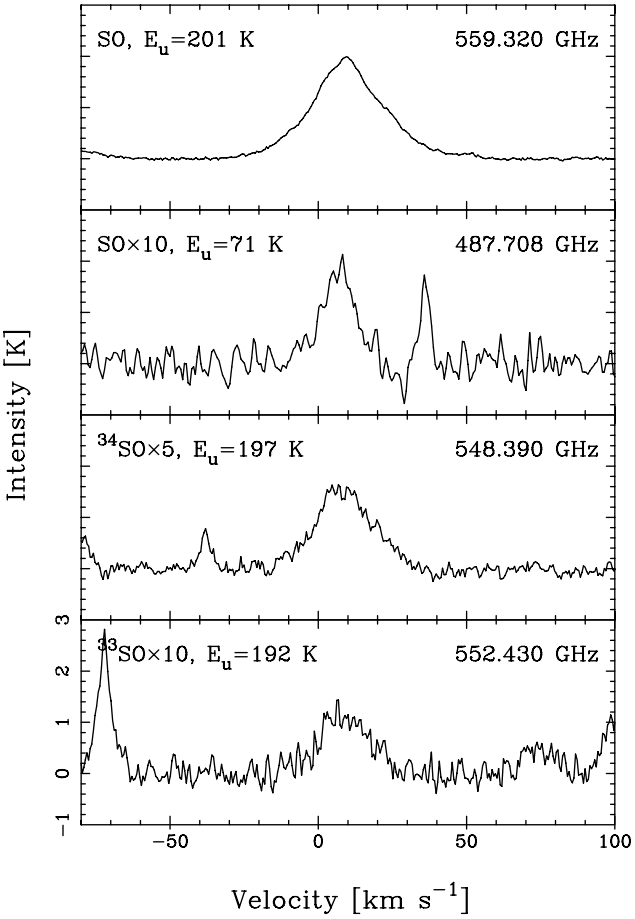

Fig. 27. SO and isotopologues. The SO line in the top panel is optically thick, and shows clear HVF line wings. The low-energy SO transition is optically thin. An intensity scale factor is given after the molecular species.

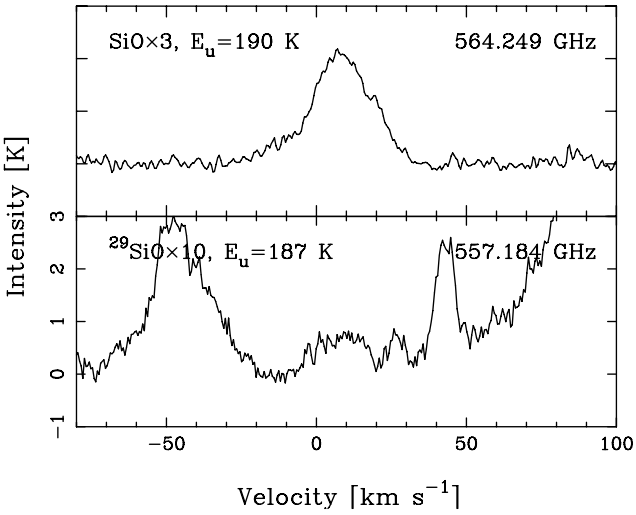

Fig. 28. The J = 13–12 transition for both SiO and ^{29}SiO. The SiO line is optically thick and also exhibits pronounced HVF line wings. A blend from CH_3OH and $^{13}CH_3OH$ is visible at 19.6 km s^{-1} in the SiO line. An intensity scale factor is given after the molecular species.

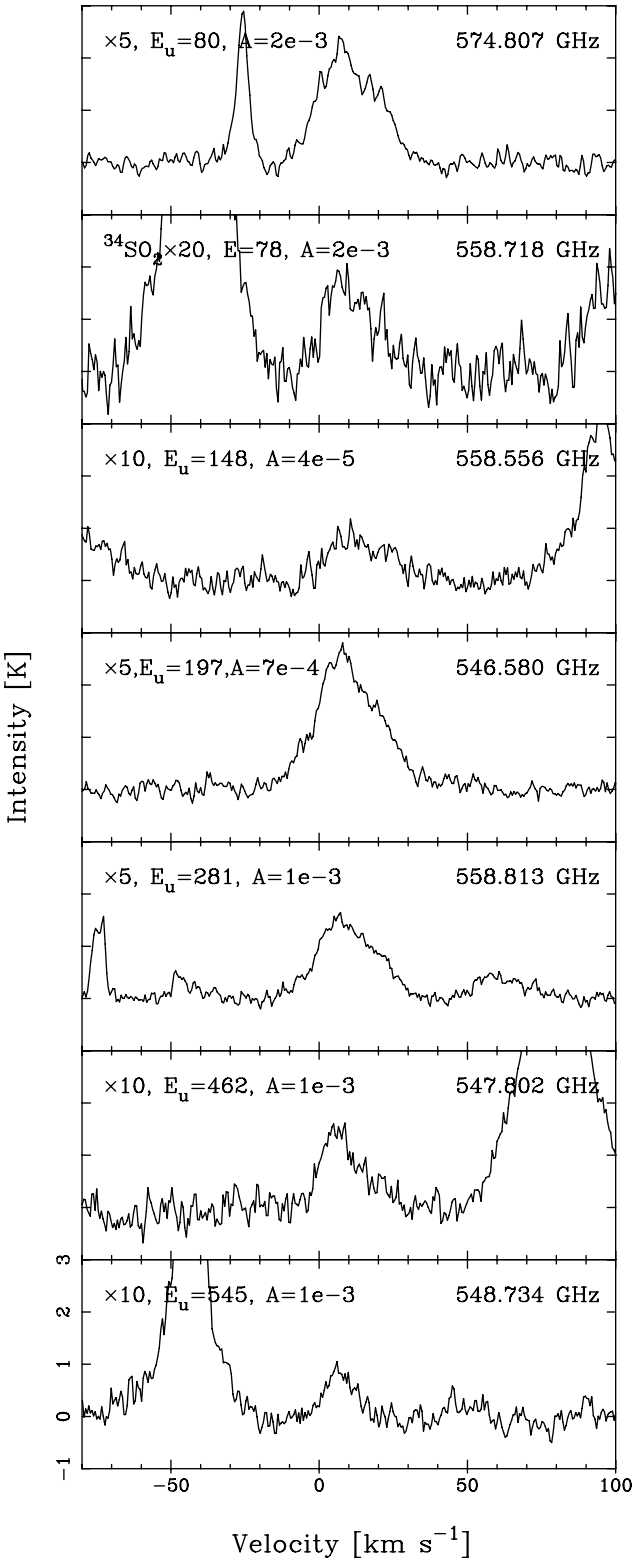

Fig. 29. SO_2 with different upper state energy levels and A-coefficients. The $^{34}SO_2$ line is the same transition as the SO_2 transition with E_u = 80 K. An intensity scale factor is given in the top left corners.

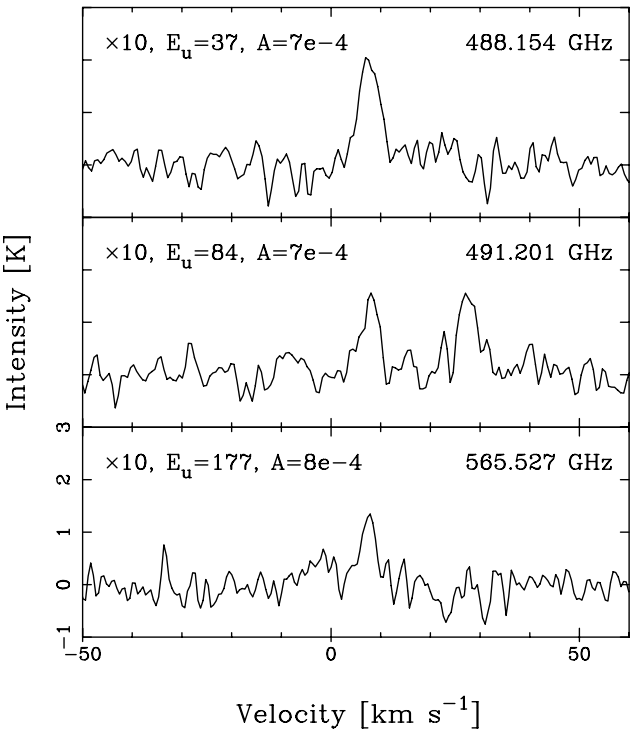

Fig. 30. $^{13}CH_3OH$ with emission from the CR. An intensity scale factor is given in the top left corners, upper state energies given in K and A-coefficients in s^{-1}.

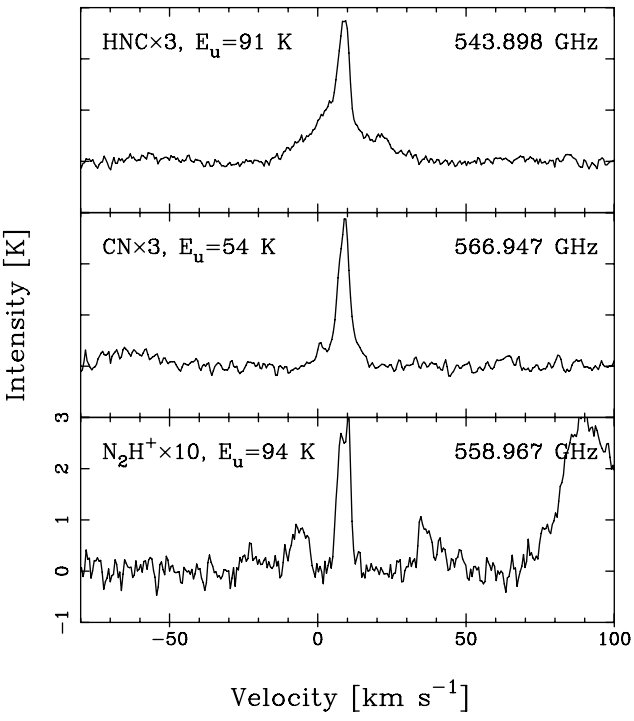

Fig. 31. The line profile of HNC shows emission from the ER, HC and LVF, CN from the PDR/ER and HC, and N_2H^+ from the ER. The line at $v \approx -8$ km s^{-1} next to N_2H^+ is OCS, which is also shown in Fig. 25. An intensity scale factor is given after the molecular species.

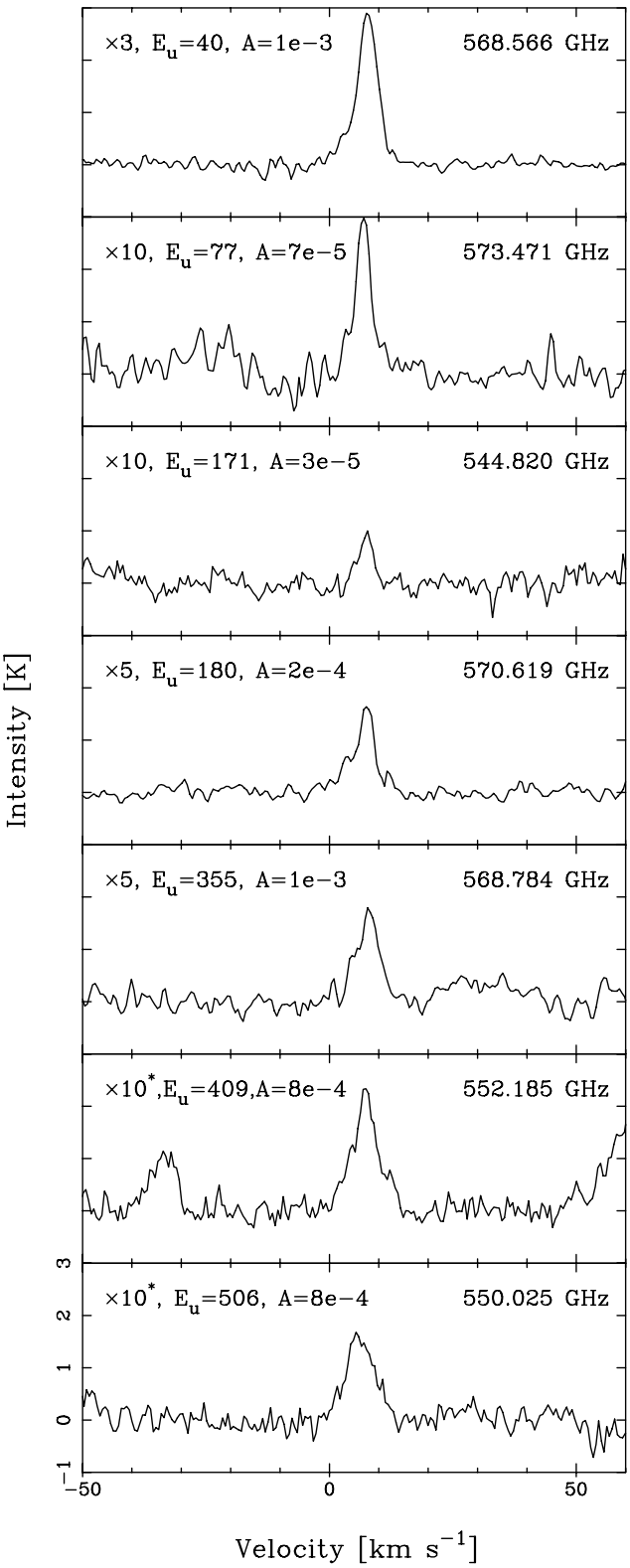

Fig. 32. CH_3OH with emission from both the CR and HC. Vibrationally excited transitions are marked by $*$ after the intensity scale factor given in the top left corners, with upper state energies given in K and A-coefficients in s^{-1}.

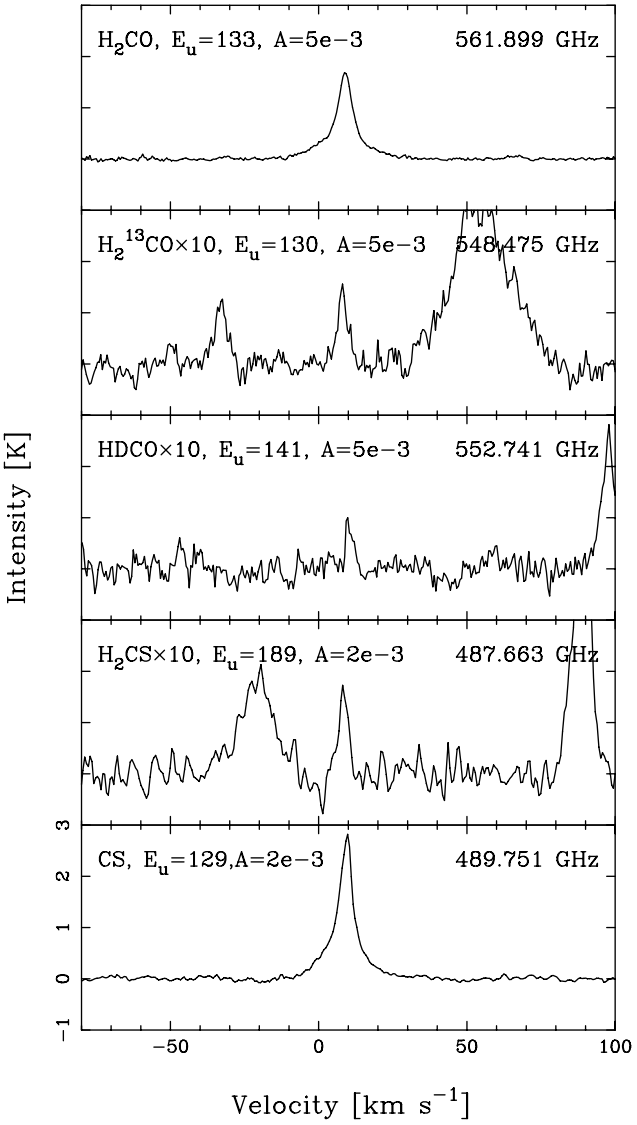

Fig. 33. The optically thick line profile of H_2CO show emission from the CR and LVF. The optically thin transitions of $H_2^{13}CO$, HDCO, and H_2CS show only emission from the CR. The CS line profile shows emission from the HC, LVF and a narrow component from the CR or ER. An intensity scale factor is given after the molecular species, the upper state energies are given in K and the *A*-coefficients in s^{-1}.

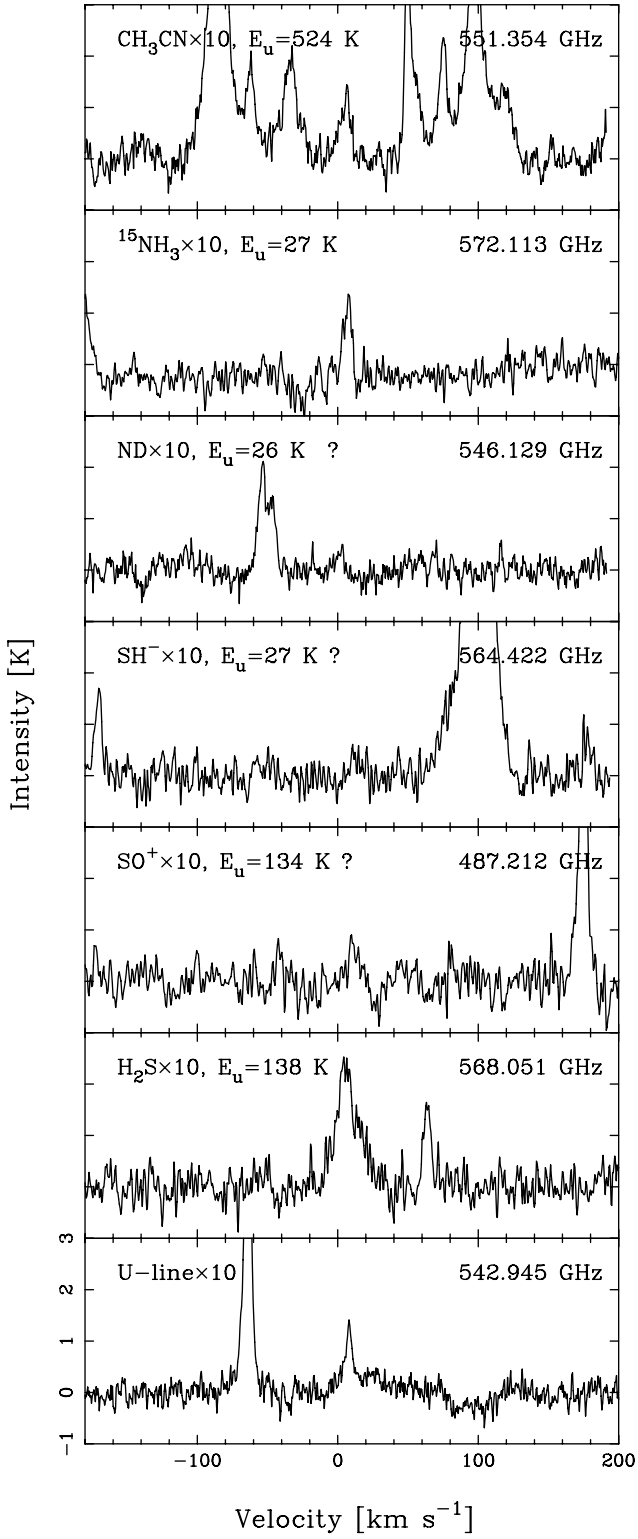

Fig. 34. Identification suggestions for a few U-lines together with $^{15}NH_3$, H_2S and CH_3CN as comparison lines. The U-line at 542.945 GHz is our strongest non-identified U-line. An intensity scale factor is given after the molecular species.

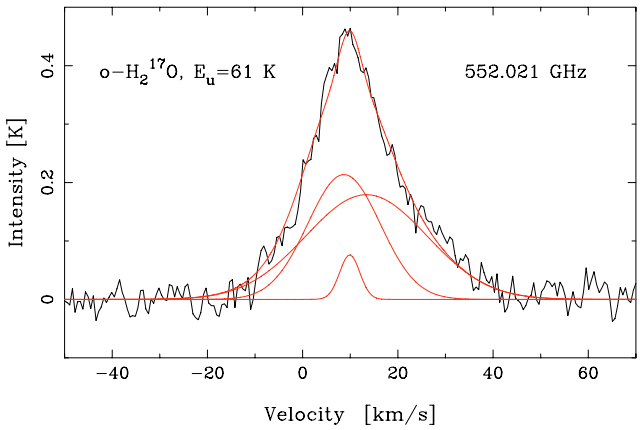

Fig. 35. A three-component Gaussian fit to $H_2^{17}O$ shown together with the individual Gaussians. The line widths are 5 km s^{-1}, 18 km s^{-1}, and 30 km s^{-1} from the CR, LVF and HVF, respectively.

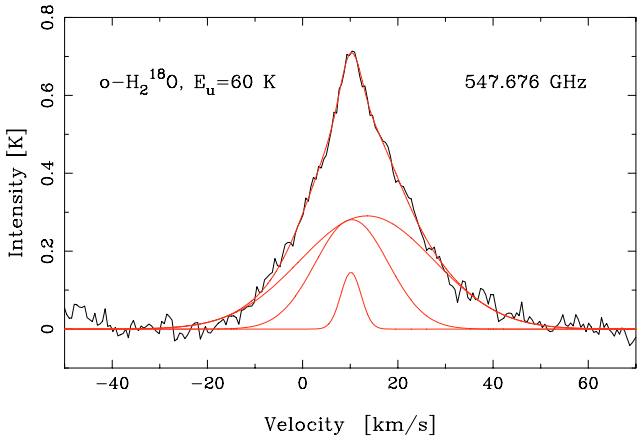

Fig. 36. A three-component Gaussian fit to $H_2^{18}O$ shown together with the individual Gaussians. The line widths are 5 km s^{-1}, 18 km s^{-1}, and 33 km s^{-1} from the CR, LVF and HVF, respectively.

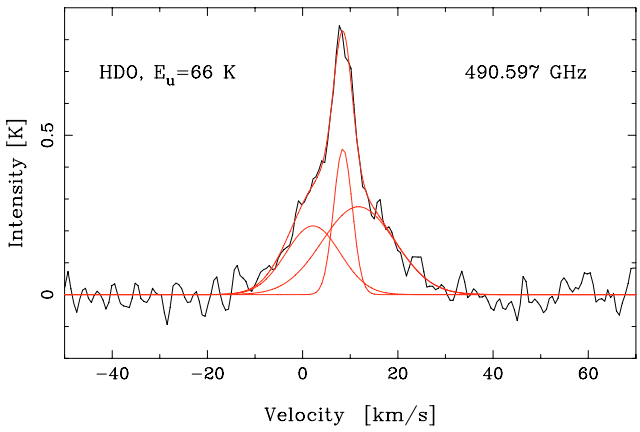

Fig. 37. A three-component Gaussian fit to HDO shown together with the individual Gaussians. The line widths are 5 km s^{-1}, 13 km s^{-1}, and 18 km s^{-1} for the CR, HC, and LVF, respectively.

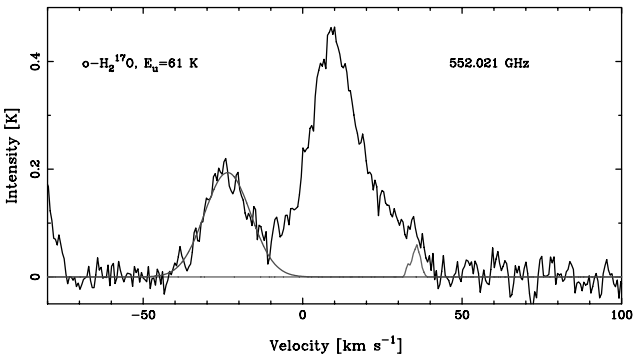

Fig. 38. $H_2^{17}O$ before removal of blends with reconstructed lines from SO_2 and CH_3OH shown.

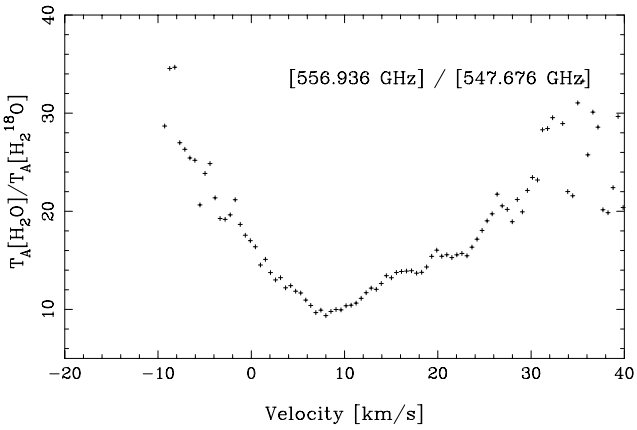

Fig. 39. Ratio of *o*-H_2O over *o*-$H_2^{18}O$.

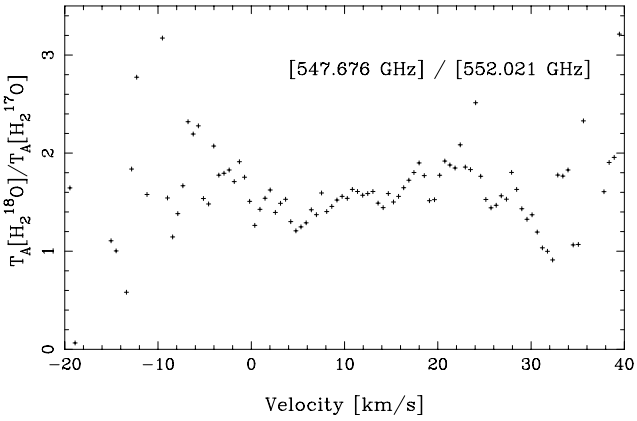

Fig. 40. Ratio of *o*-$H_2^{18}O$ over *o*-$H_2^{17}O$.

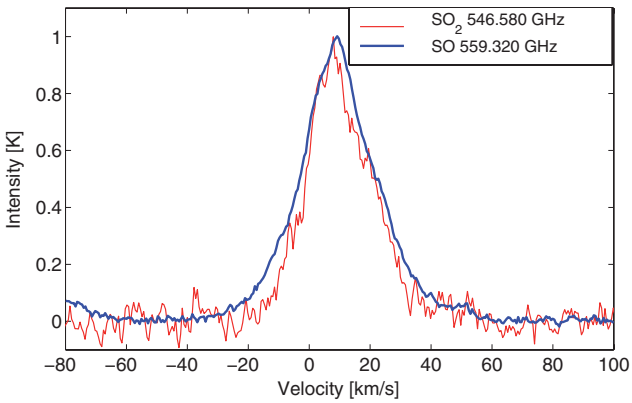

Fig. 41. Comparison of the SO and SO_2 line profiles. Both lines are normalised to unity.

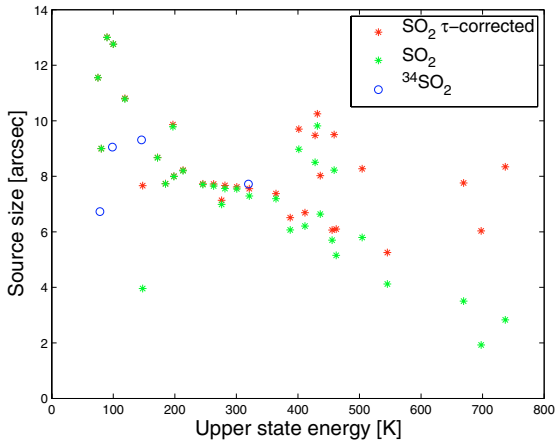

Fig. 42. Source sizes for opacity-corrected SO_2 (calculated with T_{ROT} = 103 K and source size = 8″) vs. non corrected SO_2 together with $^{34}SO_2$ (calculated with T_{ROT} = 125 K).

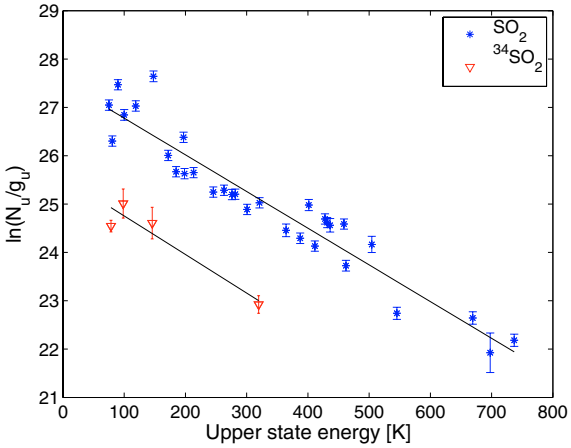

Fig. 43. Rotation diagram for SO_2, not corrected for opacity, produces T_{ROT} = 132 K and $N_{ROT} = 3.9 \times 10^{17}$ cm^{-2} (extended source). The $^{34}SO_2$ fit give T_{ROT} = 125 K and $N_{ROT} = 5.4 \times 10^{16}$ cm^{-2}.

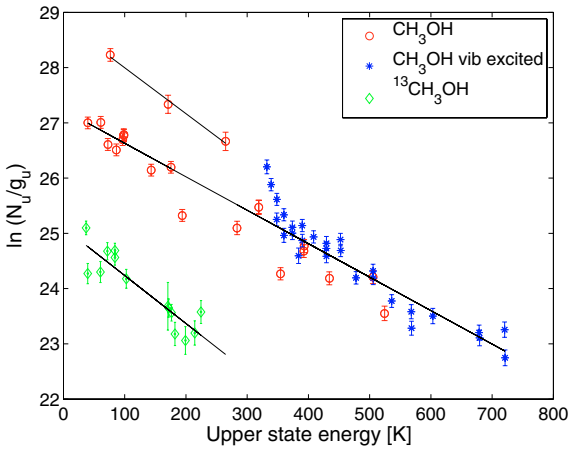

Fig. 44. Rotation diagrams: CH_3OH producing T_{ROT} = 165 K and $N_{ROT} = 9.3 \times 10^{17}$ cm^{-2} (not opacity corrected); three optically thin CH_3OH lines produces T_{ROT} = 120 K and $N_{ROT} = 2.6 \times 10^{18}$ cm^{-2}; $^{13}CH_3OH$ producing T_{ROT} = 115 K and $N_{ROT} = 5.9 \times 10^{17}$ cm^{-2} (extended source).

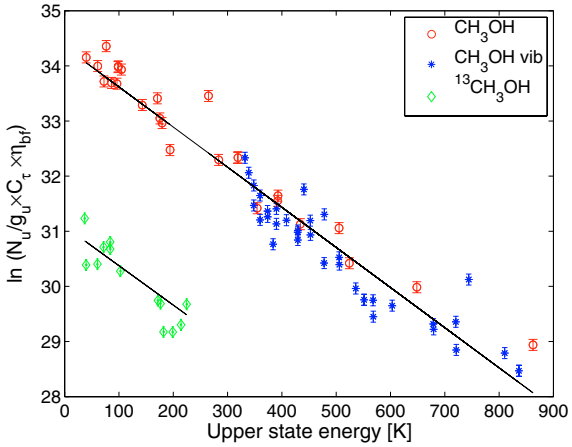

Fig. 45. CH_3OH forward model producing $T_{ROT} = 136^{+3}_{-4}$ K, $N = (1.3 \pm 0.1) \times 10^{18}$ cm^{-2} and a source size of $6''^{+0.1}_{-0.3}$. The $^{13}CH_3OH$ forward model use the rotation temperature and source size obtained from CH_3OH.

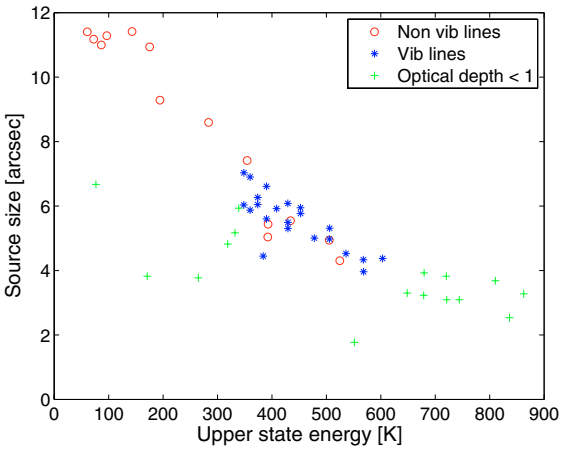

Fig. 46. Source size variation with energy for CH_3OH (no opacity corrections). The low-energy transitions have larger source sizes than higher-energy transitions. Note that all lines with an optical depth less than one, fall below the general trend of decreasing source size with higher energy, since Eq. (14) is only valid for optically thick lines.

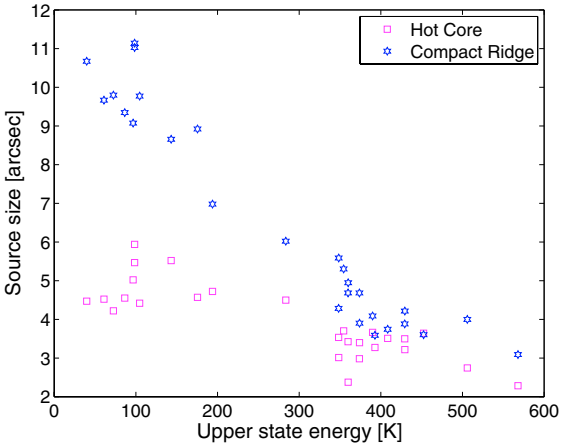

Fig. 47. Source size variation with energy for two components of CH_3OH with no opacity correction.

Table 5. Summary of all detected species.

Species	Number of lines	Upper state energy range [K]	$\int T_A^* d\upsilon$ [K km s^{-1}]
CH_3OCH_3	47	106–448	18.3
SO_2	42	75–737	239.9
$^{34}SO_2$	5	79–457	2.6
SO	5	71–201	181.5
^{33}SO	3	191–199	6.5
^{34}SO	2	191–197	15.6
CH_3OH υ_t=1	42	332–836	
CH_3OH	34	38–863	108.6
$^{13}CH_3OH$	21	37–499	6.8
$^{13}CH_3OH$ υ_t=1	2	373–670	
CH_3CN	17	410–1012	9.3
NO	12	84–232	11.1
CN	8	54	8.5
H_2CS	5	138–343	1.7
H_2CO	3	106–133	38.5
$H_2^{13}CO$	1	130	0.6
HDCO	3	114–141	2.8
OCS	3	604–658	1.3
o-H_2O	1	61	320.3
p-H_2O	1	867	2.2
o-$H_2^{17}O$	1	61	9.4
o-$H_2^{18}O$	2	60–430	16.2
HDO	1	66	10.7
HC_3N	2	648–799	0.6
CO	1	83	1 100
^{13}CO	1	79	174.3
$C^{17}O$	1	81	6.0
$C^{18}O$	1	79	24.3
C	1	24	38.7
NH_3	1	27	20.6
$^{15}NH_3$	1	27	0.7
HNC	1	91	10.7
N_2H^+	1	94	1.5
H_2S	1	166	4.4
CS	1	129	24
^{13}CS	1	173	v blend
SiO	1	190	17.6
^{29}SiO	1	187	1.4
^{30}SiO	1	185	0.5
HCS^+	1	186	v blend
NS	1	442	v blend
U-line	28		9.1
T-line	36		7.2
No. of species	38		
No. of lines	344		
Total $\int T_A^* d\upsilon$			2455

Table 6. Isotopologue abundance ratios from our survey, or from the literature, as compared to terrestrial values. The molecular abundance O/S ratios are also included.

	$[^{12}C/^{13}C]$	$[^{32}S/^{34}S]$	$[^{34}S/^{33}S]$	$[^{18}O/^{17}O]$	$[^{16}O/^{18}O]$	[D/H]	[O/S]	$[^{14}N/^{15}N]$	$[^{28}Si/^{29}Si]$
This survey	57 ± 14^a	21 ± 6^b–23 ± 7^c	4.9^d	3.6^e		0.001^f–0.03^g	15^h–20^i		
Terrestrial	89^j	22.5^j	5.5^j	5.5^k			35^v	273^l	19.6^m
K88[j]	47^{+6}_{-5}	$20.2^{+2.6}_{-2.1}$	$5.7^{+0.8}_{-0.6}$						
W&R94[n]	77 ± 7	~ 22		3.2 ± 0.2	560 ± 25			450 ± 22	
C96[o]	75 ± 21	35 ± 10	7.53 ± 0.45						
B01[p]	65.0 ± 9.2			4.15 ± 0.59					
P81b[q]				3.9 ± 0.2					
Various surveys	43 ± 7^r			4.17 ± 0.26^s	330 ± 69^t	2×10^{-5} [u]			16.9 ± 2.0^m

[a] From $^{12}CH_3OH/^{13}CH_3OH$. [b] From $^{32}SO/^{34}SO$. [c] From $^{32}SO_2/^{34}SO_2$. [d] From $^{34}SO/^{33}SO$. [e] From $C^{18}O/C^{17}O$. [f] From $HDO/H_2^{17}O$ Hot Core. [g] From $HDO/H_2^{17}O$ Compact Ridge. [h] From $H_2^{13}CO/H_2^{12}CS$ CR. [i] From $H_2^{17}O/H_2S$ LVF. [j] Kahane et al. (1988), the envelope of IRC+10216. [k] Blake et al. (1987). [l] Ho & Townes (1983). [m] Penzias (1981a). [n] Wilson & Rood (1994) and references therein, local ISM. [o] Chin et al. (1996), towards Orion KL. [p] Bensch et al. (2001), towards ρ Ophiuchi Molecular Cloud. [q] Penzias (1981b), towards Orion A. [r] Savage et al. (2002), towards Orion A using CN and ^{13}CN. [s] Wouterloot et al. (2005), towards ρ Ophiuchi Molecular Cloud, value from LTE column densities. [t] Olofsson (2003), from $S^{18}O$ observations of molecular cloud cores. [u] Neufeld et al. (2006). [v] Standard abundances, Grevesse et al. (1996).

Table 7. H_2O and isotopologue parameters and derived column densities.

Species	Comp[a]	υ_{LSR} [km s^{-1}]	$\Delta\upsilon$ [km s^{-1}]	T_A^* [K]	T_k [K]	Size ["]	N^b	τ cm^{-2}]	$N^c_{\tau\,corr}$ cm^{-2}]	N^d_{ISO} [cm^{-2}]
o-$H_2^{16}O$	Total				72	(15)[e]		$\sim 1100^f$		1.7×10^{18}
	CR				115	(6)[e]		$\sim 860^f$		5.6×10^{17}
	LVF				72	(15)[e]		$\sim 1900^f$		8.7×10^{17}
	HVF	5.3	67.1	2.452	72	70	8.7×10^{14}	$\sim 910^f$	8.0×10^{17}	8.8×10^{17}
p-$H_2^{16}O$	HC	4.4	12.0	0.181	200	10	1.2×10^{19}	0.3^g		
o-$H_2^{17}O$	Total				72	15	8.6×10^{14}	0.9^f	1.3×10^{15}	
	CR	9.9	5.0	0.076	115	6	3.2×10^{14}	0.7^f	4.4×10^{14}	
	LVF	8.7	18.0	0.214	72	15	3.5×10^{14}	1.5^f	6.7×10^{14}	
	HVF	13.4	30.1	0.179	72	15	4.9×10^{14}	0.7^f	6.8×10^{14}	
o-$H_2^{18}O$	Total				72	15	1.4×10^{15}	3.4^f	5.0×10^{15}	5.0×10^{15}
	CR	10.1	5.0	0.145	115	6	6.2×10^{14}	2.6^f	1.8×10^{15}	1.7×10^{15}
	LVF	10.5	18.0	0.275	72	15	4.6×10^{14}	5.9^f	2.7×10^{15}	2.6×10^{15}
	HVF	13.4	33.4	0.298	72	15	9.3×10^{14}	2.8^f	2.8×10^{15}	2.7×10^{15}
HDO	Total				72	15	9.1×10^{15}	$\sim 1.5^g$		
	CR	8.5	4.6	0.459	115	6	1.8×10^{16}	$\sim 3^g$		
	LVF	11.8	18.0	0.273	72	15	4.5×10^{15}	$\sim 0.3^g$		
	HC	2.2	13.4	0.216	200	10	1.5×10^{16}	$\sim 0.5^g$		

[a] Total = the total integrated intensity is used, CR = Compact Ridge, LVF = Low Velocity Flow, HVF = High Velocity Flow, HC = Hot Core.
[b] Corrected for beam-filling.
[c] Corrected for beam-filling, and for optical depth with factor $\tau/(1 - e^{-\tau})$.
[d] Column calculated from isotopologue *o*-$H_2^{17}O$, beam-filling and optical depth corrected.
[e] Size from isotopologues. The full LVF *o*-$H_2^{16}O$ emission may have a larger extent.
[f] Calculated from the ratio of $H_2^{18}O$ and $H_2^{17}O$ column densities.
[g] Calculated with Eq. (15).

Table 8. CO and isotopologue parameters and derived column densities.

Species	Comp[a]	$\upsilon_{\rm LSR}$	$\Delta\upsilon$	$T_{\rm A}^*$ [K]	$\int T_{\rm A}^* {\rm d}\upsilon$ [K km s^{-1}]	$T_{\rm k}$ [K]	Size [″]	N [cm^{-2}]	τ	$N_{\rm ISO}(\rm C^{17}O)$ [cm^{-2}]	$N_{\rm ISO}(\rm C^{18}O)$	$N_{\rm ISO}(^{13}\rm CO)$
CO	PDR[b]					100	...			1.6×10^{18}	1.5×10^{18}	1.2×10^{18}
	LVF					100	(30)[d]			2.5×10^{19}	2.2×10^{19}	2.3×10^{19}
	HVF					100	(70)[d]					2.2×10^{18}
^{13}CO	N[c]	8.1	4.8	21.6	109.9	100	...	5.7×10^{16}		5.4×10^{16}	4.9×10^{16}	
	LVF	7.8	18.0	2.18	41.6	100	30	3.9×10^{17}		4.2×10^{17}	3.7×10^{17}	
	HVF	6.7	48.7	0.470	24.2	100	70	5.2×10^{16}				
$\rm C^{17}O$	N[c]	8.8	4.2	1.11	4.95	100	...	2.5×10^{15}	0.07			
	LVF	9.9	18.0	0.116	2.21	100	30	2.0×10^{16}	0.1			
$\rm C^{18}O$	N[c]	8.7	4.2	3.81	17.0	100	...	8.9×10^{15}	0.3	9.8×10^{15}		
	LVF	7.8	18.0	0.367	7.00	100	30	6.7×10^{16}	0.3	7.7×10^{16}		
$\rm H_2$	PDR[b]						...			2.0×10^{22}	1.8×10^{22}	1.5×10^{22}
	ER[b]						...			2.0×10^{22}	1.8×10^{22}	1.5×10^{22}
	LVF						(30)[d]			3.2×10^{23}	2.8×10^{23}	2.3×10^{23}
	HVF						(70)[d]					3.9×10^{22}

[a] N = Narrow, LVF = Low Velocity Flow, HVF = High Velocity Flow.
[b] This is half of the column density obtained from the narrow components of the isotopolouges, since CO narrow component only has emission from the PDR, while the isotopologues have ~equal emission from PDR and ER (as discussed in W06).
[c] Consists of approximately equal emission from PDR and ER.
[d] Size from CO isotopologues. The size of the full LVF CO emission is larger than the isotopologues and calculated to be 45″.

Table 9. SO_2 parameters[a].

ν_{ul} [MHz]	$\Delta\nu_p$ [MHz]	$\Delta\nu_g$ [MHz]	Transition $J_{Ka,Kc}$	E_u [K]	A_{ul} [s^{-1}]	T_A^*(peak) [mK]	Ampl. [mK]	Width [km s^{-1}]	$\int T_A^* d\upsilon$ [K km s^{-1}]	Note
491934.7			$7_{4,4}-6_{3,3}$	65.0	9.49e-4					blend HDCO
541750.9	0.9		$14_{3,11}-13_{2,12}$	119.0	6.31e-4	695			15.80	
		0.0					143	5.0		3G: CR
		-0.1					266	18.0		3G: LVF
		3.2					301	34.9		3G: HVF
541810.6			$30_{6,24}-30_{5,25}$	516.7	1.34e-3					weak
543413.5	−2.5	−0.5	$29_{2,28}-28_{1,27}$	401.5	1.64e-3	457	411	25.5	10.70	blend CH_3OH & SO_2
543467.7			$37_{3,35}-37_{2,36}$	664.0	7.77e-4					v blend CH_3OH & SO_2
545318.5	3.5	5.5	$37_{6,32}-37_{5,33}$	736.9	1.43e-3	66	41	17.5	0.72	
545517.3	−0.7	−2.7	$35_{6,30}-35_{5,31}$	669.3	1.42e-3	99	63	16.5	1.07	
546579.8	−1.2	2.8	$19_{3,17}-18_{2,16}$	197.0	7.40e-4	546	488	25.1	12.90	
547802.2	1.2	−1.8	$28_{6,22}-28_{5,23}$	462.2	1.36e-3	160	136	16.8	2.41	
548734.3	−3.7	−2.7	$31_{6,26}-31_{5,27}$	545.3	1.40e-3	102	87	11.3	1.02	
548838.9			$40_{4,36}-39_{5,35}$	808.3	5.52e-4					blend $C^{18}O$
549303.3	3.3	11.3	$10_{4,6}-9_{3,7}$	89.8	1.07e-3	890	857	32.8	29.20	blend CH_3OH, $^{13}CH_3OH$ & ^{34}SO
549566.4	15.4	5.4	$30_{1,29}-29_{2,28}$	427.9	1.73e-3	455	369	24.7	9.38	blend CH_3OCH_3
550946.7			$29_{6,24}-29_{5,25}$	488.9	1.40e-3					blend ^{13}CO
551622.9	−3.1		$38_{2,36}-38_{1,37}$	697.7	7.94e-4	43			0.31	weak
552069.4	−11.6		$34_{1,33}-34_{0,34}$	542.8	4.43e-4					blend $H_2^{17}O$, SO_2
552078.9	−2.1	0.0	$26_{6,20}-26_{5,21}$	411.4	1.37e-3	223	197	17.1	3.33	blend $H_2^{17}O$, SO_2
553164.9	2.9	2.9	$27_{6,22}-27_{5,23}$	436.3	1.39e-3	224	225	22.5		v blend & 3G CH_3OH;
554212.8	7.8	1.8	$31_{1,31}-30_{0,30}$	431.5	2.34e-3	545	490	21.4	10.90	blend CH_3OH
555121.5	−2.5		$24_{6,18}-24_{5,19}$	364.4	1.37e-3	264			4.20	blend $(CH_3)_2O$
555204.1	−6.9		$25_{6,20}-25_{5,21}$	387.4	1-38e-3	223	188	19.9	3.75	
555666.3	0.7	−0.7	$5_{5,1}-4_{4,0}$	75.1	2.18e-3	742	677	28.1	20.00	blend CH_3OCH_3
556959.9			$23_{6,18}-23_{5,19}$	342.2	1.37e-3					blend H_2O
557283.2	−3.8	0.2	$22_{6,16}-22_{5,17}$	321.0	1.36e-3	303	271	22.9	6.72	
558101.2			$15_{9,7}-16_{8,8}$	308.6	1.54e-3					blend SO
558390.9	−1.1	−1.1	$21_{6,16}-21_{5,17}$	300.8	1.35e-3	335	290	20.0	5.55	blend & 3G CH_3OH;
558555.8	4.8	9.2	$16_{3,13}-16_{0,16}$	147.8	3.90e-5	115	80	23.8	1.93	
558812.5	−2.5	2.5	$20_{6,14}-20_{5,15}$	281.4	1.34e-3	327	291	23.7	7.17	
559500.4	−0.6	−0.6	$19_{6,14}-19_{5,15}$	263.0	1.32e-3	352	298	23.1	7.31	
559882.1	−1.9	0.1	$18_{6,12}-18_{5,13}$	245.5	1.31e-3	331	302	21.7	6.59	
560318.9	−1.1	−1.1	$17_{6,12}-17_{5,13}$	229.0	1.29e-3	393	376	18.1		v blend & 2G CH_3OH;
560613.5	−1.5	1.5	$16_{6,10}-16_{5,11}$	213.3	1.27e-3	354	342	23.4	8.52	blend $^{34}SO_2$
560891.0	−3.0		$15_{6,10}-15_{5,11}$	198.6	1.25 e-3	378	325	22.6	7.68	
561094.8	−1.2	−1.2	$14_{6,8}-14_{5,9}$	184.8	1.22e-3	326	304	23.0	7.30	
561265.6	−0.4	1.4	$13_{6,8}-13_{5,9}$	171.9	1.19e-3	467	382	23.2	9.26	blend CH_3OH
561361.4			$21_{3,19}-20_{2,18}$	234.7	8.31e-4	522				blend SO_2
561392.9	0.9		$12_{6,6}-12_{5,7}$	160.0	1.14e-3	436				blend CH_3OH & SO_2
561490.5	0.5		$11_{6,6}-11_{5,7}$	149.0	1.09e-3	383				blend SO_2
561560.3	−1.7		$10_{6,4}-10_{5,5}$	138.8	1.02e-3	402				v blend SO_2
561608.6	−0.4		$9_{6,4}-9_{5,5}$	129.7	9.37e-4	502				v blend SO_2
561639.3	−0.7		$8_{6,2}-8_{5,3}$	121.4	8.18e-3	564				v blend SO_2
561656.7	16.7		$7_{6,2}-7_{5,3}$	114.0	6.50e-4	547				v blend SO_2
561664.2	24.2		$6_{6,0}-6_{5,1}$	107.6	3.99e-4	547				v blend SO_2
567592.7	−1.3		$11_{4,8}-10_{3,37}$	100.0	1.12e-3	822			16.80	
571532.6	−7.4	−1.4	$32_{2,30}-31_{3,29}$	504.3	1.34e-3	465	171	21.3		blend & 2G SO_2;
571553.3	−2.7	0.3	$32_{0,32}-31_{1,31}$	459.0	2.58 e-3	465	343	21.2	11.30	blend & 2 G SO_2;
574587.8	−7.2	−3.2	$23_{3,21}-22_{2,20}$	276.0	9.46e-4	276	248	21.4	5.47	
574807.3	−2.7	3.3	$6_{5,1}-5_{4,2}$	80.7	2.07e-3	478	410	23.4	9.97	blend $^{34}SO_2$
576042.1	−5.9	−4.9	$31_{2,30}-30_{1,29}$	455.6	2.03e-3	200	165	16.0	2.72	
Total No.	49									

[a] ν_{ul} = rest frequency of the transition $u \rightarrow l$; $\Delta\nu_p$ = the difference between freq and the observed frequency at the peak temperature; $\Delta\nu_g$ = the difference between freq and the frequency of the Gaussian fit; Transition = the quantum numbers for the transition; E_u = the upper state energy; A_{ul} = the Einstein A-coefficient; T_A^*(peak) = the observed peak temperature of the transition; Ampl. = the peak temperature of the Gaussian fit; Width = the width of the transition from the Gaussian fit; $\int T_A^* d\upsilon$ = the integrated intensity from the observed spectra; Note: 2G or 3G denotes a two- or three-component Gaussian fit, v blend denotes a visible blend, Total No. = the total number of transitions of the molecule in the table. All these lines are also marked in the spectra shown in Paper I Appendix A, and listed in the online Table of Paper I. These total numbers of lines include not visible blends, which are not counted in Table 5.

Table 10. $^{34}SO_2$ parameters[a].

ν_{ul} [MHz]	Δv_p [MHz]	Δv_g [MHz]	Transition $J_{Ka,Kc}$	E_u [K]	A_{ul} [s^{-1}]	T_A^*(peak) [mK]	Ampl. [mK]	Width [km s^{-1}]	$\int T_A^* dv$ [K km s^{-1}]	Note
542097.7	−0.3	4.7	$11_{6,6}-11_{5,7}$	145.8	9.83e-4		102	16.0		from 3G CH_3OH
542177.4			$10_{6,4}-10_{5,5}$	135.7	9.23e-4					
542233.5			$9_{6,4}-9_{5,5}$	126.5	8.44e-4					weak
542270.1			$8_{6,2}-8_{5,3}$	118.3	7.37e-4					weak
542291.7			$7_{6,2}-7_{5,3}$	110.9	5.86e-4					weak
542302.3			$6_{6,0}-6_{5,1}$	104.5	3.60e-4					weak
547613.5			$21_{3,19}-20_{2,18}$	233.5	7.87e-4					blend $H_2^{18}O$
551767.4			$31_{1,31}-30_{0,30}$	429.7	2.32e-3					blend CH_3OH, weak
554708.2		−6.8	$11_{4,8}-10_{3,7}$	98.5	1.04e-3	141	123	20.1		v blend ^{13}CS; from 2G ^{13}CS
558717.5	2.5	3.5	$6_{5,1}-5_{4,2}$	78.5	1.90e-3	98	83	19.5	1.67	
560590.2			$23_{3,21}-22_{2,20}$	274.7	9.02e-4					blend SO_2
569091.6	−3.4		$32_{0,32}-31_{1,31}$	457.0	2.55e-3	74			0.33	weak
573527.3	2.3		$25_{3,23}-24_{2,22}$	319.5	1.05e-3	92			0.68	weak
574797.9			$12_{4,8}-11_{3,9}$	109.5	1.10e-3					blend SO_2
Total No.	14									

[a] Notation as in Table 9.

Table 11. SO parameters[a].

ν_{ul} [MHz]	Δv_p [MHz]	Δv_g [MHz]	Transition N_J	E_u [K]	A_{ul} [s^{-1}]	T_A^*(peak) [mK]	Ampl. [mK]	Width [km s^{-1}]	$\int T_A^* dv$ [K km s^{-1}]	Note
487708.5	0.5	−1.5	7_7-6_7	71.0	1.70e-5	206	178	13.8	2.67	
558087.7	2.7		$13_{12}-12_{11}$	194.4	2.28e-3	2094			59.00	blend SO_2
		2.7					160	4.7		3G; CR
		0.7					759	18.0		3G; LVF
		2.7					1178	35.5		3G; HVF
559319.8	3.8		$13_{13}-12_{12}$	201.1	2.30e-3	1996			56.90	
		3.8					165	5.0		3G; CR
		−0.2					674	18.0		3G; LVF
		4.8					1163	35.3		3G; HVF
560178.7	2.7		$13_{14}-12_{13}$	192.7	2.32e-3	2168			61.70	
		2.7					213	5.0		3G; CR
		0.7					666	18.0		3G; LVF
		1.7					1285	35.6		3G; HVF
568741.6	9.6	1.6	9_9-8_9	106.1	1.90e-5	105	78	15.9	1.24	
Total No.	5									

[a] Notation as in Table 9.

Table 12. ^{33}SO parameters[a].

ν_{ul} [MHz]	Δv_p [MHz]	Δv_g [MHz]	Transition N_J	E_u [K]	A_{ul} [s^{-1}]	T_A^*(peak) [mK]	Ampl. [mK]	Width [km s^{-1}]	$\int T_A^* dv$ [K km s^{-1}]	Note
552429.8	−2.2	1.8	$12_{13}-11_{12}$	192.5	2.18 e-3	138	112	20.3	2.41	
553681.3	−6.7	−2.7	$13_{13}-12_{12}$	199.2	2.20e-3	113	85	17.0		Blend 2 U-lines & CH_3CN
554555.6	−3.4	−3.4	$14_{13}-13_{12}$	190.8	2.24e-3	110	100	20.5	2.06	
Total No.	3									

[a] Notation as in Table 9.

Table 13. ^{34}SO parameters[a].

ν_{ul} [MHz]	Δv_p [MHz]	Δv_g [MHz]	Transition N_J	E_u [K]	A_{ul} [s^{-1}]	T_A^*(peak) [mK]	Ampl. [mK]	Width [km s^{-1}]	$\int T_A^* d\upsilon$ [K km s^{-1}]	Note
547119.6	−5.4	−2.4	$12_{13}-11_{12}$	190.7	2.15e-3	380	326	27.6	9.35	
548389.8	−2.2	0.8	$13_{13}-12_{12}$	197.4	2.17 e-3	324	304	22.8	7.31	
549278.7			$14_{13}-13_{12}$	189.0	2.19e-3					blend CH_3OH, SO_2 & $^{13}CH_3OH$
561700.4			9_9-9_8	104.3	1.83e-5					blend SO_2 & $C^{17}O$
Total No.	4									

[a] Notation as in Table 9.

Table 14. SiO and isotopologue parameters[a].

Species	ν_{ul} [MHz]	Δv_p [MHz]	Δv_g [MHz]	Transition J	E_u [K]	A_{ul} [s^{-1}]	T_A^*(peak) [mK]	Ampl. [mK]	Width [km s^{-1}]	$\int T_A^* d\upsilon$ [K km s^{-1}]	Note
SiO	564249.2	−2.8		13−12	189.6	9.66e-3	729			17.60	
			2.2					391	18.0		2G; LVF
			−1.8					315	31.5		2G; HVF
^{29}SiO	557184.4	2.4	1.4	13−12	187.2	9.31e-3	82	72	21.2	1.39	blend H_2O
^{30}SiO	550605.2	−9.8	−5.8	13−12	185.0	8.98e-3	71	59	7.5	0.45	?
Total No.	3										

[a] Notation as in Table 9.

Table 15. H_2S parameters[a].

ν_{ul} [MHz]	Δv_p [MHz]	Δv_g [MHz]	Transition J_{K_a,K_c}	E_u [K]	A_{ul} [s^{-1}]	T_A^*(peak) [mK]	Ampl. [mK]	Width [km s^{-1}]	$\int T_A^* d\upsilon$ [K km s^{-1}]	Note
567079.6			$6_{4,2}-6_{3,3}$	540.2	6.52e-4					blend NO
568050.7	−7.3		$3_{3,1}-3_{2,2}$	165.9	3.32e-4	247			4.41	
		−7.3					106	7.5		2G; HC
		−0.3					145	24.4		2G; Plateau
Total No.	2									

[a] Notation as in Table 9.

Table 16. CH_3CN parameters[a].

ν_{ul} [MHz]	$\Delta\nu_p$ [MHz]	$\Delta\nu_g$ [MHz]	Transition J_K	E_u [K]	A_{ul} [s^{-1}]	T_A^*(peak) [mK]	Ampl. [mK]	Width [km s^{-1}]	$\int T_A^* d\upsilon$ [K km s^{-1}]	Note
550671.7			30_9-29_9	984.6	1.34e-2					blend CH_3OH
550850.0	−6.0		30_8-29_8	864.2	1.37e-2					v blend ^{13}CO
551007.4	0.4		30_7-29_7	758.0	1.39e-2					v blend ^{13}CO
551143.9	−5.1	−5.1	30_6-29_6	665.8	1.41e-2	145	125	13.2		v blend NO; from 5G CH_3CN, NO & CH_3OH
551259.6		−8.4	30_5-29_5	587.8	1.43e-2	159	160	10.6		v blend CH_3OCH_3; from 2G CH_3OCH_3
551354.2	−1.8	−4.8	30_4-29_4	524.0	1.45e-2	144	112	9.4	1.09	
551427.9	−1.1	−4.1	30_3-29_3	474.3	1.46e-2	221	198	9.9	1.80	
551480.6	−2.4	−4.4	30_2-29_2	438.8	1.47e-2	210	173	9.0	1.43	
551512.2			30_1-29_1	417.5	1.47e-2					v blend NO
551522.7			30_0-29_0	410.4	1.48e-2					v blend NO
552646.6*	−1.4		30_1-29_1 $\ell=+1$	930.2	1.48e-2					weak
552970.8*	−3.2		30_0-29_0 $\ell=\pm1$	936.7	1.49e-2					weak
553007.8*	−6.2		30_2-29_2 $\ell=-1$	991.9	1.48e-2					weak
553029.1*	−0.9		30_1-29_1 $\ell=-1$	957.2	1.49e-2					weak
553240.3*	−2.7		30_3-29_3 $\ell=+1$	961.1	1.48e-2					weak
553362.2*			30_2-29_2 $\ell=+1$	938.9	1.48e-2					weak & narrow
553707.6				931.8						weak
568999.3	−1.7		31_9-30_9	1011.9	1.49e-2	81				weak
569486.9	−3.1	−5.1	31_6-30_6	693.2	1.57e-2	144	98	7.8	0.77	strange shape
569606.3	−1.7	−3.7	31_5-30_5	615.2	1.58e-2	91	77	3.3	0.25	
569704.0	−6.0	−5.0	31_4-30_4	551.3	1.60e-2	130	124	3.6	0.45	
569780.1	−6.9	−6.9	31_3-30_3	501.6	1.61e-2	241	165	8.4	1.26	
569834.5	−1.5	−3.5	31_2-30_2	466.2	1.62e-2	126	126	5.8	0.71	
569867.1	−4.9	−2.9	31_1-30_1	444.9	1.63e-2	159	151	5.1	0.66	blend CH_3CN
569878.0	−3.0	−2.0	31_0-30_0	437.8	1.63e-2	220	208	5.5	0.95	blend CH_3CN
Total No.	25									

[a] Notation as in Table 9. * Vibrationally excited transition, $v_8 = 1$.

Table 17. NH_3 and $^{15}NH_3$ parameters[a].

Species	ν_{ul} [MHz]	$\Delta\nu_p$ [MHz]	$\Delta\nu_g$ [MHz]	Transition J_K	E_u [K]	A_{ul} [s^{-1}]	T_A^*(peak) [mK]	Ampl. [mK]	Width [km s^{-1}]	$\int T_A^* d\upsilon$ [K km s^{-1}]	Note
NH_3	572498.2	1.2		1_0-0_0	27.5	1.61e-3	2409			20.60	
			1.2					1704	4.9		2G fit; CR
			2.2					694	16.2		2G fit; HC
$^{15}NH_3$	572112.8	–0.2		1_0-0_0	27.5	1.57e-3	167	150	6.7	1.02	
Total No.	2										

[a] Notation as in Table 9.

Table 18. HC_3N parameters[a].

ν_{ul} [MHz]	$\Delta\nu_p$ [MHz]	$\Delta\nu_g$ [MHz]	Transition J	E_u [K]	A_{ul} [s^{-1}]	T_A^*(peak) [mK]	Ampl. [mK]	Width [km s^{-1}]	$\int T_A^* d\upsilon$ [K km s^{-1}]	Note
490955.7	−6.3	−5.3	54–53	648.2	9.50e-3	91	86	6.4	0.53	blend CH_3OH
545417.1	−3.9		60–59	798.7	1.30e-2	70	57	10.3	0.60	
Total No.	2									

[a] Notation as in Table 9.

Table 19. OCS parameters[a].

ν_{ul} [MHz]	$\Delta\nu_p$ [MHz]	$\Delta\nu_g$ [MHz]	Transition J	E_u [K]	A_{ul} [s^{-1}]	T_A^*(peak) [mK]	Ampl. [mK]	Width [km s^{-1}]	$\int T_A^* d\upsilon$ [K km s^{-1}]	Note
546859.8	−3.2		45−44	603.9	4.81e-4	67			0.31	blend SO_2, $^{13}CH_3OH$
558990.5	−4.5	−2.5	46−45	630.7	5.14e-4	88	88	6.5	0.58	
571119.7	−2.3		47−46	658.1	5.49e-4	68			0.41	?
Total No.	3									

[a] Notation as in Table 9.

Table 20. CH_3OH parameters[a].

ν_{ul} [MHz]	$\Delta\nu_p$ [MHz]	$\Delta\nu_g$ [MHz]	Transition J_{K_a,K_c}	E_u [K]	A_{ul} [s^{-1}]	T_A^*(peak) [mK]	Ampl. [mK]	Width [km s^{-1}]	$\int T_A^* d\upsilon$ [K km s^{-1}]	Note
486940.9	0.9		$4_{2,3}-4_{1,4}$ A	60.9	5.45e-4	884			5.13	
		0.9					635	3.8		2G; CR
		−0.1					241	10.1		2G; HC
487531.9	0.9		$10_{1,9}-9_{1,8}$ A	143.3	5.15e-4	855			4.85	
		0.9					509	3.3		2G; CR
		−0.1					359	8.1		2G; HC
488945.5*	−0.5	−1.0	$7_{2,5}-8_{3,5}$ E	429.4	5.79e-4	191	188	5.0	1.01	
489037.0	0.0		$5_{2,4}-5_{1,5}$ A	72.5	5.70e-4	849			4.36	
		0.0					652	3.7		2G; CR
		−2.0					210	8.5		2G; HC
489224.3	0.3	0.3	$23_{1,23}-22_{2,20}$ A	648.5	1.92e-4	74	69	2.9	0.21	
490960.0	−2.0		$21_{3,19}-20_{4,17}$ E	598.5	2.27e-4					blend HC_3N
491550.9	0.1		$6_{2,5}-6_{1,6}$ A	86.4	5.87e-4	821			4.76	
		−0.1					593	3.8		2G; CR
		−1.1					244	9.5		2G; HC
492278.6	0.0		$4_{1,4}-3_{0,3}$ E	37.6	7.65e-4	927	920	4.4	2.58	
542000.9	0.9		$6_{3,4}-5_{2,3}$ A	98.5	7.93e-4	1261			6.89	
		0.9					817	3.2		2G; CR
		0.9					413	9.3		2G; HC
542081.9	−0.1		$6_{3,3}-5_{2,4}$ A	98.5	7.94e-4	1230				
		−0.1					834	3.5		from 3G $^{34}SO_2$; CR
		1.9					350	9.0		from 3G $^{34}SO_2$; HC
542163.0*	−2.0	−4.0	$20_{1,20}-20_{2,19}$	810.4	7.35e-4	91	68	6.0	0.35	
543076.1	0.1		$8_{0,8}-7_{1,7}$ E	96.6	4.54e-4	856			4.75	
		0.1					614	3.8		2G; CR
		−0.9					227	9.9		2G; HC
543457.3*	−2.7		$19_{1,19}-19_{2,18}$ A	764.3	7.49e-4					v blend SO_2
544653.1*	−4.9		$18_{1,18}-18_{2,17}$ A	720.4	7.62e-4	98			0.55	?
544820.5	−0.5	−1.5	$5_{5,1}-6_{4,2}$ E	170.9	2.60e-5	98	91	3.4	0.32	
545034.8	0.8		$26_{3,23}26_{2,24}$ E	862.5	9.00e-4	72			0.31	
545755.6*	−6.4	−4.4	$17_{1,17}-17_{2,16}$ A	678.8	7.75e-4	70	70	5.6	0.50	
546226.8*	−1.2		$11_{3,9}-12_{4,9}$ E	570.1	8.26e-4					v blend CH_3OH
546239.0	−1.0		$17_{2,16}-17_{1,17}$ A	392.5	7.38e-4	212			2.13	blend CH_3OH
547698.9*			$15_{1,15}-15_{2,14}$ A	602.6	7.97e-4					blend $H_2^{18}O$
548548.7*	−1.3		$14_{1,14}-14_{2,13}$ A	568.0	8.07e-4	126			0.63	
		−2.3					64	2.7		2G; CR
		−2.3					61	7.5		2G; HC
549322.8*			$13_{1,13}-13_{2,12}$ A	535.6	8.16e-4					blend SO_2, & $^{13}CH_3OH$
550025.2*	−4.8	−2.8	$12_{1,12}-12_{2,11}$ A	505.6	8.24e-4	166	157	6.9	1.15	
550659.3*	−2.7	−3.7	$11_{1,11}-11_{1,11}$ A	477.9	8.31e-4	168	153	5.9	0.94	blend CH_3CN

[a] Notation as in Table 9. * Vibrationally excited transition, $v_t = 1$.

Table 20. continued.

ν_{ul} [MHz]	$\Delta\nu_p$ [MHz]	$\Delta\nu_g$ [MHz]	Transition J_{K_a,K_c}	E_u [K]	A_{ul} [s^{-1}]	T_A^*(peak) [mK]	Ampl. [mK]	Width [km s^{-1}]	$\int T_A^* d\upsilon$ [K km s^{-1}]	Note
551228.6*	−1.4		$10_{1,10}-10_{2,9}$ A	452.4	8.36e-4	237				blend CH_3OCH_3, NO, & CH_3CN
							90	3.3		5G CH_3CN,
							152	9.4		NO & CH_3OH
551736.2*	−0.8		$9_{1,9}-9_{2,8}$ A	429.3	8.40e-4	248			1.33	
		−0.8					101	2.5		2G; CR
		−1.8					143	8.1		2G; HC
551968.8		−2.2	$6_{6,1}-7_{5,3}$ E	227.5	2.10e-5					v blend $H_2^{17}O$
552184.8*	−1.2		$8_{1,8}-8_{2,7}$ A	408.5	8.41e-4	235			1.46	
		−1.2					94	2.3		2G; CR
		−1.2					144	8.4		2G; HC
552577.2*	−0.8		$7_{1,7}-7_{2,6}$ A	390.0	8.40e-4	293			1.58	
		−0.8					110	2.2		2G; CR
		−0.8					161	7.9		2G; HC
552915.4*	0.4		$6_{1,6}-6_{2,5}$ A	373.8	8.35e-4	263			1.32	
		−0.6					147	3.2		2G; CR
		−0.6					104	7.6		2G; HC
553146.3	0.3		$8_{1,7}-7_{0,7}$ E	104.6	4.63e-4	1036			6.35	blend SO_2
		0.3					640	3.3		from 3G SO_2
		−3.7					228	9.4		from 3G SO_2
553201.6*	−1.4		$5_{1,5}-5_{2,4}$ A	359.9	8.22e-4	319			1.48	
		−0.4					132	1.9		2G; CR
		−1.4					171	7.4		2G; HC
553437.5*	−0.5		$4_{1,4}-4_{2,3}$ A	348.4	7.96e-4	244			1.00	
		−0.5					123	1.6		2G; CR
		−2.5					146	5.3		2G; HC
553570.9	−2.1		$18_{2,17}-18_{1,18}$ A	434.2	7.56e-4	206			1.35	
		−2.1					39	3.0		2G;CR
		−3.1					149	8.0		2G; HC
553624.5*	−1.5		$3_{1,3}-3_{2,2}$ A	339.1	7.40e-4	236			1.20	
		−1.5					128	2.5		2G; CR
		−3.5					116	8.8		2G; HC
553763.7*	−1.3		$2_{1,2}-2_{2,1}$ A	332.2	5.93e-4	179			1.07	
		−1.3					106	3.5		2G; CR
		−3.3					78	8.6		2G; HC
554052.7*	−4.3		$2_{1,1}-2_{2,0}$ A	332.2	5.94e-4	549			3.19	blend CH_3OH
554055.5	−1.5		$12_{1,11}-11_{2,9}$ E	202.1	3.13e-4					blend CH_3OH
554202.9*	−1.1		$3_{1,2}-3_{2,1}$ A	339.2	7.41e-4					v blend SO_2
554402.5*	−1.5		$4_{1,3}-4_{2,2}$ A	348.4	7.99e-4	331			1.30	
		−1.5					209	2.8		2G; CR
		−4.5					106	10.6		2G; HC
554650.9*	−1.1		$5_{1,4}-5_{2,3}$ A	360.0	8.26e-4	231			0.95	
		−0.6					102	2.7		2G; CR
		−2.6					135	6.8		2G; HC
554947.4*	0.4	−1.6	$6_{1,5}-6_{2,4}$ A	373.9	8.41e-4	245	207	5.4	1.19	
555291.1*	−1.9	−2.9	$7_{1,6}-7_{2,5}$ A	390.1	8.48e-4	210	193	6.2	1.21	blend $H_2C^{18}O$
555417.7	−0.3		$8_{3,5}-8_{1,7}$ E	131.3	1.71e-6	49				v blend CH_3OH & U-line
555418.5	0.5		$10_{3,7}-10_{1,9}$ E	175.4	2.66e-6	49				v blend CH_3OH & U-line
555681.0*	−2.0		$8_{1,7}-8_{2,6}$ A	408.7	8.52e-4					v blend SO_2, $H_2C^{18}O$, & CH_3OCH_3
556115.8*	−1.2		$9_{1,8}-9_{2,7}$ A	429.5	8.53e-4	202			1.15	
		0.8					119	2.9		2G; CR
		4.2					121	6.2		2G; HC
556594.4*	−0.6		$10_{1,9}-10_{2,8}$ A	452.7	8.52e-4	223			1.41	blend CH_3OH

Table 20. continued.

ν_{ul} [MHz]	$\Delta\nu_p$ [MHz]	$\Delta\nu_g$ [MHz]	Transition J_{K_a,K_c}	E_u [K]	A_{ul} [s^{-1}]	T_A^*(peak) [mK]	Ampl. [mK]	Width [km s^{-1}]	$\int T_A^* d\upsilon$ [K km s^{-1}]	Note
556603.7	−1.3		$25_{1,25}-24_{2,22}$ A	760.8	2.66e-4					v blend CH_3OH
557115.2*	−0.8	−3.8	$11_{1,10}-11_{2,9}$ A	478.2	8.50e-4	257	250	9.1	2.27	
557147.0*	−4.0		$11_{9,3}-10_{8,2}$ A	836.5	1.40e-3	86	74	7.2	0.26	blend CH_3OH
557147.0*	−4.0		$11_{9,2}-10_{8,3}$ A	836.5	1.40e-3	86	74	7.2	0.26	blend CH_3OH
557676.6*	−0.4		$12_{1,11}-12_{2,10}$ A	506.0	8.46e-4	189			1.01	
		0.6					107	3.5		2G; CR
		−3.4					88	6.9		2G; HC
558004.6*		−2.4	$4_{3,2}-3_{2,2}$ E	440.6	1.95e-4		55	6.4		v blend SO; from 3G SO
558276.8*	−0.2	−1.2	$13_{1,12}-13_{2,11}$ A	536.1	8.42e-4	137	134	5.2	0.71	
558344.5	0.5		$11_{2,9}-10_{1,9}$ E	175.5	5.16e-4	801			4.09	blend SO_2
		0.5					533	3.1		from 3G SO_2
		−2.5					244	10.5		from 3G SO_2
558606.4	0.4		$26_{2,25}-26_{1,26}$ E	843.0	7.47e-4	49				(too) weak
558890.2*	−2.8		$8_{6,2}-9_{5,5}$ A	551.5	8.90e-5	42			0.04	
558890.2*	−2.8		$8_{6,3}-9_{5,4}$ A	551.5	8.90e-5	42			0.04	
558904.6*	−0.4		$16_{5,11}-17_{4,14}$ E	744.1	1.27e-4	64			0.18	
558914.0*	−3.0		$14_{1,13}-14_{2,12}$ A	568.5	8.37e-4	105			0.46	
559586.1*	−2.9	−3.9	$15_{1,14}-15_{2,13}$ A	603.2	8.31e-4	128	116	5.3	0.61	
560291.0*	−9.0	−1.0	$16_{1,15}-16_{2,14}$ A	640.2	8.24e-4		177	9.0		v blend SO_2; from 2G SO_2
561026.4*	0.4		$17_{1,16}-17_{2,15}$ A	679.5	8.17e-4	103	90	4.8	0.46	
561269.1			$19_{2,18}-19_{1,19}$ A	478.2	7.75e-4					blend SO_2
561402.9			$18_{7,12}-19_{6,4}$ E	646.3	2.25e-4					blend SO_2
561789.7*	0.7	−2.3	$18_{1,17}-18_{2,16}$ A	721.2	8.09e-4	64	59	5.9	0.33	
564221.6			$21_{1,20}-21_{2,19}$ A	606.0	7.81e-4					v blend SiO
564759.8	−1.2	−2.2	$17_{2,16}-16_{3,13}$ A	392.5	3.52e-4	170	164	5.6	0.93	
567942.6	−3.4	−2.4	$20_{1,19}-19_{2,18}$ A	505.4	5.28e-4	163	163	6.1	1.02	
568566.1	−0.9		$3_{2,2}-2_{1,2}$ E	39.8	1.00e-3	965			5.32	
		0.1					761	3.9		2G; CR
		−2.9					233	9.0		2G; HC
568783.6	−0.4		$17_{0,17}-16_{1,16}$ A	354.5	1.10e-3	367			1.91	
		0.6					107	2.2		2G; CR
		−0.4					255	6.5		2G; HC
569324.5	−4.5	−3.5	$20_{2,19}-20_{1,20}$ A	524.4	7.95e-4	124	125	6.1	0.78	
570261.5	−1.5		$12_{5,8}-13_{4,9}$ A	318.9	2.31e-4	310			0.95	blend CH_3OH
		−2.5					123	2.8		2G; CR
		−3.5					199	7.2		2G; HC
570264.0	1.0	−3.5	$12_{5,7}-13_{4,10}$ A	318.9	2.31e-4	310	289	5.9	0.95	blend CH_3OH
570619.0	−1.0		$8_{4,4}-9_{3,6}$ E	179.5	2.02e-4	327			1.86	blend $^{13}CH_3OH$
		−1.0					216	2.4		2G; CR
		−4.0					143	8.5		2G; HC
572676.2	−1.8	−1.8	$14_{1,13}-13_{2,12}$ E	264.8	1.70e-5	95	76	3.3	0.26	weak
572898.8	−1.2		$15_{1,15}-14_{0,14}$ E	283.61	8.61e-4	493			2.99	
		0.8					242	3.6		2G; CR
		−1.2					236	8.6		2G; HC
573471.1	−1.9		$3_{3,1}-4_{2,3}$ E	76.6	7.30e-5	297	282	4.1	1.31	
573912.7	−2.3		$17_{2,15}-16_{3,14}$ A	392.9	3.84e-4	197			1.08	
		−2.3					86	2.5		2G; CR
		−4.3					125	6.7		2G; HC
574868.5	−2.5		$12_{1,12}-11_{1,11}$ A	193.9	8.53e-4	575			2.97	
		−2.5					325	3.1		2G; CR
		−3.5					260	7.0		2G; HC
575547.2*	−3.8	−3.8	$8_{0,8}-7_{1,7}$ E	383.9	4.15e-4	132	120	3.7	0.47	
Total No.	82									

Table 21. $^{13}CH_3OH$ parameters[a].

ν_{ul} [MHz]	$\Delta\nu_p$ [MHz]	$\Delta\nu_g$ [MHz]	Transition $J_{Ka,Kc}$	E_u [K]	A_{ul} [s^{-1}]	T_A^*(peak) [mK]	Ampl. [mK]	Width [km s^{-1}]	$\int T_A^* d\upsilon$ [K km s^{-1}]	Note
488153.5	−1.5	−0.5	$4_{1,4}-3_{0,3}$ A	37.0	7.46e-4	204	205	4.9	1.04	
488302.6	0.6	−0.4	$4_{2,3}-4_{2,3}$ A	60.5	5.50e-4	154	151	2.3	0.34	
490299.4	0.4		$5_{2,4}-5_{1,5}$ A	71.8	5.75e-4	168			0.59	
491170.0	0.0	1.0	$5_{3,3}-4_{2,2}$ A	84.0	6.52e-4	155	155	4.4	0.73	
491201.3	0.3	0.3	$5_{3,2}-4_{2,3}$ A	84.0	6.53e-4	156	145	4.2	0.64	
491310.1			$11_{1,10}-10_{2,8}$	170.6	2.15e-4	73			0.34	weak
544140.5*			$17_{1,17}-17_{2,16}$ A	670.5	7.71e-4	63			0.12	
544206.7	−1.3	−0.3	$8_{1,7}-7_{0,7}$	102.6	4.41e-4	93	76	4.9	0.37	
547457.8	−1.2	−2.2	$11_{2,9}-10_{1,9}$	171.9	4.90e-4	90	82	3.9	0.32	
549297.1*			$10_{1,10}-10_{2,9}$ A	449.5	8.29e-4					blend SO_2 & CH_3OH
552835.1*			$6_{1,5}-6_{2,4}$ A	372.9	8.32e-4	48			0.10	weak
555700.1			$15_{1,15}-14_{0,14}$ E	277.0	7.72e-4					blend SO_2 & CH_3OH
561138.5	−0.5		$12_{1,12}-11_{1,11}$ A	189.7	7.93e-4					v blend SO_2
564223.7	−4.3		$12_{0,12}-11_{0,11}$	189.4	8.10e-4					v blend SiO
565245.2	−1.8	−0.8	$12_{1,12}-11_{1,11}$ E	182.1	8.10e-4	89	72	4.2	0.30	
565527.8	−0.2	−1.2	$12_{0,12}-11_{0,11}$ A	176.6	8.17e-4	133	135	3.5	0.51	
565737.4	1.4	1.4	$12_{8,4}-11_{8,3}$ A	499.3	4.53e-4	68	65	2.0	0.07	too weak?
565737.4	1.4	1.4	$12_{8,5}-11_{8,4}$ A	499.3	4.53e-4	68	65	2.0	0.07	too weak?
565895.0			$12_{2,11}-11_{2,10}$ A	214.4	8.01e-4	85			0.34	?
565914.4	4.4	3.4	$12_{6,7}-11_{6,6}$	356.4	6.11e-4	108	103	3.2	0.32	
565946.2	−1.8	0.2	$12_{6,6}-11_{6,5}$ A	371.3	6.13e-4	68	51	4.7	0.23	
566411.9	−0.1		$12_{3,9}-11_{3,8}$	224.7	7.70e-4	110			0.48	blend U-line?
566662.8	−0.2	−1.2	$3_{2,2}-2_{1,2}$ E	39.6	9.96e-4	115	108	3.2	0.35	
566840.7	1.7		$12_{2,10}-11_{2,9}$	199.1	7.92e-4	69			0.30	
570624.2	−2.8		$12_{1,11}-11_{1,10}$ A	192.7	8.35e-4	140				v blend CH_3OH
Total No.	25									

[a] Notation as in Table 9. * Vibrationally excited transition, $v_t = 1$.

Table 22. $(CH_3)_2O$ parameters[a].

ν_{ul} [MHz]	$\Delta\nu_p$ [MHz]	$\Delta\nu_g$ [MHz]	Transition $J_{Ka,Kc}$	E_u [K]	A_{ul} [s^{-1}]	T_A^*(peak) [mK]	Ampl. [mK]	Width [km s^{-1}]	$\int T_A^* d\upsilon$ [K km s^{-1}]	Note
490795.3	−4.7		$15_{4,11}-14_{3,12}$ AE	131.9	3.56e-4	194			2.05	blend 3 groups
490795.3			$15_{4,11}-14_{3,12}$ EA	131.9	3.56e-4					
490797.5			$12_{5,8}-11_{4,7}$ EA	106.2	2.26e-4					
490798.3			$15_{4,11}-14_{3,12}$ EE	131.9	3.56e-4					
490801.3			$15_{4,11}-14_{3,12}$ AA	131.9	3.56e-4					
490804.3			$12_{5,8}-11_{4,7}$ AE	106.2	4.84e-4					
490804.7			$12_{5,8}-11_{4,7}$ EE	106.2	3.01e-4					
490810.3			$12_{5,8}-11_{4,7}$ AA	106.2	4.84e-4					
490811.4			$12_{5,7}-11_{4,7}$ EA	106.2	2.58e-4					
490812.1			$12_{5,7}-11_{4,7}$ EE	106.2	1.82e-4					
490864.4			$12_{5,8}-11_{4,8}$ EA	106.2	2.58e-4					
490869.8			$12_{5,8}-11_{4,8}$ EE	106.2	1.82e-4				0.88	blend 2 groups
490871.5			$12_{5,7}-11_{4,8}$ AE	106.2	4.84e-4					
490877.2			$12_{5,7}-11_{4,8}$ EE	106.2	3.01e-4					
490877.6			$12_{5,7}-11_{4,8}$ AA	106.2	4.84e-4					
490878.3			$12_{5,7}-11_{4,8}$ EA	106.2	2.26e-4					
542257.7	−1.3	−3.3	$19_{4,16}-18_{3,15}$ AE	195.8	4.30e-4	112	111	4.8	0.48	entire group
542257.7	−1.3	−3.3	$19_{4,16}-18_{3,15}$ EA							
542260.1	1.1	−0.9	$19_{4,16}-18_{3,15}$ EE							
542262.4	3.4	1.4	$19_{4,16}-18_{3,15}$ AA							

[a] Notation as in Table 9.

Table 22. continued.

ν_{ul} [MHz]	$\Delta\nu_p$ [MHz]	$\Delta\nu_g$ [MHz]	Transition J_{K_a,K_c}	E_u [K]	A_{ul} [s^{-1}]	T_A^*(peak) [mK]	Ampl. [mK]	Width [km s^{-1}]	$\int T_A^* d\upsilon$ [K km s^{-1}]	Note
543753.9	−5.1		$18_{3,15}-17_{2,16}$ AE	169.8	1.94e-4	45			0.20	entire group
543753.9	−5.1		$18_{3,15}-17_{2,16}$ EA							
543756.9	−2.1		$18_{3,15}-17_{2,16}$ EE							
543759.8	0.8		$18_{3,15}-17_{2,16}$ AA							
546827.8	−4.2	−3.2	$15_{5,11}-14_{4,10}$ EA	144.4	5.50e-4	116	119	3.5	0.60	entire group
546829.2	−2.8	−1.8	$15_{5,11}-14_{4,10}$ AE							
546831.5	−0.5	0.5	$15_{5,11}-14_{4,10}$ EE							
546834.5	2.5	3.5	$15_{5,11}-14_{4,10}$ AA							
547284.8	−2.2	−3.2	$15_{5,10}-14_{4,11}$ AE	144.4	5.90e-4	187	170	3.1	0.56	entire group
547286.2	−0.8	−1.8	$15_{5,10}-14_{4,11}$ EA		5.59e-4					
547287.8	0.8	−0.2	$15_{5,10}-14_{4,11}$ EE		5.82e-4					
547290.1	3.1	2.1	$15_{5,10}-14_{4,11}$ AA		5.90e-4					
549504.7	−3.3		$30_{1,29}-29_{2,28}$ EA	420.3	1.16e-4	82			0.39	entire group
549504.7	−3.3		$30_{1,29}-29_{2,28}$ AE							
549504.9	−3.1		$30_{1,29}-29_{2,28}$ EE							
549505.2	−2.8		$30_{1,29}-29_{2,28}$ AA							
549543.8			$12_{66}-11_{56}$ EA	121.6	7.76e-4					2 groups bl SO_2
549546.5			$12_{67}-11_{56}$ AE							
549547.4			$12_{66}-11_{56}$ EE							
549547.7			$12_{66}-11_{57}$ AE							
549550.4			$12_{67}-11_{57}$ EA							
549550.6			$12_{67}-11_{56}$ AA							
549550.8			$12_{67}-11_{57}$ EE							
549551.7	0.7		$12_{66}-11_{57}$ AA							
551270.8	−6.2	−6.2	$9_{7,3}-8_{6,2}$ EA	109.8	1.09e-4	383	312	4.3		blend CH_3CN; 2G CH_3CN
551273.6	−3.4	−3.4	$9_{7,3}-8_{6,2}$ EE							
551275.1	−1.9	−1.9	$9_{7,2}-8_{6,3}$ AE							
551275.1	−1.9	−1.9	$9_{7,3}-8_{6,2}$ AE							
551276.5	−0.5	−0.5	$9_{7,3}-8_{6,2}$ AA							
551276.5	−0.5	−0.5	$9_{7,2}-8_{6,3}$ AA							
551277.9	0.9	0.9	$9_{7,2}-8_{6,3}$ EE							
551279.4	2.4	2.4	$9_{7,2}-8_{6,3}$ EA							
552258.9	−3.1		$18_{4,14}-17_{3,15}$ EA	178.6	4.35e-4	112			0.67	entire group
552258.9	−3.1		$18_{4,14}-17_{3,15}$ AE							
552261.4	−0.6		$18_{4,14}-17_{3,15}$ EE							
552264.0	2.0		$18_{4,14}-17_{3,15}$ AA							
554619.8	−5.2		$25_{10,15}-25_{9,16}$ AA	436.3	7.47e-4	64			0.13	entire group
554619.8	−5.2		$25_{10,16}-25_{9,17}$ AA							
554621.0	-4.0		$25_{10,16}-25_{9,17}$ EE							
554621.5	−3.5		$25_{10,15}-25_{9,16}$ EE							
554622.1	−2.9		$25_{10,16}-25_{9,17}$ EA							
554622.6	−2.4		$25_{10,15}-25_{9,16}$ AE							
554622.6	−2.4		$25_{10,16}-25_{9,17}$ AE							
554623.2	−1.7		$25_{10,15}-25_{9,16}$ EA							
554811.5	−2.5		$24_{10,14}-24_{9,15}$ AA	413.5	7.36e-4	60		2.2	0.12	entire group
554811.5	−2.5		$24_{10,15}-24_{9,16}$ AA							
554812.7	−1.3		$24_{10,15}-24_{9,16}$ EE							
554813.4	−0.6		$24_{10,14}-24_{9,15}$ EE							
554813.9	−0.1		$24_{10,15}-24_{9,16}$ EA							
554814.6	0.6		$24_{10,14}-24_{9,15}$ AE							
554814.6	0.6		$24_{10,15}-24_{9,16}$ AE							
554815.3	1.3		$24_{10,14}-24_{9,15}$ EA							
554888.3	−2.7		$20_{4,17}-19_{3,16}$ EA	214.1	4.50e-4	118			0.32	entire group
554888.3	−2.7		$20_{4,17}-19_{3,16}$ AE							
554890.4	−0.6		$20_{4,17}-19_{3,16}$ EE							
554892.5	1.5		$20_{4,17}-19_{3,16}$ AA							

Table 22. continued.

ν_{ul} [MHz]	$\Delta\nu_p$ [MHz]	$\Delta\nu_g$ [MHz]	Transition $J_{Ka,Kc}$	E_u [K]	A_{ul} [s^{-1}]	T_A^*(peak) [mK]	Ampl. [mK]	Width [km s^{-1}]	$\int T_A^* d\upsilon$ [K km s^{-1}]	Note
554979.1	−4.9		$23_{10,13}-23_{9,14}$ AA	391.7	7.23e-4	90			0.21	entire group
554979.1	−4.9		$23_{10,14}-23_{9,15}$ AA							
554980.4	−3.6		$23_{10,14}-23_{9,15}$ EE							
554981.2	−2.8		$23_{10,13}-23_{9,14}$ EE							
554981.7	−2.3		$23_{10,14}-23_{9,15}$ EA							
554982.5	−1.5		$23_{10,13}-23_{9,14}$ AE							
554982.5	−1.5		$23_{10,14}-23_{9,15}$ AE							
554983.3	−0.7		$23_{10,13}-23_{9,14}$ EA							
555124.5			$22_{10,12}-22_{9,13}$ AA	370.7	7.08e-4					entire group
555124.5			$22_{10,13}-22_{9,14}$ AA							bl SO_2
555125.9			$22_{10,13}-22_{9,14}$ EE							
555126.8			$22_{10,12}-22_{9,13}$ EE							
555127.3			$22_{10,13}-22_{9,14}$ EA							
555128.2			$22_{10,12}-22_{9,13}$ AE							
555128.2			$22_{10,13}-22_{9,14}$ AE							
555129.1			$22_{10,12}-22_{9,13}$ EA							
555249.8	−11.2	−9.2	$21_{10,11}-21_{9,12}$ AA	350.7	6.92e-4	129	104	8.2	0.82	entire group
555249.8	−11.2	−9.2	$21_{10,12}-21_{9,13}$ AA							
555251.3	−9.7	−7.7	$21_{10,12}-21_{9,13}$ EE							
555252.3	−8.7	−6.7	$21_{10,11}-21_{9,12}$ EE							
555252.7	−8.3	−6.3	$21_{10,12}-21_{9,13}$ EA							
555253.8	−7.2	−5.2	$21_{10,12}-21_{9,13}$ AE							
555253.8	−7.2	−5.2	$21_{10,11}-21_{9,12}$ AE							
555254.9	−6.1	−4.1	$21_{10,11}-21_{9,12}$ EA							
555356.8	−6.2	−6.2	$20_{10,10}-20_{9,11}$ AA	331.6	6.73e-4	75	71	4.9	0.37	entire group
555356.8	−6.2	−6.2	$20_{10,11}-20_{9,12}$ AA							
555358.3	−4.7	−4.7	$20_{10,11}-20_{9,12}$ EE							
555359.5	−3.5	−3.5	$20_{10,10}-20_{9,11}$ EE							
555359.9	−3.1	−3.1	$20_{10,11}-20_{9,12}$ EA							
555361.1	−1.9	−1.9	$20_{10,10}-20_{9,11}$ AE							
555361.1	−1.9	−1.9	$20_{10,11}-20_{9,12}$ AE							
555362.3	−0.7	−0.7	$20_{10,10}-20_{9,11}$ EA							
555447.3	−3.7	−5.7	$19_{10,9}-19_{9,10}$ AA	313.4	6.52e-4	104		5.1	0.39	entire group
555447.3	−3.7	−5.7	$19_{10,10}-19_{9,11}$ AA							
555448.9	−2.1	−4.1	$19_{10,10}-19_{9,11}$ EE							
555450.2	−0.8	−2.8	$19_{10,9}-19_{9,10}$ EE							
555450.6	−0.4	−2.4	$19_{10,10}-19_{9,11}$ EA							
555451.9	0.9	−1.1	$19_{10,9}-19_{9,10}$ AE							
555451.9	0.9	−1.1	$19_{10,10}-19_{9,11}$ AE							
555453.1	2.1	0.1	$19_{10,9}-19_{9,10}$ EA							
555522.9	−4.1	−6.1	$18_{10,8}-18_{9,9}$ AA	296.1	6.28e-4	110			0.51	entire group
555522.9	−4.1	−6.1	$18_{10,9}-18_{9,10}$ AA							
555524.6	−2.6	−4.6	$18_{10,9}-18_{9,10}$ EE							
555526.0	−1.0	−3.0	$18_{10,8}-18_{9,9}$ EE							
555526.4	−0.6	−2.6	$18_{10,9}-18_{9,10}$ EA							
555527.8	0.8	1.2	$18_{10,8}-18_{9,9}$ AE							
555527.8	0.8	1.2	$18_{10,9}-18_{9,10}$ AE							
555529.2	2.2	0.2	$18_{10,8}-18_{9,9}$ EA							
555585.3	−5.7	−5.7	$17_{10,7}-17_{9,8}$ AA	279.7	5.99e-4	83		4.2	0.35	entire group
555585.3	−5.7	−5.7	$17_{10,8}-17_{9,9}$ AA							
555587.1	−3.9	−3.9	$17_{10,8}-7_{9,9}$ EE							
555588.6	−2.4	−2.4	$17_{10,7}-17_{9,8}$ EE							
555589.0	−2.0	−2.0	$17_{10,8}-17_{9,9}$ EA							
555590.4	−0.6	−0.6	$17_{10,7}-17_{9,8}$ AE							
555590.4	−0.6	−0.6	$17_{10,8}-17_{9,9}$ AE							
555591.9	0.9	0.9	$17_{10,7}-17_{9,8}$ EA							

Table 22. continued.

ν_{ul} [MHz]	$\Delta\nu_p$ [MHz]	$\Delta\nu_g$ [MHz]	Transition J_{K_a,K_c}	E_u [K]	A_{ul} [s^{-1}]	T_A^*(peak) [mK]	Ampl. [mK]	Width [km s^{-1}]	$\int T_A^* d\upsilon$ [K km s^{-1}]	Note
555635.9			$16_{10,6}-16_{9,7}$ AA	264.2	5.66e-4					blend SO_2
555635.9			$16_{10,7}-16_{9,8}$ AA							
555637.9			$16_{10,7}-16_{9,8}$ EE							
555639.4			$16_{10,6}-16_{9,7}$ EE							
555639.8			$16_{10,7}-16_{9,8}$ EA							
555641.4			$16_{10,6}-16_{9,7}$ AE							
555641.4			$16_{10,7}-16_{9,8}$ AE							
555642.9			$16_{10,6}-16_{9,7}$ EA							
555676.3			$15_{10,5}-15_{9,6}$ AA	249.7	5.27e-4					blend SO_2, CH_3OH
555676.3			$15_{10,6}-15_{9,7}$ AA							
555678.3			$15_{10,6}-15_{9,7}$ EE							
555679.9			$15_{10,5}-15_{9,6}$ EE							
555680.3			$15_{10,6}-15_{9,7}$ EA							
555681.9			$15_{10,5}-15_{9,6}$ AE							
555681.9			$15_{10,6}-15_{9,7}$ AE							
555683.6			$15_{10,5}-15_{9,6}$ EA							
555707.6			$14_{10,4}-14_{9,5}$ AA	236.0	4.80e-4					blend SO_2
555707.6			$14_{10,5}-14_{9,6}$ AA							
555709.7			$14_{10,5}-14_{9,6}$ EE							
555711.4			$14_{10,4}-14_{9,5}$ EE							
555711.8			$14_{10,5}-14_{9,6}$ EA							
555713.5			$14_{10,4}-14_{9,5}$ AE							
555713.5			$14_{10,5}-14_{9,6}$ AE							
555715.2			$14_{10,4}-14_{9,5}$ EA							
555731.2	−4.8	−6.8	$13_{10,3}-13_{9,4}$ AA	223.3	4.23e-4	96		6.2	0.61	entire group
555731.2	−4.8	−6.8	$13_{10,4}-13_{9,5}$ AA							
555733.4	−2.6	−4.6	$13_{10,4}-13_{9,5}$ EE							
555735.2	−0.8	−2.8	$13_{10,3}-13_{9,4}$ EE							
555735.5	−0.5	−2.5	$13_{10,4}-13_{9,5}$ EA							
555737.3	1.3	−0.7	$13_{10,3}-13_{9,4}$ AE							
555737.3	1.3	−0.7	$13_{10,4}-13_{9,5}$ AE							
555739.1	3.1	1.1	$13_{10,3}-13_{9,4}$ EA							
555748.2			$12_{10,2}-12_{9,3}$ AA	211.5	3.53e-4					blend 3 groups
555748.2			$12_{10,3}-12_{9,4}$ AA							
555750.5			$12_{10,3}-12_{9,4}$ EE							
555752.3			$12_{10,2}-12_{9,3}$ EE							
555752.7			$12_{10,3}-12_{9,4}$ EA							
555754.6			$12_{10,2}-12_{9,3}$ AE							
555754.6			$12_{10,3}-12_{9,4}$ AE							
555756.4			$12_{10,2}-12_{9,3}$ EA							
555759.7			$11_{10,1}-11_{9,2}$ AA	200.6	2.64e-4					blend 3 groups
555759.7			$11_{10,2}-11_{9,3}$ AA							
555762.1			$11_{10,2}-11_{9,3}$ EE							
555764.0			$11_{10,1}-11_{9,2}$ EE							
555764.4			$11_{10,2}-11_{9,3}$ EA							
555766.3			$11_{10,1}-11_{9,2}$ AE							
555766.3			$11_{10,2}-11_{9,3}$ AE							
555766.8			$10_{10,0}-10_{9,1}$ AA	190.5	1.50e-4					blend 3 groups
555766.8			$10_{10,1}-10_{9,2}$ AA							
555768.2			$11_{10,1}-11_{9,2}$ EA	200.6	2.64e-4					
555769.2			$10_{10,1}-10_{9,2}$ EE	190.5	1.50 e-4					blend 3 groups
555771.2			$10_{10,0}-10_{9,1}$ EE							
555771.6			$10_{10,1}-10_{9,2}$ EA							
555773.5			$10_{10,0}-10_{9,1}$ AE							
555773.5			$10_{10,1}-10_{9,2}$ AE							
555775.5			$10_{10,0}-10_{9,1}$ EA							

Table 22. continued.

ν_{ul} [MHz]	$\Delta\nu_p$ [MHz]	$\Delta\nu_g$ [MHz]	Transition J_{K_a,K_c}	E_u [K]	A_{ul} [s^{-1}]	T_A^*(peak) [mK]	Ampl. [mK]	Width [km s^{-1}]	$\int T_A^* d\upsilon$ [K km s^{-1}]	Note
556179.4	−1.6	−0.6	$31_{0,31}-30_{1,30}$ EA	431.3	1.50e-4	65	60	3.5	0.17	entire group
556179.4	−1.6	−0.6	$31_{0,31}-30_{1,30}$ AE							
556179.4	−1.6	−0.6	$31_{0,31}-30_{1,30}$ EE							
556179.5	−1.5	−0.5	$31_{0,31}-30_{1,30}$ AA							
556212.0			$31_{1,31}-30_{0,30}$ EA							(Too) weak
556212.0			$31_{1,31}-30_{0,30}$ AE							(Too) weak
556212.1			$31_{1,31}-30_{0,30}$ EE							(Too) weak
556212.2			$31_{1,31}-30_{0,30}$ AA							(Too) weak
560648.9			$29_{3,27}-28_{2,26}$ AA	407.3	8.54e-4					v blend SO_2
560648.9			$29_{3,27}-28_{2,26}$ EE							
560649.0			$29_{3,27}-28_{2,26}$ EA							
560649.0			$29_{3,27}-28_{2,26}$ AE							
565262.1	−3.9	−3.9	$16_{5,12}-15_{4,11}$ EA	159.0	6.18e-4	154	120	5.7	0.69	entire group
565262.8	−3.2		$16_{5,12}-15_{4,11}$ AE							
565265.2	−0.8		$16_{5,12}-15_{4,11}$ EE							
565267.9	1.9		$16_{5,12}-15_{4,11}$ AA							
566046.6	−3.4	−4.4	$16_{5,11}-15_{4,12}$ AE	159.0	6.29e-4	204	198	3.4	0.71	entire group
566047.3	−2.7	−3.7	$16_{5,11}-15_{4,12}$ EA							
566049.3	−0.7	−1.7	$16_{5,11}-15_{4,12}$ EE							
566051.7	1.7	0.7	$16_{5,11}-15_{4,12}$ AA							
566606.7	−2.3	−2.3	$21_{4,18}-20_{3,17}$ AE	233.3	4.71e-4	90	73	3.9	0.28	entire group
566606.7	−2.3	−2.3	$21_{4,18}-20_{3,17}$ EA							
566608.5	−0.5	−0.5	$21_{4,18}-20_{3,17}$ EE							
566610.4	1.4	1.4	$21_{4,18}-20_{3,17}$ AA							
568430.6	−7.4		$13_{6,7}-12_{5,7}$ EA	133.4	8.10e-4	331	330	5.1	1.79	entire group
568432.6	−5.4		$13_{6,8}-12_{5,7}$ AE							
568433.9	−4.1		$13_{6,7}-12_{5,7}$ EE		7.85e-4					
568435.3	−2.7		$13_{6,7}-12_{5,8}$ AE		8.19e-4					
568436.3	−1.7		$13_{6,8}-12_{5,7}$ AA							
568437.2	−0.8		$13_{6,8}-12_{5,8}$ EA		8.10e-4					
568437.7	−0.3		$13_{6,8}-12_{5,8}$ EE		7.85e-4					
568439.2	1.2		$13_{6,7}-12_{5,8}$ AA		8.19e-4					
568690.1	−2.9		$31_{2,30}-30_{1,29}$ AE	447.6	1.30e-4	92			0.29	entire group
568690.1			$31_{2,30}-30_{1,29}$ EA							
568690.3	−2.7		$31_{2,30}-30_{1,29}$ EE							
568690.4	−2.6		$31_{2,30}-30_{1,29}$ AA							
570219.1	−5.9		$10_{7,4}-9_{6,3}$ EA	118.9	1.12e-4	351	342	4.3	1.55	entire group
570221.9	−2.9		$10_{7,4}-9_{6,3}$ EE							
570223.3	−1.7		$10_{7,3}-9_{6,4}$ AE							
570223.3	−1.7		$10_{7,4}-9_{6,3}$ AE							
570224.7	−0.3		$10_{7,4}-9_{6,3}$ AA							
570224.7	−0.3		$10_{7,3}-9_{6,4}$ AA							
570226.1	1.1		$10_{7,3}-9_{6,4}$ EE							
570227.5	2.5		$10_{7,3}-9_{6,4}$ EA							
574090.9	−7.1	−6.1	$19_{4,15}-18_{3,16}$ EA	196.0	4.59e-4	92	89	2.8	0.29	entire group
574090.9	−7.1	−6.1	$19_{4,15}-18_{3,16}$ AE							
574093.3	−4.7	−3.7	$19_{4,15}-18_{3,16}$ EE							
574095.7	−2.3	−1.3	$19_{4,15}-18_{3,16}$ AA							
Total No.	236									

Table 23. H_2CO and isotopologue parameters[a].

Species	ν_{ul} [MHz]	Δv_p [MHz]	Δv_g [MHz]	Transition $J_{Ka,Kc}$	E_u [K]	A_{ul} [s^{-1}]	T_A^*(peak) [mK]	Ampl. [mK]	Width [km s^{-1}]	$\int T_A^* dv$ [K km s^{-1}]	Note
H_2CO	491968.4	2.4	1.4	$7_{1,7}-6_{1,6}$	106.3	3.44e-3	2040	1954	5.2	11.30	
	561899.3	1.3		$8_{1,8}-7_{1,7}$	133.3	5.20e-3	1705			16.3	
			1.3					1167	4.9		2G; CR
			−0.7					504	19.0		2G; LVF
	576708.3	−0.7		$8_{0,8}-7_{0,7}$	125.1	5.70e-3	1116			11.30	blend NS
			0.3					742	4.8		2G; CR
			−6.7					392	18.7		2G; LVF
$H_2^{13}CO$	548475.2	0.2	0.2	$8_{1,8}-7_{1,7}$	130.4	4.84e-3	155	135	4.3	0.62	
HDCO	491937.0	2.0	3.0	$8_{1,8}-7_{1,7}$	114.4	3.48e-3	370	360	6.1	2.41	blend U-line?
	552740.9	−0.1	0.9	$9_{1,9}-8_{1,8}$	141.0	4.99e-3	101	88	3.0	0.27	
	565857.5	2.5		$9_{0,9}-8_{0,8}$	137.3	5.40e-3	60			0.19	weak
Total No.	7										

[a] Notation as in Table 9.

Table 24. H_2CS parameters[a].

ν_{ul} [MHz]	Δv_p [MHz]	Δv_g [MHz]	Transition $J_{Ka,Kc}$	E_u [K]	A_{ul} [s^{-1}]	T_A^*(peak) [mK]	Ampl. [mK]	Width [km s^{-1}]	$\int T_A^* dv$ [K km s^{-1}]	Note
487663.4	0.4	0.4	$14_{1,13}-13_{1,12}$	188.8	1.76e-3	172	161	3.7	0.62	
547308.2	−3.8	−2.8	$16_{0,16}-15_{0,15}$	223.7	2.51e-3	77	63	3	0.19	
549402.4	0.4	0.4	$16_{3,14}-15_{3,13}$	342.6	2.45e-3	62	55	1.8	0.15	
549447.5	−1.5		$16_{3,13}-15_{3,12}$	342.6	2.45e-3	98				blend U-line
557123.2	2.2		$16_{1,15}-15_{1,14}$	240.6	2.64e-3					blend CH_3OH; in H_2O wing
574140.0	−2.0	−2.0	$17_{1,17}-16_{1,16}$	261.4	2.90e-3	130	125	2.9	0.38	
Total No.	6									

[a] Notation as in Table 9.

Table 25. CS and ^{13}CS parameters[a].

Species	ν_{ul} [MHz]	Δv_p [MHz]	Δv_g [MHz]	Transition J	E_u [K]	A_{ul} [s^{-1}]	T_A^*(peak) [mK]	Ampl. [mK]	Width [km s^{-1}]	$\int T_A^* dv$ [K km s^{-1}]	Note
CS	489751.1	3.1		10−9	129.3	0.00250	2814			23.4	
			−0.9					424	9.0		HC, 3G fit
			2.1					1730	4.0		ER/CR, 3G fit
			1.1					633	18.0		LVF, 3G fit
^{13}CS	554726.0		−2.0	12−11	173.1	0.00366		88	4.8		v blend, 2G $^{34}SO_2$
Total No.	2										

[a] Notation as in Table 9.

Table 26. NO parameters[a].

ν_{ul} [MHz]	Δv_p [MHz]	Transition $J(F)$	E_u [K]	A_{ul} [s^{-1}]	T_A^*(peak) [mK]	Ampl. [mK]	Width [km s^{-1}]	$\int T_A^* dv$ [K km s^{-1}]	Note
551187.3	−0.7	$^2\Pi_{1/2}$ 5.5(5.5)−4.5(4.5) e	84.2	2.16e-5	540				entire group;
						265	5.4		5G from CH_3CN,
						284	18.6		NO & CH_3OH
551187.5		$^2\Pi_{1/2}$ 5.5(6.5)−4.5(5.5) e	84.1	2.23e-5					
551188.8		$^2\Pi_{1/2}$ 5.5(4.5)−4.5(3.5) e	84.2	2.14e-5					
551531.5	0.5	$^2\Pi_{1/2}$ 5.5(6.5)−4.5(5.5) f	84.3	2.24e-5	644			9.331	entire group;
									blend CH_3CN
551534.0	3.0	$^2\Pi_{1/2}$ 5.5(4.5)−4.5(3.5) f	84.2	2.15e-5					blend CH_3CN, NO
551534.1	3.1	$^2\Pi_{1/2}$ 5.5(5.5)−4.5(4.5) f	84.3	2.16e-5					blend CH_3CN, NO
567064.2	−11.8	$^2\Pi_{3/2}$ 5.5(6.5)−4.5(5.5) e	231.7	2.27e-5	122	97	19.1	1.805	entire group;
567069.6		$^2\Pi_{3/2}$ 5.5(5.5)−4.5(4.5) e	231.7	2.63e-5					blend H_2S
567073.4		$^2\Pi_{3/2}$ 5.5(4.5)−4.5(3.5) e	231.7	1.82e-5					blend H_2S
567077.9		$^2\Pi_{3/2}$ 5.5(6.5)−4.5(5.5) f	231.7	2.27e-5					blend H_2S
567082.7		$^2\Pi_{3/2}$ 5.5(5.5)−4.5(4.5) f	231.7	2.19e-5					blend H_2S
567086.6		$^2\Pi_{3/2}$ 5.5(4.5)−4.5(3.5) f	231.7	2.18e-5					blend H_2S
Total No.	12								

[a] Notation as in Table 9.

Table 27. HNC parameters[a].

ν_{ul} [MHz]	Δv_p [MHz]	Δv_g [MHz]	Transition J	E_u [K]	A_{ul} [s^{-1}]	T_A^*(peak) [mK]	Ampl. [mK]	Width [km s^{-1}]	$\int T_A^* dv$ [K km s^{-1}]	Note
543897.6	1.6		6−5	91.4	8.04e-3	913			10.70	v blend U-line
		1.6					600	3.8		ER; from 4G U-line
		−4.4					171	9.3		HC; from 4G U-line
		−1.4					224	26.8		Plateau; from 4G U-line
Total No.	1									

[a] Notation as in Table 9.

Table 28. CN parameters[a].

ν_{ul} [MHz]	Δv_p [MHz]	Δv_g [MHz]	Transition $N(J, F)$	E_u [K]	A_{ul} [s^{-1}]	T_A^*(peak) [mK]	Ampl. [mK]	Width [km s^{-1}]	$\int T_A^* dv$ [K km s^{-1}]	Note
566729.9	1.9	0.9	5(4.5, 5.5)–4(3.5, 4.5)	54.4	1.98e-3	690			3.345	entire group;
							570	3.5		2G; PDR/ER
							122	10.0		2G; HC
566730.7			5(4.5, 3.5)–4(3.5, 2.5)	54.4	1.86e-3					blend CN
566730.8			5(4.5, 4.5)–4(3.5, 3.5)	54.4	1.88e-3					blend CN
566946.8	1.8		5(5.5, 5.5)–4(4.5, 4.5)	54.4	1.96e-3	965			5.15	entire group;
										blend CN
		1.8	5(5.5, 5.5)–4(4.5, 4.5)	54.4	1.96e-3		736	3.8		3G CN; PDR/ER
		0.8	5(5.5, 5.5)–4(4.5, 4.5)	54.4	1.96e-3		214	10.8		v blends; HC
566946.9			5(5.5, 6.5)–4(4.5, 5.5)	54.4	2.03e-3					blend CN
566947.2			5(5.5, 4.5)–4(4.5, 3.5)	54.4	1.95e-3					blend CN
566962.0	1.0	0.0	5(5.5,4.5)–4(4.5,4.5)	54.4	8.00e-5		100	2		entire group;
										3G CN
566963.7			5(5.5,5.5)–4(4.5,5.5)	54.4	6.7e-5					
Total No.	8									

[a] Notation as in Table 9.

Table 29. N_2H^+ parameters[a].

ν_{ul} [MHz]	Δv_p [MHz]	Δv_g [MHz]	Transition J	E_u [K]	A_{ul} [s^{-1}]	T_A^*(peak) [mK]	Ampl. [mK]	Width [km s^{-1}]	$\int T_A^* dv$ [K km s^{-1}]	Note
558966.6	4.6	1.6	6−5	93.9	1.08e-2	315	300	4.8	1.46	
Total No.	1									

[a] Notation as in Table 9.

Table 30. HCS^+ parameters[a].

ν_{ul} [MHz]	$\Delta\nu_p$ [MHz]	$\Delta\nu_g$ [MHz]	Transition J	E_u [K]	A_{ul} [s^{-1}]	T_A^*(peak) [mK]	Ampl. [mK]	Width [km s^{-1}]	$\int T_A^* d\upsilon$ [K km s^{-1}]	Note
554576.6			13−12	186.3	3.66e-3		57	3.4		v blend ^{33}SO
										2G ^{33}SO
Total No.	1									

[a] Notation as in Table 9.

Table 31. NS parameters[a].

ν_{ul} [MHz]	$\Delta\nu_p$ [MHz]	$\Delta\nu_g$ [MHz]	Transition J	E_u [K]	A_{ul} [s^{-1}]	T_A^*(peak) [mK]	Ampl. [mK]	Width [km s^{-1}]	$\int T_A^* d\upsilon$ [K km s^{-1}]	Note
576720.2			$^2\Pi_{1/2}$ 12.5−11.5	187.36						v blend H_2CO
Total No.	1									

[a] Notation as in Table 9.

Table 32. CO and C parameters[a].

Species	ν_{ul} [MHz]	$\Delta\nu_p$ [MHz]	$\Delta\nu_g$ [MHz]	Transition J	E_u [K]	A_{ul} [s^{-1}]	T_A^*(peak) [mK]	Ampl. [mK]	Width [km s^{-1}]	$\int T_A^* d\upsilon$ [K km s^{-1}]	Note
CO	576267.9	−0.1		5−4	83.0	1.22e-5	62200			785.50	
^{13}CO	550926.3	0.3		5−4	79.3	1.10e-5	24300			174.30	
			0.3					21600	4.8		3G; N
			−0.7					2180	18.0		3G; LVF
			−0.7					470	48.7		3G;HVF
$C^{17}O$	561712.8	1.8	1.8	5−4	80.9	1.14e-5	1169			6.03	blend
											^{34}SO, SO_2
			1.8					1070	4.2		3G; N
			3.8					116	18.0		3G; LVF
$C^{18}O$	548831.0	2.0		5−4	79.0	1.06e-5	4219			24.30	
			1.0					3810	4.2		3G; N
			0.0					367	18.0		3G; LVF
C	492160.7			1−0	23.6	7.99e-8	7800	7794	4.5	38.7	
Total No.	5										

[a] Notation as in Table 9.

Table 33. Water parameters[a].

Species	ν_{ul} [MHz]	$\Delta\nu_p$ [MHz]	$\Delta\nu_g$ [MHz]	Transition J_{K_a,K_c}	E_u [K]	A_{ul} [s^{-1}]	T_A^*(peak) [mK]	Ampl. [mK]	Width [km s^{-1}]	$\int T_A^* d\upsilon$ [K km s^{-1}]	Note
$o-H_2O$	556936.0	−7.0		$1_{1,0}-1_{0,1}$	61.0	3.46e-3	7600			320.30	
$p-H_2O$	488491.1	−0.9	−5.9	$6_{2,4}-7_{1,7}$	867.3	1.22e-5	196	181	12.0	2.24	
$o-H_2^{17}O$	552021.0	2.0		$1_{1,0}-1_{0,1}$	60.7	3.37e-3	464			9.44	blend SO_2
											&CH_3OH
			4.0					76	5.0		3G; CR
			1.0					214	18.0		3G; LVF
			10.0					179	30.1		3G; HVF
$o-H_2^{18}O$	489054.3	−6.7	−7.7	$4_{2,3}-3_{3,0}$	429	8.84e-6	83	58	5.7	0.33	?
	547676.4	3.4		$1_{1,0}-1_{0,1}$	60.5	3.29e-3	715			15.90	blend $^{34}SO_2$
											& CH_3OH
			4.4					145	5.0		3G; CR
			4.4					275	18.0		3G; LVF
			11.4					298	33.4		3G; HVF
HDO	490596.7	−0.3		$2_{0,2}-1_{1,1}$	66.4	5.25e-4	841			10.70	
			0.7					459	4.6		3G; CR
			6.7					273	18.0		3G; LVF
			−11.3					216	13.4		3G; LVF
Total No.	6										

[a] Notation as in Table 9.

Table 34. U-line parameters[a].

ν_{ul} [MHz]	T_A^*(peak) [mK]	Ampl. [mK]	Width [km s^{-1}]	$\int T_A^* \, d\upsilon$ [K km s^{-1}]	Note
487 209	91			0.673	SO^+ ?
488 598	94	73	3.4	0.256	CH_3OCHO?
488 633	83	76	4.3	0.313	CH_3CHO?
491 496	104			1.438	CH_3OCHO?
491 892	157			0.64	tripple peaked
541 981	109	87	4.5	0.38	CH_3OCHO?
542 945	140	122	6.7	0.813	
543 873		72	3.9		v blend HNC; from 4G HNC
546 138	50			0.368	ND?
549 449					blend with H_2CS
552 308	64	50	13	0.663	
553 667		62	3.4		blend ^{33}SO, 3G fit with ^{33}SO, CH_3OCHO?
553 716		80	2.4		blend ^{33}SO, 3G fit with ^{33}SO
559 239					v blend SO; CH_3OCHO?
559 861					v blend SO_2, CH_3OCHO?
559 913					v blend SO_2
561 971	57			0.187	
562 960	106	107	5.4	0.593	
563 033	94	79	5.1	0.395	
564 105	111	75	6.2	0.495	
566 066	117	108	2.7	0.306	
567 485	143	133	2	0.278	
569 138	148	135	3.1	0.41	HNCO?
570 303	68	85	2.6	0.158	
572 596	90	84	2.4	0.202	
572 678	95	74	3.1	0.268	
574 184	80	81	2	0.155	
576 446					v blend CO wing
Total No.	28				

[a] Notation as in Table 9.

Table 35. T-line parameters[a].

ν_{ul} [MHz]	T_A^*(peak) [mK]	Ampl. [mK]	Width [km s^{-1}]	$\int T_A^* \, d\upsilon$ [K km s^{-1}]	Note
486 845	80	83	3.3	0.275	SO^+ ?
487 507	70	77	2.7	0.213	CH_3CHO?
488 477	49	47	3.2	0.147	
489 193	107	114	1.7	0.412	
489 709					SiS?; v blend CS
541 926	104	93	2.7	0.292	
544 016	51			0.396	SiS?
546 176	50			0.060	ND?
546 662	67			0.141	
546 805	79	68	2.3	0.213	
547 080					v blend ^{34}SO
547 162					v blend ^{34}SO
547 262	69			0.115	HNCO?
549 142	53			0.217	HNCO?
549 199	43			0.199	HNCO? or H_2CS?
549 719	68	62	3.6	0.278	CH_3OCHO? or SO_2?
550 132	64			0.375	SO_2?
552 846	62			0.131	
555 312	52	46	2.5	0.117	
555 914	63			0.194	
555 933	49			0.124	
556 267	40			0.193	
556 633	52	51	1.9	0.1	
559 816	45			0.060	weak, HDO?
560 753	43			0.212	
562 118	70	60	3.6	0.219	
563 481	96			0.278	weak, HNCO?
564 418	61	36	9.3	0.336	SH^-?
570 335	79	81	1.6	0.112	
570 790	76	69	2.1	0.141	
570 814	72	71	1.7	0.124	
571 151	49			0.138	HNCO?
571 217	59			0.168	HNCO?
571 477	58			0.118	$H_2C^{18}O$?
575 397	69	62	1.8	0.104	
577 160	144	93	6.0	0.503	
Total No.	36				

[a] Notation as in Table 9.

Chapter 5

Introduction to Paper III: Water and ammonia in S140

5.1 The molecular cloud S140

In PDRs and outflows, the requirements of high temperature and density to produce a high gas-phase water abundance are well meet. We have therefore performed observations towards the well-known photon dominated region Sh 2-140, more commonly known as S140. It is located at a distance of 910 pc in the large L1202/L1204 dark cloud, extending over more than $30'$ (8 pc). The PDR is caused by the energetic radiation from the nearby B0.5V star HD 211880, creating a bright HII region and an almost edge-on PDR adjacent to the molecular cloud. Figure 5.1 shows an image in visible light from the Sloan Digital Sky Survey. The HII region is clearly seen with the illuminating star in the centre, about $7'$ (1.8 pc) from the bright transition zone at the PDR edge extending into the dark molecular cloud in the north-east (upper left corner).

The darkness in visible in the north-east does not reveal the star forming region observed in infrared (e.g. Preibish et al. 2000). The core in S140 contains a small cluster of about 50 deeply embedded protostars illuminating the cloud from within, thereby producing the infrared radiation. The brightest infrared source, with a mass about 10 $M_\odot$, is called IRS 1, which on small scales is composed of several sources. Two of these sources are believed to power bipolar molecular outflows in almost perpendicular directions on scales from a few to one hundred arcseconds. The outflows are bursting into the surrounding HII region and molecular cloud, thereby creating shocked gas. Outflows from high-mass stars are often observed to be less well collimated than those from low-mass stars outflows, which also seems to be the case in S140. The north-west to south-east (NW-SE) outflow axis (from upper right to lower left) has been observed to be close to the line-of-sight. The structures of the outflows and the PDR have been observed to be clumpy.

In addition to the observations presented in paper III, we have performed

Figure 5.1: Sloan Digital Sky Survey image of the S140 molecular cloud in visible light covering $25' \times 25'$ (from `http://galaxymap.org/`). The observations performed by Odin covered strip maps from the north-eastern corner (upper left) across the bright rim extending over $6'$.

observations of HCO^+ $J = 1-0$ at 89.188 GHz with the Onsala 20-m telescope. Although not as sensitive as water, this molecule has also been shown to react to outflow chemistry and may give additional information on the source structure. Figure 5.2 shows maps of the blue and red outflow wings of HCO^+ within the indicated velocity ranges.

5.2 Results of Paper III

1. We have used the Odin satellite to simultaneously observe five-point strip maps across the bright rim in S140 of the *ortho*-H_2O $1_{1,0} - 1_{0,1}$ and the *ortho*-NH_3 $1_0 - 0_0$ transitions, as well as CO(5 – 4) and ^{13}CO(5 – 4). The NH_3 transition has never previously been observed in S140. Observations of $H_2^{18}O$ in the central position resulted in a non-detection at an rms level of 8 mK. To support these observations we also mapped ^{13}CO(1 – 0) line with the Onsala 20m telescope.

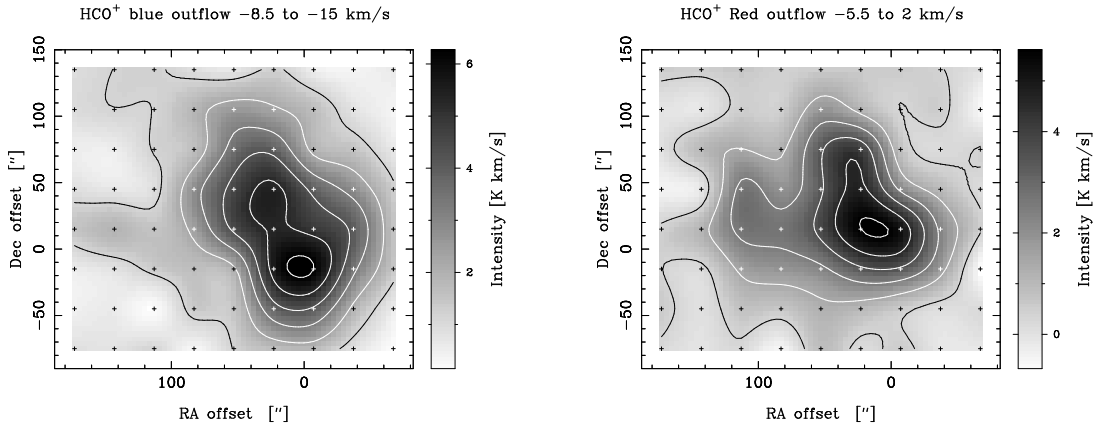

Figure 5.2: HCO^+ maps of S140 obtained with the Onsala 20m telescope showing the red and blue outflows. The zero position corresponds to IRS 1.

2. Water and CO:
   Like CO, the water line-profile is dominated by emission from a NW − SE outflow, however, mainly in the red wing. Strong self-absorption is seen in the optically thick CO emission, while no obvious signs of self-absorption are seen in the *ortho*-H_2O, *ortho*-NH_3 or the almost optically thin ^{13}CO line profiles. The lack of self-absorption in water may be caused by a lower water abundance in the blue outflow. In addition to the outflow, water shows emission from a more extended NE − SW elongated PDR. Both these components, outflow and PDR, originate approximately around the central position. No additional water emission is detected closer to the bright rim or further into the molecular cloud where the water most likely is adsorbed onto dust grains.

3. Water and ammonia:
   The *ortho*-NH_3 emission seems to emanate from the same high density clumps in the PDR and the outflow as water, but also shows additional emission further into the cloud where the ambient gas temperature drops to about 30 K. This is in agreement with chemical models predicting that ammonia is not as sensitive to depletion in cold, high density regions as is water. Compared to water in the central position, ammonia has a weaker outflow emission in the red wing, although similar in the blue outflow. Close to the bright rim, where the outflow contribution to the emission is very low, the water and ammonia line profiles are almost identical. This suggests an origin in the same gas and velocity fields of the PDR. The ^{13}CO line also shows a very similar line profile to H_2O and NH_3 in this position with a narrow line width of $\sim 3\,\mathrm{km\,s^{-1}}$.

4. PDR abundance with a clumpy PDR model:
   Abundances in the PDR, with respect to H_2, are estimated both with an enhanced version of the homogeneous `RADEX` code and with a clumpy PDR model. This model suggests low mean abundances of water and ammonia in the PDR of 5×10^{-9} and 4×10^{-9}, respectively. In the high-density clumps both the average abundances of water and ammonia increase to 5×10^{-8}. To match the observed PDR antenna temperatures with Odin and SWAS, a clumpy medium is required by the model with a high molecular hydrogen density in the clumps of $\gtrsim1\times10^{6}\,\mathrm{cm}^{-3}$. The PDR model also confirms a rather low water opacity, with an unweighted mean opacity of 17 and a model range of $\sim10^{-5}-800$.

5. PDR abundances with the homogeneous `RADEX` model:
   The resulting `RADEX` mean abundances are twice as high as the clumpy PDR model: 1.0×10^{-8} and 8×10^{-9} for water and ammonia, respectively, using a mean molecular hydrogen density of $4\times10^{5}\,\mathrm{cm}^{-3}$ and a kinetic temperature of 55 K. The differences between the models most likely arise from the uncertainty in density, beam-filling, and volume filling of the clumps. The opacity of the narrow PDR component of the $1_{1,0}-1_{0,1}$ transition is constrained by the narrow line width, and is estimated by `RADEX` to be $\sim$7. The `RADEX` model also suggests that the strongly emitting molecules occupy only a 7% fraction of the volume.

6. Water abundance in the outflow:
   Water abundances may be estimated using a simple two-level approximation considering the water emission to be effectively optically thin. This approximation is valid when the water opacity is $\lesssim$10 (Poelman et al., 2007) and is therefore justified in the S140 outflow where the opacity is lower than in the narrow PDR. The approximation, however, depends on the assumed density which is poorly constrained. Assuming a density range of $5\times10^{4}-5\times10^{5}$ we find that the mean outflow water abundance is higher than in the PDR by at least one order of magnitude, $\sim4\times10^{-8}-4\times10^{-7}$, where the major abundance enhancement originates in the red outflow.

7. Predictions for Herschel:
   Predictions of antenna temperatures for observations with HIFI are given by our PDR model for the *ortho*- and *para*-H_2O $1_{1,0}-1_{0,1}$ and $1_{1,1}-0_{0,0}$ transitions for nine positions across the cloud core and the bright rim. They are found to peak close to IRS 1 around $70-80''$ from the dissociation front, in agreement also with our observations.

Paper III

Water and ammonia abundances in S140 with the Odin satellite

Carina M. Persson, M. Olberg, Å. Hjalmarson, M. Spaans, J.H. Black, U. Frisk, T. Liljeström, A.O.H. Olofsson, D.R. Poelman, and Aa. Sandqvist

Astronomy & Astrophysics, in press (2008)

Astronomy & Astrophysics manuscript no. s140˙accepted
November 18, 2008

Water and ammonia abundances in S140 with the Odin⋆ satellite

C. M. Persson[1], M. Olberg[1], Å. Hjalmarson[1], M. Spaans[2], J.H. Black[1], U. Frisk[3], T. Liljeström[4], A.O.H. Olofsson[1,5]
D.R. Poelman[6], and Aa. Sandqvist[7]

[1] Onsala Space Observatory, Chalmers University of Technology, SE-439 92 Onsala, Sweden
e-mail: carina.persson@chalmers.se
[2] Kapteyn Astronomical Institute, Rijksuniversiteit Groningen, P.O. Box 800, 9700 AV Groningen, The Netherlands
[3] Swedish Space Corporation, PO Box 4207, SE-171 04 Solna, Sweden
[4] Metsähovi Radio Observatory, Helsinki University of Technology, Otakaari 5A, 02150 Espoo, Finland
[5] GEPI, Observatoire de Paris, CNRS; 5 Place Jules Janssen, 92195 Meudon, France
[6] SUPA, School of Physics and Astronomy, University of St Andrews, North Haugh, St Andrews KY16 9SS, U.K.
[7] Stockholm Observatory, AlbaNova University Center, SE-10691 Stockholm, Sweden

Received September 8, 2008; accepted Nov 14, 2008

ABSTRACT

Aims. We investigate the effect of the physical environment on water and ammonia abundances across the S140 photodissociation region (PDR) with an embedded outflow.
Methods. We used the Odin satellite to obtain strip maps of the ground-state rotational transitions of *ortho*-water and *ortho*-ammonia, as well as CO(5 – 4) and ^{13}CO(5 – 4) across the PDR, and $H_2^{18}O$ in the central position. A physi-chemical inhomogeneous PDR model was used to compute the temperature and abundance distributions for water, ammonia, and CO. A multi-zone escape probability method then calculated the level populations and intensity distributions. These results are compared to a homogeneous model computed with an enhanced version of the RADEX code.
Results. H_2O, NH_3, and ^{13}CO show emission from an extended PDR with a narrow line width of ∼3 km s^{-1}. Like CO, the water line profile is dominated by outflow emission, but mainly in the red wing. Even though CO shows strong self-absorption, no signs of self-absorption are seen in the water line. The $H_2^{18}O$ molecule is not detected. The PDR model suggests that the water emission arises mainly from the surfaces of optically thick, high-density clumps with $n(H_2)\gtrsim10^6$ cm^{-3} and a clump water abundance, with respect to H_2, of 5×10^{-8}. The mean water abundance in the PDR is 5×10^{-9} and between $\sim4\times10^{-8}-4\times10^{-7}$ in the outflow derived from a simple two-level approximation. The RADEX model points to a somewhat higher average PDR water abundance of 1×10^{-8}. At low temperatures deep in the cloud, the water emission is weaker, likely due to adsorption onto dust grains, while ammonia is still abundant. Ammonia is also observed in the extended clumpy PDR, likely from the same high density and warm clumps as water. The average ammonia abundance is about the same as for water: 4×10^{-9} and 8×10^{-9} given by the PDR model and RADEX, respectively. The differences between the models most likely arise from uncertainties in density, beam-filling, and volume-filling of clumps. The similarity of water and ammonia PDR emission is also seen in the almost identical line profiles observed close to the bright rim. Around the central position, ammonia also shows some outflow emission, although weaker than water in the red wing. Predictions of the H_2O $1_{1,0}-1_{0,1}$ and $1_{1,1}-0_{0,0}$ antenna temperatures across the PDR are estimated with our PDR model for the forthcoming observations with the Herschel Space Observatory.

Key words. ISM: abundances – ISM: individual (S140) – ISM: molecules – Submillimeter – Line: profiles – Line: formation

1. Introduction

The chemistry and the evolution of the interstellar medium depend to a high degree on the available amount of carbon and oxygen. The carbon-based chemistry is understood fairly well, but the oxygen chemistry is not. Two molecules vital to understanding the oxygen chemistry are water and molecular oxygen, since some chemical models predict that a large fraction of oxygen could be in the form of these molecules.

Observations of the ground-state rotational water transition with NASA's Submillimeter Wave Astronomy Satellite (SWAS; Melnick et al., 2000b) and the Odin satellite (Nordh et al., 2003) have both shown very low abundances of molecular oxygen, 5×10^{-8} (Larsson et al., 2007), and water, $10^{-8}-10^{-9}$ (Olofsson et al., 2003), in the *extended* cold clouds in contrast to the predictions from chemical models. However, on smaller scales in warm or shocked regions and outflows, where the density is higher than 10^5-10^6 cm^{-3}, SWAS (e.g. Melnick et al., 2000a) and Odin (e.g. Persson et al., 2007) have also shown *locally* increased water abundance by several orders of magnitude, $10^{-6}-10^{-4}$ with respect to molecular hydrogen. The analysis of the data is, however, somewhat difficult and uncertain due to observations of a single line and large beam-widths, but is in agreement with observations of a wealth of highly excited water vapour transitions with ISO (the Infrared Space Observatory, Cernicharo & Crovisier, 2005). These locally high abundances support the predictions that water should be an important cooling agent in the star-forming process, especially at high temperatures and densities (e.g. Neufeld et al., 1995; Bergin et al., 2003). The strong

Send offprint requests to: carina.persson@chalmers.se

⋆ Odin is a Swedish-led satellite project funded jointly by the Swedish National Space Board (SNSB), the Canadian Space Agency (CSA), the National Technology Agency of Finland (Tekes) and Centre National d'Etudes Spatiales (CNES). The Swedish Space Corporation was the prime contractor and also is responsible for the satellite operation.

To be cited as: A&A preprint doi http://dx.doi.org/10.1051/0004-6361:200810930

dependence of the water chemistry on the temperature changes seen in star-forming regions also make water an excellent tracer of shocks and outflows from protostars still hidden within their dusty envelopes (e.g. Bergin et al., 1998).

The intention of this paper is to continue the previous work with ISO, SWAS, and Odin, and also to be a valuable input to future observations with the Heterodyne Instrument for the Far Infrared (HIFI) on board the Herschel[1] satellite to be launched in 2009. Our aim is to investigate how the water abundance depends on the environment in a star-forming region. The high spectral resolution ($0.5\,\mathrm{km\,s^{-1}}$) and the smaller beam-size of Odin compared to SWAS (2.′1 vs. 3.′3×4.′5), which enable higher spatial resolution maps, allow a more detailed analysis of the line profile observed at each map position. We can also obtain an estimate of the beam-filling by comparing SWAS and Odin line profiles if the same object has been observed. If not properly taken into account the beam-filling may otherwise influence the results by orders of magnitude.

In addition to the water observations a second goal of our work is to perform and analyse observations of the important ground-state rotational transition of ammonia. While ammonia has been extensively observed in the inversion transitions at cm-wavelengths (e.g. Ungerechts et al., 1986; Zhou et al., 1993), the 1_0-0_0 transition, however, cannot be observed from ground due to the opaque terrestrial atmosphere. The first observation of this transition was performed by the Kuiper Airborne Observatory (Keene et al., 1983), and was later followed up with Odin (Larsson et al., 2003; Liseau et al., 2003; Olofsson et al., 2007).

Our chosen target is the well known molecular cloud and bright nebula Sh 2-140, more commonly known as S140 (Sharpless, 1959; Blair et al., 1978). It is located at a distance of 910 pc (Crampton & Fisher, 1974) in the large L1202/L1204 dark cloud. This region is illuminated from the south-western side by the nearby B0.5V star HD 211880, creating a bright HII region and an almost edge-on PDR adjacent to the molecular cloud and extending deeply into the cloud. The core in S140 also contains a small cluster of deeply embedded young stellar objects which illuminate the cloud from within. One or more of these early B-stars are undergoing some mass-loss process and molecular outflows are observed from this dense and warm region (e.g. Rouan et al., 1977; Hayashi et al., 1987; Minchin et al., 1993; Preibisch & Smith, 2002). The brightest infrared source in S140, called IRS1, is on small scales composed of several sources, two of which might be powering bipolar molecular outflows in almost perpendicular directions (Trinidad et al., 2007). The increased temperature and density in both the PDR and the outflows are likely expected to produce a higher than average water abundance. For these reasons, S140 is a promising target for our purposes.

Both ISO (Boonman & van Dishoeck, 2003) and SWAS (Snell et al., 2000a; Ashby et al., 2000a,b; Franklin et al., 2008) have observed water in S140 and several attempts have been made to model these observations (e.g. Ashby et al., 2000a,b; Boonman et al., 2003; Poelman & Spaans, 2005, 2006). However, they all have had difficulties to explain the unusual, narrow $1_{1,0}-1_{0,1}$ emission line with no or little evidence of self-absorption. In order to obtain more information about the water emission we have conducted strip map observations of S140, starting deep within the molecular cloud and reaching outside the bright rim (see Fig. 1). Strip maps are also simultaneously performed of the previously unobserved $NH_3(1_0-0_0)$ transition.

[1] http://herschel.esac.esa.int/

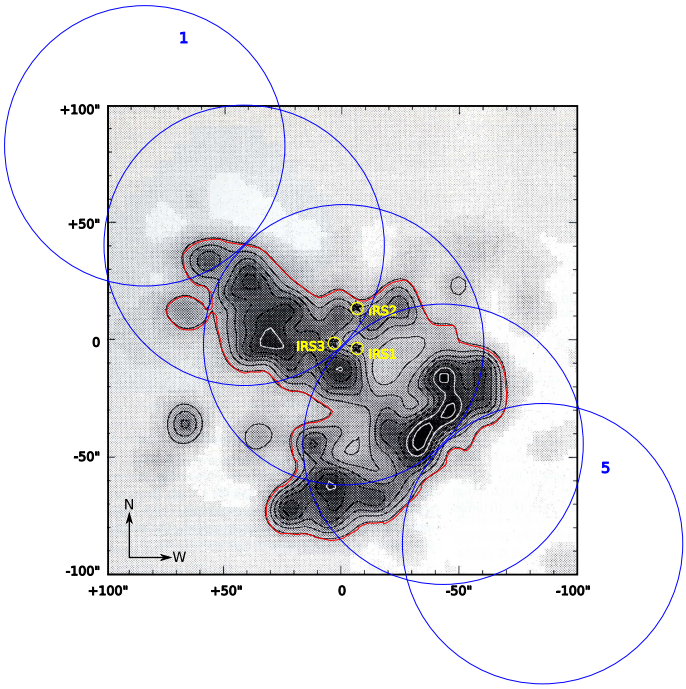

Fig. 1. A CI map (492 GHz) of S140 observed with JCMT (Minchin et al., 1993). The Odin 2.′1 beam at the five strip positions is also shown. Position 1 in NE to position 5 in SW.

To aid the analysis of water and ammonia, we have in addition performed $H_2^{18}O$ observations in the central position, strip maps of CO (5 – 4) and ^{13}CO (5 – 4) with the Odin satellite, and a ^{13}CO (1 – 0) map with the Onsala 20-m telescope.

2. Observations

All transitions, except ^{13}CO(1 – 0), were acquired with the Odin satellite from 2003 to 2006 with a total of 561 orbits (see Table 1). The calibration procedure (the chopper wheel method) is described in Olberg et al. (2003). The Odin 1.1 m offset Gregorian telescope has a circular beam at 557 GHz with a Full Width of Half Maximum (FWHM) of 2.′1 (Frisk et al., 2003). Being outside the atmosphere, and with an exceptionally high main beam efficiency, $\eta_{\mathrm{mb}} = 0.9$, our intensity calibration is very accurate. The intensity scale in the figures is expressed in terms of antenna temperature T_{A}^{*}. In all calculations, however, the main beam efficiency is properly taken into account. The reconstructed pointing offset was <15″ during most of the time. The simultaneous observations of H_2O and NH_3, and of ^{13}CO, CO and H_2O guarantee their pointing to be identical.

Three different tunable submm receivers were used, having average single-sideband (SSB) system temperatures of about 3 300 K. They were used in combination with a hybrid autocorrelator spectrometer (300 – 400 MHz working bandwidth) and an acousto-optical spectrometer (1 GHz working bandwidth), both with a channel spacing of $\sim 0.3\,\mathrm{km\,s^{-1}}$. All observations were performed in the sky-switching mode with reference sky beams at 42° distance and 4.4° FWHM. To correct for ripple, observations of a reference off position 30′ east of S140 were conducted as well.

The five point strip maps have 60″ step size with strip centre coordinates R.A. $22^{\mathrm{h}}17.^{\mathrm{m}}42.^{\mathrm{s}}0$, Dec. $+63°03.'45.''0$ (B1950) at the cloud core (our position 3, Fig. 1). Position 1 is in NE and posi-

Table 1. All molecular transitions are observed with the Odin satellite except the ^{13}CO(1 – 0) map which is observed with the Onsala 20-m telescope.

Species	Transition	Freq. [MHz]	E_u^a [K]	n_{crit}^b [cm^{-3}]	Int. time [h]
H_2O	$1_{1,0} - 1_{0,1}$	556 936.0	61	$3\times10^{8\,c}$	41
$H_2^{18}O$	$1_{1,0} - 1_{0,1}$	547 676.4	60	$3\times10^{8\,c}$	91
CO	5 – 4	576 267.9	83	$2\times10^{5\,c}$	9
^{13}CO	5 – 4	550 926.3	79	2×10^{5}	9
^{13}CO	1 – 0	110 210.4	5	7×10^{2}	2 min/pos
NH_3	$1_0 - 0_0$	572 498.1	29	$5\times10^{7\,c}$	16

[a] Upper state energy.
[b] Critical density calculated for a temperature of 40 K.
[c] Can be considerably reduced because of radiative trapping.

tion 5 in SW. The frequency scale is set relative to a source LSR velocity of $-7.5\,\mathrm{km\,s^{-1}}$.

In addition, the Onsala 20-m telescope was used in 2006 for a ^{13}CO(1 – 0) 10×11 point map of the S140 molecular cloud with a spacing of 30″. The SSB system temperature was ∼500 K, the main-beam efficiency 0.5, and the FWHM beam at 110.201 GHz is 34″.

3. Results

The observed Odin spectra of CO, H_2O, and NH_3 are shown together with ^{13}CO(5 – 4) in Figs. 2 – 4 to allow a comparison of the line profiles of the different molecules at each position. The water and ammonia spectra are also shown together in Fig. 5. No $H_2^{18}O$ emission was detected in the central position (Fig. B.1, on-line material) at an rms noise level of 8 mK. Tables with 1σ rms, integrated intensities, peak antenna temperatures, line widths and amplitudes of Gaussian fits, and centre velocities for species observed with Odin are found in the on-line Tables B.1 – B.4. The on-line material also includes figures of Gaussian fits to ^{13}CO(1 – 0) and $J = 5 - 4$, H_2O and $NH_3(1_1 - 0_0)$ (Figs. B.4 – B.7).

Below we will discuss the observations and some straight forward results, while the model results for the narrow PDR component are presented in Sect. 4 and 5.

3.1. Carbon monoxide

The CO(5 – 4) and ^{13}CO(5 – 4) observations show a narrow line from the PDR in all positions superimposed on a broader outflow feature seen in CO at positions 1 – 4 and in ^{13}CO at the centre position (Fig. 2). The emission peaks about 20″ from the central position towards position 2 deeper in the cloud. A comparison of the ^{12}CO and ^{13}CO line shapes suggests strong CO(5 – 4) self-absorption by lower excitation foreground gas. This is also discussed by e.g. Minchin et al. (1993) and Boonman et al. (2003) where the higher J-level CO lines are strongly self-absorbed. No strong self-absorption is visible in ^{13}CO.

The mean opacity of ^{12}CO and ^{13}CO can be determined by comparison of their antenna peak temperatures if the isotopologue abundance ratio R is known. Assuming that the opacity of ^{12}CO is larger than the opacity of ^{13}CO by a factor R, we will have

$$\frac{T^*_{\mathrm{A},13}}{T^*_{\mathrm{A},12}} = \frac{J(T^{13}_{\mathrm{ex}})\,(1-e^{-\tau_{13}})\,\eta_{\mathrm{bf},13}}{J(T^{12}_{\mathrm{ex}})\,(1-e^{-\tau_{12}})\,\eta_{\mathrm{bf},12}} = \frac{J(T^{13}_{\mathrm{ex}})\,(1-e^{-\tau_{13}})\,\eta_{\mathrm{bf},13}}{J(T^{12}_{\mathrm{ex}})\,(1-e^{-R\,\tau_{13}})\,\eta_{\mathrm{bf},12}}, \quad (1)$$

where the radiation temperature, $J(T_{\mathrm{ex}})$, is a function of the excitation temperature, T_{ex},

$$J(T_{\mathrm{ex}}) = \frac{h\nu}{k}\frac{1}{e^{h\nu/kT_{\mathrm{ex}}}-1}. \quad (2)$$

The beam-filling factor is calculated with

$$\eta_{\mathrm{bf}} = \frac{\theta_{\mathrm{s}}^2}{\theta_{\mathrm{s}}^2+\theta_{\mathrm{mb}}^2}, \quad (3)$$

assuming that both the source brightness distribution and the antenna response are circularly symmetric and Gaussian.

Assuming that the excitation temperatures are the same for both species, co-spatial emissions and using $R = 70$, the opacities of the narrow component of ^{12}CO and ^{13}CO are estimated to be $\lesssim 70$ and $\lesssim 1$, while the opacities in the broad outflow component are $\lesssim 7$ and $\lesssim 0.1$, respectively. Due to the self-absorption of ^{12}CO the opacities are upper limits.

The size of the emission region can be estimated by comparing Odin and SWAS antenna temperatures

$$\frac{T^*_{\mathrm{A,Odin}}}{T^*_{\mathrm{A,SWAS}}} = \frac{(3\farcm3\times60\times4\farcm5\times60)+\theta^2}{(2\farcm1\times60)^2+\theta^2}, \quad (4)$$

where θ is the effective circular Gaussian source size in arcseconds. For the central position the ratio of the Odin and SWAS ^{13}CO peak antenna temperatures is ∼2.5 which is equivalent to a mean source size of ∼100″.

A second approach to estimate the source size is performed by plotting the antenna temperatures in our Odin strip map vs. position, and fitting a Gaussian. After deconvolution with the 126″ Odin beam, the resulting one dimensional source size is about 106″. Together with the mean source size of ∼100″, this implies a relatively circular source.

The excitation temperature can be estimated by plotting a rotation diagram of several transitions. The level populations are given by the Boltzmann distribution and the excitation temperatures for all the energy levels are assumed to be the same. The beam-filling corrected integrated intensities of all lines are plotted as a function of the upper state energy in a semi-log plot based upon the relation (Persson et al., 2007)

$$\ln\frac{8\pi k\nu_{ul}^2}{hc^3 g_u A_{ul}}\int T_{\mathrm{b}}\,\mathrm{d}\upsilon = \ln\frac{N_{\mathrm{ROT}}}{Q(T)} - \frac{E_u}{kT_{\mathrm{ex}}}. \quad (5)$$

where k is the Boltzmann constant, ν_{ul} is the frequency of the transition, h is the Planck constant, c is the speed of light, A_{ul} is the Einstein A-coefficient for the transition, T_{b} is the brightness temperature (observed antenna temperature corrected for beam-efficiency and beam-filling), g_u and E_u are the statistical weight and energy of the upper state, respectively, $Q(T)$ is the partition function, T_{ex} is the excitation temperature for the transition, and N_{ROT} is the total column density of the species obtained from the rotational diagram. As customary the frequency axis ν has been converted to a velocity axis υ using the speed of light. A least-squares fit to the data will produce a straight line with slope $-1/T_{\mathrm{ROT}}$. If we extrapolate the line to $E_u = 0$ K, the total column density is found from the intersection of the y-axis.

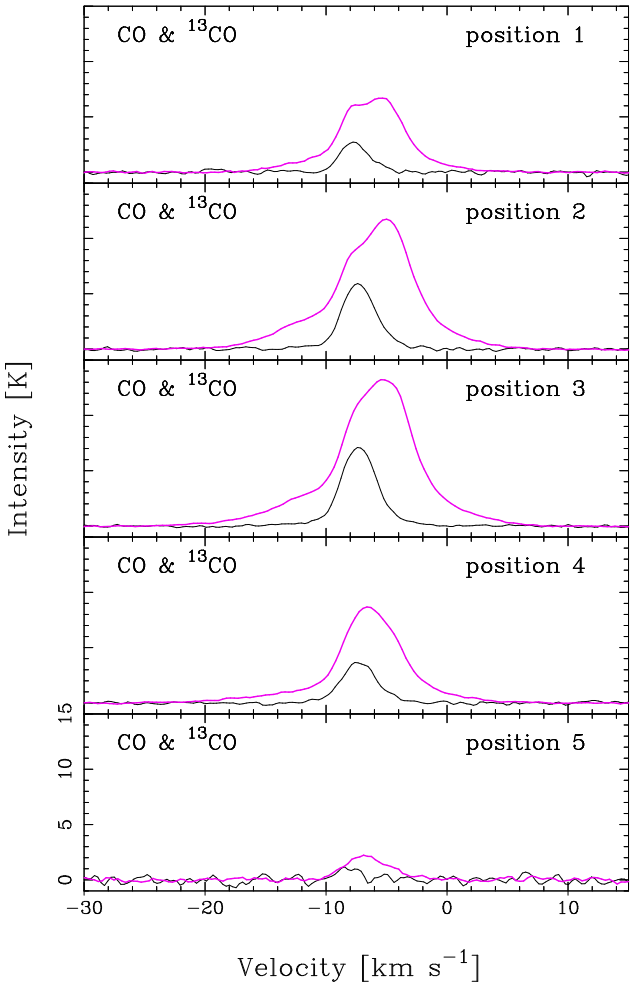

Fig. 2. Comparison of the CO(5−4) (thick magenta line) and ^{13}CO(5−4) (thin black line) line profiles in a strip map from NE to SW across the PDR.

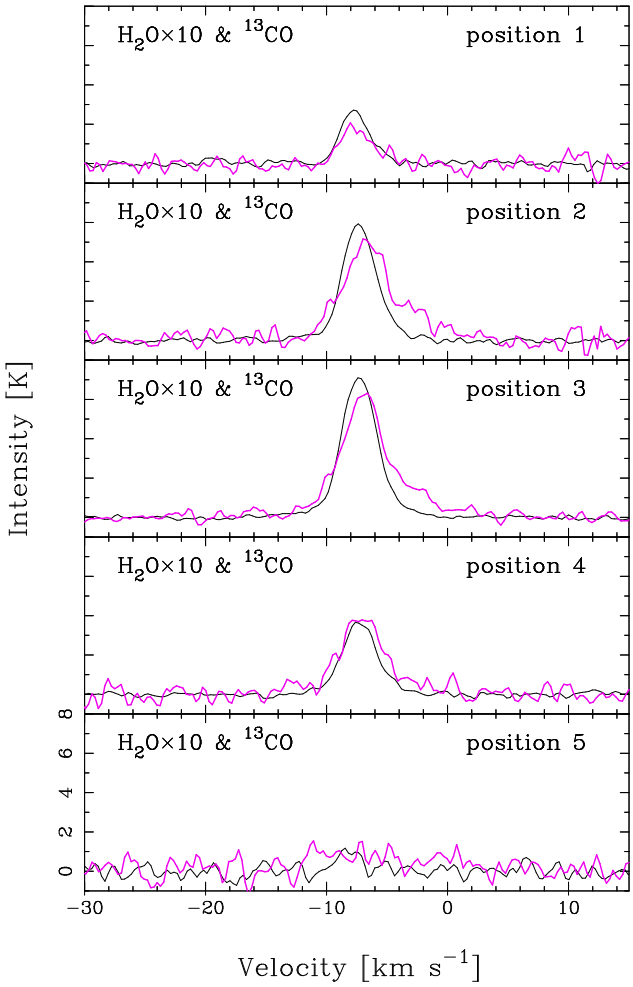

Fig. 3. Comparison of the H_2O $1_{1,0}-1_{0,1}$ (thick magenta line) and ^{13}CO(5−4) (thin black line) line profiles in a strip map from NE to SW across the PDR.

Our rotation diagram of the broad outflow ^{13}CO component in the central position (on-line Fig. B.2), including the Onsala 20-m $J=1-0$ transition, the $J=2-1$ and $3-2$ transitions from Minchin et al. (1993), and the Odin $J=5-4$ transition, produces $T_{\rm ROT}=24\pm2$ K and $N_{\rm ROT}=(2.5\pm0.4)\times10^{16}$ cm^{-2}. All antenna temperatures are corrected with respective beam-filling and beam-efficiencies. This temperature is in agreement with the previously estimated lower limit of the outflow excitation temperature of about 15 – 20 K (Minchin et al., 1993). The low temperature of the outflow indicates that the emission arises from gas far behind the shock front where the gas has already cooled (Snell et al., 1984b). .

The excitation temperature of the narrow ^{13}CO PDR emission in the central position is also estimated by means of a rotation diagram (on-line Fig. B.3), including the above mentioned transitions with addition of the $J=6-5$ line from Graf et al. (1993), but excluding $J=1-0$ which seems to originate only in the colder gas component. This produces $T_{\rm ROT}=69\pm27$ K, in agreement with Minchin et al. (1993) who find a PDR excitation temperature of about 70 K at IRS and a steep rise in temperature to about 250 K at the dissociation front 60″ – 80″ SW of IRS1. Our PDR column density, $N_{\rm ROT}(^{13}{\rm CO})=(3.2\pm1.8)\times10^{16}$ cm^{-2}, is relatively uncertain but in agreement with the RADEX result in Sect. 4, $N(^{13}{\rm CO})=2.8\times10^{16}$ cm^{-2}, and with Plume et al. (1994), 3.4×10^{16} cm^{-2}.

3.2. Water

The *ortho*-water $1_{1,0}-1_{0,1}$ ground-state rotational transition is detected in all positions except outside the bright rim (position 5). Similar to CO and ^{13}CO, a narrow component (Δv ~3 km s^{-1}) superimposed on a broader outflow component (Δv ~8.5 km s^{-1}) is observed with emission originating around the central position. Like CO, the water line profile is dominated by outflow emission, clearly seen in a two Gaussian component fit in the on-line Fig. B.6. This is in contrast to ^{13}CO which is dominated by the narrow component (on-line Fig B.4). The water outflow emission, in addition, mainly shows a red wing.

The non-detection of $H_2^{18}O$ can be used to set upper limits on the opacity of the main water line using Eq. 1. However, the calculation is not as straightforward as for CO. Because of the high critical density (the ratio of the spontaneous de-excitation and collision coefficients) of the H_2O 557 GHz line, the emission of this transition is highly sub-thermal and has a high opacity even for rather low abundances. This high optical depth allows the excitation temperature to be enhanced by radiative trapping. As a result, the corresponding lines of H_2O and $H_2^{18}O$ have quite different values of excitation temperature. Their excitation temperatures will also be much lower than the kinetic temperature. Using the RADEX code in Sect. 4 for a kinetic temperature of 55 K and a molecular hydrogen density $n(H_2)=4\times10^5$ cm^{-3}, we find excitation temperatures of 8.2 and 6.3 K for the $1_{1,0}-1_{0,1}$

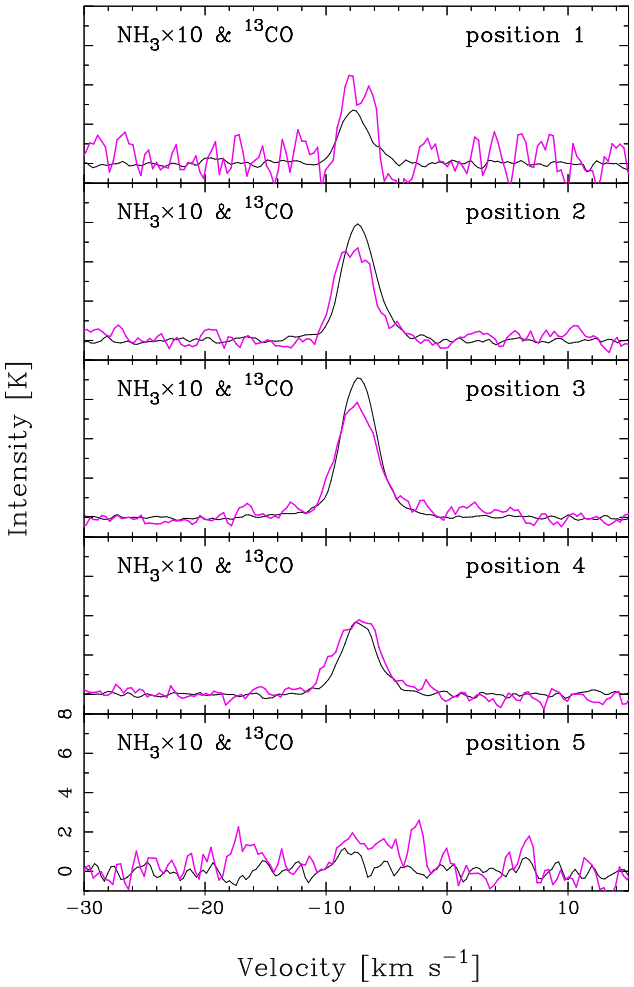

Fig. 4. Comparison of the NH_3 1_0-0_0 (thick magenta line) and $^{13}CO(5-4)$ (thin black line) line profiles in a strip map from NE to SW across the PDR.

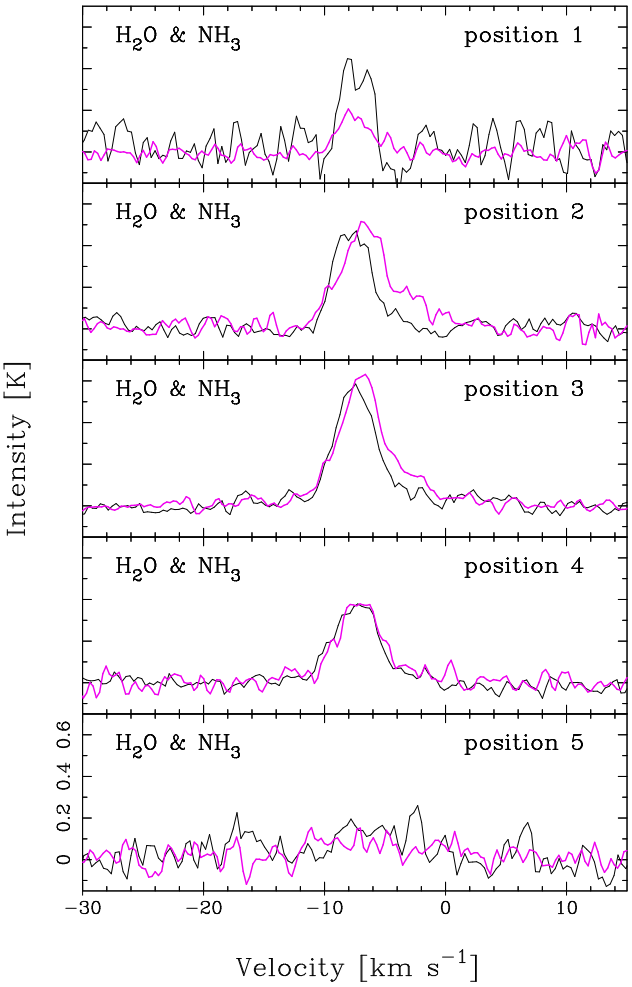

Fig. 5. Comparison of the H_2O (thick magenta line) $1_{1,0}-1_{0,1}$ and the NH_3 (thin black line) 1_0-0_0 line profiles in a strip map from NE to SW across the PDR.

transitions of H_2O and $H_2^{18}O$, respectively. If the abundance ratio $[^{16}O/^{18}O] = 330$ in water (Persson et al., 2007) and if the two isotopologues are distributed similarly, then the 5σ upper limit on the intensity of the $H_2^{18}O$ line implies that the optical depth of the H_2O line is $\lesssim 60$. If the assumed density is lower by a factor of 10, the difference in excitation temperatures will increase and change the upper limit to $\lesssim$120.

The high H_2O opacity, in addition, often produces self-absorbed spectra. Our observations, however, do not show any obvious signs of self-absorption in contrast to our CO observations. When comparing the centre velocities of the narrow components of water and CO to ^{13}CO, we find that the velocities of water and ^{13}CO are well matched (Fig. 3 and Table B.2 – B.3), while CO and ^{13}CO in positions 1 – 4 are not (Fig. 2). This supports our conclusion that there is no severe self-absorption in H_2O in contrast to observations of other sources in which corresponding self-absorptions were seen in CO(7-6) and in ISO measurements of H_2O (Boonman et al., 2003).

The lack of self-absorption points to a rather constant excitation across the region (cf. Snell et al., 1984a). It also implies a lower water abundance in the blue than in the red outflow. A higher water abundance in the red wing may be caused by outflowing gas pushing into the ambient high density cloud thereby producing water. The blue outflow, on the other hand, is leaving the molecular cloud, and expands into an ionized region with low density gas with no or very low water production as a result. This is in agreement with the results in Franklin et al. (2008) who investigated water abundance in molecular outflows with SWAS and find about five times higher abundance in the red outflow compared to the blue.

The sizes of the emitting regions are estimated in the same way as for ^{13}CO (Eq. 4). For the central position the ratio of the Odin and SWAS peak antenna temperatures is ∼2.4, equivalent to a mean source size of ∼100″. This confirms previous suggestions that the water emission does not fill the SWAS beam (Boonman et al., 2003). To obtain estimates of the size of each component, we use the amplitudes of the fitted Gaussians from the Odin and SWAS spectra. The ratios of the PDR and outflow components are ∼2.2 and ∼2.6, which corresponds to mean source sizes of 120″ and 85″, respectively.

Gaussian fits to the amplitudes in each position in the Odin strip map results in one-dimensional source sizes of $\gtrsim$150″ and $\lesssim$50″ for the PDR and outflow, respectively. Taken together, these two calculations of source sizes suggest that the water emission from the PDR is more extended in the NE – SW direction (same direction as our strip map), while the contrary applies to the outflow, indicating a NW – SE elongation.

A third approach to estimate the beam-filling can be achieved by using the radiative transfer equation. With a constant source function, the solution of the radiative transport equation is

$$T_{\rm A}^{*} = T_{\rm b}\,\eta_{\rm mb}\,\eta_{\rm bf} = (J(T_{\rm ex}) - J(T_{\rm cont}))\,(1 - e^{-\tau})\,\eta_{\rm mb}\,\eta_{\rm bf}, \quad (6)$$

where $J(T_{\rm cont})$ is the background continuum radiation.

For an optically thick line and neglecting the background radiation

$$T_{\rm A}^{*} \approx J(T_{\rm ex})\eta_{\rm mb}\,\eta_{\rm bf}. \quad (7)$$

If $T_{\rm ex}$ is known, then the beam-filling can be estimated. Using $T_{\rm ex} = 8.2$ K obtained from RADEX and Equation 7 give a beam-filling factor that corresponds to a PDR source size of about 110″, which is close to the source size of 120″ obtained from the relative temperatures from Odin and SWAS. This implies that the gas is somewhat clumped, and that the surface filling fraction of the high density PDR gas is ∼84%. The clumpy structure of the cloud is confirmed by previous observations (Snell et al., 1984a,b; Zhou et al., 1993; Minchin et al., 1993; Hayashi & Murata, 1992; Ashby et al., 2000a) and our model results in Sect. 5. The amount of surface clumping is, however, not possible to determine very accurately due to the uncertainty of the excitation temperature which is affected by the assumed density. With $T_{\rm ex} = 9$ K and 10 K the same calculations give source sizes of 86″ and 69″, with corresponding surface filling fractions of 50% and 33%, respectively. Including the background radiation in Eq. 6 also introduces additional uncertainties.

3.3. Ammonia

A complex energy level diagram with a wealth of transitions covering different temperatures and densities has made ammonia a very valuable diagnostic of physical conditions in the interstellar medium. The $1_0 - 0_0$ ground-state rotational transition, observed by Odin, has an upper state energy comparable to the extensively observed inversion transitions (e.g. Ungerechts et al., 1986; Zhou et al., 1993), but the critical density is about four orders of magnitude larger. It is therefore likely that these transitions partly probe different gas components. The $1_0 - 0_0$ transition has a high opacity and is highly sub-thermally excited in most cases like our observed water transition.

The $1_0 - 0_0$ transition of *ortho*-NH_3 is detected in all positions except outside the bright rim (position 5). The line profiles and centre velocities are very similar to those of ^{13}CO(5 – 4) with an exception in position 1 (Fig. 4). Our comparison of ammonia and water in Fig. 5 shows an almost identical line profile at the bright rim (position 4), which suggests emission from the same gas and velocity fields at this position originating in the PDR. In the central position, the water line profile is dominated by the outflow in contrast to ammonia. Both species displays, however, very similar emission in the blue outflow, while water has a more pronounced outflow in the red wing. The water emission from the outflow seems to be almost the same in position 2 and 3, while the ammonia emission from the outflow decreases in position 2. This suggests that the outflow production mechanism is more efficient for water than ammonia.

Deepest in the molecular cloud a very weak water line is seen. The ammonia emission is, however, considerably stronger than the water emission at this position. This confirms previous observations of NH_3 inversion transitions (Zhou et al., 1993; Ungerechts et al., 1986) who find an NH_3 peak further into the cloud at about 1′ northeast of IRS1. When we plot the peak antenna temperatures vs. position it is obvious that we see additional emission in position 1. A Gaussian fit to positions 2 – 4 gives a source size of ∼130″, with a peak about 10″ into the cloud from the centre. This size is relatively uncertain due to a fit to only three positions, but agrees well with the source sizes estimated from ^{13}CO and H_2O.

The Odin observations indicate that in addition to the warm, dense PDR and a weak outflow around IRS, we also observe NH_3 from the same cold and extended gas deep in the cloud (position 1) as ^{13}CO(1 – 0) at a temperature about 20 – 30 K. This is also in agreement with Ungerechts et al. (1986) and Zhou et al. (1993) who find an NH_3 rotation temperature of 40 K in between our first and second position. Chemical models predict that NH_3 is not depleted in high density regions ($\lesssim 1\times10^6$ cm^{-3}) and is therefore relatively more abundant than other molecules such as water and CO (Bergin & Langer, 1997; Bergin, 2003).

The surface filling fraction of the narrow PDR component of ammonia is also estimated using the radiative transfer equation (Eq. 7). The excitation temperature is approximately the same as for water thereby producing similar surface filling factors. Together with the similarity of the line profiles, source sizes and centre velocities of the H_2O, NH_3 and ^{13}CO(5 – 4) narrow components, this points to emission from the same high density PDR clumps with the same temperature of about 70 K for all species (cf. Boonman et al., 2003).

3.4. Outflow abundances

The collisional de-excitation of the ground-state rotational transition of *ortho*-water is very low in the density ranges considered here due to the high critical density of $\sim3\times10^8$ cm^{-3} at a temperature of 40 K. A simple analytic expression for the antenna temperature of a two-level system in the low collision rate limit can therefore be used since collisional excitation always results in a photon that escapes the cloud. Thus, even though our transition may be optically thick, it is effectively thin (Linke et al., 1977; Snell et al., 2000b). We use this approach to estimate the water abundance in the outflow (Snell et al., 2000b)

$$\int T_{\rm b}\,d\upsilon = C\,n_{\rm H_2}\frac{c^3}{2\nu^3 k}\,N({\rm o-H_2O})\frac{h\nu}{4\pi}\,\exp(-h\nu/kT_K), \quad (8)$$

where C is the collision rate which equals the product of the cross-section and velocity. Dividing Eq. (8) with $N(H_2)$ and scaling the calculated factor in Snell et al. (2000b) to our derived rotational outflow temperature of 24 K (with $\sqrt{T}$) produces the fractional abundance of *ortho*-water with respect to H_2 in the outflow

$$X(o-{\rm H_2O}) = 5.1\times10^{19}\frac{\int T_{\rm b}\,d\upsilon}{N({\rm H_2})\,n_{\rm H_2}}. \quad (9)$$

The H_2 column density in the outflow is calculated from $N_{\rm ROT}(^{13}{\rm CO})$ of the broad component. Using typical values of $[{\rm CO/H_2}] = 1\times10^{-4}$ and $[^{12}{\rm C}/^{13}{\rm C}] = 70$ we obtain $N({\rm H_2}) = 1.8\times10^{22}$ cm^{-2}. Together with a range of mean molecular hydrogen densities of $5\times10^4 - 5\times10^5$ cm^{-3} we obtain a total water outflow abundance of $\sim 4\times10^{-8} - 4\times10^{-7}$. This is in agreement with Franklin et al. (2008) who found an outflow abundance in the blue wing of 2.4×10^{-8} and 1.0×10^{-7} in the red wing using a kinetic temperature of 50 K and a molecular density of 10^5 cm^{-3}.

The ammonia abundance in the outflow is estimated using the Local Thermal Equilibrium (LTE) approximation. Assuming

Table 2. Observations and model calculations for the narrow PDR component in the RADEX homogeneous model.[a]

Species	Transition	Frequency	Observations			Ref	Model calculations			
		ν [GHz]	T_b [K]	$4\pi I$ [ergs s^{-1} cm^{-2}]	$\Delta\upsilon$ [km s^{-1}]		T_{ex} [K]	τ	T_b [K]	$4\pi I$ [ergs s^{-1} cm^{-2}]
H_2O	$1_{1,0}-1_{0,1}$	556.936	0.92	...	3.1	*c*	8.2	6.6	0.92	6.8×10^{-6}
$H_2^{18}O$	$1_{1,0}-1_{0,1}$	547.676	< 0.051	...	(3.1)[b]	*c*	6.3	0.2	< 0.05	$< 3.5\times10^{-7}$
NH_3	1_0-0_0	572.498	1.1	...	3.3	*c*	9.0	6.1	1.1	9.2×10^{-6}
	(1, 1)	23.695	2.9	...	...	*d*	54	0.02	0.87	2.5×10^{-10}
	(2, 2)	23.723	2.0	...	...	*d*	47	0.01	0.50	1.7×10^{-10}
	(3, 3)	23.870	1.4	...	...	*d*	−5.1	−0.25	2.2	9.0×10^{-10}
	(4,4)	24.139	0.15	...	...	*d*	46	0.001	0.06	3.8×10^{-11}
^{13}CO	2 – 1	220.399	12	...	3.3	*e*	55	0.2	9.1	4.3×10^{-6}
	5 – 4	550.926	14.7	...	3.2	*c*	51	0.5	14.7	1.1×10^{-4}
CS	2 – 1	97.981	8.6	...	3.0	*f*	47	0.2	9.1	3.5×10^{-7}
	3 – 2	146.969	10.2	...	3.0	*f*	20	1.0	10.0	1.3×10^{-6}
	5 – 4	244.936	5.4	...	3.0	*f*	13	1.3	5.5	3.3×10^{-6}
	6 – 5	293.912	3.3	...	2.2	*f*	12	0.7	3.1	3.3×10^{-6}
[C I]	1 – 0	492.161	3.7	...	3.5	*g*	54	0.1	3.7	2.1×10^{-5}
[C II]	3/2 – 1/2	1900.537	...	4.4×10^{-3}	...	*h*	55	1.0	13.4	4.4×10^{-3}
[O I]	1 – 2	4744.778	...	4.1×10^{-3}	...	*h*	46	0.9	0.88	4.5×10^{-3}

[a] All results for $T_K = 55$ K, $n(H_2) = 4\times10^5$ cm^{-3}. T_b = Rayleigh-Jeans brightness temperature, $4\pi I$ = flux, $\Delta\upsilon$ = line width, T_{ex} = excitation temperature, τ = line-centre peak opacity. [b] From H_2O. [c] This work. [d] Ungerechts et al. (1986). [e] Minchin et al. (1993). [f] Snell et al. (1984a). [g] Plume et al. (1994). [h] Emery et al. (1996).

LTE and adding corrections for opacity and beam-filling, the total source averaged column density can be calculated as

$$N_{\rm LTE} = \frac{C_\tau}{\eta_{\rm bf}} \frac{8\pi k\nu_{ul}^2}{hc^3} \frac{1}{A_{ul}} \frac{Q(T)}{g_u} \exp\left(E_u/kT_{\rm ex}\right) \int T_{\rm b}\, d\upsilon, \qquad (10)$$

where $C_\tau = \tau/(1 - \exp(-\tau))$ is the opacity correction factor. Using $C_\tau = 1$, a source size of 85″ to calculate $\eta_{\rm bf}$ and an excitation temperature of 10 K, the ammonia outflow column density is estimated to be $\sim1.2\times10^{13}$ cm^{-2}. This column density is thus not opacity-corrected and may therefore be underestimated. The ammonia outflow abundance is then calculated as $X(NH_3) = N_{NH_3}/N_{H_2}$ and is found to be $\sim7\times10^{-10}$.

4. Model results: RADEX – a homogeneous model

In this section we use an enhanced version of the RADEX[2] (van der Tak et al., 2007) code to compute the intensities of the narrow components of the transitions observed by Odin, and the intensities of several atomic and molecular transitions that previously have been observed in S140. The RADEX codex applies a very simple method of mean escape probabilities to the radiative transfer and yields results that are similar to those in the large-velocity-gradient approximation, assuming an isothermal and homogeneous medium, but without an implicit assumption of a gradient in velocity. Although much more sophisticated methods of radiative transfer have been used to construct models of the atomic and molecular line emission from this region, it is useful to examine a simple, internally consistent model of a homogeneous cloud that reproduces the principal observed facts. Such a model can be used in particular to assess the role of radiative coupling of molecular excitation to the intense continuum radiation within the PDR. In Sect. 5, these results are compared to the results from a 3D inhomogeneous PDR model that calculates the temperature and abundance distributions, and a multi-zone escape probability method that calculates the level populations and intensity distributions of water and ammonia (Poelman & Spaans, 2005, 2006).

The molecular data files for H_2O and NH_3 have been enlarged, compared with those previously available through the Leiden Atomic and Molecular Database (LAMDA)[3]. Data for the *ortho* and *para* forms of these molecules have been combined into a single file and infrared transitions have been added. Collision rates published by Faure et al. (2007) for H_2 + H_2O and by Faure et al. (2004) for e^- + H_2O are now used. Two different data files have been used to analyse the excitation of NH_3. The smaller includes only the lowest 112 levels of the vibrational ground state and 140 radiative transitions between them. A larger file, derived mainly from the HITRAN[4] database, has also been tested: it contains 2 392 levels and 15 067 radiative transitions, including lines of several ν_2 and ν_4 vibrational bands in the mid-infrared.

We include a simple dust model of the broad-band spectrum (Thronson et al., 1983; Minchin et al., 1995; Ney & Merrill, 1980) at submm and far-infrared wavelengths in order to characterise the internal radiation sensed by the molecules (a detailed description is found in Appendix A of the on-line material).

The principal parameters needed to specify a model are the kinetic temperature T_K and the average number density of molecular hydrogen $n(H_2)$. Our adopted dust model implies $N(H_2) = 4.7\times10^{22}$ cm^{-2} and an average density $n(H_2) = 3\times10^4$ cm^{-3} in a homogeneous, spherical cloud with a source size $L = 0.5$ pc (derivation in Appendix A, on-line material). Unfortunately, this average density is inconsistent with our observations. Although a uniform RADEX model can be constructed based upon this density, this low-density model cannot

[2] The published version will soon include these enhancements, see http://www.sron.rug.nl/~vdtak/radex/index.shtml

[3] http://www.strw.leidenuniv.nl/~moldata

[4] http://cfa-www.harvard.edu/hitran

explain the observed intensities of the pure rotational lines of H_2O and NH_3 unless the line-centre optical depths are of the order of 200 and 100, respectively. Such large opacities would imply significant line broadening through saturation of the emission, which conflicts with the observed narrow profiles.

High densities of 7×10^5 cm^{-3} are found by multitransition CS observations (Snell et al., 1984a), and 5×10^5 cm^{-3} from NH_3 inversion transitions (Ungerechts et al., 1986). We include the CS transitions in our RADEX model in addition to our own observations, and our best fit suggests a mean molecular density of 4×10^5 cm^{-3} and a temperature of 55 K. This suggests that the strongly emitting molecules occupy only a 7% fraction of the volume. The H_2 column density, which is needed to obtain the abundances, $X(\mathrm{x}) = N(\mathrm{x})/N(H_2)$, is calculated from the $N(^{13}CO)$ obtained with RADEX. This column density is also in agreement with $N_{ROT}(^{13}CO)$ found in Sect. 3.1. Using $[^{12}C/^{13}C] = 70$ and $[CO/H_2] = 10^{-4}$ we obtain $N(H_2) = 2.0\times10^{22}$ cm^{-2} for the narrow PDR component.

Table 2 collects the observed intensities and the corresponding values calculated from the model. A source size of 120″, derived in Sect. 2, is used to correct the antenna temperatures T_A^* to Rayleigh-Jeans brightness temperatures T_b according to the scaling in Eq. 6. The estimated abundances and column densities are summarized in Table 3. Note that the best-fitting model of the [C II] $\lambda157\,\mu$m line emission implies a density of carbon ions, $n(C^+) = 7.7$ cm^{-3}. This is taken to be equal to the electron density, which implies an average electron fraction of $X(e^-) = 1.9\times10^{-5}$. This electron fraction is large enough that electron-impact on polar molecules like H_2O must be competitive with H_2 collisions in exciting rotational states. However, the results presented for NH_3 so far neglect electron collisions.

The model reproduces nicely all the observations except the ammonia inversion transitions which are predicted to be lower than the observed intensities. The $^{13}CO(2-1)$ transition is also predicted to be slightly lower than what is observed. These discrepancies may be caused by a co-existing, extended lower excitation gas component, which is not contributing much to the emission of the $^{13}CO(5-4)$ or $NH_3(1_0-0_0)$ lines. Even so, the column densities of C, ^{13}CO and CS agree well with Plume et al. (1994) and Snell et al. (1984a), and the C abundance is also in agreement with Franklin et al. (2008). The water abundance was previously estimated by Snell et al. (2000a) to be 9×10^{-9}, and by Ashby et al. (2000a) to be 2×10^{-8}, both very similar to the abundance calculated by RADEX.

The RADEX model is also tested for higher transitions of H_2O and shows that some lines are sensitive to various effects. For example, the intensity ratio of the 1661 and 1670 GHz lines appears to be sensitive to the total column density. When the internal radiation field is switched off in the models, the intensities of the transitions involving the lowest rotational levels increase slightly, while the intensities of lines involving more highly excited states are diminished. In particular, the 1661 GHz line is enhanced by radiative excitation and is very sensitive to the total column density. This line will appear in absorption if the opacity in the 557 GHz transition is small since photon-trapping is ineffective at column densities around 10^{14} cm^{-2} or less.

The excitation of NH_3 also shows some interesting effects in these models. Due to the rather high density of C^+ ions, the reaction of C^+ with NH_3 will destroy ammonia at a rate exceeding 10^{-8} s^{-1}, which is rapid enough to affect the excitation of the metastable levels involved in several of the inversion transitions near 23 GHz. Indeed, the calculations indicate that the $(J,K) = (3,3)$ inversion transition is a weak maser (cf. Walmsley & Ungerechts, 1983). In addition, NH_3 has strong vibrational transitions in the mid- and near-infrared. When these are included, the intensity of the 572 GHz transition is somewhat suppressed while the lowest inversion transitions are somewhat enhanced.

Table 3. Results of the homogeneous RADEX model for the narrow PDR component: column densities and abundances.[a]

Species x	Column Density N(x) [cm^{-2}]	Abundance X(x)
H_2O	2.0×10^{14}	9.8×10^{-9}
$H_2^{18}O$	$< 4.9\times10^{12}$	$< 2.5\times10^{-10}$
NH_3	1.5×10^{14}	7.5×10^{-9}
^{12}CO	2.0×10^{18}	1.0×10^{-4}
^{13}CO	2.9×10^{16}	1.4×10^{-6}
CS	1.5×10^{14}	7.5×10^{-9}
C	2.0×10^{17}	1.0×10^{-5}
C^+	9.0×10^{17}	4.5×10^{-5}
O	6.3×10^{17}	3.2×10^{-5}

[a] All results for $T_K = 55$ K, $n(H_2) = 4\times10^5$ cm^{-3}, $n(e^-) = 7.7$ cm^{-3}, $N(H_2) = 2.0\times10^{22}$ cm^{-2}.

Table 4. Clumpy PDR model parameters.

size [pc]	n_c(H) [cm^{-3}]	n_{ic}(H) [cm^{-3}]	F^a [%]	l_c^b [pc]	T_{gas} [K]	T_{dust} [K]
0.5	2×10^6	1×10^4	8	0.03	$9-40^c$ $35-195^d$	18- 32[c]

[a] Volume filling fraction of clumps.
[b] Clump size.
[c] Temperatures in clumps.
[d] Temperatures in interclump medium.

5. Model results: clumpy PDR model

A self-consistent physi-chemical 3D inhomogeneous model is used to compute the temperature of the gas and dust, and the abundance distributions inside the clumpy cloud (detailed descriptions are found in Spaans, 1996; Spaans & van Dishoeck, 1997; Poelman & Spaans, 2005). This clumpy PDR model has three free parameters; the volume filling factor F (fraction of the cloud that is occupied by clumps), a clump size l_c, and the clump-interclump ratio $n_c(H)/n_{ic}(H)$. The total hydrogen density $n_H = n(H) + 2n(H_2)$. In the dense clumps, hydrogen is entirely molecular, thus $n(H) = 2n(H_2)$. The PDR model parameters used in this paper are given in Table 4. We use a velocity dispersion of 1.2 km s^{-1} (Zhou et al., 1994) equivalent to a FWHM line width of 2.0 km s^{-1} for an optically thin line. With an opacity of about 5 – 10 the line is broadened by a factor of ∼1.5 – 2 to 3 – 4 km s^{-1}, consistent with our observations. The incident radiation field is taken to be $I_{UV} = 140$ with respect to the Draine (1978) field. The clumps are randomly distributed in the interclump medium and the volume filling fraction is taken to be 8% (Spaans & van Dishoeck, 1997; Ashby et al., 2000a; Poelman & Spaans, 2005). The grid size is 81x81x81, corresponding to a

resolution of 0.006 pc and a total size of 0.5 pc (about 110″ at a distance of 910 pc).

In the PDR computation, each clump is joined smoothly to the inter-clump medium through a power-law $\propto 1/R^2$ density distribution. This envelope contains very little molecular material and the bulk of the impinging radiation field is always absorbed by the clumps and not the inter-clump medium. The definition of the mean H_2 density and the mean molecular abundances X of species x is thus made through $< n >= F n_c + (1 - F)\, n_{ic}$ and $X_{mean}(x) = F\, X_c(x) + (1 - F)\, X_{ic}(x)$ to allow an unambiguous comparison with molecular line observations .

A high molecular hydrogen density of $\gtrsim 1{\times}10^6\,cm^{-3}$ in the clumps is required to match the intensities observed by Odin and SWAS. Note that this clump density is considerably higher than that used by Poelman & Spaans (2005, 2006). The high density and clumpy medium suggested by our PDR model is, however, also supported by previous density estimates. For example, density variations between $10^4 - 10^6\,cm^{-3}$ are necessary to explain the apparent coincidence of the C I and CO ridges as well as the distance between the C I ridge and the bright rim (Hayashi & Murata, 1992). Emission from numerous, small, dense ($10^5 - 2{\times}10^6\,cm^{-3}$) and optically thick clumps of gas, where the number density of clumps decreases with distance from the CS cloud centre close to IRS, is the best explanation of the CS column density variations, as well as the observed opacities and temperatures obtained from multitransition observations of CS (Snell et al., 1984a; Zhou et al., 1994). As molecular hydrogen density in the interclump medium we use $5{\times}10^3\,cm^{-3}$.

Table 5. Resulting abundances with respect to n_{H_2} for the narrow PDR components of water and ammonia from the clumpy PDR model.

Species	Comp.	n_{H_2} [cm^{-3}]	Abundance
H_2O	Interclump	$5.0{\times}10^3$	$8.9{\times}10^{-10}$
	Clump	$1.0{\times}10^6$	$4.8{\times}10^{-8}$
	Mean	$8.5{\times}10^4$	$4.6{\times}10^{-9}$
NH_3	Interclump	$5.0{\times}10^3$	$1.1{\times}10^{-10}$
	Clump	$1.0{\times}10^6$	$4.5{\times}10^{-8}$
	Mean	$8.5{\times}10^4$	$3.7{\times}10^{-9}$

The resulting abundances, with respect to H_2, in the clumps and the inter-clump medium, as well as a mean value over the whole region, are found in Table 5. The mean value is about half than found by RADEX. In the clumps, the water abundances vary between $10^{-7} - 10^{-9}$ with an average of $4.8{\times}10^{-8}$. The low density in the interclump medium results in low water abundances between $1{\times}10^{-11} - 5{\times}10^{-9}$ with an average of $8.9{\times}10^{-10}$. Ammonia is found to have about the same average abundance as water, $4.3{\times}10^{-8}$, in the clumps, while lower by almost an order of magnitude in the inter-clump medium, $1.1{\times}10^{-10}$.

Table 6. Observed and predicted T_A^* in the PDR for o-$H_2O(1_{1,0} - 1_{0,1})$ with SWAS and Odin at the central position.

Satellite	Obs. T_A^* [mK]	Pred. T_A^* [mK]
SWAS	186	120
Odin	416	345

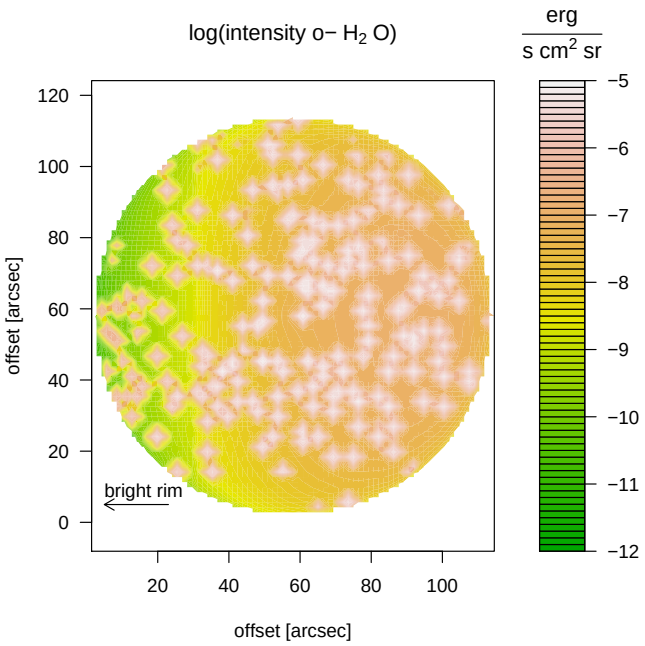

Fig. 6. Result of the PDR high-density model. The water intensity is shown on a logarithmic scale. The ionizing star is located on the left side of the displayed region.

The result from our PDR model is used as input to a three-dimensional multi-zone escape probability method which computes the level populations of *ortho*- and *para*-H_2O (up to ~350 K), CO and NH_3, as well as line intensities and opacities (Poelman & Spaans, 2005, 2006). The excitation due to dust emission is fully included. The dust temperature in the model varies between 18 and 32 K. However, due to geometry the highest T_{dust} is only achieved at the edge of the PDR and the dust component fills only a small part of the region. The bulk of the dust has a temperature of about 25 K and the dust continuum opacity $\lambda 100\,\mu$m is 0.02 or smaller. Results from this code differ at most by 10% compared to other Monte Carlo/Accelerated Lambda Iteration codes. Fig. 6 shows the predicted water intensities on a logarithmic scale. Note that the ionizing star is located on the left side of the displayed region. The peak emission is found about 70 – 80″ from the bright rim, in agreement with our observations of all species.

The resulting model intensities are then used to calculate the expected antenna temperature via

$$T_A^* = \frac{1}{2}\frac{S A_{eff}}{k\,\Delta\nu} = \frac{1}{2}\frac{b\,\eta_{bf}\,\Omega_{mb}}{k\,\Delta\nu}\frac{\lambda^2}{\Omega_A} = \\ = \frac{1}{2}\frac{b\,\lambda^2}{k\,\Delta\nu}\,\eta_{bf}\,\eta_{mb} = \frac{b\,\lambda^3}{2\,k\,\Delta\upsilon}\,\eta_{mb}\,\eta_{bf}\ \ [\mathrm{K}], \qquad (11)$$

where S is the integrated flux density in [erg s^{-1} cm^{-2}], the intensity b is in [erg s^{-1} cm^{-2} sr^{-1}], A_{eff} is the effective antenna area $\eta_A\,A_{geo} = \lambda^2/\Omega_A$ [cm^2], $\Delta\nu$ is the observed line width in Hz, Ω_{mb} is the main beam solid angle in [sr], $\Delta\upsilon$ is the observed line width in cm s^{-1}, and the wavelength λ is in cm. We convolve the intensities to the Odin beam, and in addition predict the intensities of the forthcoming observations of the Herschel Space Observatory using a telescope diameter of 350 cm and a beam-efficiency of 0.7. The observed and modelled SWAS and Odin antenna temperatures for the $1_{1,0} - 1_{0,1}$ transition are provided in Table 6 for the central position. In addition, the predicted antenna tempera-

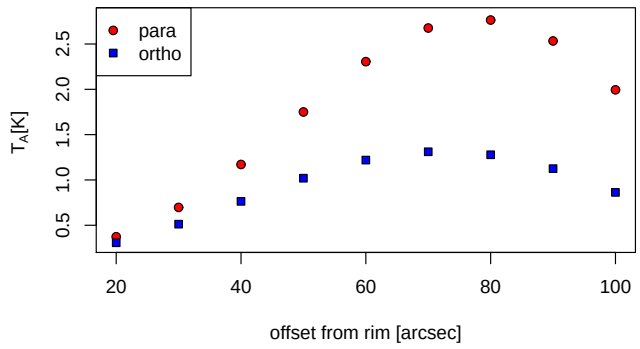

Fig. 7. Predicted antenna temperatures of the *ortho*-$H_2O(1_{1,0}-1_{0,1})$ and *para*-$H_2O(1_{1,1}-0_{0,0})$ transitions for the forthcoming Herschel-HIFI observations along a cut 20 – 100″ from the bright rim.

tures for Herschel-HIFI of both the *ortho*- and *para*-H_2O $1_{1,0}-1_{0,1}$ and $1_{1,1}-0_{0,0}$ transitions along a cut from the bright rim are shown in Fig. 7.

The model *ortho*-water opacities are relatively low with a unweighted mean opacity of 17 over the entire source, with a range between $10^{-5}-800$.

The antenna temperatures from the PDR model agree well with our observations, especially considering uncertainties in source and clump size, as well as the volume filling fraction, which is the main uncertainty and can be varied to obtain slightly higher or lower T_A^*. The dust background continuum is also lower than in the RADEX model, which diminishes the effect of radiative excitation of water. A clumpy medium with high clump densities above $10^6\,\mathrm{cm}^{-3}$ is, however, necessary to produce model antenna temperatures close to the observed values. This is also supported by the resulting low density of $3{\times}10^4\,\mathrm{cm}^{-3}$ obtained by the dust model in Sect. 4 assuming a homogeneous, spherical cloud, which is about 7% of the density in our best fitting model.

A clump-interclump density ratio of ∼100 is in general agreement with observations of dense PDRs. Data in CO, sensitive to $n\sim10^{3-4}\,\mathrm{cm}^{-3}$, and high density tracers like CS and HCN, probing $n\sim10^{5-6}\,\mathrm{cm}^{-3}$, often show an extended morphology in CO lines and clump-like features in the CS and HCN gas. Maintaining such a density contrast is a challenge, since the clumps likely evolve on a sound crossing time of $\sim10^5$ yr (∼ 0.1 pc clumps). If the interclump medium has a much higher temperature or a higher degree of turbulent motion than the clumps, then a rough pressure equilibrium might hold for times exceeding the sound crossing time, supporting our best-fit density contrast. This would, however, require interclump temperatures of $>10^3$ K or turbulent motions of $>3\,\mathrm{km\,s}^{-1}$.

6. Summary and conclusions

We have used the Odin satellite to observe water, ammonia, and carbon-monoxide in the well-known molecular cloud S140. We have simultaneously observed five-point strip maps across the bright rim in S140 of the *ortho*-H_2O $1_{1,0}-1_{0,1}$ and the *ortho*-NH_3 1_0-0_0 transitions, as well as CO(5 – 4) and ^{13}CO(5 – 4). The NH_3 transition has never previously been observed in S140. Observations of $H_2^{18}O$ in the central position resulted in a non-detection at an rms level of 8 mK. As support observation we also mapped ^{13}CO(1 – 0) with the Onsala 20m telescope.

Like CO, the water line-profile is dominated by emission from a NW – SE outflow, however, mainly in the red wing. Strong self-absorption is seen in the optically thick CO emission, while no obvious signs are seen in the *ortho*-H_2O, *ortho*-NH_3 or the almost optically thin ^{13}CO line profiles. In addition to the outflow, our water line shows emission from a more extended NE – SW elongated PDR. Both these components originate approximately around our central position. No additional emission is detected closer to the bright rim or further into the molecular cloud where the water most likely is adsorbed onto dust grains. Close to the bright rim the temperature is most likely too high for a detection of our transition with an upper state energy of 61 K. Instead, higher-lying transitions, observable with the Herschel Space Observatory, will have their peak intensity shifted towards the bright rim (Poelman & Spaans, 2005, 2006). Even closer to the bright rim at a few magnitudes of A_V, water is, however, photo-dissociated by the UV field.

The *ortho*-NH_3 emission seems to emanate from the same high density clumps in the PDR and the outflow as water, but also shows additional emission further into the cloud where the ambient gas temperature drops to about 30 K. Compared to water in the central position, ammonia has a weaker outflow emission in the red wing although similar in the blue outflow. Close to the bright rim, where the outflow contribution to the emission is very low, the water and ammonia line profiles are almost identical, suggesting an origin in the same gas and velocity fields of the PDR. The ^{13}CO line also shows a very similar line profile as H_2O and NH_3 in this position with a narrow line width of $\sim3\,\mathrm{km\,s}^{-1}$.

Abundances, with respect to H_2, in the PDR are estimated both with an enhanced version of the homogeneous RADEX code and with a clumpy PDR model. This model points to low mean water and ammonia abundances in the PDR of $5{\times}10^{-9}$ and $4{\times}10^{-9}$, respectively. In the high-density clumps both the average water and ammonia abundances increase to $5{\times}10^{-8}$. To match the observed PDR antenna temperatures with Odin and SWAS, a clumpy medium is required by the model with a high molecular hydrogen density in the clumps of $\gtrsim1{\times}10^6\,\mathrm{cm}^{-3}$. The resulting RADEX mean abundances are twice as high: $1.0{\times}10^{-8}$ and $8{\times}10^{-8}$ for water and ammonia, respectively, using a molecular hydrogen density of $4{\times}10^5\,\mathrm{cm}^{-3}$ and a kinetic temperature of 55 K. The differences most likely arise from the uncertainty in density, beam-filling, and volume filling of the clumps. The opacity of the narrow PDR component of the $1_{1,0}-1_{0,1}$ transition is constrained by the narrow line width, and is estimated by RADEX to be ∼7. The PDR model also confirm a low water opacity with an unweighted mean opacity of 17 and a model range of $\sim10^{-5}-800$. The mean outflow water abundance, derived from a simple two-level approximation, is higher than in the PDR by at least one order of magnitude, $\sim4{\times}10^{-8}-4{\times}10^{-7}$.

Predictions of antenna temperatures for observations with HIFI are given by our PDR model of the *ortho*- and *para*-H_2O $1_{1,0}-1_{0,1}$ and $1_{1,1}-0_{0,0}$ transitions for nine positions across the bright rim, and are found to peak around 70 – 80″ from the dissociation front in agreement with our observations.

Acknowledgements. We thank Per Bergman, Per Bjerkeli, Magnus Gustavsson, Matthijs Klomp and also Steve Shore and the organizers of the A&A and EDP sciences school: Scientific Writing for Young Astronomers for helpful discussions. Generous financial support from the Research Councils and Space Agencies in Sweden, Canada, Finland and France is gratefully acknowledged.

References

Ashby, M. L. N., Bergin, E. A., Plume, R., et al. 2000a, ApJ, 539, L119
Ashby, M. L. N., Bergin, E. A., Plume, R., et al. 2000b, ApJ, 539, L115
Bergin, E. A. 2003, in SFChem 2002: Chemistry as a Diagnostic of Star Formation, proceedings of a conference held August 21-23, 2002 at University of Waterloo, Waterloo, Ontario, Canada N2L 3G1. Edited by Charles L. Curry and Michel Fich. NRC Press, Ottawa, Canada, 2003, p. 63., ed. C. L. Curry & M. Fich, 63–+
Bergin, E. A., Kaufman, M. J., Melnick, G. J., Snell, R. L., & Howe, J. E. 2003, ApJ, 582, 830
Bergin, E. A. & Langer, W. D. 1997, ApJ, 486, 316
Bergin, E. A., Neufeld, D. A., & Melnick, G. J. 1998, ApJ, 499, 777
Blair, G. N., Evans, II, N. J., Vanden Bout, P. A., & Peters, III, W. L. 1978, ApJ, 219, 896
Boonman, A. M. S., Doty, S. D., van Dishoeck, E. F., et al. 2003, A&A, 406, 937
Boonman, A. M. S. & van Dishoeck, E. F. 2003, A&A, 403, 1003
Cernicharo, J. & Crovisier, J. 2005, Space Science Reviews, 119, 29
Crampton, D. & Fisher, W. A. 1974, Publications of the Dominion Astrophysical Observatory Victoria, 14, 283
Draine, B. T. 1978, ApJS, 36, 595
Emery, R., Aannestad, P., Minchin, N., et al. 1996, A&A, 315, L285
Faure, A., Crimier, N., Ceccarelli, C., et al. 2007, A&A, 472, 1029
Faure, A., Gorfinkiel, J. D., & Tennyson, J. 2004, MNRAS, 347, 323
Franklin, J., Snell, R. L., Kaufman, M. J., et al. 2008, ApJ, 674, 1015
Frisk, U., Hagström, M., Ala-Laurinaho, J., et al. 2003, A&A, 402, L27
Graf, U. U., Eckart, A., Genzel, R., et al. 1993, ApJ, 405, 249
Hayashi, M., Hasegawa, T., Omodaka, T., Hayashi, S. S., & Miyawaki, R. 1987, ApJ, 312, 327
Hayashi, M. & Murata, Y. 1992, PASJ, 44, 391
Keene, J., Blake, G. A., & Phillips, T. G. 1983, ApJ, 271, L27
Larsson, B., Liseau, R., Bergman, P., et al. 2003, A&A, 402, L69
Larsson, B., Liseau, R., Pagani, L., et al. 2007, A&A, 466, 999
Linke, R. A., Goldsmith, P. F., Wannier, P. G., Wilson, R. W., & Penzias, A. A. 1977, ApJ, 214, 50
Liseau, R., Larsson, B., Brandeker, A., et al. 2003, A&A, 402, L73
Melnick, G. J., Ashby, M. L. N., Plume, R., et al. 2000a, ApJ, 539, L87
Melnick, G. J., Stauffer, J. R., Ashby, M. L. N., et al. 2000b, ApJ, 539, L77
Minchin, N. R., Ward-Thompson, D., & White, G. J. 1995, A&A, 298, 894
Minchin, N. R., White, G. J., & Padman, R. 1993, A&A, 277, 595
Neufeld, D. A., Lepp, S., & Melnick, G. J. 1995, ApJS, 100, 132
Ney, E. P. & Merrill, K. M. 1980, AFGL Report, 80, 50
Nordh, H. L., von Schéele, F., Frisk, U., et al. 2003, A&A, 402, L21
Olberg, M., Frisk, U., Lecacheux, A., et al. 2003, A&A, 402, L35
Olofsson, A. O. H., Olofsson, G., Hjalmarson, Å., et al. 2003, A&A, 402, L47
Olofsson, A. O. H., Persson, C. M., Koning, N., et al. 2007, A&A, 476, 791
Persson, C. M., Olofsson, A. O. H., Koning, N., et al. 2007, A&A, 476, 807
Plume, R., Jaffe, D. T., & Keene, J. 1994, ApJ, 425, L49
Poelman, D. R. & Spaans, M. 2005, A&A, 440, 559
Poelman, D. R. & Spaans, M. 2006, A&A, 453, 615
Preibisch, T. & Smith, M. D. 2002, A&A, 383, 540
Rouan, D., Lena, P. J., Puget, J. L., de Boer, K. S., & Wijnbergen, J. J. 1977, ApJ, 213, L35
Sharpless, S. 1959, ApJS, 4, 257
Snell, R. L., Goldsmith, P. F., Erickson, N. R., Mundy, L. G., & Evans, II, N. J. 1984a, ApJ, 276, 625
Snell, R. L., Howe, J. E., Ashby, M. L. N., et al. 2000a, ApJ, 539, L101
Snell, R. L., Howe, J. E., Ashby, M. L. N., et al. 2000b, ApJ, 539, L93
Snell, R. L., Scoville, N. Z., Sanders, D. B., & Erickson, N. R. 1984b, ApJ, 284, 176
Spaans, M. 1996, A&A, 307, 271
Spaans, M. & van Dishoeck, E. F. 1997, A&A, 323, 953
Thronson, Jr., H. A., Lada, C. J., Smith, H. A., et al. 1983, ApJ, 271, 625
Trinidad, M. A., Torrelles, J. M., Rodríguez, L. F., & Curiel, S. 2007, AJ, 134, 1870
Ungerechts, H., Winnewisser, G., & Walmsley, C. M. 1986, A&A, 157, 207
van der Tak, F. F. S., Black, J. H., Schöier, F. L., Jansen, D. J., & van Dishoeck, E. F. 2007, A&A, 468, 627
Walmsley, C. M. & Ungerechts, H. 1983, A&A, 122, 164
Zhou, S., Butner, H. M., Evans, II, N. J., et al. 1994, ApJ, 428, 219
Zhou, S., Evans, II, N. J., Mundy, L. G., & Kutner, M. L. 1993, ApJ, 417, 613

Appendix A: RADEX – construction of a dust model

In order to relate the molecular column densities, N(x) of species x, to fractional abundances, $X(\mathrm{x}) = N(\mathrm{x})/N(\mathrm{H_2})$, a uniform, homogeneous sphere of diameter $L = N(\mathrm{H_2})/n(\mathrm{H_2})$ is assumed here. The adopted physical diameter of the PDR corresponding to an angular diameter of 120″ (Sect. 3) at a distance of 910 pc is 0.53 pc. This is assumed to be equal to the line-of-sight depth.

The observed intensity of the continuum is used to estimate the internal radiation field sensed by the molecules. We construct a simple model of the broad-band spectrum at submm and far-infrared wavelengths in order both to characterise the internal radiation and to estimate the total column densities of dust and hydrogen. Thronson et al. (1983) measured the far-infrared emission of S140 and found a peak flux density of the order of 10^4 Jy slightly shortward of $\lambda 100\,\mu$m in a 49″ beam. Minchin et al. (1995) presented total broad-band fluxes in a 1.′5×1.′5 box. We represent the latter results with a two-component model of thermal emission by dust over a solid angle of $\Omega = 1.9\times10^{-7}$ sr. The main component has a dust temperature $T_{\rm dust} = 40$ K and a long-wavelength ($\lambda > 40\,\mu$m) form of the opacity law

$$\tau_{\rm dust} = 0.0679(100/\lambda)^{1.2}$$

where λ is the wavelength in μm. The opacity law is smoothly matched to a standard interstellar extinction law at shorter wavelengths, which is also used to describe the second component at $T_{\rm dust} = 140$ K. The opacity of the first dust component corresponds to a visual extinction $A_V = 58.8$ mag. The second component has a smaller optical depth $A_V = 0.023$ mag, but is assumed to cover the same solid angle. In addition, the mid-infrared measurements of Ney & Merrill (1980) have been adapted in order to specify the radiation field at even shorter wavelengths. In the calculations, the molecules are assumed to be exposed to an average intensity of continuous radiation

$$I_\nu = B_\nu(T_{\rm CMB}) + \eta\frac{f_\nu^{\rm dust}}{\Omega}$$

where B_ν is the Planck function, $T_{\rm CMB} = 2.73$ K is the temperature of the cosmic background radiation, $f_\nu^{\rm dust}$ is the flux density of the 2-component dust model, $\Omega = 1.9\times10^{-7}$ sr, and $\eta = 0.72$ is a dilution factor to scale the brightness of the dust source to the larger beam area of the Odin measurements. It is important to keep in mind that we observe this strong far-infrared radiation; therefore, the co-extensive molecules must sense it also.

For the adopted interstellar extinction law and a standard gas/extinction ratio,

$$2N(\mathrm{H_2}) = 1.6\times10^{21}A_V\ \mathrm{cm^{-2}},$$

the adopted dust model implies $N(\mathrm{H_2}) = 4.7\times10^{22}$ cm^{-2} and an average density $n(\mathrm{H_2}) = 2.9\times10^4$ cm^{-3} over the source size $L = 0.53$ pc. This average density is, however, inconsistent with the observed molecular line emission in large beams ($\theta \geq 1'$). Although a uniform RADEX model can be constructed based upon this density, the line-centre optical depths of the pure rotational lines of H_2O and NH_3 would be of the order of 200 and 100, respectively. Such large opacities would imply significant line broadening through saturation of the emission, which conflicts with the observed narrow profiles of ~3 km s^{-1}.

Appendix B: Figures and Tables

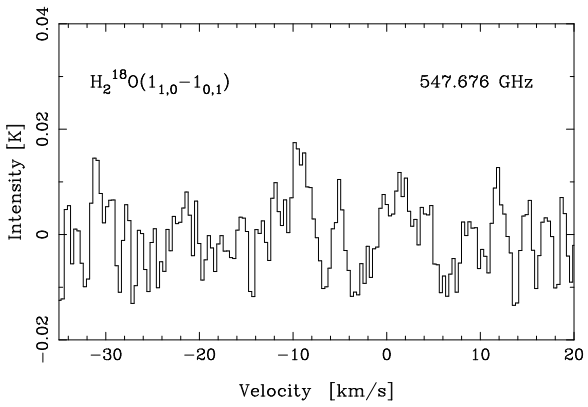

Fig. B.1. Odin observations of $H_2^{18}O$ in the central position.

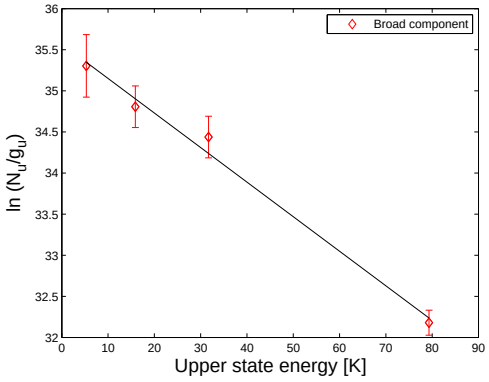

Fig. B.2. Rotation diagram of the broad component of ^{13}CO(1 – 0) with the Onsala 20-m telescope, $J = 2-1$ and $J = 3-2$ from Minchin et al. (1993), and $J = 5-4$ with Odin, producing $T_{\rm ROT} = 24\pm2$ K and $N_{\rm ROT} = (2.5\pm0.4)\times10^{16}$ cm^{-2}.

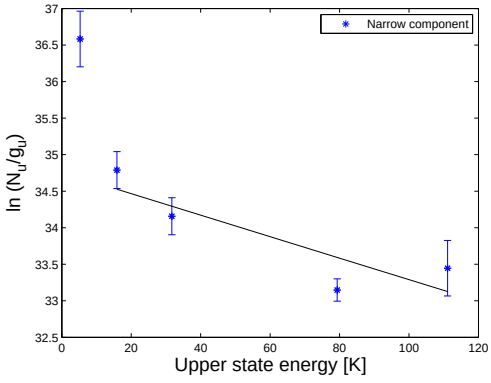

Fig. B.3. Rotation diagram of the narrow component of ^{13}CO(2 – 1) and $J = 3-2$ from Minchin et al. (1993), $J = 5-4$ with Odin, and $J = 6-5$ from Graf et al. (1993), producing $T_{\rm ROT} = 69\pm27$ K and $N_{\rm ROT} = (3.2\pm1.8)\times10^{16}$ cm^{-2}. $J = 1-0$ is not included in the fit.

Table B.1. Observed transitions and their parameters[a] in S140 with the Odin satellite in a five point NE-SW strip.

Species	Transition	Freq [GHz]	E_u [K]	A-coeff [s^{-1}]	Δv [kms^{-1}]	Pos.	v_{LSR} [kms^{-1}]	T_{peak} [mK]	$\int T_A^* dv$ [K kms^{-1}]	rms [mK]	note
H_2O	$1_{1,0}-1_{0,1}$	556.936	61.0	3.46e-3	0.27	1	-8.0	207	0.64	39	
						2	-6.9	517	2.74	68	
						3	-6.6	632	3.34	19	
						4	-7.0	379	1.84	57	
						5	–	–	–	44	No detection.
$H_2^{18}O$	$1_{1,0}-1_{0,1}$	547.676	60.5	3.29e-3	0.34	3	–	–	–	~8	No detection.
CO	5 – 4	576.258	83.0	1.22e-5	0.32	1	-5.4	6 680	47.1	67	
						2	-5.0	11 760	94.2	47	
						3	-5.5	13 240	108.8	43	
						4	-6.6	8 690	60.1	50	
						5	-6.9	2 220	10.1	160	
^{13}CO	5 – 4	550.926	79.3	1.10e-5	0.27	1	-7.8	2 740	8.29	115	
						2	-7.4	5 930	21.4	81	
						3	-7.4	7 110	27.7	61	
						4	-7.6	3 640	13.2	119	
						5	-8.5	1 190	2.5	291	
NH_3	1_0-0_0	572.498	27.5	1.61e-3	0.32	1	-8.0	444	1.18	99	
						2	-7.4	467	1.83	33	
						3	-7.4	588	2.66	29	
						4	-7.3	381	1.86	36	
						5	–	–	–	91	No detection

[a] Transition = the quantum numbers for the transition; Freq = rest frequency of the transition; E_u = the upper state energy; Acoeff = the Einstein A-coefficient; Δv = the velocity resolution; Pos = the strip position from NE to SW. v_{LSR} = the peak LSR velocity; T_{peak} = the observed peak temperature of the transition; $\int T_A^* dv$ = the integrated intensity from the observed spectra not corrected for beam-efficiency or beam-filling; rms = noise.

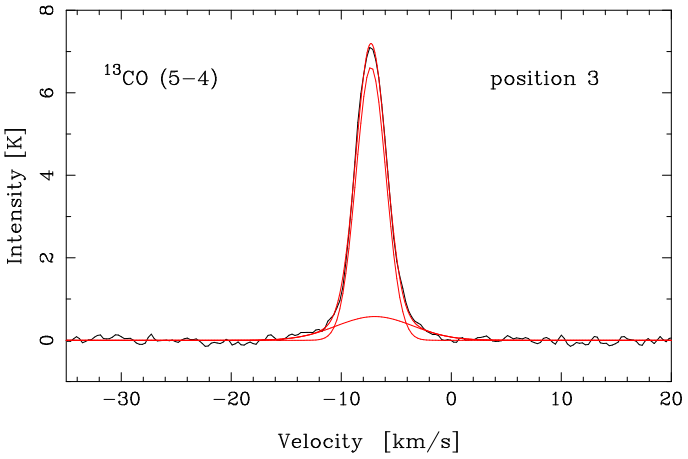

Fig. B.4. Gaussian fits to $^{13}CO(5-4)$ at the central position. The widths, amplitudes and centre velocities are 3.2 km s^{-1} and 8.2 km s^{-1}; 6.610 K and 0.612 K; −7.3 km s^{-1} and −6.8 km s^{-1}, respectively.

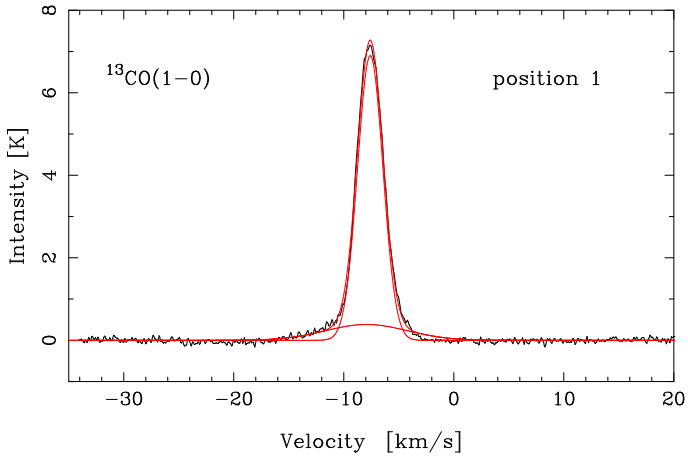

Fig. B.5. Gaussian fits to the convolved (to the Odin 126″ beam) spectra of $^{13}CO(1-0)$ at position 1. The widths, amplitudes and centre velocities are 2.7 km s^{-1} and 8.6 km s^{-1}; 6.982 K and 0.395 K; −7.6 km s^{-1} and −8.0 km s^{-1}, respectively.

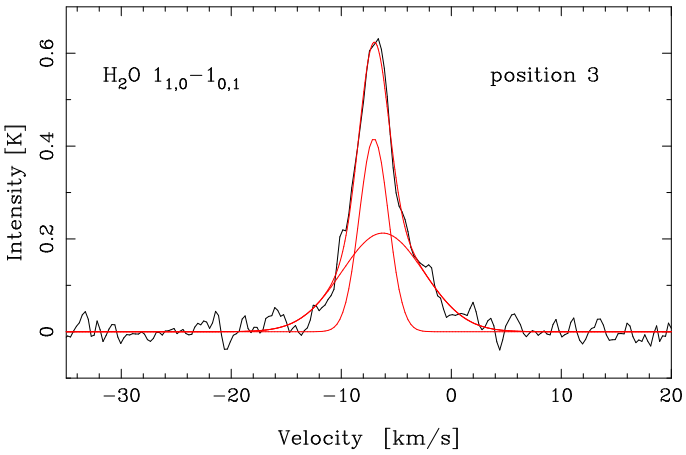

Fig. B.6. Gaussian fits to H_2O at the central position. The widths, amplitudes and centre velocities are 3.1 km s^{-1} and 8.8 km s^{-1}; 416 mK and 213 mK; −7.1 km s^{-1} and −6.1 km s^{-1}, respectively.

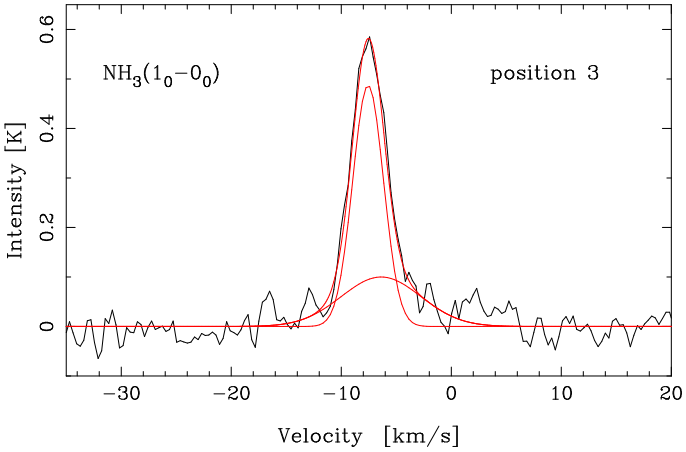

Fig. B.7. Gaussian fits to NH_3 at the central position. The widths, amplitudes and centre velocities are 3.3 km s^{-1} and 8.5 km s^{-1}; 487 mK and 100 mK; -7.6 km s^{-1} and -6.4 km s^{-1}, respectively.

Table B.2. ^{13}CO Gaussian fits[a]. T_b uses a source size for the PDR (narrow component) of 120″→ $\eta_{bf} = 2$, and a source size for the broad outflow component of 85″→ $\eta_{bf} = 3$.

Pos.	v_{LSR} [km s^{-1}]	err [km s^{-1}]	T_{A^*} [mK]	T_b [mK]	err [mK]	Δv [km s^{-1}]	err [km s^{-1}]
1	-7.7	0.04	2 665	5 920	68	2.8	0.08
2	-7.3	0.02	5 877	13 060	56	3.3	0.04
3	-7.3	0.01	6 610	14 690	199	3.2	0.07
3	-6.8	0.33	612	2 040	207	8.2	1.54
4	-7.3	0.03	3 620	8 040	66	3.5	0.07
5	-8.2	0.25	1 124	2 500	282	2.1	0.62

[a] Gaussian fits (including errors) to the spectra in 5 positions. For most positions two Gaussians are needed to fit the spectra. Parameters: v_{LSR} = the LSR velocity at the peak temperature, amp = the amplitude of the Gaussian fit, Δv = FWHM line width.

Table B.3. H_2O Gaussian fits[a]. T_b(PDR) uses a source size of 120″→ $\eta_{bf} = 2$, while T_b(outflow) uses a source size of 85″→ $\eta_{bf} = 3$.

Pos.	v_{LSR} [km s^{-1}]	err [km s^{-1}]	T_{A^*} [mK]	T_b [mK]	err [mK]	Δv [km s^{-1}]	err [km s^{-1}]
1	-7.5	0.10	180	400	12	3.1	0.2
2	-6.9	0.08	340	756	28	3.5	0.3
	-5.4	0.39	171	570	27	8.8	0.7
3	-7.1	0.06	416	924	30	3.1	0.20
	-6.1	0.24	213	710	31	8.8	0.60
4	-7.1	0.08	316	702	44	3.5	0.4
	-6.6	0.8	78	260	45	10.0	4.1

[a] Notation as in Table B.2 .

Table B.4. NH_3 Gaussian fits[a]. T_b(PDR) uses a source size of 120″→ $\eta_{bf} = 2$, while T_b(outflow) uses a source size of 85″→ $\eta_{bf} = 3$.

Position	v_{LSR} [km s^{-1}]	err [km s^{-1}]	T_{A^*} [mK]	T_b [mK]	err [mK]	Δv [km s^{-1}]	err [km s^{-1}]
1	-7.5	0.14	438	973	46	2.6	0.3
2	-7.9	0.25	412	916	200	3.3	0.9
	-6.1	3.4	111	370	160	5.8	2.6
3	-7.6	0.12	487	1 080	90	3.3	0.50
	-6.4	1.4	100	333	92	8.5	4.3
4	-7.4	0.23	321	713	185	3.9	1.2
	-6.8	2.6	61	203	192	8.7	12.1

[a] Notation as in Table B.2 .

Chapter 6

Introduction to Paper IV: The search for the unknown

The most exciting projects of all, are those where we do not know what to expect or what to do. Our goal is to explore, in every way we can possibly think of.

The fact that light travels with a finite speed has an intriguing consequence. When we look far away in the Universe we look back in time.

According to the standard Big Bang model our Universe started out extremely hot and dense about 13.7 billion years ago. The model predicts that it took about 20 minutes to finish the synthesis of the lightest elements, and another 400 million years to form the first stars in the Universe. These first stars then rapidly produced all other elements occurring in nature, and reionised the Universe with their intense radiation. It is during the epoch of the Dark Ages before reionisation that the evolution from the tiny density fluctuation present in the very early Universe to gravitationally collapsed structures took place. Information about this evolution is of very high interest, but no observational data from this time exists today.

A fascinating idea concerns the prospect of actually detecting signals from the cosmic Dark Ages. A detection would for the first time ever give *direct* evidence of a protostructure from the early Universe and would therefore be of utmost importance. However, the search for these signals, described in paper IV, is also extremely difficult. We search for signals from unknown species, from unknown sources, and from an unknown time. The signals are expected to either arise from colliding or collapsing primordial perturbations or from the Cosmic Microwave Background (CMB) radiation scattering off molecules in the pristine gas.

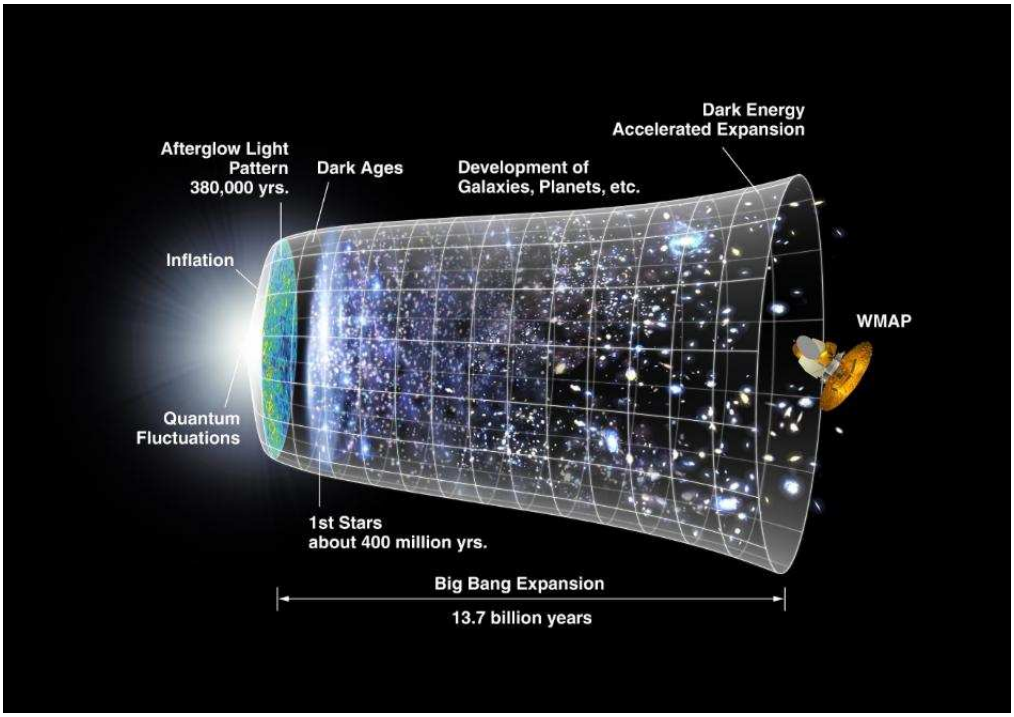

Figure 6.1: The history of our Universe; from the Big Bang, via the Dark Ages, to the formation of the first stars and galaxies to present time (Credit: NASA and WMAP Science Team: `http://map.gsfc.nasa.gov/`).

6.1 The Cosmic Microwave Background radiation

New discoveries are often found by "accident", and the discovery of the relic radiation from the Big Bang radiation is a good example of such serendipity.

Scientists had been puzzled for ages about the origin of the elements and many theories had been proposed. Thermonuclear processes in stars could not account for the high helium abundance in the Universe. New ideas arose when Edwin Hubble discovered the expansion of the Universe in 1929, described by

$$v = H_0\, d, \tag{6.1}$$

where v is the recessional velocity of an object, H_0 is the Hubble constant, and d is the distance. This expansion of the Universe causes the emitted light from a distant object to be redshifted as

$$z = \frac{\lambda - \lambda_0}{\lambda_0}, \tag{6.2}$$

where λ_0 is the wavelength of the transition in a reference frame at rest with respect to us, and λ is the received wavelength. Note, that the shift of wavelengths by the

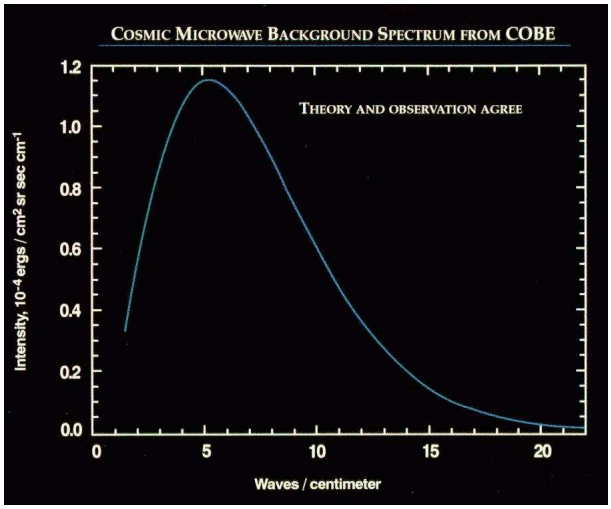

Figure 6.2: The CMB spectrum plotted in waves/cm vs. intensity. The FIRAS data on-board the COBE satellite were taken at 34 positions equally spaced along this curve. The data is a perfect match to a blackbody curve with a temperature of 2.725±0.001 K. The error uncertainties are less than the width of the theoretical curve (`http://lambda.gsfc.nasa.gov/product/cobe/slide_captions.cfm`).

expansion of the Universe is not the same as a Doppler shift, which is caused by the motion of an object through space. The cosmological redshift is caused by the expansion of space itself. A redshift of zero corresponds to the present time, and a high redshift corresponds to an early Universe. The size of the Universe scales with redshift as

$$R = \frac{1}{1+z}, \tag{6.3}$$

where R is the scale factor.

An interesting property of this expansion was discovered by George Gamov in connection with his analysis of primordial nucleosynthesis in 1946. If the Universe is expanding at present, then if we look backwards in time, at some point a long time ago, the Universe must have been extremely small and dense. The idea of an extremely hot and dense Big Bang was born. Together with his student Ralph Alpher, Gamow proposed reactions in the early Universe that could produce all elements in the Universe. They also predicted that the Universe immediately after the Big Bang was so hot that thermonuclear processes occurred everywhere in space. This would create a blackbody radiation *filling the entire space*, which by now would have been shifted towards longer wavelengths due to the expansion of the Universe and correspond to 5 K. Ralph Alpher and Robert Herman, continued to work on this idea and showed a few years later that it was impossible to produce elements heavier than helium in the Big Bang. In his PhD thesis, Alpher also calculated the amount of He to be 25% in the Universe.

The catchy phrase "Big Bang" was ironically coined by an opponent of this theory, Fred Hoyle, on a BBC radio program in 1949. Hoyle worked on nucleosynthesis in stars and had an idea of a non-expanding, steady state Universe. This theory cannot explain all the present day cosmological observations and has been rejected by most scientists.

Apparently unaware of Gamows' idea, Robert Dicke and his student James Peebles also realized in the early 1960s how to explain the high helium abundance in the Universe and began to build an antenna to search for the CMB radiation. Before they were finished, the CMB was inadvertently discovered by Arno Penzias and Robert Wilson in 1965 as an "excess noise" corresponding to 3 K in their measurements using the Bell Labs Horn Antenna (originally designed to relay telephone calls to Earth-orbiting communication satellites). In their discovery paper they state that this radiation was, within the uncertainties of their observations, "isotropic, un-polarized, and free from seasonal variations". This is a perfect portrait of the cosmological principle describing the Universe as homogeneous and isotropic on large scales. Together with general relativity, it constitutes the pillars of cosmology. The interpretation of their results was made by Dicke and Peebles, and in 1978 Penzias and Wilson received the Nobel prize in physics for their discovery.

Shortly after Penzias and Wilson's discovery, it was realized that the CMB radiation already had been indirectly discovered ten years before it was even predicted by Gamow in 1946. It was during the first pioneering years of molecular astronomy, in 1935 – 1939, when Adams and Dunham discovered faint absorption lines identified as CH, CH^+, and CN. The excitation temperature for CN was found to be 2.3 K. Little attention was paid to this derived temperature, which was assumed to be the result of some interstellar excitation process, while in fact it was the CMB radiation.

After many attempts to observe the CMB with ground-based and balloon-borne observations, it became clear that the measurements needed to be done from space above the Earths bright and obscuring atmosphere. NASAs Cosmic Background Explorer (COBE) satellite was launched in November 1989. The first result, only nine months afterwards, showed the most perfect blackbody radiation ever observed, with a peak at 1.9 mm and a temperature of 2.725 K. This was in very strong support to the Big Bang theory.

Moreover, in 1992, COBE showed weak but definite anisotropies, revealing the spatial temperature variations of the CMB. The strongest such anisotropy is the dipole anisotropy. This is a Doppler shift caused by the motion of our solar system relative to the CMB background. The amplitude of this anisotropy is proportional to the ratio of the peculiar velocity to the speed of light. The peculiar velocity of our solar system is measured to be $371\,\mathrm{km\,s^{-1}}$ in a direction towards a point between the constellations of Leo and Crater. Our Sun is also moving around the center of the Milky Way, and the Milky Way is moving relative to our closest

neighboring galaxies called the Local Group. When these velocities are accounted for, it is found that the Local Group moves with a velocity of $627\,\mathrm{km\,s^{-1}}$ relative to the CMB. This kind of velocity will be shown to be very important for the emergence of resonant lines in paper IV.

When the dipole anisotropy is removed, residual small anisotropies are seen with an amplitude of the order of 1/100 000. These tiny fluctuations are the true seeds of stars and structure in the Universe and show the density fluctuations at a redshift of 1 080. All these observations were major achievements and the 2006 Nobel prize in physics was awarded to John Mather and George Smoot who were in charge of these measurements.

The Wilkinson Microwave Anisotropy Probe (WMAP) was launched in June of 2001 to continue the mapping of the CMB temperature fluctuations with higher resolution, sensitivity, and accuracy than COBE. In February 2003, the WMAP team released results from the first year of flight data, and the latest results were released in 2008. Their results, combined with other observations, for example of high redshift supernova, have been used to very accurately determine the Hubble constant H_0 defined in Eq. 6.1, and the age of the Universe to be 13.7 billion years. The amount of matter in the Universe, described by a dimensionless density parameter Ω_{M}, is also very accurately determined. It turns out that 5/6 of all matter in the Universe consists of dark matter and only the remaining 1/6 being ordinary baryonic matter. The dark matter can be detected by the gravitational influences on its surroundings and the Universe as a whole.

In addition, all results points to a flat geometry of the Universe which cannot be attained unless the Universe presently is filled to 72% with an unknown form of collisionless energy. Similar to the matter density, it is described by the dimensionless dark energy density parameter Ω_Λ. This mysterious energy is accelerating the expansion of the Universe at present times, an effect seen in supernovae observations. In the early Universe this energy was very small and has no, or only a very small, effect on our calculations in paper IV.

6.2 Big Bang Nucleosynthesis and molecular synthesis

In the beginning the Universe was extremely hot, but it was cooling because of the expansion as

$$T = T_0\,(1 + z), \tag{6.4}$$

where T_0 is the present temperature of the CMB, $2.725 \pm 0.001\,\mathrm{K}$.

The abundances of the light elements produced in the Big Bang Nucleosynthesis (BNN) depend for instance on the baryon nucleon density, neutrino content, neutrino-antineutrino asymmetry, and the expansion rate of the Universe controlling the temperature. Nucleosynthesis is only efficient within certain temperature ranges. A few minutes after the Big Bang, the temperature had dropped to about

900 billion K, and the existing protons and neutrons could combine into helium and trace amounts of lithium. In the standard BBN model this was over about another 20 minutes later when the temperature had become too low. If we measure the primordial abundances today and compare with predictions, we can test Big Bang models as well as particle physics.

In the standard BBN model, the resulting abundances of the light elements by mass are 75 % H, 25 % He, and trace amounts of lithium. By number, for each 10^{12} H atoms there were $7{\times}10^{10}$ ^{4}He atoms, $2.67{\times}10^7$ D atoms, $1.06{\times}10^7$ ^{3}He atoms, and only 430 Li atoms. All elements were ionised since the temperature was too high to allow combination with electrons. The photons and particles were in close interaction with each-other, keeping their temperatures the same, via Thompson scattering where photons mainly scatter off free electrons.

Approximately 380 000 years after the Big Bang, the temperature had dropped to about 3 000 K. This time is called the epoch of *recombination* with a corresponding redshift of 1 080. The protons could now combine with the electrons and produce neutral hydrogen without being immediately reionised by energetic radiation. Helium started to recombine to He^+ from He^{2+} at a redshift $\sim$6000 and to neutral He at $z{\sim}2\,500$, since higher energy photons are required to ionise this atom. Lithium similarly started to recombine at $z{\sim}10\,000$ to Li^{2+} and the final neutral Li atom appeared around $z{\sim}600$.

The epoch of recombination is also referred to as the *last scattering surface*, describing the Universe as transparent from us to this epoch and completely opaque prior to this time. It is considered to be the last time that the photons scattered off matter, producing the CMB radiation seen with COBE and WMAP.

After the recombination the close thermal coupling between matter and radiation was lost since the number density of free electrons decreased dramatically. From this time forward, the temperatures of matter and radiation started to evolve separately, even though their temperatures are believed to stay about the same to a redshift of $\sim$200.

Also the matter density in the Universe decreases when space is expanding as

$$n = n_0(1+z)^3, \tag{6.5}$$

where n_0 is the average density of hydrogen in the Universe at present time, with a value of only $2{\times}10^{-7}\,\mathrm{cm}^{-3}$. At recombination, the hydrogen density was about $200\,\mathrm{cm}^{-3}$. This is still a very low density medium compared to the conditions in local star forming regions in our Galaxy. Although the low density and the expansion of the Universe acted against molecular formation, di-atomic molecules formed in gas-phase reactions through radiative association as soon as neutral atoms appeared.

These molecules were crucial to the formation of the first stars in the Universe since atomic hydrogen alone cannot cool the gas to below a temperature of about 8 000 K. Molecular hydrogen is able to cool it further to $\sim$500 K and HD to even

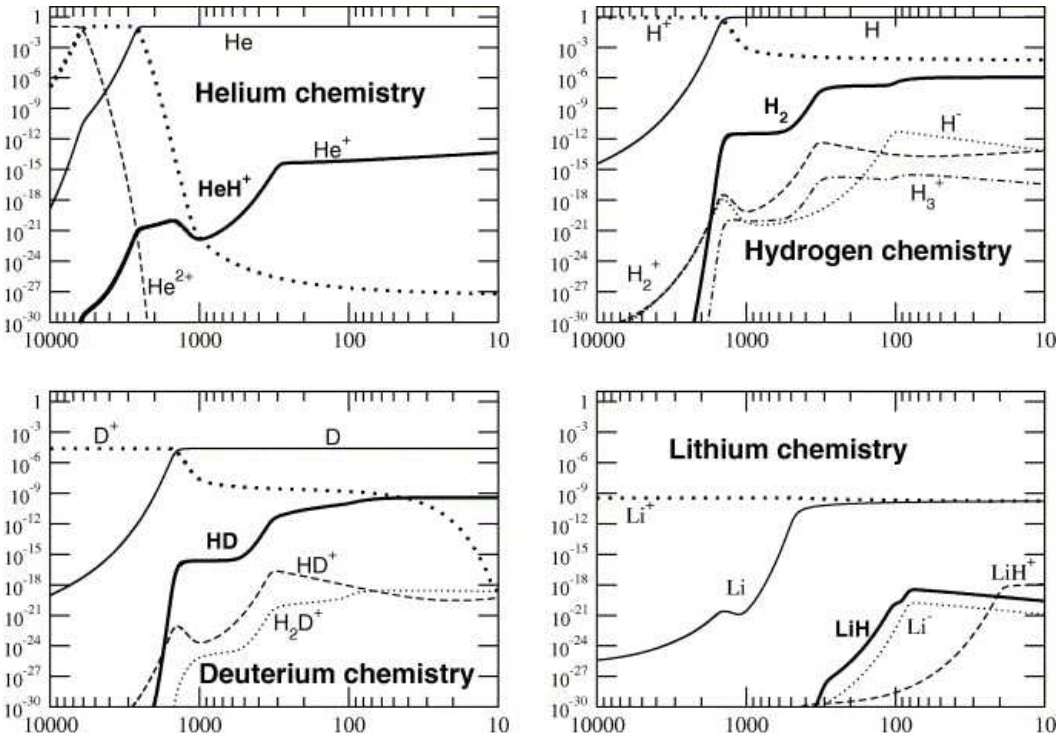

Figure 6.3: Evolution of the chemical abundances with redshift: helium, hydrogen, deuterium and lithium chemistries. The ordinates show the resulting relative abundances using a standard Big Bang Chemistry model (Puy & Signore, 2007).

lower temperatures of ∼100 K. Their abundances are therefore highly interesting and many authors have presented chemical models which follow the evolution of molecular abundances. Even though only a few species and ions are present in the early Universe, there are several hundreds of different reactions to take into account. Several non-standard BBN theories have also been suggested, and in addition there may exist high density regions creating heavier elements than lithium such as flourine. Magnetic fields and turbulence, which are considered very important in star formation today, are believed to be very weak and are therefore most often neglected. A presence of magnetic fields in the early Universe may change substantially the standard theory of star and structure formation during the Dark Ages.

All estimated molecular abundances are therefore very uncertain and may be off by orders of magnitudes. The abundance of HeH^+ relative to H have for example been estimated to be in the range $10^{-8} - 10^{-15}$, the one for LiH between 10^{-11} and 10^{-18}, and H_2 between 10^{-1} and 10^{-8}. The abundance of deuterated molecular hydrogen HD relative to ordinary H_2 is predicted to be within $10^{-1} - 10^{-5}$. Figure 6.3 shows one of these models and their predicted molecular abundances

from Puy & Pfenniger (2008), already presented in Signore et al. (2006) and in Puy & Signore (2007).

6.3 Primordial signals

All observations today of the high redshift Universe are either from high redshift quasars ($z{\sim}6$) and clouds in their line of sight, or the CMB at $z{\approx}1\,080$. No observations from the era of the evolution from primordial gas to the observed structures in the Universe exist. Model-dependent theoretical modelling and computer simulations have therefore been the main tool to follow perturbations of different scales in the primordial medium to predict when and how the first stars and structure in the Universe evolved. This depends on a number of things including the chemistry in the early Universe and dark matter properties. The question is: does anything exist that we can directly *observe* between these redshifts?

The early Universe consisted of an extremely smooth neutral gas of hydrogen, helium, trace amounts of lithium, and a small residual fraction of electrons left over from the recombination. There were also CMB photons and, with time, molecules. Within this smooth gas there were tiny density perturbations present at the epoch of recombination of the order of $6{\times}10^{-5}$ compared to the average density. The perturbations grew with time and eventually collapsed to form the first stars in the Universe about 400 million years after the Big Bang according to the latest WMAP results. All numerical models indicate that these stars must have been very massive, about $100-1\,000\,\mathrm{M}_{\odot}$ and had a very short life before they exploded as a supernova or collapsed into a black hole.

In the early phases of growth the perturbations followed the expansion of the Universe. The density contrast grew linearly with redshift, and at a certain point, a given perturbation was able to resist the expansion and appeared non-moving. This is the turn-around point at which gravity counterbalances the expansion. The perturbation then enters a collapse phase during which the density and temperature quickly increase and a star is eventually formed.

The hierarchical model predicts that small perturbations or galaxies formed first and then merged or accreted gas to form even more massive objects. The latest WMAP results suggest that the reionisation of the Universe took place between $z{\sim}\,6-11$, implying that the first stars must have formed at redshifts higher than this. They are predicted to form in overdense regions of $10^5-10^6\,\mathrm{M}_{\odot}$ at redshifts about $30-40$, while larger mass perturbations would collapse at lower redshift and may be the sources of reionisation. Mass perturbations of $10^{13}-10^{14}\,\mathrm{M}_{\odot}$ are not predicted to have reached their collapse phase yet. Note, that this mass describes the total mass, and the ratio of baryonic to the total matter content is 1/6.

Before the onset of the first stars, there is thus only gas and CMB photons. To be observable the species need to be excited somehow, by increased density or temperature. They may also absorb radiation if temperature gradients exist. The

problem is that collisional excitation is most likely almost non-existing in the linear phase of growth. The average density is very low and decreases towards lower redshift. This implies that collisions between the species are negligible and that excitation is dominated by absorption of CMB photons followed by emission in a process called resonant scattering. This alone is not enough to produce a signal since spontaneous emission has random directions. However, another emerging property of the growing perturbations on all scales, is that with time, they will be increasingly affected by other growing mass-concentrations. This gravitational potential induces peculiar velocities of the primordial clouds, and thus the scattered CMB will obtain the same reference frame as that of the cloud. The CMB will simply be Doppler shifted and produces a frequency dependent signal.

The drawback of this process is that the amplitude of this process is proportional to the ratio of the peculiar velocity of the moving cloud to the speed of light. This ratio is 2×10^{-3} today and decreases with increasing redshift. Thus the signals will be very weak. They will in addition be very broad and therefore even more difficult to detect. Despite their weakness, these lines are the only predicted signals possible from the evolutionary phase before the formation of the first stars, and should therefore not be forgotten.

At the turn-around phase the lines will be stronger and very narrow, and thus this epoch is the most favourable for detection of primordial resonant lines. In the case of colliding or collapsing perturbations in which the density and temperature will increase, "normal" emission and absorption will arise and may be orders of magnitude stronger than the resonant lines. Another problem emerging problem then concerns their size. Perturbations with higher than average density or temperature will most likely only exist in smaller parts of larger low density clouds. These objects are located extremely far away and will therefore only fill a very small fraction of the beam of our receiving antenna, thereby diluting the signal by many orders of magnitude. If a small cluster of objects could be observed, the possibility of a detection increases. Predictions of expected emission or absorption have to take many considerations into account, resulting in very uncertain results.

Two previous observational attempts were made in 1993 and 2002 without success in the search for resonant lines from the Dark Ages. We now want to continue the search and further develop the analysis.

6.4 Results of Paper IV

Our aim is to observationally investigate the previously unexplored epoch of Dark Ages in order to constrain cosmological models of star and structure formation as well as the chemical evolution.

1. Since any signals from this epoch are expected to be very weak, we have as a first step in our searches used the Odin satellite in order to avoid spectral

line contamination from the terrestrial atmosphere.

2. We have performed spectral line surveys towards six positions without any known sources of emission in the search for primordial lines from the Dark Ages. Considering both standard BBN, as well as inhomogeneous and non-standard BBN, the most likely species to search for are H_2, H_2^+, H_2D^+, HD, HD^+, HeH^+, LiH, LiH^+, CH, CH^+, OH, OH^+, NH, HF, H, C, O, N, and F.

3. The first survey covered a broad band of 31 GHz between 547 – 578 GHz towards two positions with fixed reference positions. The second survey covered 11 GHz in the bands 542.0 – 547.5 GHz and 486.5 – 492.0 GHz towards four positions.

4. No lines are detected, and hence the results are upper limits in terms of noise level. Typical 1σ values are 5 – 20 mK in the 11 GHz survey, and 20 – 60 mK in the 31 GHz survey.

5. The major improvement made by the Odin observations compared to the previous attempt in 1993, is the broad bandwidth covered. In this way a wide range of redshifts can be explored for a number of atomic and molecular species.

6. We have taken into account the unknown sizes of the clouds testing a new observational strategy in the second survey. Here we have observed towards four positions in a sequence with different angular distances between the reference and signal positions.

7. We predict the intensities of HeH^+ resonant lines from different redshifts.

8. Our analysis shows that at low densities and equilibrium of temperatures, the only possible signal is from resonant scattering between CMB photons and matter moving with respect to the expansion of the Universe. These signals may at most be of the order of a few mK at low frequencies around 100 GHz, and orders of magnitude lower at higher frequencies. At both high and low frequencies, emission or absorption lines may be detected from higher density and temperature regions arising from colliding or collapsing primordial perturbations.

9. The Odin observations can be considered as pilot studies for deep searches with future much more sensitive antennas such as the Herschel Space Observatory which has orders of magnitude higher sensitivity, or interferometer arrays as ALMA. Our observing methods and resulting limits, paired with a sensitivity analysis taking into account the evolution of primordial perturbations, should be a valuable input to the planning of these observations.

Paper IV

The first spectral line surveys searching for signals from the Dark Ages

Carina M. Persson, R. Maoli, P. Encrenaz, Å. Hjalmarson, M. Olberg, G. Rydbeck, M. Signore, U. Frisk, Aa. Sandqvist, and J-Y. Daniel

Intended for Astronomy & Astrophysics (2009)

Astronomy & Astrophysics manuscript no. primol
December 10, 2008

The first spectral line surveys searching for signals from the Dark Ages

C.M. Persson[1], R. Maoli[2,3], P. Encrenaz[4], Å. Hjalmarson[1], M. Olberg[1,5], G. Rydbeck[1], M. Signore[4]
U. Frisk[6], Aa. Sandqvist[7], and J.Y. Daniel[3]

[1] Onsala Space Observatory (OSO), Chalmers University of Technology, SE-439 92 Onsala, Sweden
e-mail: carina.persson@chalmers.se
[2] Department of Physics, University of Rome "La Sapienza", Pl. A: Moro 2, 00185, Roma, Italy
[3] Institut d'Astrophysique de Paris, 95 bis boulevard Arago, 75014 Paris, France
[4] LERMA , Observatoire de Paris and U.P.M.C., 61, av de l'Observatoire, 75014 Paris, France
[5] SRON, Landleven 12, NL-9747 AD Groningen, The Netherlands
[6] Swedish Space Corporation, PO Box 4207, SE-171 04 Solna, Sweden
[7] Stockholm Observatory, AlbaNova University Center, SE-10691 Stockholm, Sweden

Draft December 10, 2008

ABSTRACT

Aims. We want to observationally investigate the cosmic Dark Ages in order to constrain star and structure formation models, as well as the chemical evolution in the early Universe.
Methods. We attempt to detect spectral line signals from atoms and molecules in primordial perturbations at high redshifts. Since these signals will be very weak, we have as a first step in our searches used the Odin⋆ satellite in order to avoid spectral line poisoning from the terrestrial atmosphere. We have performed two sets of spectral line surveys towards several positions, which may be considered as pilot studies for future more sensitive observations. The first survey covered the band 547 – 578 GHz towards two positions. The second survey covered the bands 542.0 – 547.5 GHz and 486.5 – 492.0 GHz selected to test different sizes of the primordial clouds.
Results. No lines are detected at an rms level of 13 – 20 and 5 – 8 mK for the two surveys, respectively. The broad bandwidth covered allows a large redshift range to be explored for a number of atomic and molecular species. Our sensitivity analysis shows that resonant scattering lines will be observable only at frequencies below 200 GHz, while thermal emission or absorption lines from colliding or collapsing primordial perturbations may be possible to detect at both high and low frequencies.

Key words. cosmology: early Universe – cosmology: large-scale structure of Universe – cosmology: observations – line: formation – line: identification – submillimeter

1. Introduction

One of the most important topics in astronomy today concerns the formation of the first stars and structure formation in the Universe. The cosmic microwave background radiation observed by NASAs Cosmic Background Explorer[1] (COBE) satellite and the Wilkinson Microwave Anisotropy Probe[1] (WMAP) shows small density fluctuations at a redshift of ∼1100 and a temperature of ∼3000 K. After this epoch of recombination the Universe became neutral and entered the cosmic Dark Ages which did not end until the formation of the first stars and quasars, which are believed to have reionised the Universe. During this time the transition from the small density fluctuations left over from the Big Bang to strong non-linear growth took place.

The main method to obtain information about physical and chemical conditions in star forming regions is by means of atomic and molecular line observations. Molecular observations of high redshift objects have indeed been performed, for example by Bertoldi et al. (2003) where high excitation CO is found in a Sloan Digital Sky Survey quasar at z = 6.4. Other CO observations include observations of a damped Lyman-α system at $z = 2.4$ (Srianand et al., 2008), in a field containing an over-density of Lyman break galaxies at z = 5.1 (Stanway et al., 2008), and the detection of a massive CO reservoir at $z = 3.9$ (Papadopoulos et al., 2001). Recently an unusually high amount of hydrogen was found in a 14 Mpc region surrounding a young galaxy at z = 4.9 (Frye et al., 2008). However, no observational evidence exists at all from the cosmic Dark Ages at even higher redshifts or during the earliest epochs of the first star formation.

Model-dependent theoretical modelling and computer simulations have therefore been the main tool to follow perturbations of different scales in the primordial medium to predict when and how the first stars and structure in the Universe evolved. This depends on a number of parameters including the chemistry in the Early Universe and the properties of dark matter. The chemistry constitutes a very important part in the Early Universe since star formation requires a cooling mechanism provided by the molecules.

The standard Big Bang Nucleosynthesis (BBN) model predicts the formation of H, D, He and Li a few minutes after the Big Bang (e.g. Steigman, 2007). Their primordial abundances

Send offprint requests to: carina.persson@chalmers.se

⋆ Odin is a Swedish-led satellite project funded jointly by the Swedish National Space Board (SNSB), the Canadian Space Agency (CSA), the National Technology Agency of Finland (Tekes) and Centre National d'Etudes Spatiales (CNES). The Swedish Space Corporation was the prime contractor and also is responsible for the satellite operation.

[1] http://lambda.gsfc.nasa.gov/

depend only on the density of baryons which has been measured with high precision, $\Omega_b = 0.0462 \pm 0.0015$ (Komatsu et al., 2008). In the expanding and cooling Universe, molecular synthesis of for example H_2, H_2^+, HeH^+, HD, HD^+, LiH, and LiH^+, could begin as soon as neutral atoms appeared, attaining maximum abundances around redshifts of $200-400$ depending on species. The molecular primordial abundances depend on many parameters and many attempts have been made to follow the chemical evolution during the Dark Ages, with results that often differ by orders of magnitude (e.g. Lepp & Shull, 1984; Puy et al., 1993; Galli & Palla, 1998, 2002; Lepp et al., 2002; Puy & Signore, 2007; Schleicher et al., 2008; Sethi et al., 2008).

In addition, there also exist non-standard BBN models. An important class of these non-standard scenarios supposes that the baryons were spatially inhomogeneously distributed during the epoch of nucleosynthesis. In the framework of these inhomogeneous BBN models, there were small regions in the early Universe with a high baryon density where heavy elements could form already during the primordial nucleosynthesis (Applegate et al., 1987; Rauscher et al., 1994; Kurki-Suonio et al., 1997; Lara et al., 2006). Primordial chemistry of these heavy elements has been poorly studied, although Puy et al. (2007) analysed the possibility to form molecular fluorine HF, and more recently Vonlanthen & Puy (2008) calculated the possible amounts of hydride molecules, such as CH, OH, NH, and their respective molecular ions.

To be able to discriminate between the proposed models of structure formation and primordial chemistry we need to *test theory with observations* from the Dark Ages. We do know that during this epoch, the Universe is filled with atoms, molecules, ions, electrons and Cosmic Microwave Background (CMB) photons. The question is if these species have high enough abundances to produce a detectable signal. Since the average density is predicted to be very low, $n_H \sim 0.2\,\mathrm{cm}^{-3}$ at $z \sim 100$ and decreasing towards lower redshift, excitation is dominated by absorption of CMB photons followed by spontaneous or stimulated emission in a process known as resonant scattering. This alone is not enough to produce a signal since the spontaneous emission scattering has random directions. However, another emerging property of the growing perturbations on all scales is, that with time they will be increasingly affected by other growing mass-concentrations. This gravitational potential induces peculiar velocities of the primordial clouds, and thus the scattered CMB will obtain the same reference frame as that of the cloud. The cross-sections for this scattering are several orders of magnitudes larger than the Thomson scattering between CMB and electrons, and as a result of the frequency dependence of the cross-sections, resonant rotational or rotational-vibrational lines will appear.

Since the original idea by Dubrovich (1977) a number of papers have already analysed the possibility of detecting the resonant lines (e.g. Maoli et al., 1994, 1996; Shakhvorostova et al., 2003; Núñez-López et al., 2006; Dubrovich et al., 2008) and two previous observational attempts have been made without success (de Bernardis et al., 1993; Gosachinskij et al., 2002). The main problems are the expected very weak signals from unknown species in unknown sources at unknown redshifts. The amplitude and width of the lines are also uncertain and depend, in addition to the density of the species, on the dynamical phase of the primordial perturbation which is a function of mass and redshift. All these issues guarantee extremely difficult observations.

Possible signals from the Dark Ages may not only be caused by resonant scattering, since the growing potentials may further induce adiabatic heating as well as shock heating of colliding primordial clouds (e.g. Barkana & Loeb, 2001; Santoro & Shull, 2006; Johnson & Bromm, 2006). This introduces for the first time emission or absorption from overdense or high temperature regions. During the collapse phase there will also be emission of resonant lines which does not depend on peculiar velocities. However, many considerations have to be taken into account to predict all these types of emission, with uncertain results.

We emphasise, however, that every possibility to obtain observations from the Dark Ages should be seriously considered. A detection would be extremely important and would allow *direct* evidence of a very high redshift protostructure within a wide range of angular sizes, from arcsecond to arcminute scales, depending on cosmological model. These small scales are not observable in the CMB anisotropies due to the finite depth of the last scattering surface. The "primordial spectral lines" will also probe the chemistry throughout a wide range of redshifts, the heating and cooling processes as well as the dynamics of the primordial clouds before and during the gravitational collapse of a protostructure. Even upper limits would be very valuable in order to constrain all of the above mentioned issues. Thus, with this method, new otherwise unobtainable, information on star and structure formation and their consequent evolution during the Dark Ages epoch can be obtained.

Given the expected weakness of the lines, ground observations are very limited by the terrestrial atmospheric lines. The ozone molecule, O_3, including all the isotopes ^{16}O, ^{17}O and ^{18}O, emits numerous lines. Moreover, most of the vibrationally excited lines can not be found in catalogues. Observations with the IRAM 30-m telescope (de Bernardis et al., 1993) experienced much difficulties from these lines at a low level. It is therefore of great importance that these observations are performed from space. Interferometer observations may also be of interest for searches like this, due to the many advantages for rejecting both broad band and narrow atmospheric emissions.

As a first test, we have chosen to use a satellite to search for and put upper limits on primordial signals from the Dark Ages. The satellite is required to have tunable receivers in order to cover a broad spectral band, which is absolutely necessary in order to explore a wide redshift range. In this work, we have used the only available satellite with the above mentioned requirements: the Odin satellite (Nordh et al., 2003). This satellite has the unique capability to cover a broad spectral band with a high spectral resolution of about 1 MHz using the tunable SSB receivers.

A very important aspect of this work is to test different observational strategies to prepare for future observations with more sensitive telescopes also in other wavelength regions, such as the Herschel Space Observatory[2] to be launched in 2009. Other interesting facilities to consider are the 50 m Large Millimeter Telescope[3] (LMT), the Combined Array for Research in Millimeter-Wave Astronomy[4] (CARMA), the Atacama Large Millimeter Array[5] (ALMA), and the IRAM Plateau de Bure Interferometer[6].

In the second part of this work, we assume a ΛCDM cosmology, and make an attempt to predict the observed line width and amplitude of resonant HeH^+ lines. Even though these pre-

[2] http://herschel.esac.esa.int/
[3] http://www.lmtgtm.org/
[4] http://www.mmarray.org/
[5] http://www.alma.info/
[6] http://www.iram.fr/

dictions have large uncertainties, our observations provide limits for any cosmological/chemical model.

2. The Odin observations

Our approach in all observations has been to perform spectral line surveys in order to cover a wide redshift range. Our objects are located at an unknown redshift and the expansion of the Universe causes the frequency of an emitted photon to be redshifted as

$$\frac{\nu_0}{\nu_{\rm obs}} = 1 + z\,, \tag{1}$$

where ν_0 is the rest frequency, $\nu_{\rm obs}$ the observed frequency of the transition, and z is the redshift. When we choose an observation frequency, we thus determine the emitting redshift for each transition given by Eq. 1. Each transition may also be detected at different frequencies, emitted from several objects at different redshifts along the line of sight. This is similar to the the Lyman α forest where clouds in the line of sight absorb the light from bright quasars and galaxies. The strong frequency dependence of the scattering and emission processes allows a separation of the signals.

We search for any molecule or atom that may be present in the high redshift Universe. This includes molecules that form from the primordial elements H, D, He and Li (Steigman, 2007) such as: H_2, H_2^+, H_2D^+, HD, HD^+, HeH^+, LiH and LiH^+. There are also suggestions that lines from neutral hydrogen H could be seen during the time of recombination and at later times (e.g. Rubiño-Martín et al., 2005). Moreover, non-standard BBN models predict heavy nuclei such as carbon, oxygen, nitrogen, and flourine, which may have created molecules like CH, OH, NH, HF, and their respective molecular ions (Puy et al., 2007; Campos et al., 2007; Vonlanthen & Puy, 2008). In addition, regardless of BBN model, the first generation stars of a primordial composition formed at $z \gtrsim 10$ might quickly have polluted the medium with small amounts of metals with subsequent chemistry.

If we assume a cosmological model and a primordial chemistry, then there will exist a certain redshift range where the molecule is able to exist.

$$1 + z_f < 1 + z < 1 + z_d\,, \tag{2}$$

where z_f is the formation redshift, $\sim 100 - 400$, and z_d is the dissociation redshift which is located where the energetic radiation from new-born stars and quasars destroy the molecules. This allows an estimate of the frequency ranges in which a line can be expected to be observable. The redshift ranges from where the lowest rotational lines of HeH^+, HD and H_2 fall in our observed bands are found in Table 7 (on-line material).

At redshifts higher than about $z \gtrsim 200$ the matter and radiation temperature are expected to be the same due to Compton scattering, evolving as

$$T_{\rm CMB} = T_{\rm K} = T_0(1 + z)\,, \tag{3}$$

where $T_0 = 2.725\,{\rm K}$ is the cosmic microwave background radiation (CMB) today, as measured by the FIRAS instrument onboard the COBE satellite (Fixsen et al., 1996). At redshifts below 200, the matter temperature evolves in line with adiabatic expansion which implies a kinetic temperature decrease faster than for the CMB (Glover, 2005)

$$T_{\rm K} = \frac{T_0}{1 + 200}\,(1 + z)^2. \tag{4}$$

The gas will eventually be heated from collisions and collapse of the growing perturbations, and eventually from the first stars and quasars.

The coupling of the excitation temperature to the radiation or matter temperature differs with species. Polar molecules like HeH^+ probably continue to have $T_{\rm ex}$ coupled to the CMB temperature, while H_2 may remain more strongly coupled to the matter temperature. There are also situations where the excitation temperature may depend on molecular formation processes, by which for instance primordial H_2 may remain superthermal relative to the matter temperature.

The strongest emitting transitions are those with upper state energies of the order of the excitation temperature at the emission redshift. Detection of rotational-vibrational lines, with upper state energies of thousands of Kelvin, are therefore only expected for very high redshift sources, or from from colliding or collapsing high-temperature regions at lower redshifts. In such regions the density may be increased above average. The increased collision rate in these regions will drive the level populations and the excitation temperature towards the matter temperature. Since the kinetic temperature is lower than the CMB at low redshifts, this will force the excitation further away from equilibrium with the radiation, and should enhance spectral absorption distortions.

A detection of several spectral lines is required to secure a detection and a redshift of an emitting source. For rotational lines, this is often only possible when observing at frequencies below $100 - 200\,{\rm GHz}$ since the spectral distance between these lines is rather wide even for high redshifted sources. It is thus more likely that a single transition from each object would be seen in the Odin observations. The rotational-vibrational transitions would, however, be more closely spaced, but have a lower probability of detection.

Neither the amplitude nor the line widths are known and therefore we use high spectral resolution to enable detection of narrow lines, and later re-bin the data to lower resolution. The choice of spectral resolution also affect the noise level seen from the radiometer formula

$$T_{\rm rms} = \frac{T_{sys}}{\sqrt{t\,\Delta f}}\,K\,, \tag{5}$$

where Δf is the frequency resolution of the spectrometer, t is the integration time, T_{sys} is the system temperature from the whole system, which includes the receiver noise, and K is a constant which depends on observation strategy.

Table 1. Coordinates of observations.

Position	R.A. ($J2000$)	DEC. ($J2000$)
Hot Spot 1	$05^h26^m00^s0$	$-48^\circ\,30'\,00''.0$
Hot Spot 2	$05^h09^m36^s0$	$-43^\circ\,24'\,00''.0$

The expected signals most likely originate from every direction in the sky, even though they will be stronger from rare high density peaks. However, we need to observe positions with as low contamination as possible from any known source, and in addition they must be observable with the Odin satellite for long periods. For these reasons we have observed towards two of the WMAP hot spots in the CMB radiation, out of the Galactic plane. The coordinates are listed in Table 1.

Two different sets of observations were performed with different observation strategies as described below. The first survey was performed in 2004 and the second in 2006 – 2007.

The Odin 1.1 m offset Gregorian telescope has a circular beam at 557 GHz with a width (FWHM) of 2.′1 (Frisk et al., 2003). Being outside the atmosphere, and with an exceptionally high main beam efficiency, $\eta_{\rm mb} = 0.9$, our intensity calibration is very accurate. The calibration procedure (the chopper wheel method) of the Odin satellite is described in Olberg et al. (2003). The intensity scale in the figures is expressed in terms of antenna temperature $T_{\rm A}^*$. The reconstructed pointing offset was $\lesssim$15″ during most of the time.

Two different single sideband (SSB) receivers, with a typical side-band suppression of $\lesssim$20 dB, were used simultaneously in combination with one auto-correlator (AC) and one acousto-optical spectrometer (AOS). The bandwidths for the AOS is 1.040 GHz, and 690 MHz for AC, with a frequency resolution of 0.62 and 1.0 MHz for the AOS and AC, respectively. Our spectral resolution thus give $\Delta\nu/\nu \approx 2\times10^{-6}$ at $\nu = 545$ GHz. The Odin average system temperature is around 3 300 K (SSB) and therefore many hours of observations are demanded to produce sensitive observations. The resulting noise levels may very well be too high to allow a detection, but the intensity of the lines is really not known. We have therefore taken a pure observational approach in the search for any signal from whatever redshift. If no detection is obtained, the resulting upper limits will be used as input to the noise levels required in future observations.

In each LO setting, the resulting AOS spectra have a very stable baseline except at the band edges where the calibration spectra exhibit a steep increase. The noisy edges are excluded, and then a first or second order polynomial baseline is subtracted before we join all spectra together to form a long spectrum. The AC consists of 7 bands of 100 MHz each in each setting. We subtract a linear baseline in each band before we align and average all spectra. All averages are then joined to form a continuous spectrum.

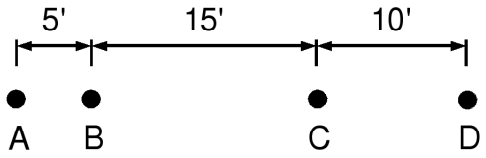

Fig. 1. Observation strategy during the second spectral survey 2006/07. The Odin beam has a width of 2.′1.

Table 2. Observation strategy 2006/07: every weekend we observed during ∼40 orbits with one frequency setting towards four positions, A – D, as listed below and shown in Fig. 1.

		Sig	Ref	Spacing
1	10 orbits	A	B	5′
2	10 orbits	B	C	15′
3	10 orbits	C	D	10′
4	10 orbits	D	A	30′

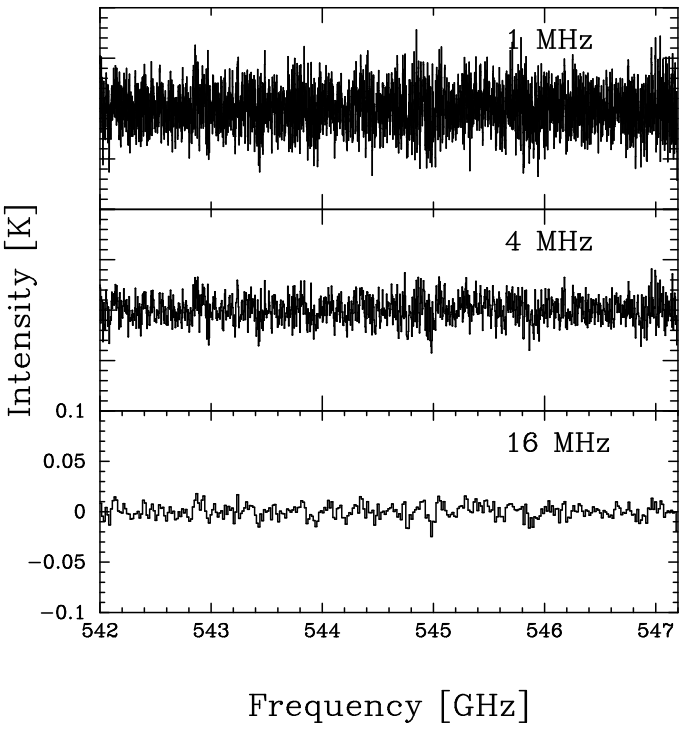

Fig. 2. Examples of the resulting spectra: 2006/07 observations towards Hot Spot 1 (position A) with B used as reference and shown with three different resolutions: 1, 4, and 16 MHz. The Odin $T_{\rm mb}$-scale is related to the flux density by $F_\nu/T_{\rm mb} = 2\,400$ Jy/K at 543 GHz.

2.1. Observation strategy summer 2004

Our first goal was to cover as wide a frequency band as possible. We were awarded 337 orbits (1 orbit∼1 hour of observation) and performed independent position switching observations towards the two positions listed in Table 1, using reference positions offset by −45 arcminutes in declination. Using simultaneous observations covering 15.5 GHz each with the AC (∼563 – 578 GHz) and AOS (∼547 – 563 GHz) the total observed frequency band is 31 GHz covering 547 – 578 GHz. We spent 5 orbits for each Local oscillator (LO) setting and the step size in frequency was 0.5 GHz. The settings and steps were the same as in the first spectral line survey performed by the Odin satellite towards the Orion KL nebulae (Olofsson et al., 2007; Persson et al., 2007).

2.2. Observation strategy winter 2006/07

In the next attempt during nine weekends in winter 2006/07 and one weekend in Aug 2007 (in total 464 orbits) we changed our observational strategy. We wanted to lower the noise compared to what we obtained in the 2004 observations, but still needed to cover a wide frequency band. Since the sizes of the primordial objects are unknown, we also wanted to test different spacings between the signal and reference positions in order to avoid subtraction of the signal if present in both positions. A compromise of the above requirements resulted in the scheme shown in Fig. 1. Four positions, A – D, were observed where position A is the previously Hot Spot 1 observed during 2004. The minimum offset was determined by the Odin beam size of 2.′1, and thus we chose the following offsets: −5′, −15′, and −10′ in DEC, keeping the same R.A. During 10 weekends of observations (∼40 orbits/weekend) we observed all four positions with one frequency setting each weekend. Table 2 shows how we performed

the observations: 10 orbits towards each pair of positions were observed in a sequence. First towards position A with B as reference (AB), then B with C as a reference (BC), C with D as reference (CD), and finally D with A as a reference (DA). Thus, in total we have ten orbits/setting/position for ten different LO settings.

As in the first observation run in 2004, we performed simultaneous observations with the AC and the AOS, but covering other frequency ranges. The final results are spectral surveys in the frequency ranges 542.0 – 547.5 GHz (AOS) and 486.5 – 492.0 GHz (AC) towards four positions.

Table 3. Upper limits from observations during 2004 using 1, 4 and 16 MHz frequency resolution. The limits are for the data observed with the AOS(AC) and for frequencies between 547 – 563 (563 – 578) GHz. Note that these values are preliminary.

Position	1σ [mK]	Peak Intensity [σ]
1 MHz resolution		
HotSpot 1	37 (88)	3.5 (3.0)
HotSpot 2	40 (83)	4.1 (3.5)
4 MHz resolution		
HotSpot 1	23 (46)	3.3 (2.8)
HotSpot 2	25 (44)	2.9 (3.1)
16 MHz resolution		
HotSpot 1	14 (27)	3.4 (3.6)
HotSpot 2	16 (25)	3.2 (3.1)

3. Results

No lines were detected and thus we are limited to measure the noise level and use 5σ as upper limits of the amplitudes of the signals. The noise is rather stable over the covered band of all surveys, with a few exceptions where we had loss of observation time. We therefore measure the 1σ noise level across the total band covered, towards each position. We have re-binned the AOS data to the AC frequency resolution, 1 MHz, and then re-binned both AOS and AC to resolutions of 4 and 16 MHz, with an example shown in Fig. 2. This should lower the noise by a factor of 2 and 4, respectively, if the noise is Gaussian distributed. Our measurements, however, do suffer from baselines at a low level which prevents the noise to follow Eq. 5 exactly. All 1σ results are found in Tables 3 and 5, which also include the peak intensity of the noise given in terms of the measured σ.

Figures 6 and 7 (on-line material) show the original AOS spectra used to produce Fig. 2. The intensity is plotted vs. channel numbers and shown for all ten frequency settings.

3.1. Comments on results from 2004 observations

The observations from summer 2004 resulted in a wide frequency band, but with a rather high noise level. Table 3 shows that a typical 1σ is about 38 (85), 24 (45), and 15 (26) mK for the AOS(AC) observations with 1, 4 and 16 MHz resolution, respectively.

Table 4. Observational strategy 2006/07: different combinations of signal and reference positions are sensitive to different angular sizes of the primordial perturbations.

Position	Angular sensitivity θ			
	$2-5'$	$5-10'$	$10-15'$	$15-30'$
A	AB+AD	AD	AD	AD
B	BC+BA	BC	BC	–
C	CD+CB	CD+CB	CB	–
D	DA+DC	DA+DC	DA	DA

3.2. Comments on results from 2006/07 observations

The analysis of these observations is somewhat different from the 2004 observations due to the new scheme. We do not know if the signals we seek are absorption or emission lines, or if they are located in the signal or in the reference position. As seen from Fig. 1, each pair of observations is sensitive to different angular scales of the perturbations. As an example, if we assume that the signal is in position A and use B as reference, this combination is sensitive to a perturbation size between $2-5'$. If the primordial cloud is larger than $5'$ the signal will be present in both A and B and will disappear in the resulting AB average. We are, however, also sensitive to larger sizes of the perturbations in A since we have observations towards position D with A as a reference. If we switch and use A as signal and D as reference, we will have an AD average which is sensitive to scales between $2-30'$. Therefore, we can add both AB and AD together to further lower the noise with a sensitivity of scales $2-5'$. For larger scales we can only use AD. A summary of all average combinations for each position with corresponding angular scale sensitivity is given in Table 4.

This observation strategy is also a way to check if the signal is in the signal or reference position. For example, if there is a signal in position A, and the size of the perturbation is $2-5'$, the signal-to-noise (S/N) will increase by $\sqrt{2}$ if we average AB and AD. If the signal is in B, the signal will be lowered by a factor of two in the AB+AD average. A signal in the B position would also be seen in the BC average with $\sqrt{2}$ increase of the S/N in the BA+BC average.

Table 5 shows that the noise is considerably lower than in the 2004 observations.

4. Analysis

We want to interpret our observations in a cosmological context and start with a summary of the cosmological background and the tools by which we estimate the amplitude and line width of the resonant lines in Sect. 5. This is model dependent and we adopt the currently favoured hierarchical ΛCDM cosmology with a cosmological constant in which cold dark matter dominates the evolution of structure. The latest results from five-years of WMAP data (Komatsu et al., 2008) are used with a Hubble constant $H_0 = 70\,\mathrm{km\,s^{-1}\,Mpc^{-1}}$, a dimensionless matter density parameter $\Omega_M = 0.28$, a dark energy density parameter $\Omega_\Lambda = 0.72$, and a baryon density $\Omega_b = 0.0462$. This implies a flat geometry where $\Omega_M + \Omega_\Lambda = 1$.

The proper length $L(z)$ of a primordial perturbation can be estimated by using the small-angle limit of the relation between

Table 5. Upper limits in mK as a function of angular size on the sky from observations during 2006/07 using 1, 4 and 16 MHz frequency resolution. The limits are for the data taken with the AOS(AC) and for frequency ranges 542.0 – 547.5 (486.5 – 492) GHz. Note that these values are preliminary.

Position	2 – 5′ 1σ [mK]	Peak intensity [σ]	5 – 10′ 1σ [mK]	Peak intensity [σ]	10 – 15′ 1σ [mK]	Peak intensity [σ]	15 – 30′ 1σ [mK]	Peak intensity [σ]
				1 MHz resolution				
A	16 (22)	3.4 (3.9)	22 (32)	3.9 (4.0)	22 (32)	3.9 (4.0)	22 (32)	3.9 (4.0)
B	17 (24)	3.1 (2.7)	23 (35)	3.6 (3.3)	23 (35)	3.6 (3.3)	–	–
C	17 (23)	3.4 (4.1)	17 (23)	3.4 (4.1)	25 (35)	3.3 (3.7)	–	–
D	15 (22)	4.1 (3.3)	15 (22)	4.1 (3.3)	22 (33)	2.8 (3.1)	22 (33)	2.8 (3.1)
				4 MHz resolution				
A	10 (14)	3.4 (2.6)	14 (20)	3.3 (3.9)	14 (20)	3.3 (3.9)	14 (20)	3.3 (3.9)
B	10 (16)	2.6 (3.2)	15 (23)	2.7 (3.6)	15 (23)	2.7 (3.6)	–	–
C	11 (16)	3.3 (3.5)	11 (16)	3.3 (3.5)	16 (23)	2.9 (4.0)	–	–
D	9 (14)	2.7 (2.6)	9 (14)	2.7 (2.6)	13 (21)	3.6 (3.9)	13 (21)	3.6 (3.9)
				16 MHz resolution				
A	5 (8)	3.7 (3.8)	7 (11)	3.5 (3.9)	7 (11)	3.5 (3.9)	7 (11)	3.5 (3.9)
B	6 (9)	2.7 (3.6)	8 (13)	3.1 (3.2)	8 (13)	3.1 (3.2)	–	–
C	6 (9)	2.7 (2.5)	6 (9)	2.7 (2.5)	8 (12)	3.1 (3.3)	–	–
D	5 (8)	3.6 (3.3)	5 (9)	3.6 (3.3)	7 (11)	3.6 (3.1)	7 (11)	3.6 (3.1)

the angular size θ a cloud subtends on the sky, its linear extent L, and the angular-diameter distance $D_{\rm A}$:

$$\theta = \frac{L(z)}{D_{\rm A}(z)} \quad [\rm rad], \tag{6}$$

where $D_{\rm A}(z)$ is the angular diameter distance. In a flat Universe, this distance is described by

$$D_{\rm A}(z) = \frac{c}{(1+z')H_0} \int_0^{z'} \frac{\rm dz}{\sqrt{\Omega_{\rm M}(1+z)^3 + \Omega_\Lambda}} \ [\rm Mpc] \,, \tag{7}$$

where c is the speed of light. Assuming a spherical geometry, the proper length $L(z)$ can be used to calculate the mass of a density perturbation $\Delta\rho/\rho$ following the expansion of the Universe

$$M = \frac{4\pi}{3}\frac{L(z)^3}{8}\,\Omega_{\rm M}\,\rho_{\rm cr}(1+z)^3(1+\Delta\rho/\rho) \,, \tag{8}$$

where $\rho_{\rm cr} = 1.88{\times}10^{-29} h^2\,{\rm g\,cm^{-3}}$ is the critical density of the Universe at present time with $h = H_0/100$, and where $\Delta\rho/\rho$ is initially very small but increases with decreasing redshift. Equations 6 – 8 then give a relation between angular size and mass.

All structure formation models predict large primordial perturbations at redshifts below 1100. The hierarchical model predicts that the smaller perturbations or galaxies formed first and then merged or accreted gas to form even more massive objects. The latest WMAP results suggest that the re-ionization of the Universe took place between $z \sim 6$–11 implying that the first stars must have formed at $z \gtrsim 11$ (Komatsu et al., 2008). They are predicted to form in overdense dark matter regions of $10^5 - 10^6\,{\rm M}_\odot$ at redshifts about 30 – 40 (Glover, 2005) while larger mass perturbations collapse at lower redshift and may be the sources of reionisation (e.g. Barkana & Loeb, 2001; Bromm & Larson, 2004). Mass perturbations $\gtrsim 10^{13} - 10^{14}\,{\rm M}_\odot$ are predicted not to have reached their collapse phase yet.

The density contrast $\Delta\rho/\rho$ is predicted to scale linearly with the scale factor as 1/(1+z). Sufficiently dense perturbations reach a turn-around point at which their gravity counterbalances the expansion. They then enter a collapse phase during which the density and temperature quickly increase.

Note that during the linear phase, the only predicted possible signal is by the resonant scattering process, while in colliding or collapsing perturbations emission and absorption lines will arise. The amplitude and line width of these lines depend among many things on the dynamics of the primordial clouds, which conveniently can be divided into the above mentioned phases: the linear phase, the turn-around phase and the collapse phase.

4.1. Linear phase:

In the linear phase, the width of the resonant lines will depend on the proper length $L(z)$ of the object. This size will occupy a redshift interval Δz in the Hubble flow, and, assuming a spherical geometry and that every part of the cloud moves with the same peculiar velocity, we have (e.g. Maoli et al., 1996; Dubrovich et al., 2008)

$$\frac{\Delta\nu}{\nu} = \frac{\Delta z}{1+z} = \frac{H_0\,L(z)}{c}\sqrt{\Omega_{\rm M}(1+z)^3 + \Omega_\Lambda} \,, \tag{9}$$

where $\Delta\nu$ is the Doppler line width.

A relation between line width and mass in the linear phase can be found using Eq. 8 with $\Delta\rho/\rho \ll 1$ and Eq. 9. The line widths increase with redshift and mass and are very broad, $\Delta\nu/\nu \sim 10^{-1} - 10^{-5}$, implying line widths of the order of a few thousand $\rm km\,s^{-1}$. Note, that this is true assuming that the density contrast is very small. When the perturbations grow the line widths will start to deviate from Eq. 9 and become more narrow. Another addition of uncertainty to the line width is our homogeneous assumption of no substructure within the cloud. Within each mass at its turn-around, there will be smaller mass perturbations which already have reached their respective turn-around. These perturbations will carry the bulk mass and may thus dominate the emission even on large scales. As a first order approximation in our analysis, we will therefore use a line width of $100\,\rm km\,s^{-1}$ in our predictions of HeH^+ resonant lines in Sect. 6.

The intensity of the resonant lines is estimated to be (e.g. de Bernardis et al., 1993; Maoli et al., 1996; Dubrovich et al., 2008)

$$\frac{\Delta I}{I_{\rm CMB}} = (3-\alpha_\nu)\,(1-e^{-\tau})\,\frac{\upsilon_{\rm p}}{c}\cos\theta\,, \tag{10}$$

where ΔI is the observed intensity, $I_{\rm CMB}$ the CMB intensity, α_ν is the spectral index, $\upsilon_{\rm p}$ is the peculiar velocity of the perturbation, $\cos\theta$ is the cosine of the angle with respect to the line of sight of the peculiar velocity, and τ is the opacity of the transition. The determining factors resulting in a positive or negative sign of $\Delta I/I$ are the $\cos\theta$ factor, and the possibility of inverted populations in which case maser emission will appear. If the populations are not inverted, then the only way to produce emission lines is therefore to have a source that moves along the line of sight towards us, while absorption lines appear when the source moves away from us. The resonant lines do not require temperature differences, only a moving cloud, CMB photons and the scattering species.

The spectral index $\alpha_\nu = (\nu/I)(\mathrm{d}I/\mathrm{d}\nu)$ is derived in Maoli et al. (1996) where $I_\nu = B_\nu(T_{\rm CMB})$ and has the general expression

$$\alpha_\nu = 3 - \frac{h\,\nu/kT}{1-\exp^{-h\,\nu/k\,T}}\,. \tag{11}$$

The peculiar velocity describes the motion of primordial perturbations with respect to the Hubble flow. In the ΛCDM model these perturbations evolve due to potential gradients and increase with time as (Longair, 2008)

$$\upsilon_{\rm p} = \frac{\upsilon_{\rm p0}}{\sqrt{1+z}}\,. \tag{12}$$

The most commonly used peculiar velocity at present time for the size of a galaxy cluster is $\upsilon_{\rm p0}\sim 600\,\mathrm{km\,s^{-1}}$, derived from the CMB dipole anisotropy, which together with our spatially flat ΛCDM model, is considered to reproduce the characteristics of the large-scale matter distribution at low redshifts (e.g. Jenkins et al., 1998). Smaller mass perturbations most likely move with a factor of 2 – 5 higher peculiar velocity (Dubrovich et al., 2008). The present ratio of the peculiar velocity to the speed of light is $\sim 2\times10^{-3}$ and decreases with increasing redshift. This is a very limiting factor in the search for resonant lines. Even with a very high molecular abundance and an opacity of one, the observed antenna temperature will be about 2 mK for high mass perturbations and about 4 – 10 mK for lower mass perturbations, if the observations are performed at 200 GHz and twice as high if observed around 100 GHz (see Table 6).

As pointed out by Dubrovich (1997), a luminescence effect may also produce lines when high energy photons are scattered and decay into several lower energy photons. The amplitude of lines produced by luminescence is given by Eq. 10 times an additional gain coefficient factor K. For simple elastic scattering $K = 1$ and for luminescence $K \lesssim 1000$. Dubrovich & Lipovka (1995) investigated luminescence produced by excited rotational-vibrational (ro-vib) transitions of H_2D^+ which decay to the lowest vibrational state emitting via several rotational transitions. This effect is, however, limited to high temperature or high density regions.

The scattering efficiency of resonant lines is very frequency dependent and here mainly on two parameters: the number density of the species and the spontaneous transition probability described by the Einstein coefficient A_{ul}. Those species which have a high product of these quantities are of special interest.

The density of the species depends on redshift and can be described in terms of the total density of hydrogen and the fractional abundance of species x as $X_x = n_x/n_{\rm H}$. For simplicity, as a first approximation we assume that the density is high enough to allow the number density of the species in an excited state to be described by the Boltzmann distribution

$$n_{x,\rm u}(z) = \frac{g_{\rm u}}{Q(T)} e^{-E_{\rm u}/{\rm k}T_{\rm ex}}\, n_x\,, \tag{13}$$

where $g_{\rm u}$ and $E_{\rm u}$ are the statistical weight and energy of the upper state, respectively, $Q(T)$ is the partition function, $T_{\rm ex}$ is the excitation temperature, $n_x = n_{\rm H,0}\,X_{x,0}\,(1+z)^3$ with $X_{x,0}$ as the abundance at present time and the present density of hydrogen atoms $n_{\rm H,0} = \rho_{\rm crit}\Omega_{\rm B}/m_{\rm p} \approx 2\times10^{-7}\,\mathrm{cm^{-3}}$. We thus assume that the molecular abundances have reached their asymptotic limit at the redshifts of interest $\lesssim 200-400$. The possibility of a detection prior to a redshift of a maximum abundance is very limited due to the very low abundances and weak signals at even higher redshifts. In reality, the population distribution also will depend on the molecular formation process, and the radiation field with possible population inversion (maser effects).

The optical depth at the centre of the line can be calculated, assuming LTE and a Gaussian line profile, using

$$\tau_{\rm max} = \int_{l_1}^{l_2} \sqrt{\frac{\ln 2}{16\,\pi^3}}\,\frac{c^3\,n_x}{\nu_{\rm ul}^3\,\Delta\upsilon}\,\frac{A_{\rm ul}\,g_{\rm u}}{Q(T)}\,e^{-E_{\rm u}/kT_{\rm ex}}(e^{\,h\nu_{\rm ul}/kT_{\rm ex}}-1)\,{\rm d}l, \tag{14}$$

where we have included an additional factor for stimulated emission. As customary we have converted the line width in frequency $\Delta\nu$ to a Doppler velocity width $\Delta\upsilon$. The integration is performed over the path length of the cloud, $l_2 - l_1 = L(z)$.

If the excitation is governed by the CMB radiation temperature, the argument of the exponential functions in Eq. 11 and 14 can be written as

$$\frac{h\,\nu_{\rm ul}}{kT_{\rm ex}} = \frac{h\nu_0}{kT_0(1+z)} = \frac{h\nu_{\rm obs}}{kT_{\rm CMB}}\,. \tag{15}$$

At redshifts lower than $z \lesssim 200$ the excitation is closer to the kinetic temperature described by Eq. 4.

4.2. Turn-around phase:

During this phase the tendency of a perturbation to collapse under its gravity just balances its tendency to expand with the rest of the Universe. The perturbation will appear non-moving and all species from every part of the perturbation will emit from the same redshift. This will produce the strongest and the most narrow lines with a line width determined by the thermal broadening (Maoli et al., 1996)

$$\frac{\Delta\nu}{\nu} = \frac{2}{c}\sqrt{\frac{2\,\ln 2\,k\,T}{m}} = 7.16\times10^{-7}\sqrt{\frac{T}{A}}\,, \tag{16}$$

where m is the atomic mass and A is the mass in atomic mass units of the species. At the low CMB temperatures this implies a line width between $0.4-4\,\mathrm{km\,s^{-1}}$ at $z = 3-400$ for HeH^+.

In fact, there will also be an additional constant broadening of about $2\,\mathrm{km\,s^{-1}}$, for every redshift, due to the finite speed of light and photon travel time across the finite size of a perturbation: A photon emitted from the far end of a cloud reaching the center at the turn-around time $t_{\rm TA}$, was emitted at a previous time when the cloud was still expanding. Therefore, this photon will be redshifted with respect to a photon emitted from the center at the same time. Likewise, photons emitted from the near end of the cloud at the time the photons from the center and far end arrive, will be redshifted precisely as much as the photons from

the far end since the cloud has then begun to contract. This produces a non-symmetric spectrum with photons from the cloud center producing a peak on the blue side, and photons from the near and far side producing lower intensity on the red side. This factor will dominate the line width over the thermal broadening at low redshifts. In addition to these broadening effects, turbulence will also contribute with an unknown amplitude.

The integrated intensity of the resonant lines has not changed compared to the linear phase, and thus the amplitude, described by Eq. 10, will increase proportionally to the decrease in line width, which may be about 3 orders of magnitude.

The turn-around and the beginning of the collapse phase are identified as the most favourable for observations (Maoli et al., 1996). It is therefore important to try to estimate at what redshift this will take place. We assume that the power spectrum of the dark matter density fluctuations is of Harrison-Zeldovich type, which means

$$\sigma_M = \left\langle \left(\frac{\Delta M}{M} \right)^2 \right\rangle^{1/2} \sim M^{-2/3} , \quad (17)$$

and that it can be normalised by the observed fluctuations $\sigma_{M_S} = 10^{-4}$ of the mass $M_S = 3.72 \times 10^{15}\,\mathrm{M}_\odot$ (cf. Eq. 15.13 Longair, 2008) within the sound horizon at the last scattering surface where $z_{\mathrm{LSS}} = 1\,080$ giving

$$\sigma_M = 10^{-4} \left(\frac{M_S}{M} \right)^{2/3} . \quad (18)$$

The turn-around redshift z_{TA} for a mass M which has $1\sigma_M$ overdensity, i.e. $\Delta M/M = \sigma_M$, can then be estimated according to

$$1 + z_{TA} = 1.35\,(1 + z_{LSS}) \left(\frac{10^9\,M_\odot}{M} \right)^{2/3} . \quad (19)$$

Figure 3 shows the turn-around z as a function of mass for one, three, and six σ_M mass perturbations. Note, that the Harrison-Zeldovich power spectrum has the power index $n = 1$, and the latest WMAP results (Komatsu et al., 2008) indicate that $n = 0.960^{+0.014}_{-0.013}$. In our calculations we have taken the total mass into account, but the baryonic to dark matter mass ratio is only 1/6. The star forming baryonic matter is predicted to subsequently fall into the dark matter potential wells at later redshifts caused by gravitational collapse.

To be able to observe these proto-objects we need to relate the turn-around mass to a linear size corresponding to an angular size of our beam. At the turn-around $(1 + \Delta\rho/\rho) = (3\pi/4)^2 \sim 5.55$ and this should be inserted in Eq. 8 to find a mass-linear size relationship at the turn-around. We then use Eq. 6 – 8 and 19 to find the relation between angular size vs. mass perturbations at turn-around redshift, shown in Fig. 4.

4.3. Non-linear collapse phase:

When $(1 + \Delta\rho/\rho) \gtrsim (3\pi/4)^2$ the collapse will begin. The amplitude and line width now depend on the collapse rate in addition to the peculiar velocity. Depending on the ratio of the two velocities the line can be in absorption, emission or have a double peak (a summary is found in Maoli et al., 1996). In the initial stages the line widths are expected to increase compared to the narrow width during the turn-around. This is also the only evolutionary stage where *the peculiar velocity is no longer required to produce resonant lines*.

The chemical abundances could also be substantially modified during the collapse phase of a primordial cloud when the increasing temperature and density would induce new chemistry.

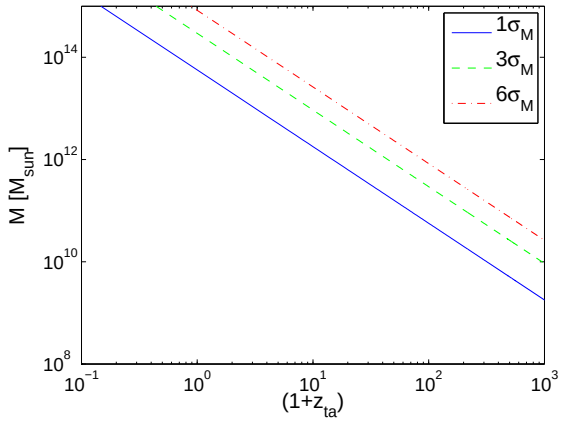

Fig. 3. Turn-around redshift for one, three and six σ_M mass primordial perturbations as determined by Eq. 19. Note, that this describes the total mass, and the baryonic to dark matter content is 1/6.

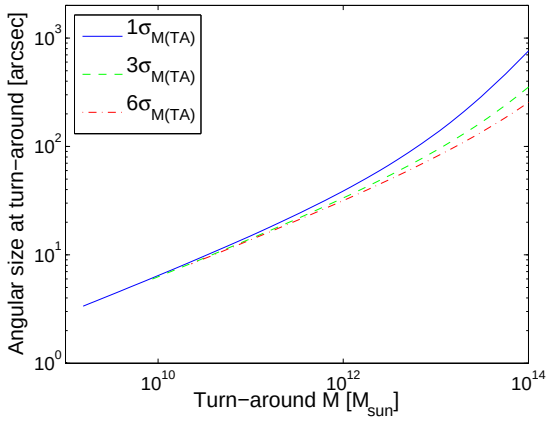

Fig. 4. The angular size vs. mass at z_{TA}, assuming one, three and six σ_M overdensities. Note, that this describes the total mass, and the baryonic to dark matter content is 1/6.

This could increase the molecular abundances, like for instance the H_2 production, and therefore the amplitudes of the primordial resonant lines (Haiman et al., 1996; Puy & Signore, 1996). The radiative feedback is, however, not always positive since the very energetic radiation from the first collapsed objects will dissociate molecular hydrogen (Haiman et al., 2000). There are, however, large uncertainties of the complex H_2 and HD chemistry (Glover & Abel, 2008).

The resonant scattering will become suppressed when the density becomes higher than some critical density depending on species, due to frequent collisions which causes thermal radiation to dominate over resonant scattering (Basu, 2007). The increasing numbers of collisions will drive the level populations and the excitation towards the lower (or higher) matter temperature. and should enhance the spectral line absorption (or emission). This effect will be greatest in molecules like H_2 and HD, which have zero or small dipole moments and thus weak transitions.

5. Sensitivity analysis for resonant lines

We now want to interpret the upper limits we have obtained using Eq. 10. This equation is, however, expressed in intensity

while sub-mm and radio antennas are usually calibrated according to the brightness temperature in the Rayleigh-Jeans limit in terms of

$$T_{\rm b} = \frac{c^2}{2\,k\nu^2}\,I_\nu = \frac{\lambda^2}{2\,k}\,I_\nu\,. \quad (20)$$

This temperature is only valid if $h\nu/kT_{\rm b} < 1$ and therefore we must use the radiation temperature

$$J(T_b) = \frac{h\nu}{k}\frac{1}{e^{h\nu/kT_{\rm b}}-1} \approx T_{\rm b}\,, \quad (21)$$

where the last approximation holds in the above mentioned limit, which is below 30 GHz when T = 2.725 K. Around 550 GHz, $J(T_b) \approx 10^{-3}$. Figure 8 (on-line material) shows $J(T_b)\times(3-\alpha)$ as a function of frequency with T = 2.725 K. As seen we lose almost two orders of magnitude in sensitivity around the Odin observation frequencies compared to frequencies below 200 GHz. This is especially limiting for detecting the already very weak rotational-vibrational transitions which cannot be observed below 200 – 400 GHz if they form at $z = 200-400$.

Combining Eq. 21 and Eq. 10, we have

$$\Delta T_b = J(T_{\rm CMB})\,(3-\alpha_\nu)\,(1-e^{-\tau})\,\frac{\upsilon_{\rm p}}{c}\cos\theta\,, \quad (22)$$

where ΔT_b is our observed 5σ noise from Table 3 and 5 (corrected for beam-efficiency), and $J(T_{\rm CMB})$ is the radiation temperature of the CMB temperature at $z = 0$.

We assume that a primordial perturbation fills the large Odin beam which thereby determines the minimum size of a perturbation which we are sensitive to. If the object is smaller we will suffer from beam-dilution by a factor of

$$\eta_{\rm bf} = \frac{\theta_{\rm s}^2}{\theta_{\rm s}^2+\theta_{\rm beam}^2}\,. \quad (23)$$

When a transition becomes optically thick the line will no longer increase its amplitude. To estimate the maximum signal possible we assume optically thick lines in Eq. 22 and calculate the observed temperature. The results are found in Table. 6, and depend on the uncertainty of the assumed peculiar velocities. Obviously, even taking this uncertainty into account, the resonant lines would be extremely difficult to detect at the high Odin frequencies. At frequencies below ~200 GHz the amplitudes are orders of magnitudes higher and hence a detection may be possible if the opacity is high.

We can also estimate the amplitude of optically thin lines and as an example we consider the rotational and first branch of ro-vib resonant HeH^+ lines for four different redshifts, shown in Fig. 5. A single perturbation is assumed, with a size corresponding to the 2.′1 Odin beam. We have also assumed a very low density of $n_{\rm H}=2\times10^{-7}(1+z)^3$ at redshifts ≥75 and increased this density 5.55 times at $z = 30$ (density at turn-around), and assumed an abundance of $X(HeH^+) = 10^{-12}$. We use an excitation temperature that follows the CMB at all redshifts, narrow lines at $z = 30$ and broad lines with $\Delta\upsilon = 100\,{\rm km\,s^{-1}}$ from $z \geq 75$ as indicated in the legends. Our choice of line widths arises from the fact that for $z \gtrsim 10-30$, the large Odin beam corresponds to much larger physical sizes and masses than the turn-around objects (Fig. 3), and at higher redshifts we are therefore most sensitive to objects in their linear phase. At high redshifts, the temperature is higher and therefore higher lying transitions will be populated. The intensities of the ro-vib lines are, however, much weaker at all redshifts than the intensities of the rotational lines. This could be compensated by the luminescence process at high redshifts of ≳200 (Dubrovich, 1997), but this possibility has not been considered here.

Table 6. Estimated maximum $\Delta T_{\rm b}$ for the resonant lines, assuming optically thick lines and $\upsilon_p(0) = 600\,{\rm km\,s^{-1}}$.

.	Maximum $T_{\rm A}$ [mK]		
Obs. Freq.	$z = 10$	$z = 100$	$z = 300$
50	1.5	0.51	0.29
100	1.3	0.42	0.24
200	0.64	0.21	0.12
300	0.24	0.078	0.045
400	0.071	0.024	0.014
500	0.019	0.006	0.004
600	0.005	0.002	9×10^{-4}

We should here stress that the predictions of Fig. 5 are based upon rather conservative assumptions. Any increase of abundance and density, or decrease of line width, would directly increase the amplitudes of the HeH^+ signals. The HeH^+ abundance is indeed very uncertain with a predicted abundance range of $10^{-8}-10^{-15}$ (Dubrovich et al., 2008). An increase of the abundance from 10^{-12}, as assumed in Fig. 5, to 10^{-9} results in predicted signal intensities which are definitivly reachable with state of the art millimetre wave telescopes.

6. Discussion – other possibilities of emission?

The advantages of the Odin satellite are the absence of adverse effects from the terrestrial atmosphere and the tunable SSB receivers, allowing the spectral coverage of a broad band. However, one severe disadvantage for detection of resonant lines is the high observing frequency. The best observing frequencies to detect the scattering lines are below 200 GHz considering the limiting factor $J(T_{\rm ex})\times(3\text{-}\alpha)$ as shown in Fig. 8. Around 550 GHz the amplitude of the lines will be at least about 100 – 10 000 times lower than the Odin noise levels. However, in the collapse phase of a primordial perturbation the density and temperature will rise substantially, thereby introducing emission and absorption for the first time in the Universe (c.f. Basu, 2007). In this phase there is no requirement on peculiar velocities and therefore this limiting factor will disappear. However, these objects may very likely be much smaller than the Odin beam and therefore any observations will severely suffer from beam-dilution. According to Figs. 3 and 4, the Odin beam size is most sensitive to $10^{10}-10^{13}\,{\rm M_\odot}$ perturbations, with turn-around redshifts about 10 – 300.

Observations of resonant lines at high frequencies have another disadvantage which concerns the molecular energy levels. To obtain detectable signals the energy levels need to be populated, and thus the upper state energy of the transitions cannot be much higher than the excitation temperature at the emission redshift which approximately follows the CMB. Since the most relevant energy levels correspond to a rather high temperature, this demands high redshifts thereby implying an observing frequency below 100 – 200 GHz. This is clearly seen by inspecting Fig. 5, where the lowest rotational transitions always are several orders of magnitude stronger than the higher lying transitions.

At high frequencies the only detectable primordial signal is therefore from thermal emission or absorption, which depends on the competition between radiation and collisions as seen in the radiative transfer equation at the appropriate redshift

$$T_{\rm b} = (J(T_{\rm ex}) - J(T_{\rm CMB}))\,(1-e^{-\tau})\,, \quad (24)$$

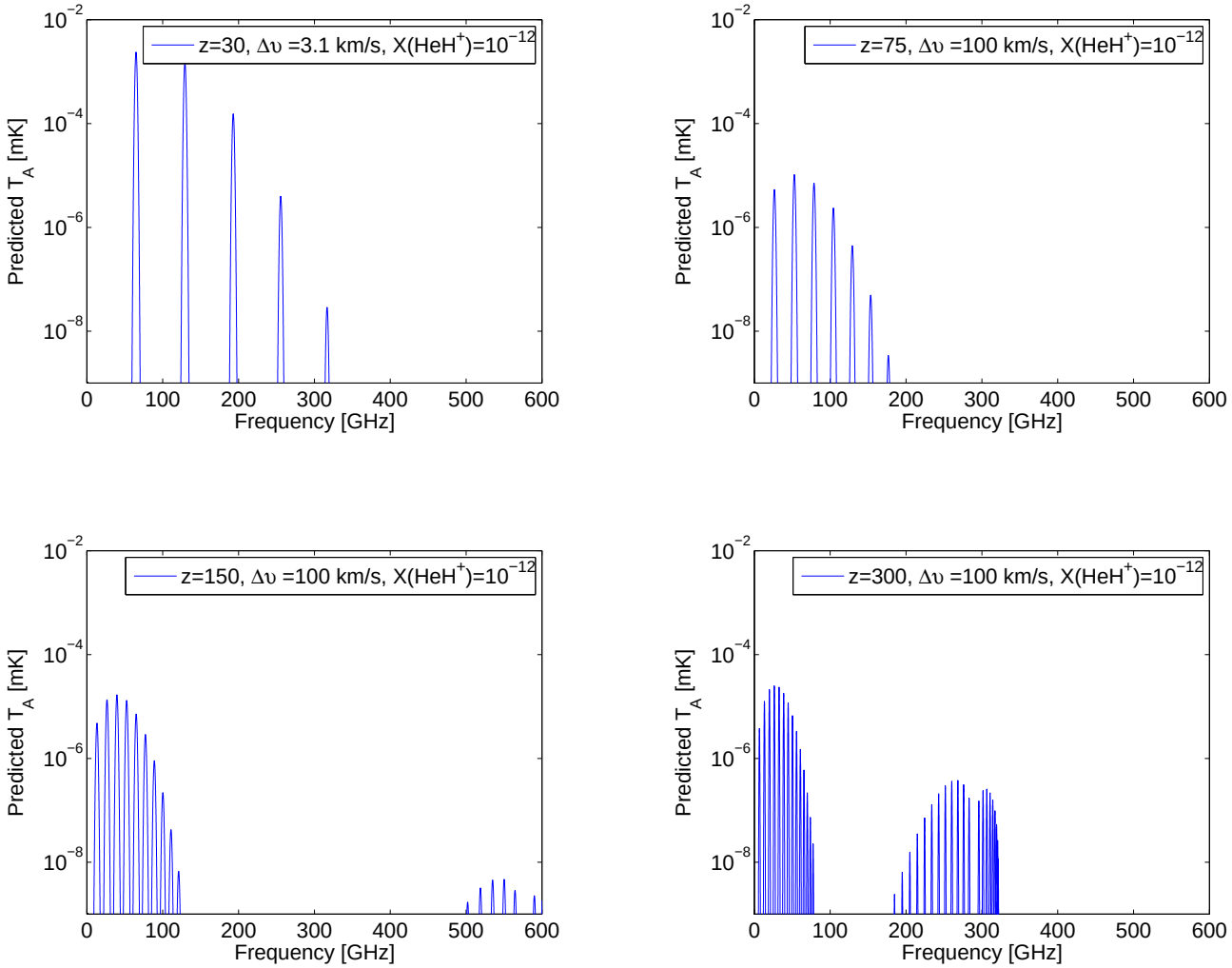

Fig. 5. Predicted antenna temperature ΔT within the 2.′1 Odin beam size for HeH^+ at $z = 30$, 75, 150, and 300. Turn-around phase is assumed for $z = 30$ and for higher z we assume linear phase and a line width of 100 km s^{-1}. We also assume a very low density $n_H = 2\times10^{-7}\,(1+z)^3$. Any increase of the density, abundance, or decrease of line width, directly increases the amplitude of the signals with an equal magnitude.

where T_b is the brightness temperature at the source, $J(T_{ex})$ is the radiation temperature from Eq. 21, and $J(T_{CMB})$ is the background CMB radiation. The excitation temperature depends on the radiation field, which is the CMB at high redshifts and at lower redshifts it is dominated by the energetic radiation from the first star formation, and on the densities through collisions. A large difference between $J(T_{ex})$ and $J(T_{CMB})$) implies a high amplitude of the lines.

A second important issue for a detection regards beam-filling. The first objects likely form in dense and small cores within larger condensations. An individual core is certainly too small for a detection due to the beam dilution, but they will probably form in a cluster and as such may be detectable (cf. Kamaya & Silk, 2003). Observations with interferometers having very high spatial resolution would therefore also be of interest.

Regardless of peculiar velocities, the resonant scattering process also has the potential of reducing the power of the CMB primary anisotropies if the molecular abundances are high enough (Maoli et al., 1994). The Planck[7] satellite, to be launched in 2009 may be able to detect this decrease in power. There are also several suggestions to use differential measurements of the broad band CMB angular power spectrum observed with Planck to the search for resonant lines (e.g. Basu et al., 2004; Dubrovich et al., 2008; Schleicher et al., 2008). To reach the required sensitivity of the order of μK, the main problem to extract these weak signals with this approach, will be the galactic and extra-galactic foreground emissions.

Other future prospects of probing the high redshift Universe include antennas like the Low-frequency Array[8] (LOFAR) which will be able to detect the redshifted 21-cm HI transition between $z \sim 6-11$ (e.g. Hogan & Rees, 1979) and the proposed Square Kilometer Array (SKA)[9] which will be able to look at higher redshift. Both instruments will, however, only be able to probe the post-reionisation Universe. The continuum of H^- has also been suggested to give rise to a detectable signal in terms of a decrease in the CMB spectrum which may superimpose a detectable absorption feature on the CMB. The strength of this effect has, however, been estimated to quite different values (Black, 2006; Schleicher et al., 2008).

The search for primordial signals from the cosmic Dark Ages is a very difficult task. However, the importance of a detection

[7] http://planck.esa.int

[8] http://www.lofar.org/

[9] http://www.skatelescope.org/

cannot be overestimated and a detection may very well be possible with the use of future, much more sensitive antennas and receivers.

7. Summary

In order to constrain cosmological models of star and structure formation as well as the chemical evolution, we have performed spectral line surveys towards several positions without any known sources of emission in a search for primordial lines from the Dark Ages. The first survey covered a broad band of 31 GHz between 547 – 578 GHz towards two positions with fixed reference-positions. The second survey covered 11 GHz in the bands 542.0 – 547.5 GHz and 486.5 – 492.0 GHz towards four positions. No lines were detected, and thus the results are upper limits in terms of noise level. Typical 1σ values are 5 – 20 mK in the 11 GHz survey, and 20 – 60 mK in the 31 GHz survey.

The major improvement made by the Odin observations compared to de Bernardis et al. (1993) is the broad bandwidth covered allowing a wide range of redshifts to be explored for a number of atomic and molecular species. In addition, in the second survey we have taken into account the unknown sizes of the clouds by testing an observational strategy, where we have observed towards four positions in a sequence with different angular distances between the reference and signal position. An important benefit of our observations is that we do no suffer from spectral line contamination from the terrestrial atmosphere.

Our analysis show that at low densities and an equilibrium of temperatures, the only expected signal is from resonant line scattering between CMB photons and matter moving with respect to the expansion of the Universe. These signals may at most be of the order of a few mK at low frequencies around 100 GHz, and orders of magnitude lower at higher frequencies. At both high and low frequencies, emission or absorption lines may be detected from higher density and temperature regions arising from colliding or collapsing primordial perturbations.

The Odin observations can be considered as pilot studies for deep searches with future much more sensitive antennas such as the Herschel Space Observatory which has orders of magnitude higher sensitivity, or interferometer arrays such as ALMA. Our observing methods and resulting limits, paired with a sensitivity analysis taking into account the evolution of primordial perturbations, should be a valuable input to the planning of these observations.

Acknowledgements. Many thanks to John H. Black and Per Bergman for valuable comments and discussions, and to the whole Odin team. Generous financial support from the Research Councils and Space Agencies in Sweden, Canada, Finland and France is gratefully acknowledged.

References

Applegate, J. H., Hogan, C. J., & Scherrer, R. J. 1987, Phys. Rev. D, 35, 1151
Barkana, R. & Loeb, A. 2001, Phys. Rep., 349, 125
Basu, K. 2007, New Astronomy Review, 51, 431
Basu, K., Hernández-Monteagudo, C., & Sunyaev, R. A. 2004, A&A, 416, 447
Bertoldi, F., Cox, P., Neri, R., et al. 2003, A&A, 409, L47
Black, J. H. 2006, in Faraday Discussions of the Royal Society of Chemistry (UK), Vol. 133, Chemistry and cosmology, 27–32
Bromm, V. & Larson, R. B. 2004, ARA&A, 42, 79
Campos, J. C., Saucedo Morales, J. C., Lipovka, A. A., & Nunes-Lopez, R. 2007, in IAU Symposium, Vol. 235, IAU Symposium, ed. F. Combes & J. Palous, 413–413
de Bernardis, P., Dubrovich, V., Encrenaz, P., et al. 1993, A&A, 269, 1
Dubrovich, V., Bajkova, A., & Khaikin, V. B. 2008, New Astronomy, 13, 28
Dubrovich, V. K. 1977, Soviet Astronomy Letters, 3, 128
Dubrovich, V. K. 1997, A&A, 324, 27
Dubrovich, V. K. & Lipovka, A. A. 1995, A&A, 296, 301
Fixsen, D. J., Cheng, E. S., Gales, J. M., et al. 1996, ApJ, 473, 576
Frisk, U., Hagström, M., Ala-Laurinaho, J., et al. 2003, A&A, 402, L27
Frye, B. L., Bowen, D. V., Hurley, M., et al. 2008, ApJ, 685, L5
Galli, D. & Palla, F. 1998, A&A, 335, 403
Galli, D. & Palla, F. 2002, Planet. Space Sci., 50, 1197
Glover, S. 2005, Space Science Reviews, 117, 445
Glover, S. C. O. & Abel, T. 2008, MNRAS, 388, 1627
Gosachinskij, I. V., Dubrovich, V. K., Zhelenkov, S. R., Il'in, G. N., & Prozorov, V. A. 2002, Astronomy Reports, 46, 543
Haiman, Z., Abel, T., & Rees, M. J. 2000, ApJ, 534, 11
Haiman, Z., Rees, M. J., & Loeb, A. 1996, ApJ, 467, 522
Hogan, C. J. & Rees, M. J. 1979, MNRAS, 188, 791
Jenkins, A., Frenk, C. S., Pearce, F. R., et al. 1998, ApJ, 499, 20
Johnson, J. L. & Bromm, V. 2006, MNRAS, 366, 247
Kamaya, H. & Silk, J. 2003, MNRAS, 339, 1256
Komatsu, E., Dunkley, J., Nolta, M. R., et al. 2008, ArXiv e-prints, 803
Kurki-Suonio, H., Jedamzik, K., & Mathews, G. J. 1997, ApJ, 479, 31
Lara, J. F., Kajino, T., & Mathews, G. J. 2006, Phys. Rev. D, 73, 083501
Lepp, S. & Shull, J. M. 1984, ApJ, 280, 465
Lepp, S., Stancil, P. C., & Dalgarno, A. 2002, Journal of Physics B Atomic Molecular Physics, 35, 57
Longair, M. S. 2008, Galaxy Formation (Galaxy Formation, by Malcolm S. Longair Berlin: Springer, 2008. ISBN 978-3-540-73477-2)
Maoli, R., Ferrucci, V., Melchiorri, F., Signore, M., & Tosti, D. 1996, ApJ, 457, 1
Maoli, R., Melchiorri, F., & Tosti, D. 1994, ApJ, 425, 372
Nordh, H. L., von Schéele, F., Frisk, U., et al. 2003, A&A, 402, L21
Núñez-López, R., Lipovka, A., & Avila-Reese, V. 2006, MNRAS, 369, 2005
Olberg, M., Frisk, U., Lecacheux, A., et al. 2003, A&A, 402, L35
Olofsson, A. O. H., Persson, C. M., Koning, N., et al. 2007, A&A, 476, 791
Papadopoulos, P., Ivison, R., Carilli, C., & Lewis, G. 2001, Nature, 409, 58
Persson, C. M., Olofsson, A. O. H., Koning, N., et al. 2007, A&A, 476, 807
Puy, D., Alecian, G., Le Bourlot, J., Leorat, J., & Pineau Des Forets, G. 1993, A&A, 267, 337
Puy, D., Dubrovich, V., Lipovka, A., Talbi, D., & Vonlanthen, P. 2007, A&A, 476, 685
Puy, D. & Signore, M. 1996, A&A, 305, 371
Puy, D. & Signore, M. 2007, New Astronomy Review, 51, 411
Rauscher, T., Applegate, J. H., Cowan, J. J., Thielemann, F.-K., & Wiescher, M. 1994, ApJ, 429, 499
Rubiño-Martín, J. A., Hernández-Monteagudo, C., & Sunyaev, R. A. 2005, A&A, 438, 461
Santoro, F. & Shull, J. M. 2006, ApJ, 643, 26
Schleicher, D. R. G., Galli, D., Palla, F., et al. 2008, ArXiv e-prints, 803
Sethi, S. K., Nath, B. B., & Subramanian, K. 2008, MNRAS, 387, 1589
Shakhvorostova, N. N., Grachev, S. I., & Dubrovich, V. K. 2003, Astrophysics, 46, 368
Srianand, R., Noterdaeme, P., Ledoux, C., & Petitjean, P. 2008, A&A, 482, L39
Stanway, E. R., Bremer, M. N., Davies, L. J. M., et al. 2008, ApJ, 687, L1
Steigman, G. 2007, Annual Review of Nuclear and Particle Science, 57, 463
Vonlanthen, P. & Puy, D. 2008, in SF2A-2008: Proceedings of the Annual meeting of the French Society of Astronomy and Astrophysics Eds.: C. Charbonnel, F. Combes and R. Samadi. Available online at http://proc.sf2a.asso.fr, p.355, ed. C. Charbonnel, F. Combes, & R. Samadi, 355–+

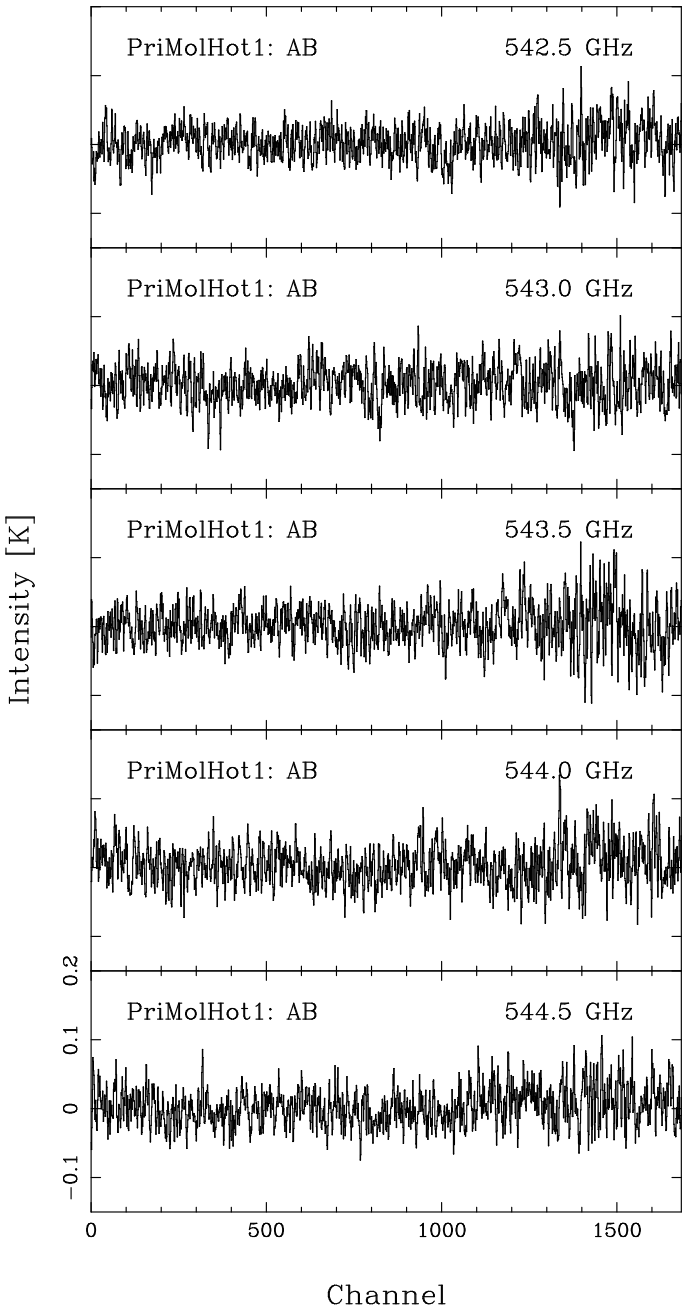

Fig. 6. Spectra from weekend 1 – 5 vs. channels for Position A with B as reference from the 2006/07 survey in original shape and resolution 0.62 MHz.

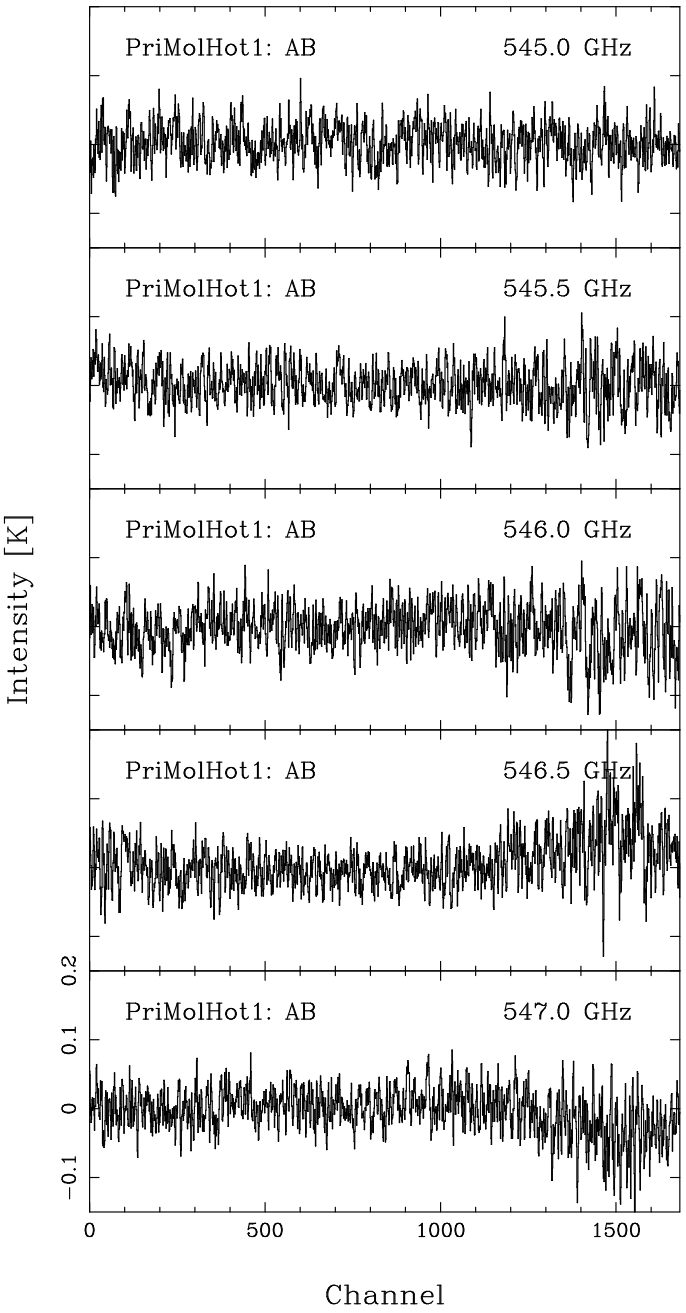

Fig. 7. Spectra from weekend 6 – 10 vs. channels for Position A with B as reference from the 2006/07 survey in original shape and resolution 0.62 MHz.

Table 8. Physical sizes corresponding to the Odin beam and the different angular steps in the 2006/07 observations.

Angular size	Redshift z					
	$z = 10$	25	50	100	200	300
θ [′]	Physical size [kpc]					
2.′1	540	270	150	78	40	28
5	1 300	640	350	190	97	66
10	2 600	1 300	700	370	190	130
15	3 800	1 900	1 050	560	290	200
30	7 700	3 800	2 100	1 100	580	400

Table 7. The ranges in redshifts covered by our observations for the five lowest rotational lines of HeH^+, H_2 and HD.

Species	Frequency	Transitions		E_u	A-coeff	AC [GHz]	AOS [GHz]	AOS [GHz]	AC [GHz]
	[GHz]	$\nu_u - \nu_l$	$J_u - J_l$	[K]	[s^{-1}]	486.5 – 492.0	542.0 – 547.5	547.0 – 563.0	563.0 – 578.0
HeH^+	2 011	0 – 0	1 – 0	94	0.10916	$z = 3.15 - 3.11$	2.73 – 2.69	2.69 – 2.59	2.59 – 2.50
	4 011	0 – 0	2 – 1	289	0.10440	$z = 7.24 - 7.15$	6.40 – 6.32	6.33 – 6.12	6.12 – 5.94
	5 988	0 – 0	3 – 2	577	0.37513	$z = 11.30 - 11.16$	10.04 – 9.93	9.94 – 9.63	9.63 – 9.35
	7 931	0 – 0	4 – 3	957	0.91401	$z = 15.29 - 15.11$	13.62 – 13.48	13.49 – 13.08	13.08 – 12.71
	9 828	0 – 0	5 – 4	1 429	0.18051	$z = 19.19 - 18.96$	17.12 – 16.94	16.95 – 16.44	16.44 – 15.99
	85 324	1 – 0	0 – 1	4 192	830.802	155			
H_2	10 631	0 – 0	2 – 0	510	2.94×10^{-11}	$z = 20.85 - 20.61$	18.61 – 18.42	18.44 – 17.88	17.88 – 17.39
	17 611	0 – 0	3 – 1	1 015	4.76×10^{-10}	$z = 35.20 - 34.79$	31.49 – 31.17	31.20 – 30.28	30.28 – 29.47
	24 433	0 – 0	4 – 2	1 682	2.76×10^{-9}	$z = 49.22 - 48.66$	44.08 – 43.63	43.67 – 42.40	42.40 – 41.27
	31 040	0 – 0	5 – 3	2 504	9.84×10^{-9}	$z = 62.80 - 62.09$	56.27 – 55.69	55.75 – 54.13	54.13 – 52.70
	37 383	0 – 0	6 – 4	3 528	2.64×10^{-8}	$z = 75.84 - 74.98$	67.97 – 67.28	67.34 – 65.40	65.40 – 63.68
HD	2 675	0 – 0	1 – 0	128	5.319×10^{-8}	$z = 4.50 - 4.44$	3.94 – 3.89	3.89 – 3.75	3.75 – 3.63
	5 332	0 – 0	2 – 1	384	5.054×10^{-7}	$z = 9.96 - 9.84$	8.84 – 8.74	8.75 – 8.47	8.47 – 8.22
	7 952	0 – 0	3 – 2	766	1.796×10^{-6}	$z = 15.35 - 15.16$	13.67 – 13.52	13.54 – 13.12	13.12 – 12.76
	10 518	0 – 0	4 – 3	1270	4.311×10^{-6}	$z = 20.62 - 20.38$	18.41 – 18.21	18.23 – 17.68	17.68 – 17.20
	13 015	0 – 0	5 – 4	1895	8.354×10^{-6}	$z = 25.75 - 25.45$	23.01 – 22.77	22.79 – 22.12	22.12 – 21.52

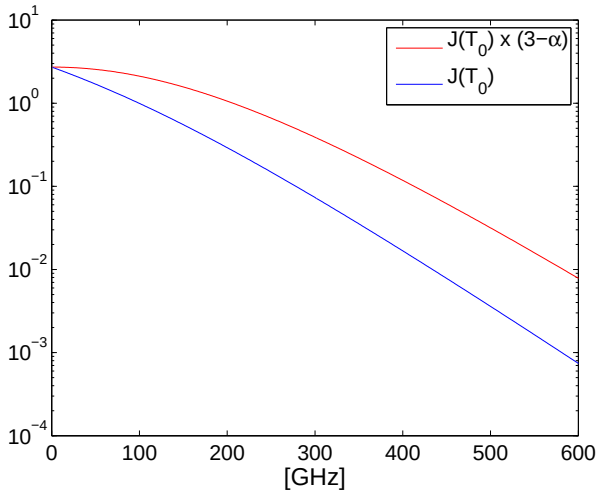

Fig. 8. Radiation temperature $J(T_0)$ times (3-α) as a function of frequency for $T_0 = 2.725$ K.

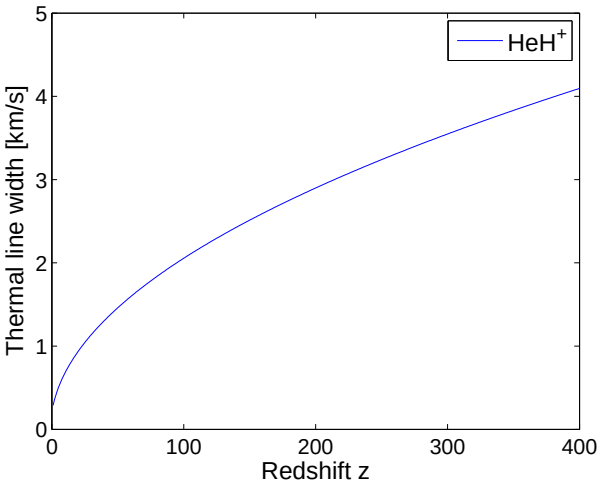

Fig. 9. Thermal line width for HeH^+ at different redshifts.

Appendix A

Tools of astronomy

A.1 Radiative transfer

The radiative transfer equation provides a description of how the intensity changes when the radiation travels from a source through a medium towards us. Photons can be *added* to the original beam of radiation from the medium it travels through. They can also be *removed* by scattering or absorption. If no local emission or extinction occurs, the intensity remains constant along the way.

To describe the amount of intensity added by local photon emission to the beam, we use the frequency-dependent *emission coefficient* j_ν, which is defined as:

$$j_\nu \equiv \frac{\mathrm{d}E_\nu}{\mathrm{d}V\,\mathrm{d}t\,\mathrm{d}\nu\,\mathrm{d}\Omega} = \frac{\mathrm{d}\,I_\nu(s)}{\mathrm{d}s}\ . \tag{A.1}$$

This expression describes the energy $\mathrm{d}E_\nu$ that is added in the form of photons to a beam with solid angle $\mathrm{d}\Omega$, over the bandwidth $\mathrm{d}\nu$, during a time $\mathrm{d}t$, within the volume $\mathrm{d}V$. This also expresses the change of intensity along the travelled path $\mathrm{d}s$. The dimensions of j_ν are [erg cm^{-3} s^{-1} Hz^{-1} sr^{-1}].

The removal of emission from the beam is proportional to the number of extinguishing particles and to the supply of photons. The frequency-dependent proportionality constant is called the *extinction coefficient*, and is defined per particle, per gram, or per cm^2.

$$\mathrm{d}\,I_\nu \equiv -\sigma_\nu\,n\,I_\nu\,\mathrm{d}\,s \equiv \kappa_\nu\,\rho\,I_\nu\,\mathrm{d}s \equiv -\alpha_\nu\,I_\nu\,\mathrm{d}s\ . \tag{A.2}$$

where n is the density of the absorbing particles [cm^{-3}], σ_ν is the effective cross-section per particle [cm^2], and κ_ν is the monochromatic mass extinction coefficient (the *opacity*, [cm^2 g^{-1}]), ρ is the mass density [g cm^{-3}], and α_ν is the monochromatic linear extinction coefficient [cm^{-1}]. In this appendix we will use α_ν.

Using the emission- and absorption coefficients, the change of intensity as it travels through a medium can be described as

$$\frac{\mathrm{d}\,I_\nu}{\mathrm{d}s} = j_\nu - \alpha_\nu\ I_\nu\ . \tag{A.3}$$

This description can be used generally except when the absorbing particles are large with respect to their mean distance, or if they are not randomly distributed in the medium.

A.1.1 Optical depth and source function

To further simplify Eq. A.3 we use the optical depth concept:

$$\mathrm{d}\tau_\nu(s') \equiv -\alpha_\nu \, \mathrm{d}s' \ . \tag{A.4}$$

The total optical depth is obtained by integrating Eq. A.4 over the total path travelled from the source to us.

$$\tau_\nu = -\int_0^s \alpha_\nu \, \mathrm{d}s' = \int_s^0 \alpha_\nu \, \mathrm{d}s' \ . \tag{A.5}$$

The optical depth is thus integrated *against* the direction of travel with $\tau_\nu = 0$ at the observer and $\tau_\nu = \infty$ at an infinite distance. It measures the photon-escape from a medium, and therefore describes the attenuation of the radiation as we see it. The opacity can also be viewed upon as the inverse of the average distance travelled between collisions within a volume $V = \sigma_\nu \, \upsilon \, t$, i.e. the *mean free path*

$$l = \frac{\upsilon \, t}{n \, \sigma_\nu \, \upsilon \, t} = \frac{1}{n \, \sigma_\nu} = \frac{1}{\alpha_\nu} \ , \tag{A.6}$$

where n is the density. If the extinction is high, a photon will only travel a very short distance before it collides, and will therefore be trapped within the medium. This is often the case for the rotational ground state transition of water observed by Odin. To escape from the medium, an opacity below one is required. Note, that the mean free path and the optical depth are frequency dependent. A cloud may be optically thick for one transition and thin for another.

The ratio of emission- and absorption coefficient is called the *source function*

$$S_\nu \equiv \frac{j_\nu}{\alpha_\nu} \ . \tag{A.7}$$

The source function depends on frequency and the local temperature of the cloud. The dimensions are the same as for the intensity, and these two quantities can be added or subtracted. The source function specifies the *addition* of photons along the path of the beam.

We can now rewrite Eq. A.3 as

$$-\frac{\mathrm{d}I_\nu}{\alpha_\nu \, \mathrm{d}s} = I_\nu - \frac{j_\nu}{\alpha_\nu} \ , \tag{A.8}$$

and by using the optical depth and source function we will have

$$\frac{\mathrm{d}I_\nu}{\mathrm{d}\tau_\nu} = I_\nu - S_\nu \ . \tag{A.9}$$

A.1.2 Solution of the transport equation

For pure extinction we have $j_\nu = 0$, and the transport equation is reduced to

$$\frac{\mathrm{d}I_\nu}{\mathrm{d}\tau_\nu} = I_\nu \ , \tag{A.10}$$

with the solution

$$I_\nu = I_{\nu,0}\ e^{-\tau_\nu} \ . \tag{A.11}$$

The infalling intensity decreases exponentially with the optical depth along the ray.

The limit between small and large extinction is found when the intensity has decreased by a factor of $1/e$, i.e. $\tau_\nu = 1$. The gas is called *optically thick* if $\tau_\nu > 1$ and *optically thin* if $\tau_\nu < 1$. An optically thin medium is one in which a photon can traverse the medium with a small chance of being absorbed, whereas in an optically thick medium the photon almost certainly will be absorbed.

Let's now add emission to the extinction:

$$\mathrm{d}I_\nu = j_\nu\,\mathrm{d}s = S_\nu\,\mathrm{d}\tau_\nu \ . \tag{A.12}$$

With the addition of a diminishing exponential to correct for the absorption of the emission travelling through the cloud, the final solution of the transport equation is

$$I_\nu(\tau_\nu) = I_{\nu,0}\ e^{-\tau_\nu} + \int_0^{\tau_\nu} S_\nu(\tau'_\nu)\ e^{-(\tau_\nu - \tau'_\nu)}\mathrm{d}\tau'_\nu \ . \tag{A.13}$$

It is often assumed that the cloud is homogeneous and the source function is constant, giving the simple solution:

$$I_\nu(\tau_\nu) = I_{\nu,0}\ e^{-\tau_\nu} + S_\nu(1 - e^{-\tau_\nu}) \ . \tag{A.14}$$

Here, the first term represents the damping of the infalling intensity when the radiation passes through the cloud. The second term is the emission contribution from the cloud, corrected for absorption when it travels through the cloud. The resulting frequency dependent intensity is thus depending on the properties of the medium it travels through, such as the absorption coefficients and the density of the gas-particles, as well as the temperature.

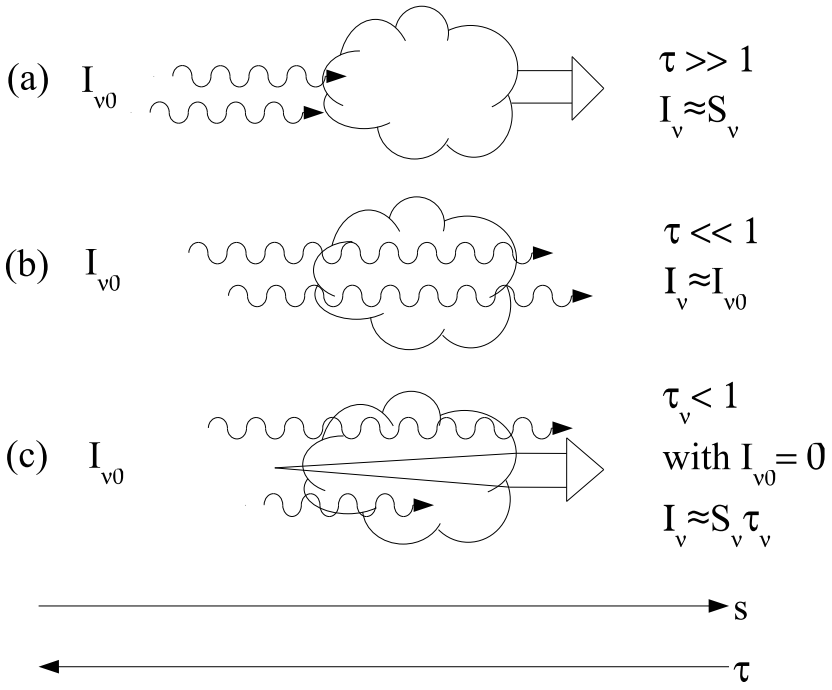

Figure A.1: Special cases in (a) the optically thick limit, (b) the extreme optically thin limit, and (c) the optically thin limit. Credit: Kaj Silander

A.1.3 Special cases

There are three special cases which have very simple solutions. These solutions arise in the optically thin and thick limits.

- Optically thick limit, $|\tau| \gg 1$.

  If the gas is very dense and opaque then the optical depth will be very large and we will have

  $$I_\nu \approx S_\nu. \tag{A.15}$$

  When we observe an optically thick medium we will obtain information about the emission from the surface of the cloud, as shown in Fig. A.1(a). The medium effectively blocks all infalling radiation and from deeper layers within the cloud. The emergent intensity depends only on the local temperature, and therefore an observation of an optically thick emission gives temperature information.

- Optically thin limit $|\tau| < 1$.

  In the less extreme thin limit, but still with little intervening gas absorbing the intensity, the optical depth will be smaller than one. The exponential can then be expanded with a Taylor-series, $e^{-\tau_\nu} \approx 1 - \tau_\nu$ and we will get:

  $$I_\nu(\tau_\nu) \approx I_{\nu,0}(1 - \tau_\nu) + S_\nu \, \tau_\nu = I_{\nu,0} + (S_\nu - I_{\nu,0})\tau_\nu \ . \tag{A.16}$$

  This simplification is correct within 5% for an opacity of 0.1. The source-function can very often vary substantially over a narrow frequency band, and this will produce emission or absorption lines depending on the difference of S_ν and $I_{\nu,0}$.

  With no infalling radiation we will have

  $$I_\nu \approx S_\nu \ \tau_\nu \ . \tag{A.17}$$

  Observations of optically thin emission or absorption give information about the total integrated emission along the line-of-sight, illustrated in Fig. A.1(c), and may be used to calculate the column density (Sect. A.2.1).

- Optically extreme thin limit $|\tau| \ll 1$.

  When the density of the intervening gas is very low and the optical depth is much below one, as seen from Eq. A.17 the emergent intensity will simply be:

  $$I_\nu(\tau_\nu) \approx I_{\nu,0} \ . \tag{A.18}$$

There is another special case, not treated in this work, arising when the optical depth is negative:

$$\tau_\nu \ll -1 \ . \tag{A.19}$$

As seen from Eq. A.13, a negative optical depth will increase the intensity *exponentially* with τ_ν. In this case we have maser amplification.

A.1.4 Discrete processes – spectral line theory

Atoms and molecules have discrete energy levels as described by quantum theory, which means that the radiation is quantised. There are various types of discrete energy levels:

- *Electronic states of atoms and ions.* Transitions involving valence electrons have energies typically a few to hundreds of eV and the spectra are seen in visible light or UV. When transitions involve inner shells the energies can be larger than keV and fall in the X-ray region.
- *Electronic states of molecules.* The energy is typically tenths to a few eV and the spectral region is infrared through the visible to the UV.
- *Vibrational states of molecules.* Molecules can also vibrate, with vibrational levels within the electronic states. The energy is typically a few tenths to one eV, and emitted in sub-mm or infrared.
- *Rotational states of molecules.* In addition to vibrational levels, the molecules can rotate at discrete energy levels. Within the vibrational levels there are rotational levels with very low energy differences. The emission of rotational lines are typically $10^{-4}-10^{-3}$ eV, and the spectra are therefore seen in the radio spectral regime.

There are five processes for excitation or de-excitation between energy levels, illustrated in a two-level system in Fig. A.2. The energy difference between the upper and lower state is $\Delta E = h\nu$. However, in any real system, there are many levels which may be connected (see example in Fig. 3.1). Note, that even though there are many energy-levels in such a diagram, there are always selection rules that determine the allowed radiative transitions.

The probabilities for radiative emission and absorption are described by the Einstein coefficients. The Einstein A-coefficient is the transition probability for a *spontaneous de-excitation* per second from an upper state energy level. This coefficient depends only on atomic or molecular parameters and not on the environment, and can be calculated as:

$$A_{\mathrm{u}l} = \frac{16\,\pi^3\,\nu_{\mathrm{u}l}^3\,\mu^2}{3\,\epsilon_0\,h\,c^3}\frac{S_{\mathrm{u}l}}{g_{\mathrm{u}}}\ , \tag{A.20}$$

where $\nu_{\mathrm{u}l}$ is the frequency of the transition, ϵ_0 is the electrical constant, μ is the molecular dipole moment, and g_{u} is the statistical weight of the upper level describing the number of states with the same energy. For linear molecules $g_{\mathrm{u}} = 2J+1$, where J is the rotational quantum number. $S_{\mathrm{u}l}$ is the rotational part of the intrinsic line strength and depends on the symmetry of the molecule. We note that high frequencies and energy levels thus have higher probabilities for a spontaneous

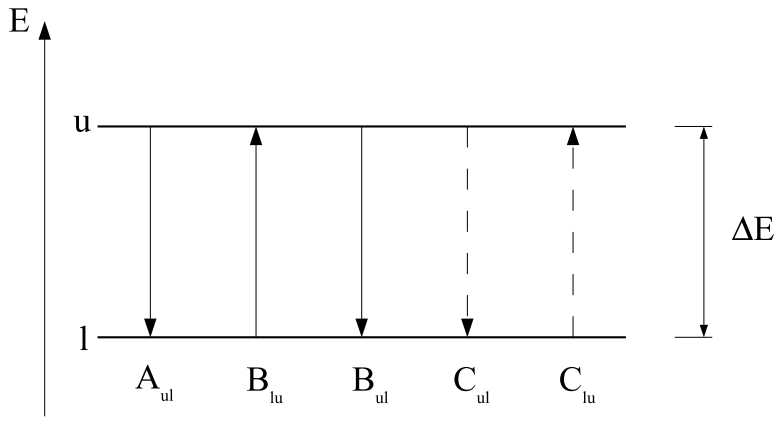

Figure A.2: A two-level system with transitions between the upper state u and the lower state l. The three radiative processes are described by the Einstein coefficients.

de-excitation. The A-coefficient, line strength and dipole moment can be found in different databases for most molecules and many transitions, and a few databases are listed at the end of this thesis.

The average lifetime in an upper state is $1/\sum_i A_{\mathrm{u}l}$, where the summation of $A_{\mathrm{u}l}$ is over all lower states l. A high A-coefficient implies that the state quickly decays before it can react with another photon or collide with another species; a very low A-coefficient forces the particle to spend a long time in the excited state. The chance for collisions with another species before it spontaneously de-excites, increases with increasing time spent in the upper level.

The probability to be *radiatively excited* depends on the Einstein $B_{\mathrm{l}u}$-coefficient together with the radiation field: $B_{\mathrm{l}u}\,\overline{I}$ describes the number of radiative excitations per second in state l, where $\overline{I}$ is the frequency- and angle averaged intensity.

A second way for radiative de-excitation is *stimulated emission* described by the Einstein coefficient $B_{\mathrm{u}l}$ and the radiation field $\overline{I}$. The de-excitation is stimulated by a photon carrying energy ΔE, and the result is two photons with the same energy, with the same phase and in the same direction as the incident photon. $B_{\mathrm{l}u}$ and $B_{\mathrm{u}l}$ have dimensions of [W^{-1} m^2 Hz s].

Generally, the Einstein coefficients are related to each other through

$$A_{\mathrm{u}l} = \frac{2h\nu_{\mathrm{u}l}^3}{c^2} B_{\mathrm{u}l} \quad \text{and} \quad B_{\mathrm{u}l} = \frac{g_{\mathrm{l}}}{g_{\mathrm{u}}} B_{\mathrm{l}u} \; . \tag{A.21}$$

The last two processes are *collisional excitation* and *collisional de-excitation*. The $C_{\mathrm{l}u}$ and $C_{\mathrm{u}l}$ coefficients describe the number of collisional excitations, or de-excitations, per second per particle in state u or l, respectively, and have dimensions [cm^{-3} s^{-1}]. The coefficients depend on the velocities between the colliding particles, on the density, and on the nature of the interaction. Collision partners

may be electrons or the most commonly found atoms and molecules, such as H, H_2 or He, with H_2 as the dominant collision agent in dense molecular clouds. A transition from state i to state j from a collision between an atom with for instance H_2 is described by:

$$n_i\, C_{ij} = n_i\, n_{\mathrm{H_2}} \int_{\upsilon_0}^{\infty} \sigma_{ij}(\upsilon)\, f(\upsilon)\, \upsilon\, \mathrm{d}\upsilon \ , \tag{A.22}$$

with n_i as the number density in state i, $n_{\mathrm{H_2}}$ is the molecular hydrogen number density, σ_{ij} is the collisional cross section, υ_o is defined via the threshold kinetic energy $(1/2 m v_0^2)$, and $f(\upsilon)$ is the Maxwell-Boltzmann velocity distribution. This function describes the number of gas particles per unit volume having speeds between υ and $\upsilon + \mathrm{d}\upsilon$ by

$$f(\upsilon) = \left(\frac{m}{2\pi k T_{\mathrm{K}}}\right)^{3/2} e^{-m\upsilon^2/2\,k\,T_{\mathrm{K}}}\, 4\pi\upsilon^2\, \mathrm{d}\upsilon \ , \tag{A.23}$$

where k is the Boltzmann constant, m is the particle mass, and T_{K} is the kinetic temperature of the species.

A.1.5 Photon creation, destruction, scattering and conversion

We have the following different kinds of interaction between discrete energy states:

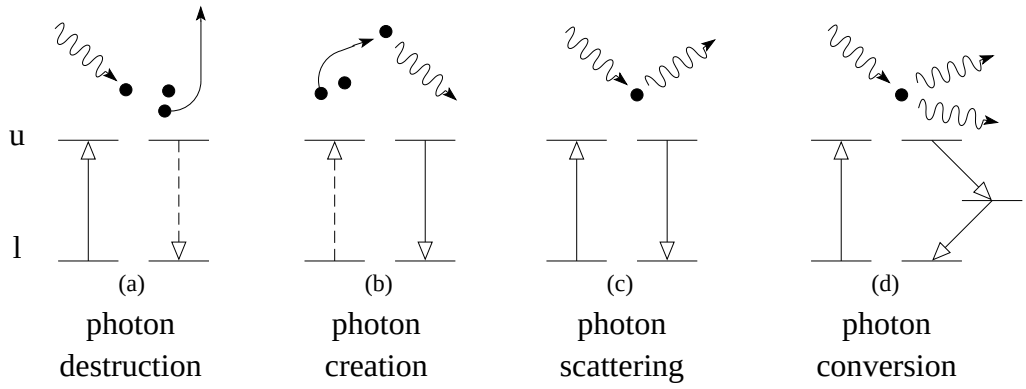

Figure A.3: An illustration of transitions between two states by different processes, which create, destroy, scatter or convert photons. Credit: Kaj Silander

- If a radiative excitation is followed by a collisional de-excitation, a photon will be destroyed. Radiation will be transferred into kinetic energy of the gas, which will *heat*. This is shown in Fig. A.3(a).

- If collisional excitation is followed by a radiative de-excitation (spontaneous or induced) a photon will be created, Fig. A.3(b). When this happens the kinetic energy in the colliding species will be transferred to radiation. Via this process the gas is able to *cool* if the optical depth is low and the created photon is able to escape from the cloud.
- When radiative excitation is followed by radiative de-excitation the photon will change direction and the radiation will be re-distributed, Fig. A.3(c). In elastic, resonant scattering (Rayleigh or Thomson scattering) the frequency is maintained, and this is the process by which the CMB radiation scatters off the primordial molecules (see paper IV). This is not the case in inelastic scattering, such as Compton or inverse Compton scattering, where the frequency will be altered. In the special case of stimulated emission, the direction, frequency and phase is preserved.
- In the last shown process in Fig. A.3(d), a species is radiatively excited, which is then followed by de-excitation in two (or several) steps. This will change the energies of an energetic photon into two or mores photons with lower frequencies and thus with lower energies. Again, the gas is able to *cool* if the cloud is optically thin and allows the created photons to escape.

In the first two processes, the local kinetic energy of the gas particles and the radiation energy in the photons are transformed into one another. If these processes are frequent, there will be strong coupling between the local radiation field and the local particle velocities, i.e. the kinetic temperature of the gas. Thus, there will be equipartition of energy and thermodynamic equilibrium (TE) or Local TE applies (see Sect.A.1.6). However, if these processes are rare the temperatures of the radiation field and the gas may not be the same (Non-LTE case). In this case the photon might have been scattered several times after its creation. Thus, the radiation we see might not tell the observer anything about the conditions from where the photons originally were emitted.

A.1.6 Types of equilibrium

- Thermodynamic Al equilibrium (TE).

  This occurs in a very optically thick medium. For *every* subprocess detailed balance holds. This means that $I_\nu = S_\nu = B_\nu$, where B_ν is the Planck function which describes the emission from a black-body

  $$B_\nu = \frac{2h\nu^3}{c^2} \frac{1}{e^{h\nu/kT} - 1} \ , \tag{A.24}$$

  where h is the Planck constant, and c is the speed of light. In TE there are no emission or absorption lines. The only emission is a thermal continuous emission as described by the Planck function.

The population of each level in TE is described by the *Boltzmann equation*, which describes the level populations, and in addition defines the *excitation temperature* $T_{\rm ex}$

$$\frac{n_{\rm u}}{n_{\rm l}} = \frac{g_{\rm u}}{g_{\rm l}}\ e^{-h\nu_{\rm ul}/kT_{\rm ex}}\ , \tag{A.25}$$

where $g_{\rm u}$ and $g_{\rm l}$ are the statistical weights of the upper and lower states, and $h\nu_{\rm ul} = E_{\rm u} - E_{\rm l}$.

To compare the number density in the upper state with the total number of particles, we may write

$$\frac{n_{\rm u}}{n_{\rm tot}} = \frac{g_{\rm u}}{Q(T)}\ e^{-E_{\rm u}/kT_{\rm ex}}\ , \tag{A.26}$$

where $Q(T)$ is the partition function which is the weighted sum of all statistical weights, g_i, from all possible states:

$$Q(T) = \sum_{i=0}^{\infty} g_i\ e^{-E_i/kT_{\rm ex}}\ . \tag{A.27}$$

The partition function depends on the excitation temperature and on molecular constants and will therefore differ between molecules. Many transitions imply a larger partition function.

The principle of detailed balance also holds for collisions, which leads to a definition of the *kinetic temperature* T_K

$$\frac{C_{\rm lu}}{C_{\rm ul}}\frac{n_{\rm u}}{n_{\rm l}} = \frac{g_{\rm u}}{g_{\rm l}} e^{-h\nu_{\rm ul}/kT_{\rm K}} \tag{A.28}$$

This relation holds generally, even without the assumption of TE.

When collisions dominate there will be strong coupling between the local radiation field and the local particle velocities. Thus, if the temperatures of the gas and radiation are in equilibrium and the same, the gas is *thermalised* and $T_{\rm rad} = T_{\rm K} = T_{\rm ex}$.

- Local thermodynamic equilibrium (LTE)

  Here, the mean free path of the particles is smaller than the scale of the temperature variations, therefore the matter will experience a *local* TE and will be in equilibrium with the ambient kinetic temperature. However, even though the radiation temperature might deviate from the kinetic temperature and can vary slowly through the medium, $T_{\rm ex} \approx T_{\rm K}$. Hence, $S_\nu = B_\nu$, but $I_\nu \neq B_\nu$. In this limit, emission or absorption lines may arise.

  The Boltzmann equation still holds in LTE since the energy-distribution of matter is maintained locally by collisions and not by radiation.

- Statistic equilibrium (SE).

  In the low density limit where collisions do not dominate, statistical equilibrium may be assumed. This implies that the radiation and the level populations are *time independent* and all upwards and downwards processes are balanced giving for a two level system:

$$\frac{\mathrm{d}n_{\mathrm{u}}}{\mathrm{d}t} = +n_{\mathrm{u}}(A_{\mathrm{u}l} + B_{\mathrm{u}l}\overline{I}_\nu + C_{\mathrm{u}l}) - n_{\mathrm{l}}(B_{\mathrm{l}u}\overline{I}_\nu + C_{\mathrm{l}u}) \equiv 0 \ , \tag{A.29}$$

$$\frac{\mathrm{d}n_{\mathrm{l}}}{\mathrm{d}t} = -n_{\mathrm{l}}(A_{\mathrm{u}l} + B_{\mathrm{u}l}\overline{I}_\nu + C_{\mathrm{u}l}) + n_{\mathrm{l}}(B_{\mathrm{l}u}\overline{I}_\nu + C_{\mathrm{l}u}) \equiv 0 \tag{A.30}$$

  with $\overline{I}_\nu$ being the mean integrated intensity of the radiation field, and n_l and n_u the level populations in the lower and upper levels, respectively. Conservation of the number of particles implies

$$n = n_{\mathrm{u}} + n_{\mathrm{l}} \ . \tag{A.31}$$

  In the case where the radiation source may be described by a black body radiation with a temperature T, $\overline{I}_\nu$ will be given by the Planck function, Eq. A.24.

  The excitation temperature in the SE case have a somewhat more complicated expression that in LTE:

$$T_{\mathrm{ex}} = T_{\mathrm{K}} \frac{T_b\, A_{\mathrm{u}l} + T_0\, C_{\mathrm{u}l}}{T_{\mathrm{K}}\, A_{\mathrm{u}l} + T_0\, C_{\mathrm{u}l}} \ , \tag{A.32}$$

  where $T_0 = h\nu_{\mathrm{u}l}/k$, and T_b is the radiation temperature. If radiation dominates and $C_{\mathrm{u}l} \ll A_{\mathrm{u}l}$ then $T_{\mathrm{ex}} \rightarrow T_{\mathrm{b}}$. If collisions dominate, then $T_{\mathrm{ex}} \rightarrow T_{\mathrm{K}}$.

  Since the temperatures are not the same, and might also differ between transitions in the same species, this calculation must be performed for *every pair of states*.

A.1.7 Critical density

When collisions in the gas start to dominate the downward transitions and the density is able to bring T_{ex} to a mean value of T_{rad} and T_{K}, the density is referred to as the *critical density*. A commonly used first order approximation in a *two level system* is

$$n_{\mathrm{crit}} = \frac{A_{ul}}{C_{ul}} \left(1 + \frac{1}{e^{\,h\nu/kT} - 1}\right) \approx \frac{A_{ul}}{C_{ul}} \ . \tag{A.33}$$

The last approximation holds if $h\nu \gg kT_{\mathrm{ex}}$ and is widely used as a first approximation of n_{crit}. A lower limit to the density required to produce observable emission may be estimated by

$$n_{\mathrm{min}} \gtrsim 10^{11} \frac{A_{\mathrm{u}l}}{\sqrt{T_{\mathrm{K}}}} \quad [\mathrm{cm}^{-3}] \tag{A.34}$$

where we have used a mean velocity of the gas particles $<v> \approx 10^4 \sqrt{T_{\rm K}}$ [cm s^{-1}], a cross-section approximated by the dimensions of a molecule, $\sigma \sim 10^{-15}$ cm^{-2}, and $C_{\rm ul} \approx n\sigma <v>$. This value must be multiplied by $T_{\rm K}/T_0$ for the excitation temperature to be at half the value of the kinetic temperature. For better estimates of the critical densities, collisional coefficients found in databases can be used.

In the *multi-level system* the critical density will often be reduced since there are usually more collisional transitions than radiative ones. This is due to the selection rules that only allow specific radiative transitions. For instance, in the second most common molecule CO, the radiative transition rules must obey $\Delta J = \pm 1$, but collisional transition are allowed between all J-levels. The situation may also be the reverse when molecules are affected by strong radiation fields and cause the critical density to increase.

When $\tau_{\rm ul} \gg 1$, the radiation in that line is trapped within the cloud. This is known as *local photon trapping* and may have substantial impact on the critical density

$$n_{\rm crit} \approx \frac{A_{\rm ul}}{C_{ul}\,\tau_{\rm ul}} \ . \tag{A.35}$$

The water transition observed by Odin often has a very high opacity. In Orion KL the opacity is estimated to about 1 800 (see paper II), thereby reducing the critical density by three orders of magnitude.

A.1.8 Self-absorption

The water and CO transitions observed by Odin in paper I – III have asymmetric line shapes, which are caused by self-absorption. This happens when lower excitation foreground gas absorbs emission from higher excitation gas deeper in the cloud. Self-absorption is most often recognised by observations and comparisons with optically thin isotopologues, which do not display any self-absorption. This is shown in paper III by comparing the line profiles of CO and ^{13}CO.

A.2 Radioastronomy

In the radio spectral region $h\nu \ll kT_{\rm ex}$ allowing Eq. A.24 to be approximated by the *Rayleigh-Jeans law*

$$B_\nu(T) = \frac{2\nu^2}{c^2} kT \ . \tag{A.36}$$

The *radiation temperature* $J(T)$ is defined as

$$J(T) = \frac{h\nu}{k} \frac{1}{e^{h\nu/kT} - 1} \approx T \ . \tag{A.37}$$

where the approximation is valid only if $h\nu \ll kT_{ex}$. For a temperature of 20 K, and a frequency of 557 GHz, the radiation temperature will be about 10 K. For the low CMB temperature of 2.7 K the difference will be even larger with $J(T) = 1$ mK.

The most important property of the Rayleigh-Jeans law is the proportionality of the temperature and the radiation. This useful when the radiation from an extended source is measured by its *brightness temperature*

$$T_b = \frac{c^2}{2k\nu^2} B_\nu \ . \tag{A.38}$$

This temperature corresponds to a brightness inserted into Rayleigh-Jeans law.

If this is applied to the equation of radiative transfer, Eq. A.14, and assuming that an isothermal source fills the beam we will get:

$$T_b = T_b(0)\ e^{-\tau_\nu} + T_{ex}(1 - e^{-\tau_\nu}). \tag{A.39}$$

With no background radiation and for an optically thin transition (A.39) simplifies to

$$T_b = T_{ex}\, \tau_\nu \tag{A.40}$$

In case of an optically thick transition (A.39) we will have

$$T_b = T_{ex} \tag{A.41}$$

Most often the source does not fill the beam and then the received radiation is lowered by the beam-filling factor:

$$\eta_{bf} = \frac{\theta_s^2}{\theta_s^2 + \theta_{mb}^2}, \tag{A.42}$$

where θ_s is the size source (FWHM) and θ_{mb} the FWHM beam size, assuming that both the source brightness distribution and the antenna response are circularly symmetric and Gaussian. An additional factor which we have to take into account is the main beam efficiency η_{mb}, which may be as low as 0.4. The Odin satellite has a very high beam-efficiency of 0.9.

The emission measured at the antenna is called the antenna temperature:

$$T_A = T_b\, \eta_{bf}\, \eta_{mb} = J(T_{ex})\, (1 - e^{-\tau})\, \eta_{bf}\, \eta_{mb}. \tag{A.43}$$

A.2.1 Column densities

Two properties of the gas are especially interesting: the temperature and column density, which is defined as

$$N = \int_0^s n\, \mathrm{d}s' \tag{A.44}$$

in units of [cm^{-2}]. If we know the geometry of the source, or assume a homogeneous spherical cloud, the density can be calculated. Note, that if the cloud is clumpy the estimated density will a mean value of the density of the clumps and the inter-clump gas.

The column density can be obtained by different methods. With observations of a single line, either LTE is assumed and then N can be calculated directly if we know the excitation temperature. We can also use a statistical equilibrium model. If a number of transitions are observed with a wide range of energy levels, the rotation diagram method, described in paper II, is an effective way to obtain both the column density and the excitation temperature at the same time.

The resulting formula for the column density is found by expressing the absorption coefficient in terms of the Einstein coefficients

$$\kappa_\nu = \frac{h\nu}{4\pi}(n_\mathrm{l}\, B_{\mathrm{l}u} - n_\mathrm{u}\, B_{\mathrm{u}l})\, \phi(\nu)\ , \tag{A.45}$$

where the normalised line profile $\phi(\nu)$ with a line width (FWHM) of $\Delta\nu$ is

$$\phi(\nu) = \frac{\sqrt{4\ln 2}}{\Delta\nu\sqrt{\pi}} e^{-4\ln 2\left(\frac{\nu}{\Delta\nu}\right)^2}\ . \tag{A.46}$$

Using (A.21) and (A.25), the optical depth of a transition from an upper state, u, to a lower state, l, may be written as

$$\begin{aligned} d\tau_\nu = \kappa_\nu\, \mathrm{d}s &= \frac{h\nu_{\mathrm{u}l}}{4\,\pi}\,(n_\mathrm{l}\, B_{\mathrm{l}u} - n_\mathrm{u}\, B_{\mathrm{u}l})\ \phi_\nu\, \mathrm{d}s \\ &= \frac{h\nu_{\mathrm{u}l}}{4\pi}\left(n_\mathrm{l}\frac{g_\mathrm{u}}{g_\mathrm{l}}\, B_{\mathrm{u}l} - n_\mathrm{u}\, B_{\mathrm{u}l}\right)\ \phi_\nu\, \mathrm{d}s \\ &= \frac{h\nu_{\mathrm{u}l}}{4\pi}\left(\frac{n_\mathrm{u}}{n_\mathrm{l}}\, n_\mathrm{l} e^{\,h\nu_{\mathrm{u}l}/kT_\mathrm{ex}} - n_\mathrm{u}\right)\frac{c^2}{2h\nu_{\mathrm{u}l}^3}\, A_{\mathrm{u}l}\, \phi_\nu\, \mathrm{d}s \\ &= \frac{c^2}{8\pi\nu_{\mathrm{u}l}^2}\, A_{\mathrm{u}l}\, n_\mathrm{u}(e^{\,h\nu_{\mathrm{u}l}/kT_\mathrm{ex}} - 1)\ \phi_\nu\, \mathrm{d}s\ . \end{aligned} \tag{A.47}$$

After integrating this along the line of sight we obtain

$$\tau_\nu = \frac{c^2}{8\pi\nu_{\mathrm{u}l}^2} A_{\mathrm{u}l} N_\mathrm{u}\left(e^{\,h\nu_{\mathrm{u}l}/kT_\mathrm{ex}} - 1\right)\ \phi_\nu\ . \tag{A.48}$$

Integrating over an assumed Gaussian line profile, using the Boltzmann equation Eq. A.25 for a relation between N_u and N_tot, and re-scaling from frequencies to equivalent Doppler velocities via the substitution $d\nu = \nu/c\ d\upsilon$, we get

$$\tau_\mathrm{max} = \sqrt{\frac{\ln\,2}{16\,\pi^3}}\frac{c^3}{\nu_{\mathrm{u}l}^3\,\Delta\upsilon}\, A_{\mathrm{u}l}\, N_\mathrm{tot}\, \frac{g_\mathrm{u}}{Q(T)}\, e^{-E_\mathrm{u}/kT_\mathrm{ex}}\left(e^{\,h\nu_{\mathrm{u}l}/kT_\mathrm{ex}} - 1\right)\ . \tag{A.49}$$

With the assumption of optically thin emission, neglecting the background radiation, and assuming that the source fills the antenna main beam, the beam averaged upper state column density can be obtained from Eq. A.48

$$N_{\rm u} = \frac{8\pi k\nu_{\rm ul}^2}{hc^3}\frac{1}{A_{\rm ul}}\int T_{\rm b}\,{\rm d}\upsilon\ . \tag{A.50}$$

The total column density of each species can then be found if we assume LTE, where all the excitation temperatures for all the energy levels are the same. The molecular population of each level is then given by the Boltzmann equation and assuming optically thin emission, the beam-averaged total column density becomes

$$N_{\rm tot}^{\rm thin} = \frac{8\pi k\nu_{\rm ul}^2}{hc^3}\frac{1}{A_{\rm ul}}\frac{Q(T)}{g_{\rm u}}e^{E_{\rm u}/kT_{\rm ex}}\int T_{\rm b}\,{\rm d}\upsilon\ . \tag{A.51}$$

If the transition is optically thick the derived total column density will be too low and needs an optical depth correction factor C_τ, which will be one or larger

$$C_\tau = \frac{\tau}{1-e^{-\tau}}\ . \tag{A.52}$$

In the case where the source do not fill the beam the beam-filling correction factor from Eq. A.42 also has to be taken into account. With corrections for optical depth and beam-filling the *true total source averaged column density* will be

$$N_{\rm tot} = \frac{C_\tau}{\eta_{\rm bf}}\,\frac{8\pi k\nu_{\rm ul}^2}{hc^3}\frac{1}{A_{\rm ul}}\frac{Q(T)}{g_{\rm u}}e^{E_{\rm u}/kT_{\rm ex}}\int T_{\rm mb}\,d\upsilon = \frac{C_\tau}{\eta_{\rm bf}}\,N_{\rm tot}^{\rm thin}\ . \tag{A.53}$$

A.2.2 Rotational diagram

If we want to calculate the total column density of a molecule we can use Eq. A.51 or A.53 as shown in previous section. However, this requires knowledge about the excitation temperature which often is unknown. A better way to establish the temperature is to use the rotational diagram method. If many transitions of the same species are observed, having a wide range of upper state energies, and assuming that only one temperature characterises all the transitions (i.e. the populations are then in LTE), the excitation temperature can be calculated.

Taking the logarithm of the Boltzmann equation, Eq. A.25, we obtain

$$\ln\frac{N_{\rm u}}{g_{\rm u}} = \ln\frac{N_{\rm tot}}{Q(T)} - \frac{E_{\rm u}}{kT_{\rm ex}}. \tag{A.54}$$

The left hand side in this equation is identical to the logarithm of Eq. A.50 divided by the statistical weight $g_{\rm u}$. We can plot this quantity as a function of the upper state energy $E_{\rm u}$ in a semi-log plot. A least squares fit to the data will then produce

a straight line with slope $-1/T_{\rm rot}$. If we extrapolate the line to $E_{\rm u} = 0\,{\rm K}$, we obtain the total column density from the intersection of the y-axis, y_0 and

$$N_{\rm tot} = Q(T)\, e^{\,y_0}. \tag{A.55}$$

The importance of a correctly calculated partition function is obvious. Beam-filling and opacity corrections may also be included if necessary in the same way as in Eq. A.53.

There are uncertainties attached to this method, not only from beam-filling and opacity, but also the possibility that the population distribution may not be characterised by a single rotational temperature. The temperature can vary due to density, excitation gradients along the line-of-sight, IR flux, sub-thermal excitation etc. See appendix in paper II for more details.

Bibliography

[1] Abel, T., Bryan, G.L., Norman, M.L. *The Formation of the First Star in the Universe*, 2002, Science, vol 295, 93

[2] Bally, J., Reipurth, B., Walawender, J. & Armond, T. *The Fountains of Youth: Irradiated Breakout of Outflows in S140*, 2002, AJ, 124, 2152

[3] Belloche, A., Menten, K. M., Comito, C., Müller, H.S.P., Schilke, P., et al. *Detection of amino acetonitrile in Sgr B2(N)*, 2008, A&A, 482, 179

[4] Bennet, J., & Shostak, S. *Life in the Universe*, 2007, 2nd ed., Pearson Education, Inc, San Fransisco

[5] Bergin, E.A., Melnick, G.J. & Neufeld, D.A. *The postshock chemical lifetimes of outflow tracers and possible new mechanism to produce water ice mantles*, 1998, ApJ, 499, 777

[6] Blake, D.F. & Jenniskens, P. *The Ice of Life*, 2001 Scientific American, Aug, 37

[7] Boogert, A.C.A. & Ehrenfreund, P. *Interstellar Ices*, 2004, Astronomical Society of the Pacific Conference Series, Witt, A.N., Clayton, G.C. & Draine, B.T. (Eds.), Vol. 309, 547

[8] Bromm, V. & Larson, R.B. *The First Stars*, 2004, ARA&A, 42, 79

[9] Cernicharo, J. & Crovisier, J. *Water in Space: The Water World of ISO*, 2005, SSRv, 119, 29

[10] Cheung, A.C., Rank, D.M., Townes, C.H., Thornton, D.D. & Welch, W.J. *Detection of NH_3 molecules in the interstellar medium by their microwave emission*, 1968, Phys Rev Letters, 21, 1701

[11] Cheung, A.C., Rank, D.M., Townes, C.H., Thornton, D.D. & Welch, W.J. *Detection of Water in Interstellar Regions by its Microwave Radiation*, 1969, Nature, Vol. 221, 626

[12] Choudhury, T.R. & Ferrara, A. *Updating reionization scenarios after recent data*, 2006, MNRAS, 371, L55

[13] de Bernardis, P., Dubrovich, V., Encrenaz, P., Maoli, R., Masi, S., et al. *Search for LiH lines at high redshift*, 1993, A&A, 269, 1

[14] Doty, S.D., van Dishoeck, E.F., van der Tak, F.F.S. & Boonman, A.M.S. *Chemistry as a probe of the structures and evolution of massive star-forming regions*, 2002, A&A, 389, 446

[15] Dubrovich, V. *Molecules of cosmological origin*, 1977 SvAL, 3, 128

[16] Duquennoy, A. & Mayor, M. *Multiplicity among solar-type stars in the solar neighbourhood. II - Distribution of the orbital elements in an unbiased sample*, 1991, A&A, 248, 485

[17] Ehrenfreund, P. & Charnley, S.B. *Organic Molecules in the Interstellar Medium, comets, and meterorites*, 2000, ARA&A, 38, 427

[18] Encrenaz, T. *Water in the Solar System*, 2008, ARA&A, 46, 57

[19] Evans II, N.J. *Physical Conditions in Regions of Star Formation*, 1999, ARA&A, 37, 311

[20] Fixsen, D.J., Cheng, E.S., Gales, J.M., Mather, J.C., Shafer, R.A. & Wright, E.L. *The Cosmic Microwave Background Spectrum from the Full COBE FIRAS Data Set*, 1996, ApJ, 473, 576

[21] Genzel, R. & Stutzki, J. *The Orion Molecular Cloud and Star-forming region*, 1989, ARA&A, 27, 41

[22] Gibb, E.L, Whittet, D.C.B., Boogert, A.C.A. & Tielens, A.G.G.M. *Interstellar Ice: The Infrared Space Observatory Legacy*, 2004, ApJS, 151, 35

[23] Glover, S. *The formation of the first stars in the universe*, 2005, SSRv, 117, 445

[24] Goldsmith, P.F. & Langer, W.D. *Molecular cooling and thermal balance of dense interstellar clouds*, 1978, ApJ, 222, 881

[25] Grevesse, N., Noels, A. & Sauval, A.J. *Standard abundances*, 1996, ASP Conference Series, Holt, S.S., & Sonneborn, G. (Eds.), Vol. 99, 1996

[26] Hartquist, T.W. (Ed.) *Molecular Astrophysics*, 1990, Cambridge University Press

[27] Hartquist, T.W. & Williams, D.A. *The chemically controlled cosmos*, 1995, Cambridge University Press

[28] Hartquist, T.W. & Williams, D.A. *The molecular astrophysics of stars and galaxies*, 1998, Oxford University Press

[29] Hjalmarson, Å., Bergman, P., Biver, N., Florn, H.-G., Frisk, U., et al. *Recent astronomy highlights from the Odin satellite*, 2005, AdSpR, 36, 1031

[30] Hjalmarson, Å., Olberg, M., Florén, H.-G. et al. *On the progress in Odin's hunt for molecules*, 2007, AdSpR, 40, 630

[31] Hollenbach, D.J. & Thronson, Jr., H.A. (Eds.) *Interstellar Processes*, 1987, Reidel Publishing Company

[32] Komatsu, E., Dunkley, J., Nolta, M.R., Bennett, C.L., Gold, B. *Five-Year Wilkinson Microwave Anisotropy Probe (WMAP) Observations: Cosmological Interpretation*, 2008, arXiv:0803.0547

[33] Larsson, B., Liseau, R., Pagani, L., Bergman, P., Bernath, P., et al. *Odin Detection of O_2*, 2007, A&A, 466, 999

[34] Lepp, S., Stancil, P.C. & Dalgarno A. *Atomic and molecular processes in the early Universe*, 2002, JPhB, 35, 57

[35] Levy, E.H., & Lunine, J.I. (Eds.) *Protostars and Planets III*, 1991, University of Arizona Press

[36] Lis, D.C., Blake, G.A. & Herbst, E. (Eds.) *Astrochemistry: Recent Successes and Current Challenges*, 2005, Proc. IAU Symposium 231, Cambridge University Press

[37] Loeb, A. *Let there be Light: the Emergence of Structure out of the Dark Ages in the Early Universe*, 2008, arXiv:0804.2258v1

[38] Longair, M.S. *Galaxy formation*, 2008, Springer Verlag

[39] Mannings, V., Boss, A.P. & Russell, S.S. (Eds.) *Protostars and Planets IV*, 2000, Tucson: University of Arizona Press

[40] Maoli, R., Melchiorri, F. & Tosti, D. *Molecules in the postrecombination universe and microwave background anisotropies*, 1994, ApJ, 425, 372

[41] Maoli, R., Ferrucci, V., Melchiorri, F., Signore M. & Tosti, D. *Molecular signals from priomordial clouds at high redshift*, 1996, ApJ, 457, 1

[42] Melnick, G.J., Stauffer,J.R., Ashby,M.L.N., Bergin, E.A., Chin, G., et al. *The Submillimeter Wave Astronomy Satellite: Science Objectives and Instrument Description*, 2000, ApJ, 539, L77

[43] Melnick, G.J. & Bergin, E.A. *The legacy of SWAS: Water and molecular oxygen in the interstellar medium*, 2005, Adv. in Space Research, 36, 1027

[44] Müller, H.S.P., Thorwirth, S., Roth, D.A. & Winnewisser, G. *The Cologne Database for Molecular Spectroscopy, CDMS*, 2001, A&A, 370, L49

[45] Müller, H.S.P., , Schlöder, F., Stutzki, J. & Winnewisser, G. *The Cologne Database for Molecular Spectroscopy, CDMS: a useful tool for astronomers and spectroscopists*, 2005, J. Mol. Struct. 742, 215

[46] Neufeld, D.A., Lepp, S. & Melnick, G.J. *Thermal balance in dense molecular clouds: Radiative cooling rate and emission-line luminosities*, 1995, ApJ, 100, 132

[47] Nordh, H.L., von Schéele, F., Frisk, U., Ahola, K., Booth, R.S., et al. *The Odin orbital observatory*, 2003, A&A, 402, L21

[48] Poelman, D.R., Spaans, M. & Tielens, A.G.G.M. *The interpretation of water emission from dense interstellar clouds*, 2007, A&A, 464, 1023

[49] Pickett, H.M., Poynter, R.L., Cohen, E.A., Delitsky, M.L., JPearson, J.C. & Muller, H.S.P. *Submillimeter, and Microwave Spectral Line Catalog*, 1998, J.Quant.Spectrosc. & Rad.Transfer, 60, 883

[50] Puy, D. & Signore, M. *Primordial chemistry from molecules to secondary cosmic microwave background anisotropies*, 2007, New Astron. Review, 51, 411

[51] Rohlfs, K., & Wilson, T.L. (Eds.) *Tools of Radio Astronomy*, 2004, Springer Verlag

[52] Rutten, R.J. *The Generation and Transport of Radiation*, 1991, 4th ed., compiled in March 1995 by Dan Kiselman

[53] Rydbeck, O. & Hjalmarson, Å. *Radio observations of Interstellar Molecules, of their behaviour, and of their physics*, 1985, Ed. Diercksen et al., Molecular Astrophysics, Reidel Publishing company, p 45-175

[54] Snell, R.L., Howe, J.E., Ashby, M.L.N., Bergin, E.A., Chin, G., et al. *Submillimeter Wave Astronomy Satellite observations of extended water emission in Orion*, 2000, ApJ, 539, L93

[55] Snell, R.L., Hollenbach, D., Howe, J.E., Neufeld, D.A., Kaufman, M.J., et al. *Detection of water in the shocked gas associated with IC 443: constraints on shock models*, 2005, ApJ, 620, 758

[56] Schöier, F.L., van der Tak, F.F.S., van Dishoeck E.F. & Black, J.H., *An atomic and molecular database for analysis of submillimetre line observation*, 2005, A&A, 432, 369

[57] Signore, M., Melchiorri, F., Olivo-Melchiorri, B. & Puy, D. *Molecular echography of the Early Universe*, 2006, Proceedings of a meeting for Pierre Encrenaz: Hunt for Molecules, Eds. Combes, F., Casoli, F., Falgarone, E., and Pagani, L., Observatoire de Paris , 197.

[58] Spergel, D.N., Bean, R., Dore, O., Nolta, M.R., Bennett, C.L., et al. *Wilkinson Microwave Anisotropy Probe (WMAP) Three Year Results: Implications for Cosmology*, 2006, astro-ph/0603449

[59] Stahler, S.W. & Palla, F. *The Formation of Stars*, 2004, WILEY-VCH Verlag GmbH & Co.KGaA, Weinheim, Germany

[60] Steigman, G. *Primordial Nucleosynthesis in the Precision Cosmology Era*, 2007, Annu.Rev.Nucl. Par.Sci. 57, 463

[61] Tielens, A.G.G.M., *The Physics and Chemistry of the Interstellar Medium*, 2005 Cambridge University Press

[62] van Dishoeck, E.F., Blake, G.A., Draine, B.T. & Lunine, J.I. *The chemical evolution of protostellar and protoplanetary matter*, 1993, in Protostars and Planets III, Levy, E.H., and Lunine, J.I., (Eds.), University of Arizona Press, 163

[63] Wirström, E.S., Bergman, P., A.O.H. Olofsson, et al. *Odin CO and* ^{13}CO *$J = 5-4$ mapping of Orion KL – a step towards accurate water abundances*, 2006, A&A, 453, 979

A.3 Some useful databases:

- The SAO/NASA Astrophysics Data System:
  `http://www.adsabs.harvard.edu/`
- The Cologne Database for Molecular Spectroscopy:
  `http://www.cdms.de`
- The Jet Propulsion Laboratory:
  `http://spec.jpl.nasa.gov/`
- Leiden Atomic and Molecular Database:
  `http://www.strw.leidenuniv.nl/~moldata/`
- The UMIST database for astrochemistry:
  `http://www.udfa.net/`

- Dave Woon's Astrochymist web page:
  `http://www.astrochymist.org/`
- Interstellar and circumstellar molecules:
  `http://www.cv.nrao.edu/~awootten/allmols.html`

A.4 On-line computer program

- `RADEX`: A computer program for performing statistical equilibrium calculations
  `http://www.strw.leidenuniv.nl/~moldata/radex.html`